MAX-PLANCK-INSTITUT FÜR RADIOASTRONOMIE
BONN

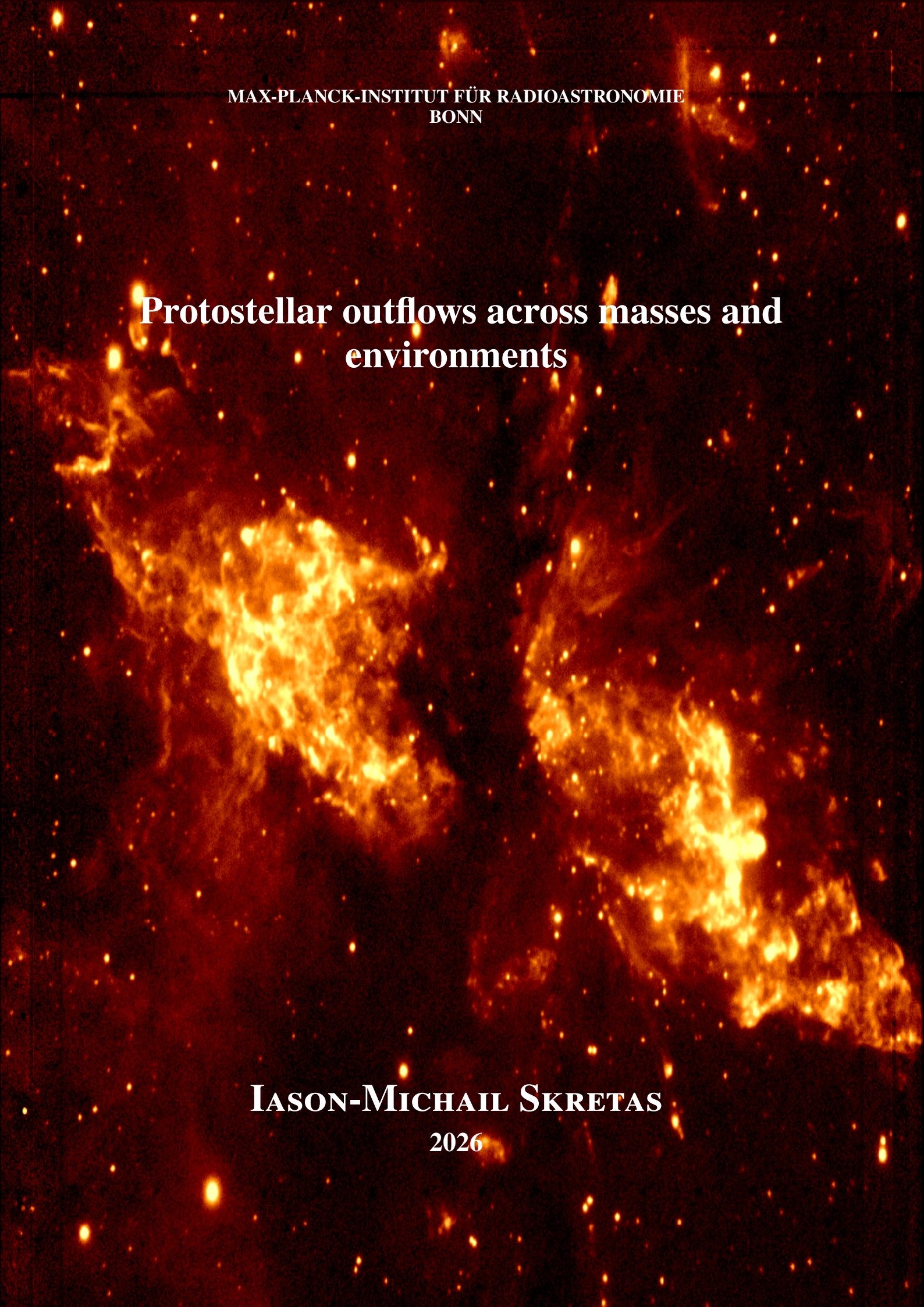

# Protostellar outflows across masses and environments

Iason-Michail Skretas

2026

# Protostellar outflows across masses and environments

Dissertation
zur
Erlangung des Doktorgrades (Dr. rer. nat.)
der
Mathematisch-Naturwissenschaftlichen Fakultät
der
Rheinischen Friedrich-Wilhelms-Universität Bonn

vorgelegt von
Iason-Michail Skretas
aus
Athens, Greece

Bonn, 17.12.2025

Angefertigt mit Genehmigung der Mathematisch-Naturwissenschaftlichen Fakultät der
Rheinischen Friedrich-Wilhelms-Universität Bonn

| | |
|---|---|
| Gutachter/Betreuer: | Prof. Dr. Peter Schilke |
| Gutachter: | Prof. Dr. Pavel Kroupa |
| Tag der Promotion: | 16.04.2026 |
| Erscheinungsjahr: | 2026 |

**RHEINISCHE FRIEDRICH–WILHELMS–UNIVERSITÄT BONN**

# *Abstract*

by Iason-Michail Skretas

for the degree of

*Doctor rerum naturalium*

Protostellar outflows mark one of the earliest, and most prominent signs of star formation, and have been detected in both low- and high-mass sources. Protostellar outflows are considered a key part of the process due to their ability to remove excess angular momentum from the protostar-disk system, which enables the accretion of material. They are typically observed via molecular transitions at radio wavelengths, but are also bright in shock excited transitions in the IR regime. Due to their close connection to the accretion process, understanding protostellar outflows is crucial in order to fully describe the formation of stars. Throughout this thesis, I aimed to investigate protostellar outflows in both the mm and IR regime, in order to investigate several of the open questions regarding their nature. A particular focus is placed on the impact of the large-scale environment onto the outflows, since this holds the potential to reveal whether the star formation process is influenced by its surroundings. In this work, I used observations from the NOEMA and IRAM 30m telescopes, as well as, observations from the JWST MIRI/MRS instrument.

In the first part of this thesis, I investigated the exceptional outflow of DR21 Main, which has been proposed to form part of a new type of protostellar outflows, known as explosive outflows. The extended bandwidth of the CASCADE observations enabled me to study this unique outflow at multiple different molecular transitions, and determine its morphological, kinematic, and energetic properties. Through comparisons with other explosive outflow candidates I aim to constrain the nature of the DR21 Main outflow thus placing further constraints in this different kind of protostellar outflows. The analysis revealed that the DR21 Main outflow, as seen in $HCO^+$ $J = 1 - 0$ is more akin a bipolar outflows than an explosive outflow. It's confirmed particularly high mass and energetic properties though still class it as one of the most extreme outflow cases known.

Subsequently, I studied the outflow activity along the entire DR21 filament, one of the most active, high-mass star-forming regions in the Galaxy. Using the $HCO^+$ $J = 1 - 0$, $H^{13}CO^+$ $J = 1 - 0$, and SiO $J = 2 - 1$ observations of the region, taken as part of the CASCADE project, I aimed to identify all protostellar outflows associated with dense molecular clumps along the DR21 ridge and estimate their physical and energetic properties. By comparing the properties of such a sample with the established correlations between outflow and source properties allowed me to investigate whether the extreme nature of the DR21 filament has any impact onto the outflows, and by extension the formation, of its sources. The results showed no clear connection between environment and outflow activity, with the sources in DR21 being indistinguishable to those of an extended literature sample. Notable exception is the location of the most prominent outflow

sources at the intersections of filaments.

In the final part of the thesis, I take advantage of the unique capabilities of the JWST, to investigate the inner workings of protostellar outflows. Namely, I study the shock excited transitions of $H_2$ along with various atomic and ionic transitions available in the MIRI range for a sample of 5 low-mass protostars in Ophiuchus. My aim with this analysis is to investigate the origin of this shock excitation, through comparisons of the observations with UV irradiated shock models. The analysis revealed the significant contribution of UV emission within these outflows. I found that the origin of this UV emission has to been from within the protostellar outflows themselves, and not from the external environment.

In this thesis, I analyzed outflows from sources across the entire mass regime, using observations in both the mm and IR regime. Throughout the multiple individual results of each project, my analysis showed that the properties of the large scale environment surrounding a forming protostar have little to no influence on the properties of its protostellar outflow. It becomes therefore apparent that the star formation process is primarily dictated from small scale processes, taking place within the star forming cores, and not impacted by the more extended environment.

*To my family*

# List of Publications

The following list indicates the relevant first-author publications that are discussed and presented in this thesis.

1. "**The Cygnus Allscale Survey of Chemistry and Dynamical Environments: CASCADE. II. A detailed kinematic analysis of the DR21 Main outflow**"
   I. M. Skretas, A. Karska, F. Wyrowski, K. M. Menten, H. Beuther, A. Ginsburg, A. Hernández-Gómez, C. Gieser, S. Li, W.-J. Kim, D. A. Semenov, L. Bouscasse, I. B. Christensen, J. M. Winters A. Hacar
   Astronomy & Astrophysics, Volume 679, id.A66. DOI: 10.1051/0004-6361/202346825

   *Author contributions: IMS performed the scientific analysis and wrote the manuscript with the supervision from AK and comments from co-authors. IMS also performed the central part of the imaging of the spectral line data used in this work. The remaining data reduction and calibration was done by HB.*

2. "**UV-irradiated outflows from low-mass protostars in Ophiuchus with JWST/MIRI**"

   I. M. Skretas, A. Karska, L. Francis, W. R. M. Rocha, M. L. van Gelder, Ł. Tychoniec, M. Figueira, M. Sewiło, F. Wyrowski, and P. Schilke
   Astronomy & Astrophysics, Volume 703, id.A139. DOI: 10.1051/0004-6361/202554977
   *Author contributions: IMS performed the scientific analysis and wrote the manuscript with the supervision of AK and comments from co-authors. The data reduction and some of the scripts used in the analysis were prepared by the co-authors LF, WRMR, MLG, and LT. The figure of the UV field in Ophiuchus was provided by MF.*

# Contents


**1 Introduction** **1**

1.1 Star formation . . . 2
1.1.1 Low-mass star formation . . . 2
1.1.2 High-mass star formation . . . 6
1.2 Emission from molecules . . . 10
1.2.1 The $H_2$ and CO molecules . . . 12
1.3 Protostellar outflows . . . 13
1.3.1 Outflow formation and launching scenarios . . . 14
1.3.2 Theoretical structure of protostellar outflows . . . 15
1.3.3 Outflows in the millimeter regime - entrained outflows . . . 17
1.3.4 Outflows in the IR regime - shock excited molecular winds and ionic jets 22
1.3.5 Explosive outflows . . . 26
1.4 Outflow shocks . . . 28
1.5 Star forming regions . . . 29
1.5.1 Cygnus-X . . . 29
1.5.2 Ophiuchus . . . 31
1.6 Scientific goals and outline of this thesis . . . 32

**2 CASCADE: A detailed kinematic analysis of the DR21 Main outflow** **35**

2.1 Context . . . 35
2.2 Aims . . . 36
2.3 Methods . . . 36
2.4 Results . . . 37
2.5 Conclusions . . . 40

**3 CASCADE: Overview of the molecular outflows along the DR21 ridge** **41**

3.1 Introduction . . . 41
3.2 Observations and data analysis . . . 43
3.2.1 Continuum observations . . . 44
3.2.2 Dense molecular clumps in the CASCADE field . . . 45
3.3 Results . . . 48
3.3.1 Core-averaged spectra . . . 48
3.3.2 $HCO^+$ outflow maps . . . 48
3.3.3 Outflow properties . . . 55

3.4 Discussion . . . 60
3.4.1 Correlation of outflow and source properties . . . 60
3.4.2 Distribution of outflow sources along the ridge . . . 64
3.4.3 Comparison of CO and $HCO^+$ outflows . . . 69
3.5 Summary and Conclusions . . . 70

**4 UV-irradiated outflows from low-mass protostars in Ophiuchus with JWST/MIRI 73**
4.1 Context . . . 73
4.2 Aims . . . 74
4.3 Methods . . . 74
4.4 Results . . . 75
4.5 Conclusions . . . 78

**5 Summary and outlook 79**
5.1 Summary . . . 79
5.2 Outlook and future steps . . . 82

**Bibliography 87**

**A CASCADE: Overview of the molecular outflows along the DR21 ridge 101**
A.1 Spectra . . . 101
A.2 Additional Contour maps . . . 106
A.3 Outflow properties correlation fits . . . 108

**B The Cygnus Allscale Survey of Chemistry and Dynamical Environments: CASCADE. II. A detailed kinematic analysis of the DR21 Main outflow 111**

**C UV-irradiated outflows from low-mass protostars in Ophiuchus with JWST/MIRI 133**

**List of Figures 157**

**List of Tables 163**

**Acknowledgements 165**

CHAPTER 1

# Introduction

Ever since humans first laid eyes upon the night sky, stars have been the cause of great admiration and curiosity. From their initial connection to various religious rites, to their use as reliable navigation tools that first enabled long distance sea travel, stars have been an integral part of the development of human civilization. Since then, our understanding of stars has improved by leaps and bounds. While Copernicus (1543) paved the way for our comprehension of the Cosmos with the establishment of the heliocentric system, it was with Giordiano Bruno's (1584) hypothesis, that stars are in reality distant suns, that the first major step in our understanding of stars was made. Tycho Brahe (1572) and later Kepler (1604) discovered what was then named "new stars", suggesting for the first time that the night sky is not immutable. Even though these "new star" were later found to actually be supernovae, this discovery eventually led to the concept of stars as "living" things which are born, evolve and eventually die.

The next big advancements in our understanding of stars came in the late 19th and 20th centuries. Initially, the advent of stellar spectroscopy enabled Cecilia Payne-Gaposchkin (1925) to establish that stars are comprised mainly of hydrogen and helium. This was followed by the construction of the Hertzsprung-Russell diagram that set up the discovery of the main sequence and forms the basis of stellar evolution. The continuous improvement of observational tools has since not only led to a much more detailed system of stellar classification, but also to a much better understanding of the internal processes powering the stars and how they connect to the different phases of stellar evolution. Still, despite our much improved knowledge surounding the composition and evolution of stars, the matter of their birth remains highly debated.

In the following sections, I provide the necessary background information relevant to the contents of this thesis. I begin with discussing the current understanding of the process of star formation for both low- and high-mass stars in Section 1.1. Subsequently, in Section 1.3, I focus on the protostellar outflows that are launched at the earlier stages of star formation, highlight both theoretical predictions as well as observational evidence of their significance, and briefly introduce the peculiar case of the explosive outflows . Next, in Section 1.4, I discuss the outflow shocks, and the role they play within the outflows of protostars, followed by some essential background on the star-forming regions which form the focus of this thesis, presented in Section 1.5. Finally, in Section 1.6 I present the goals and an outline of this thesis.

## 1.1 Star formation

Star formation takes place in the densest and coldest parts of the interstellar medium (ISM; the matter and radiation filling the space between stars), which are known as molecular clouds. These clouds have typical densities above $10^2$ cm$^{-3}$ and temperatures in the range from 10 to 20 K allowing them to maintain a primarily molecular composition (Klessen and Glover, 2016). Molecular clouds can vary significantly in size and overall mass, ranging from sub-parsec scales and masses of $\sim 5 - 50$ M$_\odot$ in the cases of isolated dark clouds (Bok globules; Launhardt, Nutter et al., 2010) all the way up to scales of $\sim 100$ pc and masses of $\sim 10^5$ M$_\odot$ for giant molecular cloud complexes (Ferrière, 2001). Despite their high-masses, molecular clouds only take up a very small fraction ($\sim 1\%$) of the total volume of the ISM. However, due to their unique ability of hosting star formation, they are instrumental in the life-cycle of galaxies.

Stars are typically split into two categories depending on their mass. Stars with a mass <8 M$_\odot$ are classed as low-mass sources, while stars with masses above 8 M$_\odot$ are referred to as high-mass. This mass limit corresponds approximately to the mass limit required in order for the final central mass, left behind at the end of a stars lifetime, to exceed the 1.4 M$_\odot$ Chandrasekhar limit, and eventually lead to the formation of a neutron star or a black hole (Chandrasekhar, 1931). As a result, low and high-mass stars follow different evolutionary paths, the first ending their lives as planetary nebulae and leaving behind a white dwarf, while the latter give rise to supernovae and leave behind a neutron star or even a black hole. Regardless, the process of star formation, for both high and low-mass stars, begins when parts of the molecular cloud begin to collapse, under the effect of their own gravity, forming small regions of even higher density, known as dense cores. Interestingly, it has been found that all molecular clouds, despite their vast differences in size and mass, all produce stars following a similar distribution of masses, the initial mass function (IMF; e.g., Kroupa, 2002). The shape of the IMF dictates that a significantly larger number of low-mass stars form compared to their high-mass counterparts. As a result, massive stars are much rarer, and are only found forming in the most massive molecular clouds, where large numbers of stars are actively forming. The large average distance of these high-mass star-forming regions from the Sun, combined with the very high dust opacity that obscures the earlier stages of high-mass star formation, have severely restricted our ability to study it in detail. As a result, the details of high-mass star formation are still unclear. In contrast, low-mass stars form also in less massive molecular clouds that can be found at shorter distances from the Sun. This has allowed us to observe them both in greater numbers, as well as, at higher spatial resolutions, thus significantly strengthening our understanding of their formation path compared to that of their high-mass counterparts. In the following subsections, I will summarize our current understanding of both low and high-mass star formation.

### 1.1.1 Low-mass star formation

Low-mass stars form within the small, high-density substructures (sizes $< 0.1$ pc, densities $n_{\rm H} > 10^5$ cm$^{-3}$; Pineda et al., 2023) of molecular clouds known as dense cores. The stability of these cores relies on the Virial theorem, which describes the equilibrium between the gravitational

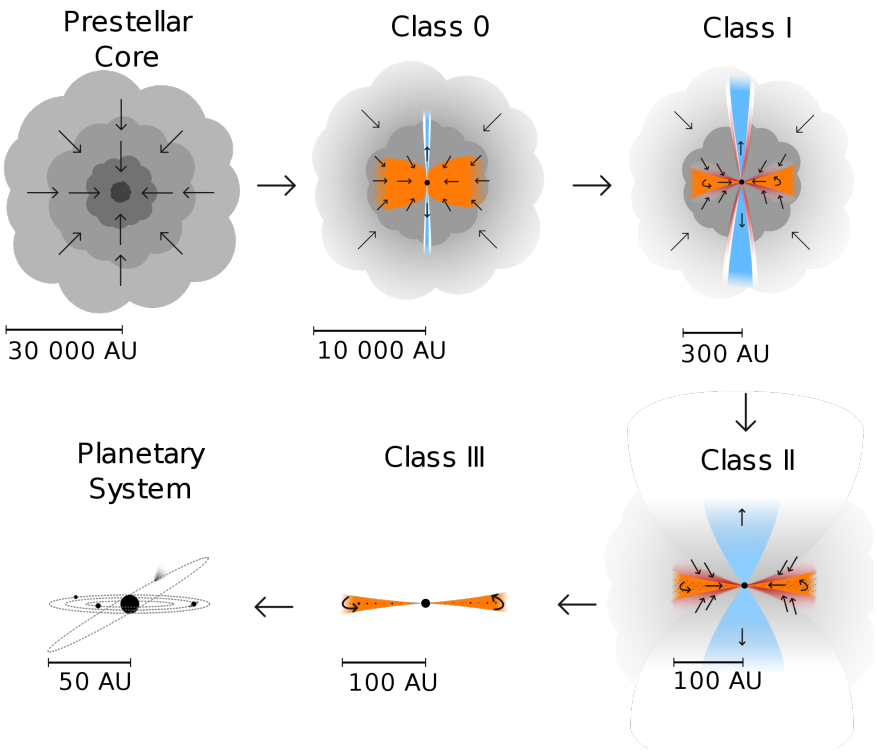


Figure 1.1: Illustration of the different evolutionary stages of a low-mass young stellar objects. Figure from Persson, 2014.

pull and the counteracting effects of thermal and magnetic pressure:

$$\frac{1}{2}\frac{\partial^2 I}{\partial t^2} = 2T + 2U + W + M, \tag{1.1}$$

where $I$ is the generalized moment of inertia, $T$ is the kinetic energy due to bulk motions of the gas, $U$ is the energy due to thermal motions, $W$ is the gravitational potential energy, and $M$ is the magnetic energy. Based on the Virial theorem, Jeans, 1928 estimated the limits, in terms of size and mass, for a stable core, known as the Jeans' length:

$$\lambda_J = \left(\frac{\pi c_s^2}{G\rho_0}\right)^{1/2}, \tag{1.2}$$

and the Jeans' mass:

$$M_J = \lambda_J^3 \rho_0 = \left(\frac{\pi c_s^2}{G}\right)^{3/2} \rho_0^{-1/2}, \tag{1.3}$$

respectively, with $c_s$ corresponding to the sound speed, $\rho_0$ to the mass density, and $G$ to the gravitational constant. The aforementioned stability criteria are applicable in both the cases of

Table 1.1: Summary of the different criteria used in protostellar classification

| Class | $\alpha_{IR}$ | $T_{bol}$ [K] | $L_{submm}/L_{bol}$ |
|---|---|---|---|
| 0 | – | ≤70 | ≥ 0.5% |
| I | ≥0.3 | 70 – 650 | < 0.5% |
| Flat | 0.3 – -0.3 | – | – |
| II | -0.3 – -1.6 | 650 – 2800 | – |
| III | ≤-1.6 | ≥ 2800 | – |

**References:** (1) Lada and Wilking, 1984, (2) Myers and Ladd, 1993; Chen et al., 1995, (3) Andre, Ward-Thompson and Barsony, 1993

low and high-mass star formation processes, and for typical values of temperature ($T$ ∼10 K) and $H_2$ number density ($n_{H_2} \sim 10^4$ cm$^{-3}$) in giant molecular clouds are found to be, $\lambda_J \sim 0.1$ pc and $M_J \sim 1$ M$_\odot$. When a core exceeds these limits, it will start collapsing under the effects of its own gravity, kick-starting the star formation process. The main stages of this collapse where first described by Larson, 1969. Initially, the collapse leads to the formation of a small, high density region at the center of the core. As more and more material is accumulated at this central region, it becomes opaque to its own radiation, and is compressed, and heated up until it reaches a hydrostatic equilibrium. This semi-stable state is called the first hydrostatic core and has a typical temperature of ∼ 850 K. At this stage, the first hydrostatic core remains stable in size, but, as material from the outer layers continues collapsing inwards, the core keeps increasing its density and temperature in order to maintain the hydrostatic equilibrium. Eventually, when the core reaches a temperature of ∼ 2000 K, collisional dissociation of $H_2$ begins, absorbing most of the released gravitational energy and stopping the increase of temperature, thus breaking the equilibrium. The second collapse ends when the hydrogen in the core becomes fully ionized allowing the gas to settle once more to a hydrostatic equilibrium; the second hydrostatic core is formed. From this stage onward, the central object is typically referred to as a protostar. The inclusion of rotation and magnetic fields in the above scenario leads to an asymmetric collapse of the material and the formation of a disk surrounding the protostar, which channels the accretion of material from the envelope onto the protostar. These disks are also connected with the launch of bipolar outflows and wide angled winds (e.g., Bjerkeli et al., 2016), that will be discussed in Section 1.3.

Low-mass protostars are divided into four classes based on their observed properties, as shown in Figure 1.1. The initial criterion used was the infrared (IR) spectral index:

$$\alpha_{IR} = \frac{d \log \lambda F_\lambda}{d \log \lambda} \tag{1.4}$$

calculated over the wavelength range between 2 and 20 $\mu$m. In this method, a positive $\alpha_{IR}$, indicating brighter emission at longer wavelengths, corresponds to younger sources (Lada and Wilking, 1984). An alternative classification method relies on the bolometric temperature ($T_{bol}$) of the sources (Myers and Ladd, 1993; Chen et al., 1995). $T_{bol}$ is defined as the temperature of a black body with the same mean frequency as that of the observed spectral energy distribution

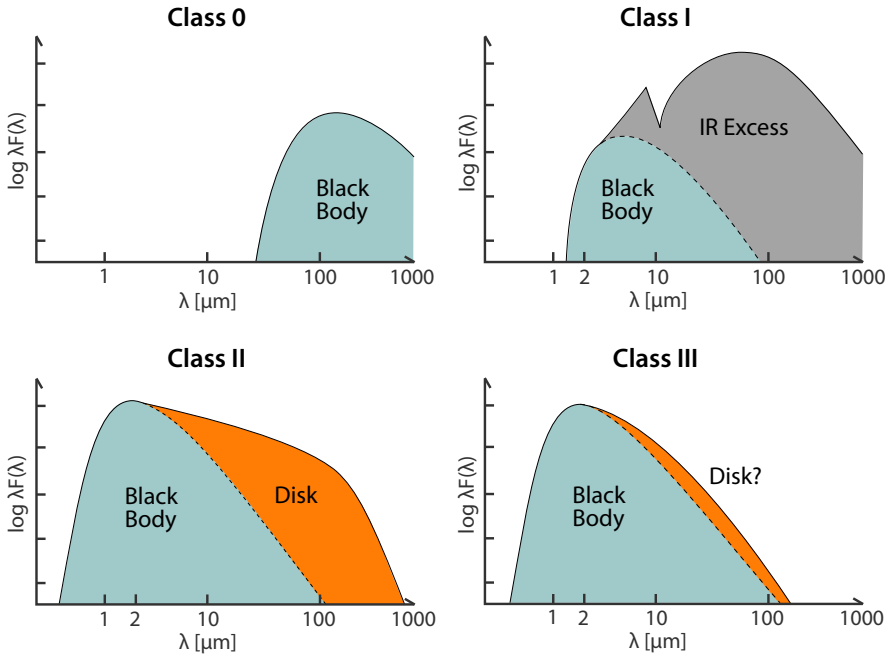


Figure 1.2: Example spectral energy distributions of the four Classes of low-mass protostars. Figure from Persson, 2014.

(SED) of the protostar. In this classification method, less evolved sources have lower values of $T_{\rm bol}$. Typical SED morphologies corresponding to the different protostellar classes are shown in Figure 1.2. Finally, after the discovery of Class 0 objects (Andre, Ward-Thompson and Barsony, 1993), the fraction of submillimeter luminosity over the total protostellar luminosity was introduced as a criterion to separate between Class 0 and Class I sources. The values of the different classification criteria corresponding to each protostellar Class are summarized in Table 1.1.

The Class 0 stage corresponds to the youngest, least evolved sources. At this stage, the protostar remains deeply embedded in the natal envelope. As a result, most of the observed continuum radiation is seen at longer wavelengths, coming from the envelope. Sources at the Class 0 stage have the highest mass accretion rates (i.e. the rate at which material from the envelope falls onto the central object) and are associated with the launch of powerful, collimated jets/outflows. At the Class I stage, most of the envelope mass has accreted onto the circumstellar disk or the protostar itself, allowing more of the protostellar and disk emission to be seen. In addition, at this stage the masses of the disks are higher, and the dust within them is generally warmer (Tychoniec, Manara et al., 2020). As a result, the SED of the source shifts towards shorter wavelengths. At this stage, sources still drive extended outflows, although these tend to be less powerful and have wider opening angles in comparison to those of their Class 0 counterparts (H. G. Arce and Sargent, 2006). In the Class II stage, the surrounding envelope is almost completely dispersed, and the central object, now referred to as a pre-main sequence star, becomes visible even at optical wavelengths. Class II sources are also called T-Tauri stars, after the prototypical source of this kind. Some outflows are still seen at this late stage, but those are far weaker than those of younger

sources (e.g., Nisini, Antoniucci et al., 2018; Rota et al., 2025). The Flat spectrum stage, referring to sources with an IR spectral index between -0.3 and 0.3, is typically considered as a transition phase between the Class I and II stages (Evans et al., 2009). By the Class III stage, only a disk remains, with most of its dust accreted either in planetisimals or onto the central protostar. The central protostar is still contracting, on its way to initiate hydrogen burning and joining the main sequence. As accretion has by that point stopped, there is no outflow activity associated with this stage.

Overall, while the formation process of low-mass protostars has been theoretically described in detail (e.g., F. H. Shu, 1977; F. H. Shu, Adams and Lizano, 1987; McKee and Ostriker, 2007), the classification system remains purely observation based. As a result, environmental factors, such as the extinction due to foreground material or the inclination angle of the disk–protostar system, can influence the assigned Class of a given source (van Kempen, van Dishoeck et al., 2009).

### 1.1.2 High-mass star formation

Overall, the basis of high-mass star formation is similar to that of the low-mass regime, with the gravitational pull overcoming the support of turbulence and magnetic fields being the key driving factor. The subsequent collapse of a core is, in principle, expected to progress similarly to the low-mass scenario (i.e. going through the first and second hydrostatic core phases) but scaled up in mass (Bhandare et al., 2018). The similarity between the high- and low-mass star formation scenarios is further supported by the detection of disks (e.g., Dutrey et al., 2014; Beltrán and de Wit, 2016; Andrews et al., 2018; Ahmadi et al., 2023) and outflows (e.g., H. G. Arce, D. Shepherd et al., 2007; Frank et al., 2014; Bally, 2016) across both mass regimes. At the same time though, there are a number of notable differences between the two cases. Namely, in order for high-mass sources to actually form, accretion needs to continue even after the star has joined the main sequence (Palla and Stahler, 1993). In addition, in high-mass sources, the ionizing flux increases strongly, leading to the formation of regions of ionized hydrogen, called H II regions, surrounding the massive star. As a result, in high-mass star formation accretion needs to be able to penetrate these H II regions. An additional difference is that high-mass star formation is found to exclusively take place in clusters, which also exhibit much higher multiplicity than those only forming low-mass stars (Motte, Bontemps and Louvet, 2018; Offner, Moe et al., 2023; Beuther, Kuiper and Tafalla, 2025). These crucial differences have led to a long debate on whether high-mass star formation is simply a scaled up version of the low-mass case or whether the increased radiation of high-mass sources leads to more fundamental differences (Zinnecker and Yorke, 2007; Beuther, Kuiper and Tafalla, 2025).

The question first became apparent when Kahn, 1974 showed that, under the assumption of spherical symmetry, the increased radiation pressure from massive protostars would not allow for the formation of stars more massive than 40 $M_{\odot}$. Since such stars have been observed, in an effort to overcome this limit, Bonnell and collaborators introduced the competitive accretion model (e.g., Bonnell, Bate and Zinnecker, 1998; Bonnell, Vine and Bate, 2004; Bonnell, Larson and Zinnecker, 2007). In this scenario, high-mass stars form at the deepest points of the gravitational wells of forming clusters (see Figure 1.3). The overall shape of the gravitational potential encourages the flow of material towards the central massive star, thus enabling faster growth to higher final masses. An alternative scenario is the turbulent core model (McKee and Tan, 2002; McKee and

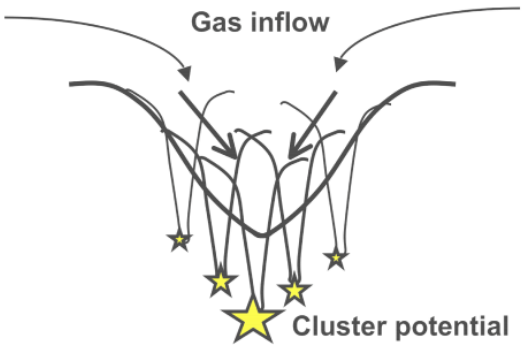


Figure 1.3: Illustration of the morphology of the cluster potential enabling the formation of massive stars in the competitive accretion scenario. Figure from Bonnell, Larson and Zinnecker, 2007.

Tan, 2003), in which high-mass stars form from the collapse of highly turbulent cores. The high turbulence of these cores supports them against collapse until they reach much higher masses than their low-mass counterparts but it also causes much higher accretion rates allowing the formation of high-mass stars on timescales of a few hundred thousands years. A schematic of the expected evolution of such a high-mass core is shown in Figure 1.4. Despite differences in their initial core conditions, the turbulent core model largely reflects a scaled-up version of the low-mass star formation scenario. While the turbulent core model forms an appealing theory, such cores remain undetected.

The difficulty in the observation of high-mass turbulent cores arises from the fact that high-mass stars are much rarer, and therefore form, on average, at larger distances from the Sun but also because they form in denser regions than their low-mass counterparts and spend most of their formation hidden deep inside dense cocoons of molecular gas that obscure them. This difficulty in observing the earliest phases of high-mass star formation has led to another crucial difference in comparison to low-mass sources when it comes to the classification of their different evolutionary steps. Namely, that high-mass star formation does not adhere to the 'Class' system established for low-mass sources, and a different sequence of evolutionary steps has been adopted. As shown in Figure 1.4, the initial stage of high-mass star formations is, similar to the low-mass scenario, comprising of a cold, collapsing core. As the high-mass protostar forms, the released energy is enough to heat up the inner parts of the core, turning it into what is known as a hot molecular core (e.g., van Dishoeck and Blake, 1998; S. Kurtz et al., 2000; Garrod, Widicus Weaver and Herbst, 2008). Eventually the material surrounding the star begins to become ionized, forming initially a hyper compact H II region, which progressively expands transitioning into an ultra compact H II region and eventually an H II region surrounding the massive star.

A fully observational classification system for high-mass protostars, based on an unbiased survey of high-mass SFR in the inner Galaxy has been proposed by König et al., 2017 and Urquhart, 2024. In this classification, the observed SED is used to determine the evolutionary stage of a source. More precisely, high-mass stars begin its formation as "quiescent", "starless", or far-IR quiet clumps, meaning that they lack any significant IR emission. As the name suggests,

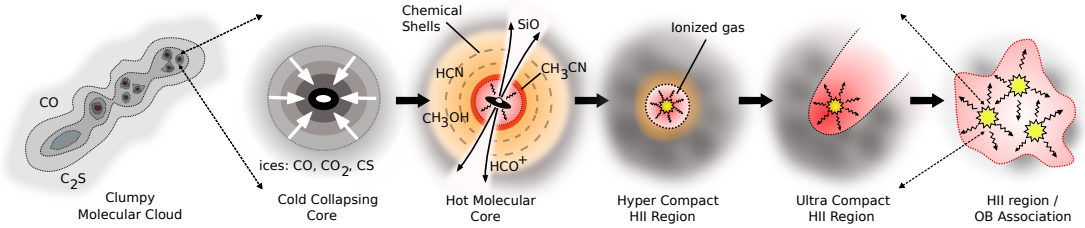


Figure 1.4: Illustration of the evolutionary scenario of high-mass stars. Image from Cormac Purcell.

this stage predates the formation of any kind of protostar. When the protostar eventually forms, the clump starts to heat up and starts emitting at shorter wavelengths. First, the clump will become bright at the far-IR (70 $\mu$m) range, entering the so called protostellar or mid-IR quiet stage. As the protostar continues accreting and heating up, the peak of the clump emission shifts to even shorter wavelengths, eventually becoming bright at the mid-IR regime. This is the mid-IR bright or the massive young stellar object (MYSO) stage. The final stage in the formation of a high-mass star, referred to as the ultra compact H II stage, comes with the formation of an H II region surrounding it. This suggests that the high-mass star has now joined the main sequence, and has begun ionizing its surroundings. Examples of observed sources in the different evolutionary stages of a high-mass sources, along with their SED are shown in Figure 1.5

Apart from the dust continuum, emission and absorption from molecules has also often been used to study key parts of the star formation process. Thanks to its ability to probe a broad range of temperatures and densities (Genzel, 1991) molecular emission allows us to disentangle energetic processes associated with star formation, while the unique formation histories of different molecular species allows them to serve as chemical clocks tracing the different star formation stages (e.g, S-bearing species tracing the earlier stages of high-mass star formation Charnley, 1997; Hatchell, Thompson et al., 1998).

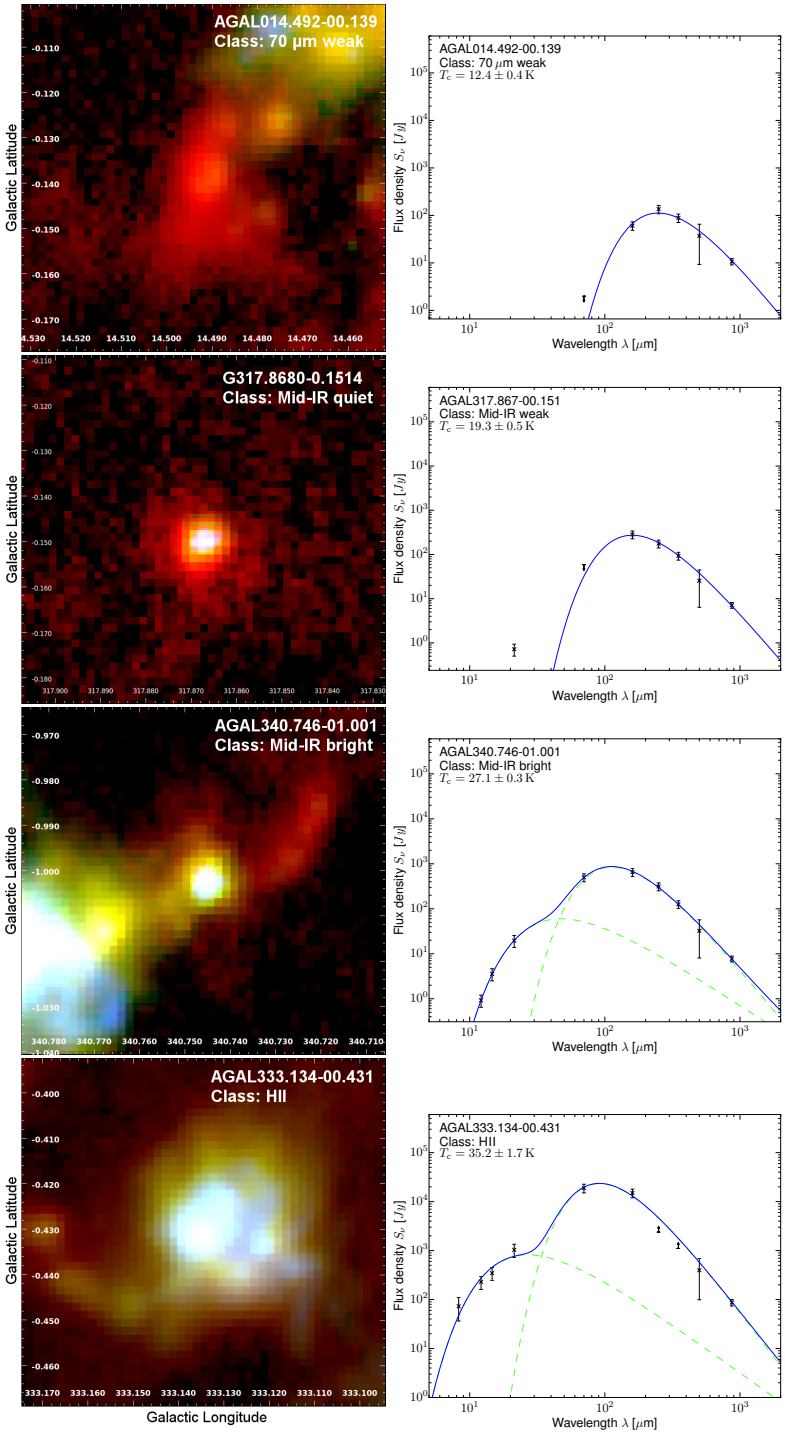


Figure 1.5: Example illustrating the classification of high-mass star forming regions. Panels on the left show three color images (red: ATLASGAL 870 $\mu$m, green: PACS 160 $\mu$m, blue: PACS 70 $\mu$m) of sources in each high-mass star formation class, while the corresponding SEDs are presented on the right. The Figure is taken from König et al., 2017.

## 1.2 Emission from molecules

Molecules emit radiation when they get de-excited, transitioning from one energy state to another with lower energy. There are three kinds of such transitions possible in molecules, electronic, vibrational, and rotational (see also Figure 1.6). The first ones are the most energetic kind of transition that can take place in molecules and take place between two different electronic levels. The energy between two electronic states is typically of the order of several eV, and therefore the radiation released in such a transition lies in the UV regime, at frequencies of $\sim 10^{15}$-$10^{16}$ Hz. Next in terms of energy are transitions between the vibrational levels of molecules, which arise from the vibration of the molecular bond along the internuclear axis. Vibrational transitions have lower energies than the electronic transitions and typically produce emission lines in the mid-IR regime (frequencies of $\sim 10^{14}$ Hz). Finally, the rotation of molecules gives rise to additional energy states within each vibrational state known as rotational levels. Rotational transitions have even lower energies than the vibrational ones, with energies in the order of meV, thus giving rise to transitions that are primarily in the centimeter or millimeter range (frequencies of $\sim 10^{9}$-$10^{11}$ Hz). As can be seen in Figure 1.6, these three types of energy levels show a nested pattern, with a single electronic state containing multiple vibrational levels; each of those in turn contains multiple rotational levels. For astrophysicists investigating the processes of star formation, the rotational transitions of molecular species are especially valuable. Owing to their low excitation energies, these transitions readily occur even under the cold, dense conditions characteristic of

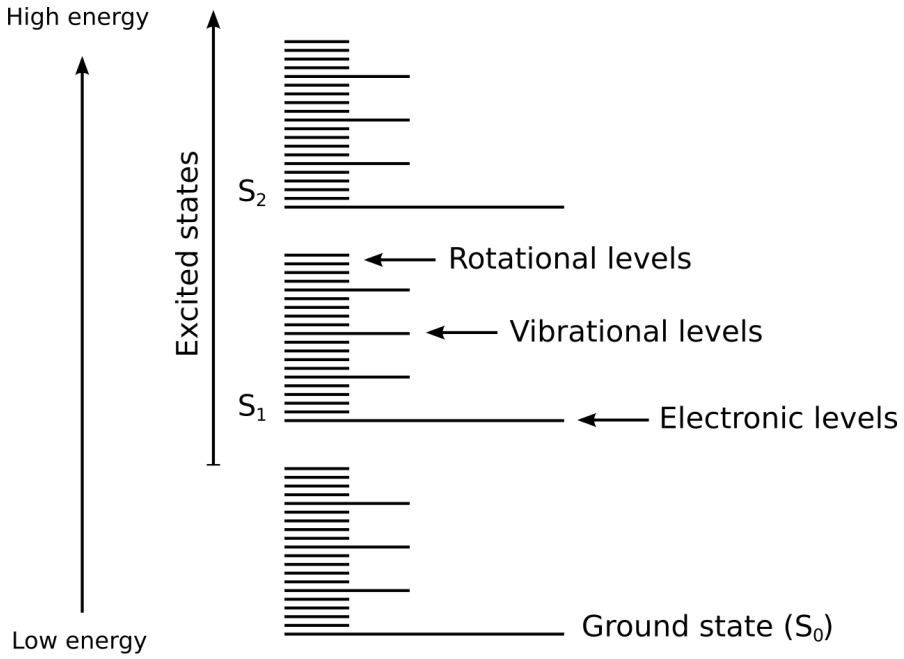


Figure 1.6: Qualitative illustration of the energy levels within a molecule. In order of increasing energy, molecular energy levels are divided into rotational, vibrational, and electronic. Figure taken from `https://commons.wikimedia.org/wiki/File:Molecular_energy_levels_en.svg`

protostellar envelopes, and have therefore been widely employed to probe the earliest phases of star formation.

Under the assumption of molecules as rigid rotors, meaning that their rotation does not affect their shape, the energy of the different rotational levels, $E_{\rm rot}$, can be estimated in terms of the angular velocity, $\omega$, and the moment of inertia, $I$ as follows:

$$E_{\rm rot} = \frac{1}{2}\begin{pmatrix} \omega_x & \omega_y & \omega_z \end{pmatrix}\begin{pmatrix} I_{xx} & I_{xy} & I_{xz} \\ I_{yx} & I_{yy} & I_{yz} \\ I_{zx} & I_{zy} & I_{zz} \end{pmatrix}\begin{pmatrix} \omega_x \\ \omega_y \\ \omega_z \end{pmatrix}, \tag{1.5}$$

where $x, y, z$ are the different rotations axes. The diagonal elements in the moment of inertia matrix correspond to the respective moments along the different axes, while the off-diagonal elements represent combinations of rotation around the different pairs of axes. One can in principle select the axes $x, y, z$ such that all off-diagonal elements in the matrix become zero. The moment of inertia, $I_{rr}$, for a given rotation axis is given as:

$$I_{rr} = \sum_{j=1}^{N} m_j r_j^2, \tag{1.6}$$

where $m_j$ is the mass of an atom $j$, $r_j$ is its distance from the center of mass, and N is the total number of atoms in the molecule. In terms of angular momentum, $P_r = \omega_r I_{rr}$, the rotational energy of a molecule (Eq. 1.5) can be written as:

$$E_{\rm rot} = \frac{P_a^2}{2I_{aa}} + \frac{P_b^2}{2I_{bb}} + \frac{P_c^2}{2I_{cc}}, \tag{1.7}$$

where $a, b, c$ are the three principal rotation axes for which all off-diagonal elements in the inertia matrix become zero.

The calculation can be further simplified in the case of diatomic molecules, as in such a case there is no rotation along the internuclear axis (i.e., the axis that runs through the nuclei of the atoms in the molecule). In the center of mass frame of the molecule, one can write $m_1 r_1 = m_2 r_2$ and $R = r_1 + r_2$, with:

$$r_1 = \frac{m_2 R}{m_1 + m_2}, \text{ and } \quad r_2 = \frac{m_1 R}{m_1 + m_2} \tag{1.8}$$

From Equation 1.6, the total angular momentum for a diatomic molecule is given as:

$$I_{rr} = m_1 r_1^2 + m_2 r_2^2 = \frac{m_1 m_2}{m_1 + m_2} R^2 = \mu R^2, \tag{1.9}$$

where $\mu$ is the reduced mass of the molecule. In a diatomic (or linear) molecule, the two available rotation axes are identical, therefore $I_{bb} = I_{cc} \equiv I$, and the total rotational energy can be written as:

$$E_{\rm rot} = \frac{1}{2I}(P_b^2 + P_c^2) \equiv \frac{P^2}{2I}, \tag{1.10}$$

with $P$ being the total angular momentum of the system. As the rotational energy levels are

Table 1.2: Spectroscopic designation of branches within ro-vibrational transitions

| Designation | Δ J | Note |
|---|---|---|
| *O* | -2 | Electric quadrupole transition |
| *P* | -1 | Electric dipole transition |
| *Q* | 0 | Electric dipole or quadrupole transition |
| *R* | +1 | Electric dipole transition |
| *S* | +2 | Electric quadrupole transition |

quantized (i.e., they can only take specific energy values arising from discrete energy levels), $P$ is replaced by its eigenvalues, $\hbar J(J+1)$, expressed in terms of the rotational quantum number, $J$, with $J = 0, 1, 2, \ldots$ and the reduced Planck constant $\hbar = h/2\pi$. The rotational energy is then given by:

$$E_{\text{rot}} = \frac{h^2}{8\pi^2 I} J(J+1) \equiv hBJ(J+1), \tag{1.11}$$

where $B = h/8\pi^2 I$ is the rotational constant. In this case, the ground rotational state corresponds to $J = 0$, and the subsequent excited states have increasing values of $J$. Of course, molecules in reality are not actually rigid rotors, and the rotation will cause some distortion to their shapes and, by extension, their moments of inertia. This distortion is typically addressed with the addition of a second-order perturbation in Eq. 1.11. While these perturbations shift the energy levels from the unperturbed values, the difference is typically orders of magnitude smaller than the values of the energy levels themselves. Molecular line emission in the millimeter regime, especially for molecules with a permanent dipole moment such as CO, typically originates from these pure rotational transitions.

In certain cases, a rotational transition can take place between rotational levels of different vibrational states, giving rise to what is known as ro-vibrational transitions. In such transitions, the change of the rotational quantum number between the upper and lower levels can be $J_{\text{upper}} - J_{\text{lower}} = \Delta J = 0, \pm 1$, and $\pm 2$. However, transitions with $\Delta J = \pm 2$ are associated with quadrupole emission and are much rarer than those associated with dipole emission. The $H_2$ molecule, due to its lack of a permanent dipole moment, is a great example of a molecule that emits primarily through such quadrupole transitions. Depending on the value of $\Delta J$, ro-vibrational transitions are often given one of the following designations, *O*, *P*, *Q*, *R*, or *S*, as shown in Table 1.2. The energy difference, between the upper and lower states in such a transition is typically higher than that of pure rotational transition, as a result ro-vibrational emission lines are often found in the IR regime.

### 1.2.1 The $H_2$ and CO molecules

The $H_2$ molecule is by far the most abundant molecule in the Universe, even so, it is challenging to observe. As the lightest molecule, $H_2$ has a very low moment of inertia, which, according to Eq. 1.11, means that even the lowest rotational energy levels of $H_2$ have high energies ($\geq$ 500 K Roueff et al., 2019). This makes the $H_2$ molecule very hard to excite within the cold environments

of molecular clouds. In addition, $H_2$ as a homonuclear molecule is perfectly symmetrical, as a result its wavefunction has to be antisymmetric under both the exchange of the two electrons or the two protons. As the two protons are spin 1/2 particles, their total spin can be either 1 (spins parallel) or 0 (spins antiparallel). To fulfill the antisymmetry requirement, if the total proton spin is 0 then the rotational quantum number $J$ must be even ($J = 0, 2, 4, ...$), while if the total proton spin is 1 $J$ must be odd ($J = 1, 3, 5, ...$). In the case with even $J$, the $H_2$ molecule is called para-$H_2$, while the odd $J$ case is referred to as ortho-$H_2$. Transitions between the ortho and para spin states of $H_2$ are very rare, as a result, the $H_2$ molecule typically only emits through quadrupole transitions, with $\Delta J = \pm 2$ or 0 that gives rise to the $S$, $Q$, and $O$ emission lines of $H_2$. The reliance on intrinsically weak quadrupole transitions makes $H_2$ emission difficult to detect, still thanks to its high abundances it can be detected.

In contrast to $H_2$, CO is a much heavier molecule, leading to its rotational transitions being more closely spaced in wavelength and starting from very low energies (5.5 K, Winnewisser et al., 1997). This makes the lower rotational levels of CO (low$-J$) easy to excite even in the low temperatures of molecular clouds, and the corresponding emission accessible at the radio regime. The rotational ladder of CO though extends also to much higher energy levels, with lines up to $J_{up} = 49$, corresponding to upper level energies of $E_{up} > 1000$ K (Karska, Kaufman et al., 2018). This high$-J$ CO emission is better suited to trace shock excited material in the ISM, more akin to that probed by the $H_2$. In addition, CO possesses a permanent dipole moment, which allows it to emit strongly when excited, despite its abundance being approximately four orders of magnitude lower than that of $H_2$ (Lacy et al., 1994). As a result, CO has been the most commonly used molecule for the studies of molecular clouds and star formation.

Irrespective of their differences, both molecules play a significant role in the studies of the most energetic processes associated with star formation: the protostellar outflows. Namely, the emission from the low rotational transitions of CO can better probe the cold environment of star formation as well as the more extended, entrained parts of molecular outflows, while $H_2$, as well as the higher $J$ transitions of CO, are capable of probing shock excited regions associated with the protostellar jets and outflows.

## 1.3 Protostellar outflows

Protostellar outflows are the most spectacular signpost of ongoing star formation, appearing during the formation of both low- and high-mass stars (e.g., Bally, 2016; Beuther, Kuiper and Tafalla, 2025). Bipolar outflows are believed to remove excess angular momentum from the protostar-disk system, thus enabling further mass accretion through the disk and onto the central protostar. At the same time, outflows inject energy and momentum into the surrounding ISM, disrupting the natal envelope and, as a result, reducing the available mass reservoir for the protostar. It is therefore clear that protostellar outflows represent key components of the star formation process by regulating the growth of the protostar.

The first sign of outflow activity associated with the formation of stars came with the discovery of small emission-line nebulae within dark clouds by Herbig, 1951 and Haro, 1952. These nebulae, now called Herbig-Haro objects (HH), are known to be shock excited nebulosities powered by the

outflows of nearby stars (e.g., Movsessian et al., 2024; Speckert, Rector and Prato, 2025). The next crucial step in the study of protostellar outflows came with the advent of radioastronomy and the first published spectra of CO. These observations revealed the presence of broad line wings in the emission from the Orion nebula (R. W. Wilson, Jefferts and Penzias, 1970), and were followed by the detection of the L1551 outflow (Figure 1.7; Snell, Loren and Plambeck, 1980). In the following years, the number of detections of protostellar outflows kept increasing, leading to the recognition that they are a common occurrence in star-forming regions (e.g Bally and Lada, 1983; Bachiller, 1996; Frank et al., 2014). However, the underlying physical processes behind this phenomenon remain uncertain, with several different models being proposed over time.

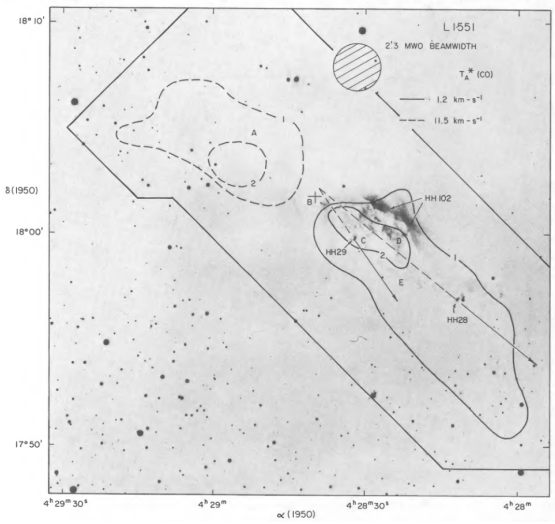


Figure 1.7: First detection of the L1551 outflow by Snell, Loren and Plambeck, 1980. The solid and dashed contours mark the blue- and red-shifted CO $J$ = 1-0 line emission respectively, overlaid on the continuum emission.

### 1.3.1 Outflow formation and launching scenarios

It is widely accepted that the launching of bipolar outflows relies on the magnetocentrifugal acceleration of material in the close vicinity ($\sim$ a few 100 AUs) of the forming star. Thus, the magnetic fields of the star and disk play crucial roles in the launching of outflows. Currently, there are two prominent types of models used for the description of the launching mechanism of protostellar outflows, the disk wind models and the X-wind models.

Disk wind models, first proposed by Pudritz and Norman, 1986, following the mechanisms outlined in Blandford and Payne, 1982, state that the initial magnetic field of the cloud gets compressed through the collapse of the core, twisted due to rotation, and further pinched due to accretion along the disk. This leads to the formation of an hourglass-shaped magnetic field, perpendicular to the disk (see Figure 1.9). Material can then be accelerated along the magnetic field lines giving rise to the outflow. In this scenario, faster moving material can be ejected at smaller radii ($\lesssim$ 1 Au Bally, 2016), close to the protostar, while slower moving outflow components

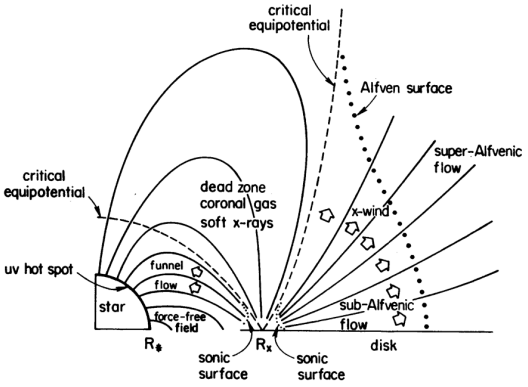


Figure 1.8: Illustration of the outflow launching configuration predicted by the X-wind model (F. Shu et al., 1994).

can be launched from larger disk radii.

In contrast, in X-wind models the stellar magnetic field extends at a distance from the surface of the star, truncating the accretion disk. At this location, the interaction between the stellar and the disk magnetic fields leads to the appearance of open magnetic field lines. It is along these lines that material can get accelerated, giving rise to the outflow (F. Shu et al., 1994; F. H. Shu, Najita et al., 2000). A detailed schematic for the X-wind model geometry is shown in Figure 1.8.

While both types of models predict the launching of the outflow very close to the location of the protostar, the collimation is observed to happen at larger distances. It was initially proposed that density gradients in the envelope material could be responsible for the re-collimation of the outflows (Canto and Rodriguez, 1980), but nowadays it is generally agreed that the hoop stress caused by toroidal magnetic fields is the most likely reason (Pudritz, Ouyed et al., 2007).Another common aspect of both models is the predicted connection between the outflow ejection and mass accretion, both in agreement with the observationally suggested values of $\dot{M}_{\rm jet} \sim 0.1\dot{M}_{\rm acc}$ (Ellerbroek et al., 2013; Nisini, Antoniucci et al., 2018). In addition, both models predict the launch of rotating outflows, which is in agreement with recent outflow observations (e.g., López-Vázquez et al., 2020; Launhardt, Pavlyuchenkov et al., 2023; Omura, Tokuda and Machida, 2024).

Overall, while it is currently hard to observe the innermost regions of outflows that differentiate between the two types of launching models, it remains crucial to study the larger scale outflow processes to understand their impact on the ISM. To that end, both types of models appear capable of reproducing the established view of protostellar outflows, in agreement with current observations.

### 1.3.2 Theoretical structure of protostellar outflows

Protostellar outflows interact heavily with the dense molecular material that surrounds the forming protostar, giving rise to the complex morphologies of their emission. Despite that, a number of common features across all protostellar outflows have been identified. Figure 1.10 shows various

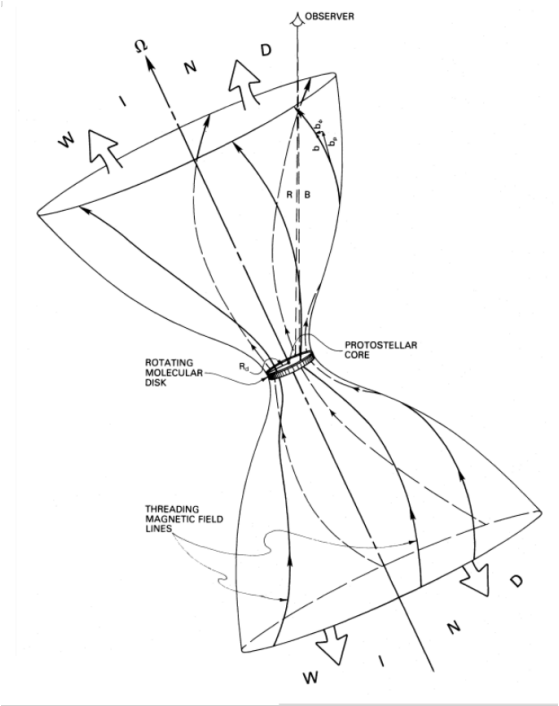


Figure 1.9: Illustration of the outflow structure as predicted by the disk-wind model (Pudritz and Norman, 1986).

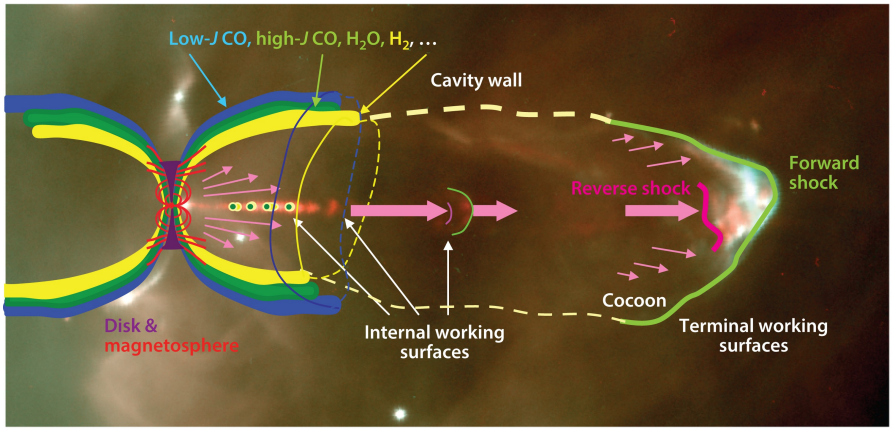


Figure 1.10: Illustration of the different components of a protostellar outflow. Background image is the jet of HH34 seen in H$\alpha$ emission (cyan) and [S II] (red). Figure from Bally, 2016.

physical components and processes associated with the protostellar outflow, as it propagates into the surrounding ISM, as well as, their respective molecular tracers.

In this established image of outflows (Bally, 2016), there is the narrow, well collimated jet, with velocities upwards of 50 km $s^{-1}$, believed to be launched from the inner radii ($\leq$ 1 AU) of the disk. All along the jet, bright emission knots are often detected. These knots are known as internal working surfaces, and they are shocks formed when faster moving material interacts with previously ejected material or other denser regions in the outflow surroundings. When detected in optical wavelengths, these shock knots correspond to the HH objects. The jet ends at the terminal working surface, where a forward bow-shock marks the limit between the outflow and the ISM. A reverse shock is also often seen at this location, propagating backwards into the outflow. Surrounding the jet is a lower density cavity, carved out as the jet propagates into the surrounding envelope, and filled by a slow-moving, wide-angle wind. In the disk-wind scenario, this wind is launched at larger disk radii ($\geq$ 1 and up to a few 10 s of AUs, Delabrosse et al., 2024), but X-wind models can also account for its presence (e.g., Shang, Krasnopolsky and C.-F. Liu, 2023). The walls of the outflow cavity form a relatively narrow layer that separates the outflow from the surrounding envelope. These walls are usually seen in molecular emission lines, like those of CO and $H_2$, and display a layered structure with the highest excitation lines seen closer to the jet and gradually decreasing towards the outer layers of the outflow. This molecular layer is also referred to as the entrained outflow, since it is believed to consist primarily of material from the dense envelope that has been swept up from the jet and wide-angle wind rather than having been launched directly from the protostar - disk system.

As physical conditions vary substantially across the different components of a protostellar outflow (i.e., the jet, cavity, cavity walls, and shock knots), a multi-wavelength approach is required in order to study all aspects of the phenomenon. More precisely, spectroscopic observations of multiple molecular species and their different transitions, capable of probing a range of gas densities and temperatures are crucial to understand the inner workings of protostellar outflows.

### 1.3.3 Outflows in the millimeter regime - entrained outflows

The millimeter regime covers a plethora of molecular rotational transitions which, thanks to their typically low excitation energies, are ideal to probe the cold and dense parts of the ISM where star formation takes place. In addition, the radio wavelength range is easily accessible from the ground, thus making molecular emission lines for a long time the primary means of studying the molecular outflows associated with star formation.

Starting with the first detection of extended line wings in spectra (R. W. Wilson, Jefferts and Penzias, 1970) and the subsequent mapping of the L1551 outflow (Snell, Loren and Plambeck, 1980), the most commonly used tracers for protostellar outflows are the low rotational transitions of $^{12}$CO. Thanks to its relatively high abundances ($N(\mathrm{CO}) \sim 10^{-4} N(\mathrm{H_2})$) and its low excitation levels, $^{12}$CO can be easily detected even in the low densities of high velocity outflow wings (see Figure 1.11 for an example). This emission originates from the more extended, entrained outflow (see Figure 1.10). Apart from CO, other molecules such as $HCO^+$ and HCN have also been reported to trace similar parts of outflows (e.g., H. G. Arce and Sargent, 2006; Walker-Smith et al., 2014; Tychoniec, van Dishoeck et al., 2021). On the other hand, molecules like SiO and SO, that are enhanced by the destruction of dust grains, have been associated with the faster moving

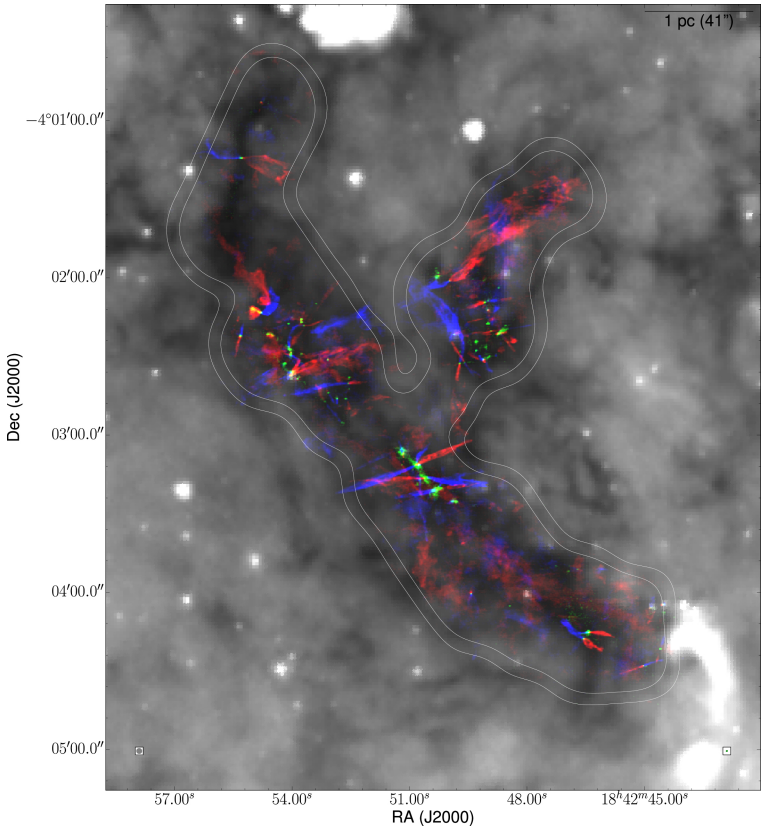


Figure 1.11: Example of outflow detections in the IR dark cloud G28.37+0.07 based on CO $J$=2-1 observations (Kong et al., 2019).

parts of the outflows and have even been detected in jets (see Figure 1.12; C.-F. Lee et al., 2017; Tychoniec, van Dishoeck et al., 2021).

Spectroscopic observations of molecular outflows at millimeter wavelengths have allowed for direct measurements of their morphological characteristics i.e., their extent and collimation factor, the ratio between the length and the width of the outflow. In addition, due to the great spectral resolution of millimeter receivers, the velocity of the outflowing gas can be estimated with high accuracy, by measuring the Doppler-shift of the line emission. Depending on the velocity and morphology of the outflow emission, two separate outflow components have been proposed (e.g., Hirano et al., 2010). The first is known as the standard high velocity component (SHV), which typically has velocities in the range of $\sim 1 - 30$ km s$^{-1}$ and a wide opening angle, tracing the cavity walls. The second component is the extreme high velocity component (EHV), which typically displays higher velocities ($> 30$ km s$^{-1}$) and much higher collimation than the SHV. The EHV is typically associated with the jet of protostellar outflows.

Observations of the emission from molecular lines allow the calculation of the molecular mass carried by the outflow ($M_{\rm out}$). This, in turn, enables the calculation of the outflow properties and energetics, such as the mass loss rate ($\dot{M}_{\rm out}$), the momentum ($P_{\rm out}$), the outflow force (or

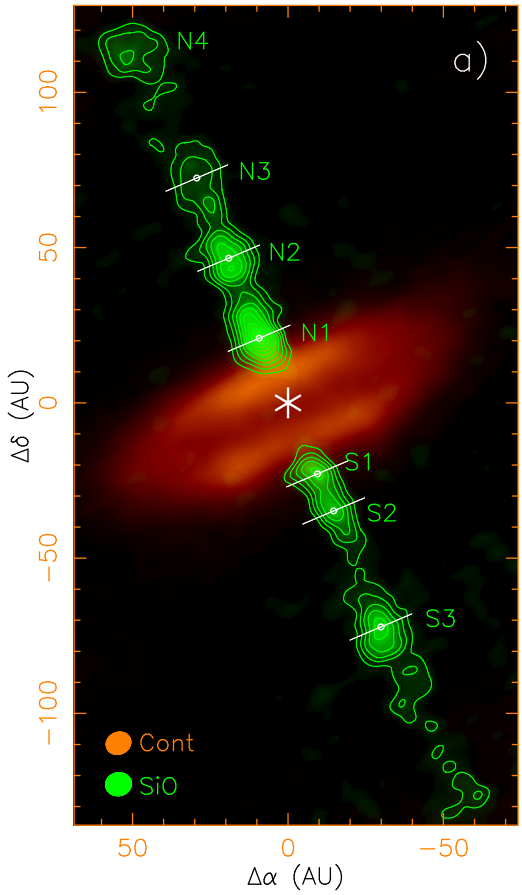


Figure 1.12: The jet of HH212 as seen in SiO emission (green contours). The disk surrounding the protostar is also seen in the continuum emission. Figure from C.-F. Lee et al., 2017.

momentum injection rate; $F$), the total kinetic energy ($E_{\rm kin}$), and the total kinetic luminosity ($L_{\rm kin}$). To measure the mass of the outflow using the observed molecular line emission, it is necessary to assume that the emission from the outflow is optically thin and that the level populations of the emitting molecule in the outflowing gas are in local thermodynamic equilibrium (LTE). Both of these assumptions are realistic in the high velocity range of protostellar outflows (Dunham, H. G. Arce et al., 2014; Maud et al., 2015). Under these conditions, the column density of the upper level of the observed transition is:

$$N_{\rm u} = \frac{8\pi k_{\rm B}}{hc^3}\frac{\nu^2 \int T_{\rm B} {\rm d}v}{A_{\rm ul}}, \tag{1.12}$$

where $k_{\rm B}$ is Boltzmann's constant, $h$ is Planck's constant, $c$ the speed of light, $\nu$ the frequency of the observed line, and $T_{\rm B}$ the measured brightness temperature, which can be converted to the observed intensity as $I_\nu = 2kT_{\rm B}\nu^2/c^2$, and is integrated over the velocity range of the outflow.

The total column density can then be calculated as:

$$N_{\rm tot} = \frac{Q(T_{\rm ex})}{g_{\rm u}} {\rm e}^{(E_{\rm u}/k_{\rm B}T_{\rm ex})} N_{\rm u}, \tag{1.13}$$

with $Q(T_{\rm ex})$ the partition function, $g_{\rm u}$ the upper level degeneracy, $E_{\rm u}$ the upper level energy, and $T_{\rm ex}$ the excitation temperature of the observed gas. Multiplying 1.13 with the abundance ratio of the observed molecule to $H_2$, $\left[N_{\rm H_2}/N_{\rm tot}\right]$, gives the total column density for $H_2$ and then the total mass can be calculated as:

$$M = \mu m_{\rm H} N_{\rm H_2} A, \tag{1.14}$$

where $\mu$ is the mean molecular weight, $m_{\rm H}$ the hydrogen mass, and $A$ is the area covered by the observations. Combining Eq. 1.12, 1.13, 1.14, the mass can be calculated as:

$$M = \mu m_{\rm H} A \left[\frac{N_{\rm H_2}}{N_{\rm tot}}\right] \frac{Q(T_{\rm ex})}{g_{\rm u}} {\rm e}^{(E_{\rm u}/k_{\rm B}T_{\rm ex})} \frac{8\pi k_{\rm B} \nu^2}{hc^3 A_{\rm ul}} \int T_{\rm B} {\rm d}v \ . \tag{1.15}$$

For convenience, the constants can be gathered in a conversion factor ($K$) which can be used to convert integrated intensity into mass. $K$ is then defined as:

$$K = \mu m_{\rm H} A \left[\frac{N_{\rm H_2}}{N_{\rm tot}}\right] \frac{Q(T_{\rm ex})}{g_{\rm u}} {\rm e}^{(E_{\rm u}/k_{\rm B}T_{\rm ex})} \frac{8\pi k_{\rm B} \nu^2}{hc^3 A_{\rm ul}}. \tag{1.16}$$

Subsequently, the time-averaged kinetic energy of the outflow is calculated as:

$$E_{\rm kin} = \frac{1}{2} M \langle v \rangle^2, \tag{1.17}$$

and its momentum as:

$$P = M \langle v \rangle \tag{1.18}$$

To calculate the corresponding rates, an estimate of the outflows age is required. Assuming that the ejection of material takes place in a steady, continuous flow, the dynamical time, defined as the ratio of the outflow extent over the maximum observed outflow velocity $\left(t_{\rm dyn} = R_{\rm lobe}/v_{\rm out}\right)$ can be used for that purpose. Although, in order to correct for the outflow inclination effects that affect both the $R_{\rm lobe}$ and $v_{\rm out}$, a number of correction factors have been introduced over the years (e.g., T. P. Downes and Cabrit, 2007). The mass loss rate can therefore be calculated as:

$$\dot{M} = \frac{M}{t_{\rm dyn}}, \tag{1.19}$$

and the power of the outflow:

$$L_{\rm kin} = \frac{E_{\rm kin}}{t_{\rm dyn}}. \tag{1.20}$$

For the outflow force, a large number of different calculation methods have been proposed among which van der Marel et al., 2013, proposed the "Separation" method as the most accurate

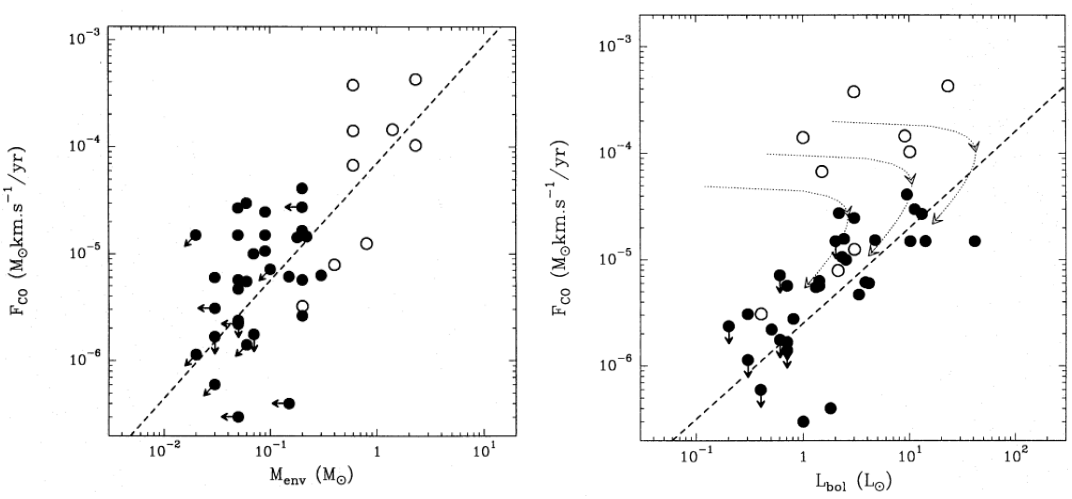


Figure 1.13: Correlation of the outflow force with the envelope mass (left) and the bolometric luminosity (right) as presented by Bontemps, Andre et al., 1996. Empty circles mark Class 0 sources and filled circles Class I, while the dotted arrows mark model evolutionary tracks based on the model presented in the same work.

way of estimating $F$. In that method $F$ is given as:

$$F = \frac{K\left(\sum_{\mathrm{j}}\left[\int_{v_{\mathrm{in}}}^{v_{\mathrm{out,j}}} T(v')v'\mathrm{d}v'\right]_{\mathrm{j}}\right)}{t_{\mathrm{dyn}}}. \tag{1.21}$$

where, $K$ is the conversion factor from Eq. 1.16, the integral $\int_{v_{\mathrm{in}}}^{v_{\mathrm{out,j}}} T(v')v'\mathrm{d}v'$ corresponds to the velocity weighted integrated intensity and the sum covers all pixels (j) that are part of the outflow.

All the above parameters are of particular interest as they not only describe the energetics of the entrained outflows, but are also found to correlate well with the envelope mass ($M_{\mathrm{env}}$) and the bolometric luminosity ($L_{\mathrm{bol}}$) of the source driving the outflow (see Figure 1.13 for an example). These correlation where first introduced for low-mass sources (e.g., Cabrit and Bertout, 1992; Bontemps, Andre et al., 1996), were subsequently expanded to cover also the high-mass regime (e.g., D. S. Shepherd and Churchwell, 1996; Beuther, Schilke et al., 2002) and are still a topic of ongoing study (e.g., Maud et al., 2015; Skretas and Kristensen, 2022). Due to the close connection between the ejection of outflows and the accretion process (Beuther, Schilke et al., 2002), the presence of such scaling relation between outflow and source properties, indicates that accretion scales with the source mass and luminosity. In addition, the shared relation between low- and high-mass sources suggests a common underlying driving mechanism for protostellar outflows across the entire mass regime.

Overall, observations of molecular line emission at the millimeter regime have been a staple of protostellar outflow research. Thanks to the continuous improvements in spectral and angular resolutions of such observations, it has been made possible to study the morphology, kinematics,

and energetics of the large scale, primarily entrained molecular outflows in ever increasing detail, thus making molecular spectroscopy instrumental in shaping our current understanding of the outflow phenomenon.

### 1.3.4 Outflows in the IR regime - shock excited molecular winds and ionic jets

Protostellar outflows are energetic phenomena, with multiple shocks along their fast moving jets as well as accretion shocks onto the central protostar serve to heat, excite, and ionize the gas along the flow. It stands therefore to reason that, protostellar outflows would emit strongly in the many ro-vibrational transitions of abundant molecules that are located in the IR regime. This was confirmed with the development of IR astronomy, both through ground based facilities, such as the Very Large Telescope (VLT), Keck (McLean et al., 1998), and the Infrared Telescope Facility (IRTF; Tokunaga et al., 2015), but especially thanks to the space observatories such as the *Infrared Space Observatory* (ISO; Kessler et al., 1996), the *Spitzer Space Telescope* (Werner et al., 2004), and the *Herschel Space Observatory* (Pilbratt et al., 2010). Through continuum observations in the IR range, these facilities enabled the detection and classification of large numbers of protostars (e.g., Furlan et al., 2008; Evans et al., 2009; Dunham, Stutz et al., 2014). At the same time, IR observatories offered access to the rotational transitions of $H_2$, and the high excitation transitions of molecules such as CO, $H_2O$, and OH, that can probe the hot ($\geq$1000 K) and warm ($\geq$300 K) gas within protostellar outflows (e.g Maret et al., 2009; Karska, Kaufman et al., 2018). They also allowed observations of multiple atomic and ionic fine structure and forbidden transitions that are strongly associated with the cooling of post-shocked gas (e.g., Karska, Herczeg et al., 2013; Nisini, Santangelo et al., 2015) and revealed widespread $H_2O$ emission in protostellar systems (Kristensen, van Dishoeck, Bergin et al., 2012; van Dishoeck, Kristensen et al., 2021). While powerful and instrumental in the development of protostellar outflow studies, these observatories were lacking significantly in terms of spatial resolution when compared to the available radio facilities, which made it difficult to study physical processes at a comparable level of detail. The recently launched *James Webb Space Telescope* (JWST) has allowed for IR observations at much higher resolutions, revealing the complex morphologies of outflows in unprecedented detail (e.g., Figure 1.14).

The Near Infrared Spectrometer (NIRSpec; Böker et al., 2023) and the Mid Infrared Instruments (MIRI; G. S. Wright et al., 2023) Medium Resolution Spectrometer (MRS; Argyriou et al., 2023) on board JWST have revealed extended $H_2$ outflows, displaying a nested structure, with high-$J$ transitions displaying a more collimated pattern and even probing the jet component, and low–$J$ transitions tracing a wide angle wind (Tychoniec, van Gelder et al., 2024; Caratti o Garatti et al., 2024). The collimated jets have also been probed with a number of atomic and ionic lines, predominantly of [Fe II] (e.g., Federman et al., 2024). Thanks to the spatial resolution of JWST, the excitation conditions, velocity distribution and chemical composition of the warm and hot components of protostellar outflows can now be mapped down to scales of a few hundreds of AUs. Still, fundamental questions remain, concerning the launching mechanism of outflows (disk winds vs X-winds, see Section 1.3.1) as well as the origin of the extended $H_2$ emission.

In order to fully understand the nature of the extended $H_2$ emission detected in JWST observations of protostellar outflows it is important to constrain the physical conditions responsible for its

Figure 1.14: The HH211 outflow as seen with JWST NIRCam. The different colors correspond to the different filters of NIRCam (Purple: F162M + F164N, Blue: F210M + F323N, Cyan: F335M, Green: F460M, Orange: F466N, Red: F470N). Figure taken from Ray et al., 2023.

emission. Rotational diagrams are a commonly employed tool for calculating the physical properties of the emitting gas using observations of multiple transitions of a single molecule. The large number of rotational transitions of $H_2$ observable in the IR range that can be accessed by JWST offer a unique opportunity for the estimation of the rotational temperature and column density of the molecular gas within protostellar outflows through the use of rotational diagrams (e.g., Francis et al., 2025).

Rotational diagrams are based on the fact that molecules, under LTE conditions, are distributed into different energy levels according to the Boltzmann distribution. For a two-level system, where $l$ marks the lower and $u$ the upper levels, respectively, the population ratio between the two levels for a fixed temperature $T$ can be written as:

$$\frac{N_u}{N_l} = \frac{g_u}{g_l} \exp\left(-\frac{E_u - E_l}{k_B T}\right), \tag{1.22}$$

where $N_i$ is the population, $g_i$ the degeneracy, and $E_i$ the energy of the $i^{\text{th}}$ level respectively. The

total population of the molecules ($N_{\rm tot}$) is:

$$N_{\rm tot} = N_0 + N_1 + N_2 + ... \tag{1.23}$$
$$= \frac{N_0}{g_0}\left(g_0 + g_0\frac{N_1}{N_0} + g_0\frac{N_2}{N_0} + ...\right) \tag{1.24}$$
$$= \frac{N_0}{g_0}\exp\left(\frac{E_0}{k_BT}\right)\left\{g_0\exp\left(\frac{-E_0}{k_BT}\right) + g_1\exp\left(\frac{-E_1}{k_BT}\right) + g_2\exp\left(\frac{-E_2}{k_BT}\right) + ...\right\} \tag{1.25}$$
$$= \frac{N_0}{g_0}\exp\left(\frac{E_0}{k_BT}\right)Q(T), \tag{1.26}$$

where the partition function, $Q(T)$, for a temperature $T$ is defined as:

$$Q(T) = \sum_{i=0} g_i\exp\left(\frac{-E_i}{k_BT}\right). \tag{1.27}$$

The upper level population of a molecule can therefore be written as:

$$N_u = N_{\rm tot}\frac{N_u}{N_{\rm tot}} = N_{\rm tot}\frac{\frac{g_u}{g_0}\exp\left(-\frac{E_u-E_0}{k_BT}\right)}{\frac{N_0}{g_0}\exp\left(\frac{E_0}{k_BT}\right)Q(T)} = g_u\frac{N_{\rm tot}}{Q(T)}\exp\left(\frac{-E_u}{k_BT}\right) \tag{1.28}$$

In the case where the emission is optically thin, the temperature $T$ is also referred to as the rotational temperature $T_{\rm rot}$, and Eq. 1.28 can be re-arranged as:

$$\ln\frac{N_u}{g_u} = \ln\frac{N_{\rm tot}}{Q(T_{\rm rot})} - \frac{1}{T_{\rm rot}}\frac{E_u}{k_B}. \tag{1.29}$$

This is a linear equation between $\ln(N_u/g_u)$ and $E_u/k_B$, where $N_u$ can be measured using the observed line intensity as described in Eq. 1.12. For observations of multiple transitions of the same molecule, performing a linear fit on the rotational diagram allows the derivation of $T_{\rm rot}$ and $N_{\rm tot}$ from the slope and intercept, respectively.

In the case where more than a single temperature component is present in the gas, the rotational diagram can display a curved shape. Still, assuming that a sufficient number of transitions are available, it is possible to carry out multiple linear fits at the same time to constrain the properties of all the different components simultaneously as shown in Figure 1.15.

In contrast to the radio wavelengths, a critical issue in the study of protostellar outflows in the IR regime is the interstellar extinction. The term, interstellar extinction, describes the wavelength dependent attenuation of starlight due to absorption or scattering by dust grains. Due to the nature of the star forming regions, namely their high density, the effects of extinction are further exacerbated.

The existence of interstellar extinction was first reported by Barnard (1907) and Barnard (1909), who noticed the dimming of stars by a, then unknown, medium. The presence of dust as the cause of extinction was later proposed by Trumpler, 1930, through the studies of the dimming of stars

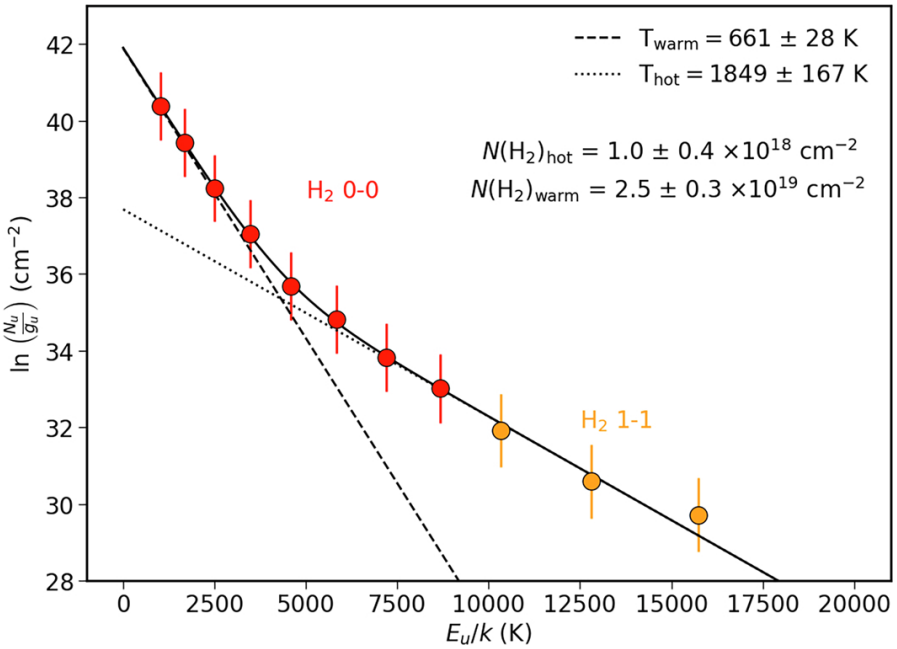


Figure 1.15: Example two-component rotational diagram of the $H_2$ rotational transitions in the wavelength range of the MIRI/MRS on board the JWST. Figure by Tychoniec, van Gelder et al., 2024.

in open clusters. Nowadays, extinction is typically measured in magnitudes, and is defined as:

$$\frac{A_\lambda}{\text{mag}} = 2.5\log_{10}[F_\lambda^0/F_\lambda] \tag{1.30}$$

where $F_\lambda$ is the observed flux, and $F_\lambda^0$ the flux that would be measured in the absence of any extinction. As the understanding of interstellar dust properties increased over time, several different extinction curves have been empirically defined (e.g., McClure, 2009; Pontoppidan et al., 2024). Among those, it was shown by Narang et al., 2024 that the so-called KP5 extinction curve by Pontoppidan et al., 2024 is ideal to de-redden the emission from deeply embedded protostellar sources. An example of the behavior of the KP5 extinction curve between 5 and 20 $\mu$m is shown in Figure 1.16. The different curves correspond to different values of extinction, $A_K$, defined as the extinction at the K-band (2.2 $\mu$m), and which determines the exact wavelength dependent distribution of the extinction, $A_\lambda$.

In protostellar outflow studies, the extinction is usually constrained through observations of the different rotational transitions of $H_2$. More precisely, the extinction can be fitted as an additional parameter in the rotational diagram of $H_2$ alongside $T_{\text{rot}}$ and $N_{\text{tot}}$ as:

$$\ln\frac{N_u}{g_u} = \ln\left(N_{\text{tot}}\frac{\exp(-x/T_{\text{rot}})}{Q(T_{\text{rot}})}10^{\frac{-A_\lambda}{2.5}}\right) \tag{1.31}$$

This method is particularly effective thanks to the strong silicate extinction feature at ~9 $\mu$m that overlaps with the S(3) transition of $H_2$, which causes the S(3) line to appear exceptionally

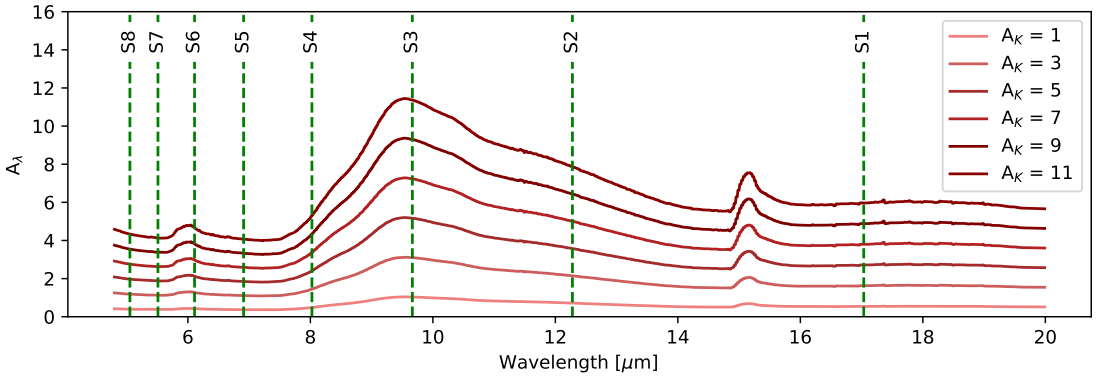


Figure 1.16: Example of the KP5 extinction curve between 5 and 20 $\mu$m. Marked in green are the locations of the pure rotational transitions of $H_2$ over the same range.

suppressed (e.g., Neufeld, Melnick and Harwit, 1998). Constraining the extinction is necessary in order to obtain accurate flux measurements for lines in the IR regime. In turn, this opens the way for the calculation of physical properties of the warm and hot components of protostellar outflows but also enables the study of shock conditions, which are primarily responsible for the gas heating.

### 1.3.5 Explosive outflows

Explosive outflows represent a class of outflows, different from the typical bipolar outflows, but which are also associated with star-forming regions. This new class of outflows was first introduced by Bally and Zinnecker, 2005, who suggested the possible explosive origin of the BN/KL outflow in Orion (Figure 1.17). Since then, the sample of proposed explosive outflows has been expanded, but their total number still remains below 10 (e.g., Zapata, Schmid-Burgk, Pérez-Goytia et al., 2013; Zapata, Ho et al., 2020; Guzmán Ccolque, Fernández-López et al., 2022; Zapata, Fernández-López et al., 2023). It is worth noting that, so far, all explosive outflows are associated with high-mass star formation, but it is unclear whether that is due to limited sample or an inherent property of the outflows (Rivera-Ortiz et al., 2025; Zapata, Fernández-López et al., 2023).

Zapata, Schmid-Burgk, Rodríguez et al., 2017 proposed a number of properties, primarily morphological, that are unique to explosive outflows, and allow their identification. Firstly, explosive outflows are expected to be, baring substantial environmental influence, largely isotropic, with no discernible red- and blue-shifted lobes. In addition, they consist of a large number of narrow, filament-like structures, which also have a Hubble flow[1]-like velocity distribution with the velocity increasing with the distance from the source. Lastly, explosive outflows are not expected to be associated with well defined bow-shock structures that arise when, in a typical bipolar outflow, the collimated jet interacts with the surrounding ISM.

[1] The term Hubble flow refers to the motion of galaxies in the universe due to its expansion. The velocity of a galaxy due to this motion is found to be proportional to its distance from the center of the flow (Hubble, 1929). Therefore, a Hubble flow-like velocity distribution refers describes a velocity structure that increases proportionally to the

The origin of explosive outflows has been suggested to be the result of protostellar mergers (Bally and Zinnecker, 2005) or the dynamical rearrangement of a non-hierarchical protostellar system into a hierarchical one (e.g., Bally, Cunningham et al., 2011; Rivera-Ortiz et al., 2025). In both cases, the release of the potential energy of the collapsing system leads to the formation of the explosive outflows. In terms of observations, explosive outflows have been exclusively discovered using low-$J$ transitions of CO, where the good spatial and spectral resolution available allows the identification of the morphological and kinematic properties that characterize them. However, shock excited $H_2$ and ionic emission, such as from [Fe II] transitions, is also prominent in such outflows (e.g., Bally, Ginsburg, Silvia et al., 2015).

distance from its origin.

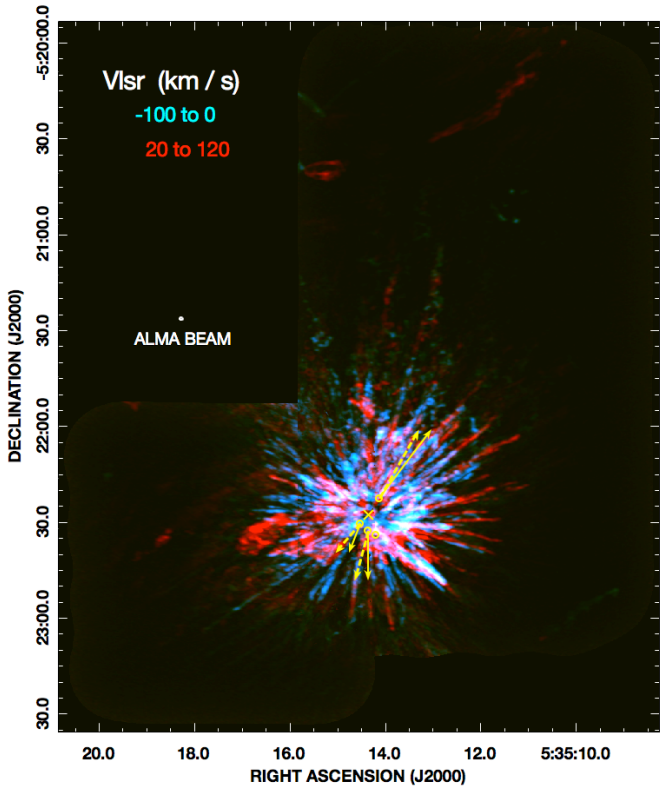


Figure 1.17: High velocity CO $J$ =2-1 emission from the prototypical explosive outflow BN/KL. Figure from Bally, Ginsburg, H. Arce et al., 2017.

## 1.4 Outflow shocks

In studies of the ISM, a shock refers to a pressure-driven disturbance that causes an irreversible change in the medium (Draine, 1980). This kind of shocks are common in protostellar outflows, caused by the interactions of the jet and wind with the surrounding envelope, and along the outflow cavity walls. Theoretically, there are two main types of shocks, the continuous (*C*-type) shocks and the jump (*J*-type) shocks. The type of the shock depends on the combination of the magnetic field strength, the shock velocity, the gas density, and the level of ionization (Draine, 1980; Draine, Roberge and Dalgarno, 1983; Hollenbach and McKee, 1989; Hollenbach, 1997).

In *J*-type shocks, the physical conditions change abruptly, leading to high peak temperatures of the shocked gas. More precisely, for shock velocities below $\sim 30$ km s$^{-1}$, *J* shocks are typically non-dissociative, heating up the gas to temperatures up to a few $10^4$ K (Flower and Pineau des Forêts, 2012). For higher velocities, *J* shocks start to break apart molecular bonds, becoming dissociative and leading up to even higher peak temperatures ($\geq 10^5$ K; Flower and Pineau des Forêts 2012). In that case, however, molecules can reform very efficiently in the post-shock regions. *C*-type shocks happen in areas with strong magnetic fields and low ionization fractions where the ions and neutrals are weakly coupled (Kaufman and Neufeld, 1996). Under such conditions, a magnetic precursor made up of ion-electron plasma carries the information ahead of the disturbance, leading to a continuous change of the physical parameters (see also Figure 1.18). Temperatures in *C* shocks only reach up to a few $10^3$ K, not sufficient to dissociate molecules.

Thanks to its high abundance, $H_2$ dominates the emission from shocked regions. As a result, it is the most commonly used tracer for shocks (e.g., Rosenthal, Bertoldi and Drapatz, 2000;

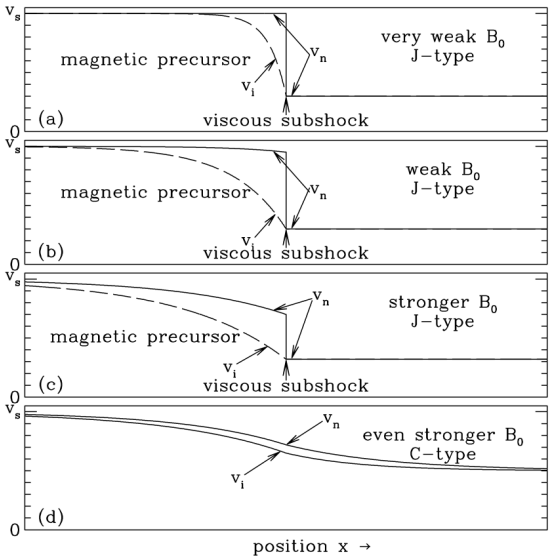


Figure 1.18: Illustration of a two fluids shock for a range of magnetic field strengths. As the magnetic field becomes stronger (from top to bottom), the magnetic precursors becomes more significant, smoothening the transition between the pre- and post-shock regions, until the *J*-type shock is eventually converted into *C*-type. Figure taken from Draine, 2011.

Davis et al., 2007; Kristensen, Ravkilde, Field et al., 2007; Kristensen, Ravkilde, Pineau Des Forêts et al., 2008; Flower and Pineau Des Forêts, 2010; Flower and Pineau des Forêts, 2012). Other abundant molecules, with emission lines in the far-IR, such as $H_2O$ and CO have also been extensively used in the study of shocks (e.g., Kaufman and Neufeld, 1996; Flower and Pineau Des Forêts, 2010; Flower and Pineau des Forêts, 2012).

In addition to the observations, shock models have played a key role in developing our understanding of the physical processes in protostellar outflows. A prominent example of such models is the Paris-Durham shock code (e.g., Flower, Pineau des Forets and Hartquist, 1985; Godard, Pineau des Forêts et al., 2019). Such models typically use a number of shock-related parameters (shock velocity, pre-shock gas density, magnetic field strength) as well as environmental properties (external radiation field, cosmic ray ionization rate, polycyclic aromatic hydrocarbon abundance) as input, in order to reproduce the expected line emission from the shocked gas allowing for direct comparisons with observations (e.g., Kristensen, Godard et al., 2023).

Overall, shocks represent a key mechanism in the studies of star formation, as they are responsible for the majority of gas heating within star forming molecular clouds. Their observed impact though, as seen through the excitation of different molecular lines, is affected by environmental factors, such as the UV radiation field. Thus, in order to properly constrain the shock properties through observations, it is necessary to take into consideration the nature of the environment in which the shock takes place. As such, studies of the different star forming regions are a vital step in understanding shock conditions, by providing constrains of the environmental factors affecting the shock.

## 1.5 Star forming regions

Star forming regions are the areas of space where stars are actively forming. Depending on the highest mass of the stars formed, they are split into high- and low-mass star forming regions. In the following, I will describe the two star forming regions that are central to the work presented in subsequent chapters of this thesis, the high-mass star forming region Cygnus-X and the low-mass star forming region of Ophiuchus.

### 1.5.1 Cygnus-X

The Cygnus-X star forming region is a molecular cloud complex, i.e., it is comprised of multiple distinct molecular clouds that form a coherent and interconnected structure (Schneider, Bontemps et al., 2006, see also Figure 1.19). It was first detected as a secondary peak in the Galactic radio continuum (at ~160 MHz) by Reber, 1944, and was subsequently named by Piddington and Minnett, 1952. Cygnus-X is estimated to have a size upwards of 100 pc in radius, and a total mass of ~3-4 $\times$ $10^6$ $M_\odot$ (Leung and Thaddeus, 1992; Schneider, Bontemps et al., 2006). The distance to Cygnus-X was estimated using parallax measurements of methanol and water masers at 6.7 GHz and 22 GHz respectively to be $\sim$ 1.4 kpc (Rygl et al., 2012). Overall, thanks to its high molecular gas content, its ability to form massive stars, along with its relatively short distance from the Sun, Cygnus-X is established as one of the closest high-mass star-forming regions in the Galaxy.

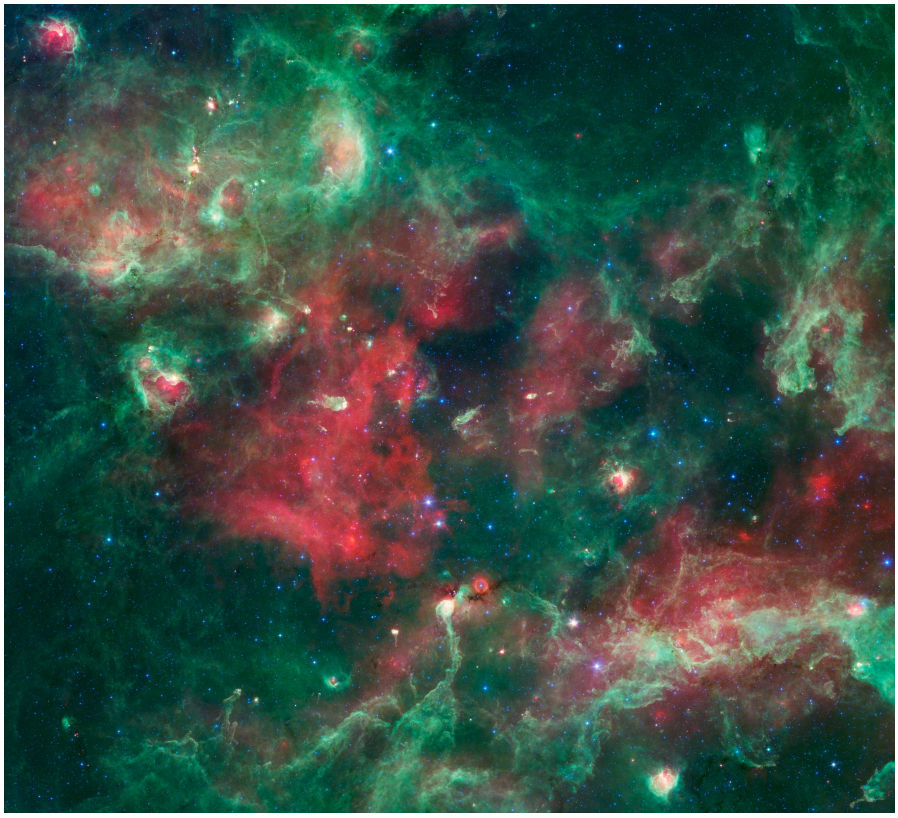

Figure 1.19: The *Spitzer space telescope* view of the Cygnus-X molecular cloud complex. The 3.6-micron light is represented in blue color, the 4.5-micron light in blue-green, the 8.0-micron light in green, and the 24-micron light in red. Image credit: NASA/JPL-Caltech/Harvard-Smithsonian CfA, and Beerer et al., 2010.

Over the years, Cygnus-X has been the target of multiple studies, which have revealed that it contains numerous high-mass protostars, across all stages of their formation. More precisely, Cygnus-X is is host to a considerable number of massive dense cores (Motte, Bontemps, Schilke et al., 2007; Cao, Qiu, Q. Zhang, Y. Wang, Hu et al., 2019; Cao, Qiu, Q. Zhang, Y. Wang and Xiao, 2021), several MYSOs including some well-known sources such as DR21 Main, DR21 (OH), W75N, AFGL 2591, and S106-IR (e.g., M. D. Smith, Eisloffel and Davis, 1998; van der Tak et al., 1999; Schneider, Simon et al., 2002; D. S. Shepherd, S. E. Kurtz and Testi, 2004), a large number of H II regions (e.g., Wendker, Higgs and Landecker, 1991; Schneider, Bontemps et al., 2006), several OB associations (e.g., Uyaniker et al., 2001), including one of the largest OB associations in the Galaxy, Cyg OB2 (Knödlseder, 2000), and some Supernova remnants (Uyaniker et al., 2001) including the so-called Cygnus loop (or Diamond ring) (e.g., Minkowski, 1958; Levenson et al., 1998; Dannhauer et al., 2025). In addition, Cygnus-X is found to have significant outflow activity, displaying a large number of molecular outflows (e.g., Duarte-Cabral, Bontemps, Motte, Hennemann et al., 2013; Skretas and Kristensen, 2022; Yang, Qiu and Pan, 2024), with the massive outflow of DR21 Main (R. Garden et al., 1986; Skretas, Karska, Wyrowski et al., 2023;

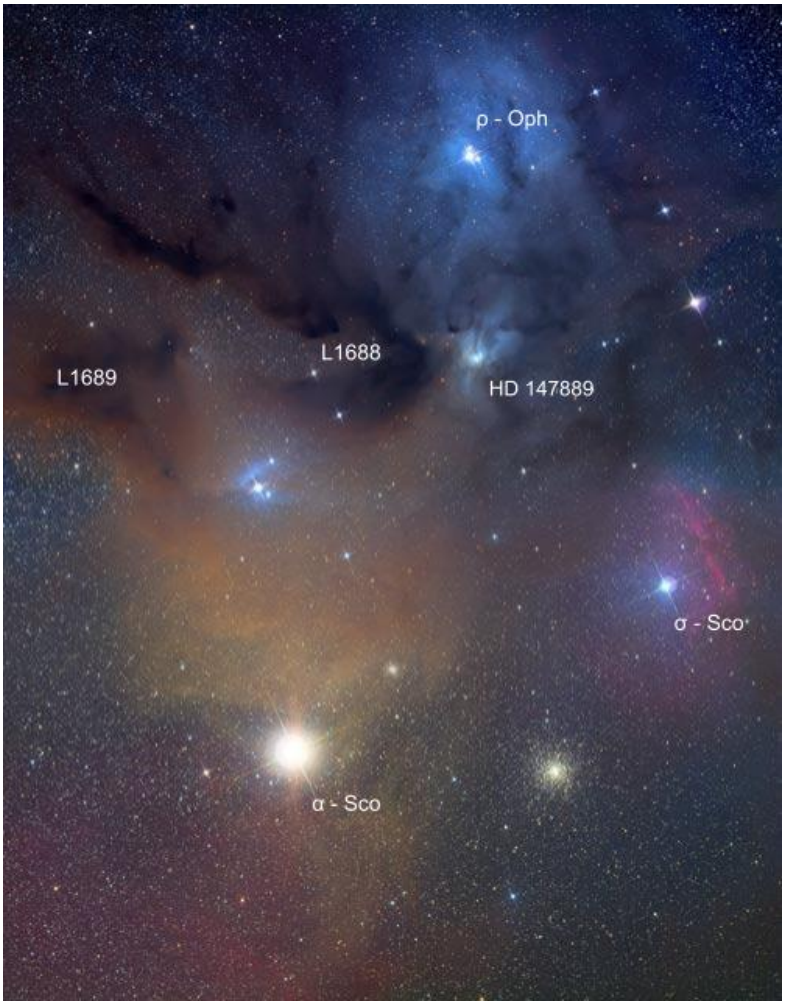


Figure 1.20: Optical image of the $\rho$ Ophiuchus cloud complex and its surroundings. Adapted from (Wilking, Gagné and Allen, 2008), background image credit: Robert Gendler, Jim Misti, and Steve Mazlin.

Karska, Figueira et al., 2025) being the most prominent example, but also collimated jets (e.g., Davis et al., 2007)

The vicinity of Cygnus-X, especially in comparison to other high-mass star-forming regions, along with its high star forming activity make it stand apart as a unique region where all the stages of high-mass star formation can be simultaneously studied in detail.

### 1.5.2 Ophiuchus

The Ophiuchus molecular cloud complex is a nearby low to intermediate mass star forming region, named after the adjacent $\rho$-Oph star system. Its distance has been measured at ~137 pc, based on trigonometric parallax measurements using Very Large Baseline Array (VLBA) radio observations (Ortiz-León et al., 2017), while its total mass has been estimated to be $\sim 10^4$ $M_\odot$

(Dame, Hartmann and Thaddeus, 2001).

Ophiuchus is comprised of two main molecular clouds, named L1688 and L1689 following the Lynds, 1962 nomenclature, along with a number of smaller, filamentary clouds that extend toward the northeast, up to distances of ∼10 pc (Loren, 1989a; Loren, 1989b, see also Figure 1.20). Out of the two main clouds, L1688 is also referred to as the core of Ophiuchus, because it is by far the most active, containing more than 300 YSOs that span all the evolutionary stages from Class 0 to Class III (e.g., Lada and Wilking, 1984; Andre, Ward-Thompson and Barsony, 1993; Gagné, Skinner and Daniel, 2004; Wilking, Meyer et al., 2005; van Kempen, van Dishoeck et al., 2009), multiple molecular outflows (e.g., Andre, Martin-Pintado et al., 1990; M. Zhang and H. Wang, 2009; Hatchell, Terebey et al., 2012; van der Marel et al., 2013), and atomic jets marked by strings of HH objects (e.g., Wilking, Schwartz et al., 1997; Wu et al., 2002; Gómez et al., 2003). These sources are spread across the six dense clumps, named Oph-A to Oph-F, detected within L1688 by Mezger et al., 1992. In contrast to L1688, L1689 is surprisingly quiescent, with only a limited number of forming stars (Nutter, Ward-Thompson and André, 2006). This difference in star formation activity, has been partially attributed to the difference in their respective mass reservoirs, with L1688 having more than twice the mass of L1689, but also to the influence of the nearby Sco-Cen association believed to trigger the star formation in L1688 (e.g., Loren, 1989a).

In addition to the members of the Sco-Cen association, there are a number of additional stars influencing the Ophiuchus region. Some examples include the namesake of the region, the $\rho$-Oph star cluster (Pillitteri et al., 2014), located to the north of the two main clouds (see also Figure 1.20), the HD 147889 star located to the west of L1688 (Liseau et al., 1999), and the S1 star hidden inside the dense dust cocoon of L1688 (Loinard et al., 2008). The influence of the surrounding stars is also held responsible for the, on average, higher UV radiation field measured in the region (van Dishoeck and Black, 1986).

Like the Cygnus X region, owing to its proximity and rich star formation activity, Ophiuchus allows for detailed observations of all the different stages of low-mass star formation. As a result it has over time consistently been the target of multi-wavelength observations, contributing significantly in furthering our understanding of the processes that govern the formation of stars. In addition, the higher than average UV radiation in the region makes Ophiuchus a prime laboratory for the study of the impact of UV radiation on the star formation process.

## 1.6 Scientific goals and outline of this thesis

As presented in the previous sections, the star formation process and the protostellar outflows that accompany it have been extensively studied over the years. Despite these efforts, many fundamental questions still remain unanswered, and new ones emerge, as observations become more sensitive and achieve higher spatial resolutions

A question that has recently arisen concerns the nature of several extreme protostellar outflows that have been detected in our Galaxy. While many of those objects where initially considered as bipolar outflows driven by a particularly massive protostar, or protocluster (e.g., the DR21 Main outflow; R. Garden et al., 1986; R. P. Garden, Hayashi et al., 1991; R. P. Garden and Carlstrom, 1992), more recent studies have proposed an entirely different scenario for their launching that relies on the explosive disintegration of the initial protostellar system (e.g., Bally

and Zinnecker, 2005; Zapata, Schmid-Burgk, Pérez-Goytia et al., 2013; Zapata, Schmid-Burgk, Rodríguez et al., 2017, and also Section 1.3.5). While the number of proposed explosive outflows has been increasing recently, it remains extremely low, with fewer than 10 cases reported to date. In addition, their detection currently relies solely upon certain morphological properties seen exclusively in the low$-J$ $^{12}$CO emission. As a result, the nature of such outflows is still unclear. Do explosive outflows really form a separate class of protostellar outflows? Or do they simply represent the extreme case of the typical bipolar outflows associated with star formation? And if indeed they form a new type of outflow, what are the best methods to identify and study them? Therefore, obtaining robust confirmation of the true nature of the currently proposed sample of explosive outflows is a vital step in understanding the importance of this newly proposed phenomenon.

Another major question that persists is whether the process of star formation is at all impacted by the broader environment in which it takes place. While existing models describe accurately the formation of isolated stars (see Section 1.1), in reality stars often form within regions containing multiple separate protostars (or protoclusters), all forming simultaneously. Do stars that form in an environment with a very high density of forming stars evolve differently from those forming in more quiescent regions? In addition, the clouds in which the stars form are not homogeneous, but instead are made up of interlocking filamentary structures and have varying morphologies and densities. Does therefore the relative location in which a star forms, within its parental molecular cloud, have an impact on its formation? Large scale surveys of entire star forming regions, such as the recent Cygnus Allscale Survey of Chemistry and Dynamical Environments (CASCADE; Beuther, Wyrowski et al., 2022) present an opportunity to investigate the overall impact of large scale environment on star formation.

Lastly, recent JWST results have shown the presence of widespread $H_2$ emission within protostellar outflows of both low and high mass sources (e.g., Caratti o Garatti et al., 2024; Tychoniec, van Gelder et al., 2024; Francis et al., 2025). While the origin of this emission has generally been attributed to shocks along the protostellar jet and cavity walls,the questions still remain: Where is $H_2$ actually excited? What are the conditions at the vicinity of protostars and the properties of shocks that lead to the observed line intensities? In addition, UV irradiation has been shown to play an important role in setting the abundances of molecular species inside protostellar outflows (e.g., Karska, Kristensen et al., 2014; Kristensen, van Dishoeck, Mottram et al., 2017), but its origin remains uncertain. Is this UV radiation produced locally, within protostellar outflows? Or is it coming from external sources, such us nearby massive stars that affect the entire star-forming region? Placing constraints on the origin of the UV radiation, as well as its impact on the shocks and how they drive the excitation of $H_2$ emission in protostellar outflows are necessary to understand the complex phenomenon of protostellar outflows.

In the following sections, I present in detail the different projects that I carried out as part of this thesis, aiming to address these questions.

In Chapter 2, I discuss the observations of the DR21 Main outflow, obtained as part of the CASCADE project. With this study, I aimed to evaluate the morphological, kinematic, and energetic properties of the outflow, using multiple different molecular tracers, in order to constrain its nature as an explosive or bipolar type of outflow. In addition, the results of this study allowed for updated comparisons between the DR21 Main outflow and other protostellar outflows and

therefore determine whether DR21 Main is truly an exceptional source, or rather it represents an upper limit of the more typical protostellar outflows.

In Chapter 3, I expanded the analysis of the CASCADE observations to investigate the outflow activity along the entire DR21 filament, the densest and most actively star forming part of the Cygnus-X complex. Using the complete sample of outflows associated with the dense molecular clumps(Motte, Bontemps, Schilke et al., 2007; Cao, Qiu, Q. Zhang, Y. Wang, Hu et al., 2019; Cao, Qiu, Q. Zhang, Y. Wang and Xiao, 2021), combined with literature information on the DR21 filament (Schneider, Csengeri et al., 2010; Hennemann et al., 2012), allowed me to identify factors that influence the outflow activity (and by extension the star formation process) within a star forming region. Furthermore, the comparison of outflows identified within DR21 – one of the most active SFRs in the galaxy, to outflows driven by sources located within more quiescent regions is ideal to investigate the impact of environmental conditions on the star formation process.

In Chapter 4, I investigated the hot, shock excited inner parts of protostellar outflows, down to scales of a few hundreds of AUs. Using spectroscopic observations from JWST, targeting five low-mass protostars in Ophiuchus, I studied the morphology of molecular outflows and ionic jets. In addition, leveraging the multiple available $H_2$ transitions, I aimed to constrain the conditions of the shock excited components of the outflows. Additionally, through comparisons with state of the art shock models, I searched for the impact of UV irradiation on shock excitation and investigated its origin.

Chapter 5 presents a summary of all the results presented in this thesis as well as a brief outlook covering the possible next steps that will allow us to expand and build upon this work in the future.

CHAPTER 2

# CASCADE: A detailed kinematic analysis of the DR21 Main outflow

*This chapter contains a summary of the first published article associated with this thesis, titled:*

"**The Cygnus Allscale Survey of Chemistry and Dynamical Environments: CASCADE. II. A detailed kinematic analysis of the DR21 Main outflow**"

I. M. Skretas, A. Karska, F. Wyrowski, K. M. Menten, H. Beuther, A. Ginsburg, A. Hernández-Gómez, C. Gieser, S. Li, W.-J. Kim, D. A. Semenov, L. Bouscasse, I. B. Christensen, J. M. Winters A. Hacar
Astronomy & Astrophysics, Volume 679, id.A66.

*The full article can be found in Appendix B.*

*Author contributions: IMS performed the scientific analysis and wrote the manuscript with the supervision from AK and comments from co-authors. IMS also performed the central part of the imaging of the spectral line data used in this work. The remaining data reduction and calibration was done by HB.*

## 2.1 Context

Protostellar outflows are a ubiquitous phenomenon, closely associated with the formation process of both high and low mass stars. The close link between outflows and accretion, along with the impact they have on the surrounding ISM, has established protostellar outflows as a key ingredient in regulating star formation. Over the past $\sim$ 20 years, a different type of outflows has been introduced. These "new" outflows have been named explosive outflows, and appear also connected with the star formation process (e.g., Bally and Zinnecker, 2005; Zapata, Schmid-Burgk, Ho et al., 2009, ; see also Section 1.3.5). The outflow of DR21 Main, located at a distance of 1.5 kpc (Rygl et al., 2012) in the Cygnus-X high-mass star-forming region, is one of the most massive protostellar outflows in the Galaxy (R. Garden et al., 1986; R. P. Garden, Hayashi et al., 1991). Recently, DR21 Main has been proposed to be part of the, still limited, sample of explosive outflows (Zapata, Schmid-Burgk, Pérez-Goytia et al., 2013).

The northern parts of the Cygnus-X region, including the entirety of the DR21 Main outflow was recently covered by the CASCADE project (Beuther, Wyrowski et al., 2022). CASCADE is a Max Planck IRAM Observatory Program (MIOP) that targeted the densest parts of the Cygnus-X North region using both the NOEMA interferometer and the Institut de Radioastronomie Millimètrique (IRAM) 30m telescope. With an extended bandwidth, covering a total of 16 GHz, and substantial spectral and angular resolutions of 62.5 kHz and 2-4 arcseconds, respectively, CASCADE offers a unique opportunity to study the DR21 Main outflows in great detail.

## 2.2 Aims

The primary aim of this project is to obtain an updated view of the DR21 Main outflow using the multiple molecular gas tracers available in the CASCADE observations. Through these observations, the morphological, kinematic and energetic properties of the outflow have been determined in an effort to constrain the true nature of the driving mechanism behind the DR21 Main outflow.

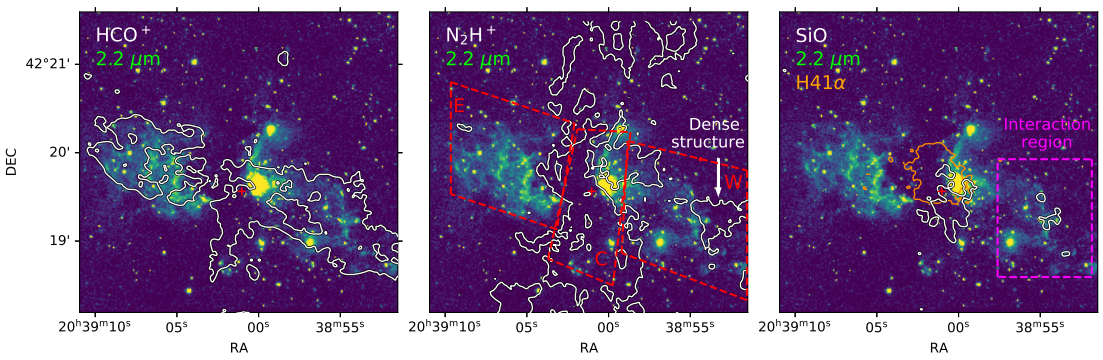


Figure 2.1: Example of the three different emission morphologies seen among the different molecular tracers covered in the CASCADE range. The background emission is the 2.2 micron continuum emission from the United Kingdom Infra-Red Telescope (UKIRT) *Wide Field Camera* (WFCAM) probing shock excited $H_2$ emission from the outflow (Warren et al., 2007). The white contours mark the $5\sigma$ $HCO^+$ (left), $N_2H^+$ (middle) and SiO (right) emission, while intensities are integrated between -50 and 50, -20 and 10 ,and -20 and 20 km $s^{-1}$ for the $HCO^+$, $N_2H^+$ and SiO emission, respectively. Figure taken from Skretas, Karska, Wyrowski et al. (2023).

## 2.3 Methods

In order to assess the morphology of DR21 Main outflow, I created a series of integrated intensity maps for all the different molecular lines in within the range of the CASCADE observations. Spectra, extracted at different positions along the outflow (east lobe, center, and west lobe), were used in order to determine the velocity range for the integration. In addition, the creation of channel maps and position-velocity (PV) diagrams provided us with information about the behavior of the emission at different velocities. By comparing the morphological and kinematic

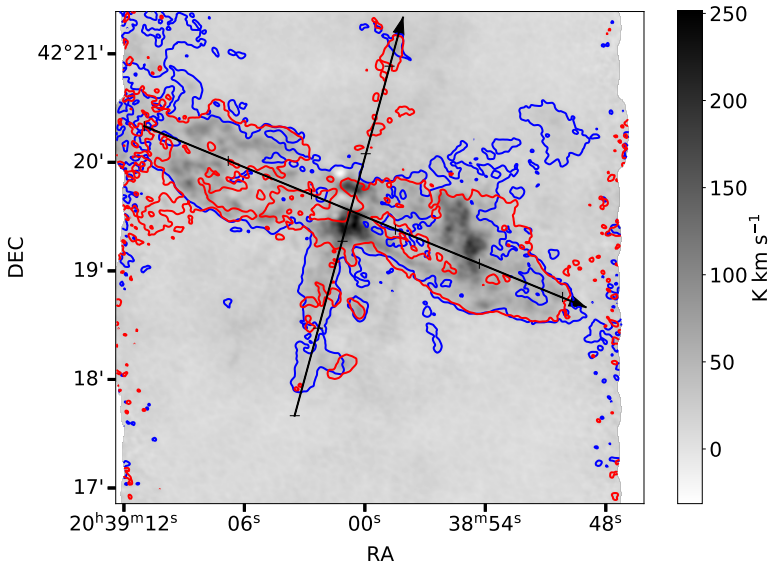


Figure 2.2: Contour of the redshifted (5 to 45 km $s^{-1}$) and blueshifted (-5 to -45 km $s^{-1}$) $HCO^+$ emission shown in red and blue respectively. The contours correspond to 5 $\sigma_{rms}$ emission and the velocity ranges are given relative to the source velocity of -3 km $s^{-1}$. Background emission is the integrated $HCO^+$ emission from -50 to 50 km $s^{-1}$. Figure taken from Skretas, Karska, Wyrowski et al. (2023).

properties of the DR21 Main outflow to those of the Orion BN/KL outflow (the prototypical explosive outflow source; see Figure 1.17), I attempted to discern its true nature. Finally, by estimating its energetic properties, I was able to more directly compare the outflow of DR21 Main to those of other sources, and determine whether it is indeed a unique, extreme case or simply represents a particularly powerful protostellar outflow.

## 2.4 Results

The integrated intensity maps of the different molecular emission lines in the CASCADE range showed the existence of three separate patterns of emission. As shown in Figure 2.1, the first type of emission is primarily associated with the molecular outflow, the second is best tracing the denser material, revealing the core of the DR21 filament that extends in the North-South direction, and lastly, the third type of emission appears more centrally concentrated around the DR21 Main H II region or sporadic. Among all the available molecular tracers, $HCO^+$, $N_2H^+$, and SiO are the most prominent examples of the three separate morphologies, with $HCO^+$ best tracing the molecular outflow, $N_2H^+$ revealing the densest regions, and SiO showing close to the outflow center and sporadic emission in the western lobe.

The integrated intensity maps of the blue- and red-shifted $HCO^+$ emission revealed an almost complete overlap of the two outflow components in both lobes of the DR21 Main outflow (see Figure 2.2). Such a behavior is not typical of bipolar outflows, where a clear separation between the blue- and red-shifted emission is expected. In contrast, explosive outflows are known to have

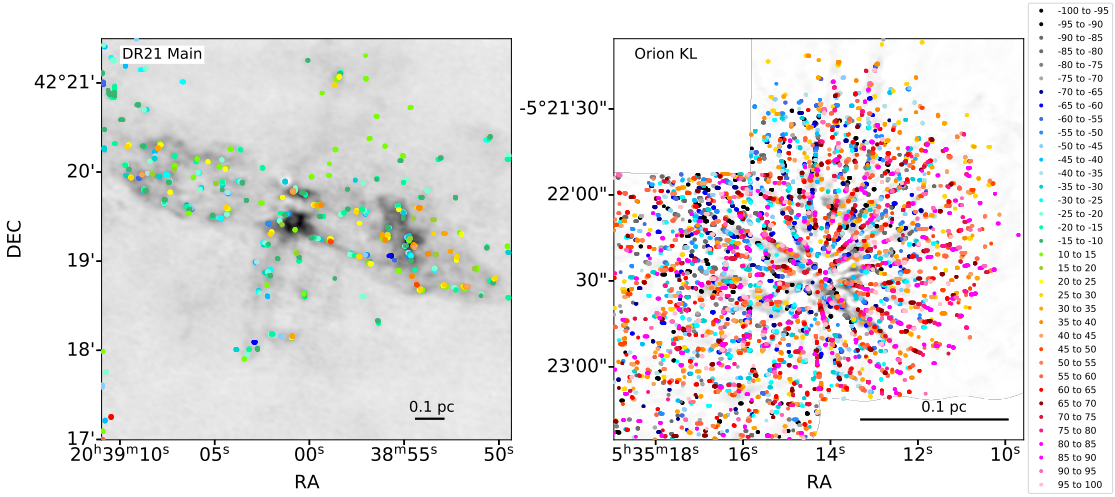


Figure 2.3: Distribution of gas velocities associated with the outflows in DR21 (left) and Orion KL (right, Bally, Ginsburg, H. Arce et al., 2017). Each point shows a local intensity peak of the $HCO^+$ emission (above 2 $\sigma$) integrated in velocity steps of 5 km $s^{-1}$. The color of the points signifies the corresponding velocity steps and are shared for the two plots. Background gray-scale shows the integrated $HCO^+$ (left panel) and CO emission (right panel) over the entire velocity range of the outflows (from $-70$ to 70 km $s^{-1}$ for DR21 Main and $-100$ to 100 km $s^{-1}$ for Orion KL). Figure taken from Skretas, Karska, Wyrowski et al. (2023).

substantial overlap of blue- and red-shifted emission. Another possible explanation for the overlap of the two components, which also aligns with the presence of two prominent lobes in the outflow emission, is that the outflow of DR21 Main extends along or very close to the plane of the sky, and the blue- and red-shifted components trace the sideway expansion of the outflow cavity walls.

To further investigate the nature of the DR21 Main outflow, Figure 2.3 shows the side by side comparison of the local intensity peaks at different velocity steps for the DR21 Main and Orion BN/KL outflows. The coherent velocity structures seen in Orion BN/KL are largely absent in the case of DR21 Main. Since these structures are believed to be a key characteristic of explosive outflows, this result suggests that the DR21 Main outflow appears more like a typical bipolar outflow instead of an explosive outflow. It is important to note though the difference in resolution between the two sources, with DR21 Main being located much further away than Orion. Still, given the length of these structures in Orion, one would expect to also see them in DR21 Main. Despite the fact that the results suggest that the outflow of DR21 Main resembles more a typical bipolar outflow, the energetic properties measured (e.g., mass loss rate, outflow force etc.) solidify it as one of the most exceptional outflows in the Galaxy, with outflow properties substantially higher than most other outflow sources.

Finally, a close look into the western lobe of the outflow revealed signs of ongoing interaction between the outflow and a dense molecular structure located there. More precisely, the $HCO^+$ outflow emission (grayscale in Figure 2.4) can be seen peaking right in front of the dense molecular structure that is traced by the $N_2H^+$ emission (blue contours in Figure 2.4). In addition, $H_2CO$ and SiO emission, typically associated with shocks is detected along the interface of the outflow

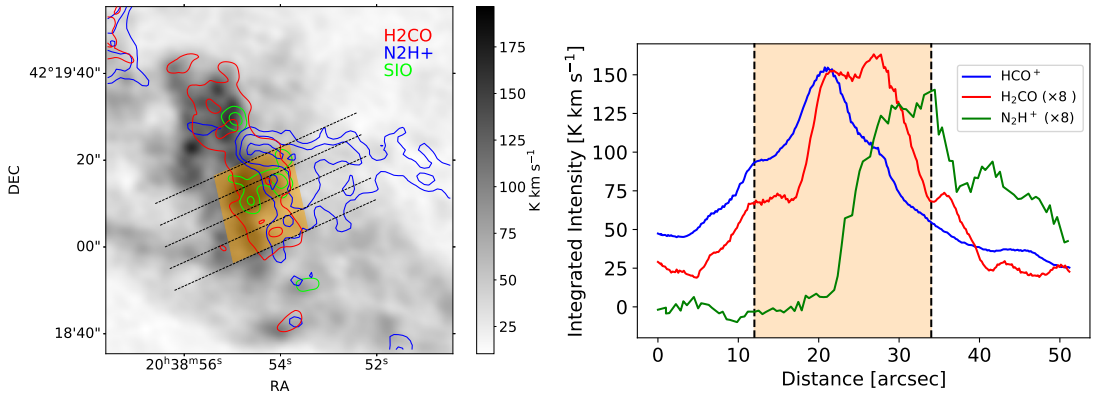


Figure 2.4: [Left:] Zoom-in on the western lobe of the DR21 Main outflow, where it is interacting with a nearby dense molecular structure. Background grayscale shows the integrated $HCO^+$ emission, integrated between -50 and 50 km $s^{-1}$ relative to the source velocity. Red contours show line emission of $H_2CO$, blue contours show the emission of $N_2H^+$ and green contours show the emission of SiO. All contour levels are at 5, 10 and 20 $\sigma_{\rm rms}$ of the corresponding emission. [Right:] Average integrated intensities of $HCO^+$ (in blue), $H_2CO$ (in red), and $N_2H^+$ (in green) across the interaction region in the western lobe of DR21. Intensities are integrated from -70 to 70, -20 to 20 and -20 to 10 km $s^{-1}$ for $HCO^+$, $H_2CO$ and $N_2H^+$, respectively. The x-axis shows the distance in arcseconds measured along the black lines shown in the left panel. The orange rectangle shows the area actively affected by the interaction and is also marked in the left panel. The intensities for $H_2CO$ and $N_2H^+$ are scaled up by a factor of 8 in order for their distributions to be more easily comparable to that of $HCO^+$. Figure adapted from Skretas, Karska, Wyrowski et al. (2023).

with the dense structure, strongly indicating the ongoing interaction between the two components.

## 2.5 Conclusions

Overall, through the analysis of the CASCADE observations covering the outflow of DR21 Main, I found that its morphology and kinematic behavior is more akin that of a bipolar outflow, rather than an explosive one. Still, the exceptionally high energetic properties measured, reaffirm the position the outflow of DR21 Main as an extreme case among protostellar outflows. Finally, the ongoing interaction detected between the outflow and a nearby dense molecular structure represents an unique opportunity for further studies of the impact of outflows in their surroundings.

CHAPTER 3

# CASCADE: Overview of the molecular outflows along the DR21 ridge

## 3.1 Introduction

Bipolar outflows serve as a clear signpost of star formation. They are a necessary bi-product of the accretion process, as by removing excess angular momentum from the protostar-disk system they enable the infall of material along the disk (Pudritz, Ouyed et al., 2007; Frank et al., 2014). Star formation models describing the launch of protostellar outflows initially proposed for low-mass stars (e.g., F. Shu et al., 1994; Pudritz and Norman, 1983) have also been developed for their high-mass counterparts (e.g., Vaidya et al., 2011; Oliva and Kuiper, 2023), and such outflows have been detected in many sources across the mass spectrum (e.g., Beuther and D. Shepherd, 2005; H. G. Arce, D. Shepherd et al., 2007; Bally, 2016). These outflows inject significant amounts of momentum and energy in the surrounding ISM and are believed to be responsible for the dispersion of the natal, protostellar envelopes. As a result, protostellar outflows play a key role in regulating the star formation efficiency (e.g., Fall, Krumholz and Matzner, 2010; Frank et al., 2014).

The protostellar outflows are most often observed in the low $J$ rotational transitions of CO (e.g., van der Marel et al., 2013), but other molecules, such as $HCO^+$ have also been used (e.g., H. G. Arce and Sargent, 2006; Skretas, Karska, Wyrowski et al., 2023). This molecular emission is tracing the cold, entrained molecular gas and allows for the calculation of several energetic properties of the protostellar outflow, such as the outflow mass $M$, momentum $p$ and kinetic energy $E_{\rm kin}$, as well as the equivalent rates, mass loss rate $\dot{M}$, force $F$ and kinetic luminosity $L_{\rm kin}$. Several correlations have been discovered, connecting these outflow properties, with the properties of the molecular core (e.g., the mass and luminosity) hosting the driving protostar, both for low- (e.g., Bontemps, Andre et al., 1996; Yıldız et al., 2015; Mottram et al., 2017) and high-mass sources (e.g., Beuther, Schilke et al., 2002; Maud et al., 2015). Recent studies of these correlations across extended mass regimes have shown significant differences between the behavior of low- and high-mass sources (Skretas and Kristensen, 2022). These differences are further highlighted by the limited amount of intermediate mass sources (e.g. van Kempen, Hogerheijde et al., 2016) included in these studies. The overall similarities and differences of low-

and high-mass star formation remain a matter of discussion (e.g., Beuther, Kuiper and Tafalla, 2025). In addition, previous studies, especially on the high-mass regime, often targeted sources in different molecular clouds with varying environments. By constraining the environment of the sources the characteristic of the driving sources that influences the outflow properties can be traced better.

In this work, I aim to identify all molecular outflows associated with dense molecular clumps, the early stage of high-mass star formation, within the DR21 filament. Using these sources, I intend to expand the existing correlations between the properties of outflows and their driving sources and investigate whether these are impacted by the environment in which the stars are formed. More precisely, the goal is to compare the outflow properties of sources along the DR21 ridge with the established correlations in order to identify whether the extreme nature of the filament impacts the formation process of stars.

To that end, I present here observations of the DR21 ridge, taken as part of the Cygnus Allscale Survey of Chemistry and Dynamical Environments (CASCADE) (Beuther, Wyrowski et al., 2022). CASCADE is a large Max Planck IRAM Observatory Program (MIOP) covering the densest regions of the Cygnus-X molecular cloud complex in the 3 mm window, with high angular resolution and with a broad bandpass. The observations where carried out using both the Northern Extended Array for Millimeter Astronomy (NOEMA) and the 30 m telescope, both operated by the Institut de Radioastronomie Millimètrique (IRAM). The combined use of single-dish and interferometric observations is crucial as it provides the angular resolution required to identify molecular outflows while at the same time, maintaining the full information of the more extended spatial scales. For more details on the scope and goals of CASCADE I refer the reader to the original publication of the project in Beuther, Wyrowski et al. (2022).

The Cygnus-X giant molecular cloud complex, located at a distance of $\sim$ 1.4 kpc (Rygl et al., 2012) is one of the nearest active high-mass star-forming regions. It is also one of the largest molecular cloud complexes in the Milky Way, with an estimated total molecular mass of $\sim 3 \times 10^6$ $M_\odot$ and a projected size of $\sim$ 130 pc (Cao, Qiu, Q. Zhang, Y. Wang, Hu et al., 2019). The complex hosts all stages of high-mass star-formation, containing a large number of ultra-compact H II regions (Cyganowski et al., 2003) and a significant population of OB stars (N. J. Wright et al., 2010), along with one of the largest known OB associations in the Galaxy, Cyg OB2 (Knödlseder, 2000).

The DR21 filament is the most active region within Cygnus-X thus offering an ideal target to study the impact of a clustered environment on the process of star formation. It spans a length of $\sim$ 4 pc with a total mass of $\sim 10^4$ $M_\odot$ and typical $H_2$ column densities of $\sim 10^{23}$ cm$^{-2}$ (Schneider, Csengeri et al., 2010; Hennemann et al., 2012). At the southern end of the DR21 filament is the prominent compact H II region DR21 Main (D. Downes and Rinehart, 1966; Immer et al., 2014) driving a massive outflow perpendicular to the filament (R. Garden et al., 1986; R. P. Garden, Hayashi et al., 1991; Skretas, Karska, Wyrowski et al., 2023) while, the OH, $H_2O$, and $CH_3OH$ maser source DR21 (OH) is located further north (Mangum, Wootten and Mundy, 1992). In addition, Motte, Bontemps, Schilke et al. (2007) using IRAM 30m telescope observations at 1.2 mm identified a significant number of dense molecular cores along the DR21 filament. These cores display a gradient of evolutionary stages, with the northern end of the ridge being less evolved than the southern end (Hennemann et al., 2012). The list of dense cores in DR21 was

Table 3.1: Continuum and spectral line parameters for the lines studied in this work

| Species | Trans. | Freq. [GHz] | $\sigma_{\rm rms}$ $\left[\frac{\rm mJy}{\rm beam}\right]$ | Beam [arcsec] | $E_{\rm up}/k$ [K] | $\log_{10}(A_{\rm ij})$ [$s^{-1}$] |
|---|---|---|---|---|---|---|
| $H^{13}CO^+$ | 1-0 | 86.754 | 7.5 | 2.74×2.49 | 4.16 | -4.41 |
| SiO | 2-1 | 86.847 | 9.6 | 3.25×2.70 | 6.25 | -4.53 |
| $HCO^+$ | 1-0 | 89.189 | 7.7 | 3.29×2.74 | 4.28 | -4.38 |
| Cont. | - | 90.0 | 0.05 | 2.80×2.54 | - | - |

**Notes:** The rms noise level, $\sigma_{\rm rms}$, is calculated for channels of 2.0 km $s^{-1}$. Rest frequencies are from NIST recommended rest frequencies (Lovas, 2004) and the Cologne Database for Molecular Spectroscopy (CDMS, Müller et al. (2001)), while the upper level energy, $E_{\rm up}$, and the Einstein coefficient for spontaneous emission, $A_{\rm ij}$, are taken from CDMS.

expanded by Cao, Qiu, Q. Zhang, Y. Wang, Hu et al. (2019) and Cao, Qiu, Q. Zhang, Y. Wang and Xiao (2021), who made use of additional continuum observations of the complex at shorter wavelengths (70 - 850 $\mu$m) taken with *Herschel* PACS and SPIRE cameras as well as with the James Clerk Maxwell Telescope (JCMT) SCUBA receiver.

The present chapter is organized as follows. Section 3.2 describes the observations from CASCADE as well as the different dense core catalogs covering the DR21 ridge. Section 3.3 presents $HCO^+$ and $H^{13}CO^+$ spectra along with the associated integrated intensity maps for the high velocity $HCO^+$ emission for all cores along DR21. In addition, outflow properties for all detected outflows are calculated. In Section 3.4 the derived outflow properties are discussed both in context with the known properties of the DR21 filament but also in comparison with additional literature samples. A brief comparison between $HCO^+$ and CO outflows from previous studies is also presented in this section. Finally, Section 3.5 contains the summary and conclusions.

## 3.2 Observations and data analysis

The observations of the DR21 filament, presented in this work, were taken as part of the CASCADE project (Beuther, Wyrowski et al., 2022). The DR21 filament was covered by a total of six NOEMA mosaic tiles, each covering an area of 16 $arcmin^2$ and corresponding to 78 NOEMA pointings. Observations were carried out using both the C and D configurations and have a total bandwidth of 16 GHz in the 3 mm atmospheric window. The spectral resolution in the full frequency range probing the continuum is 2.0 MHz (or $\sim$ 6.5 km $s^{-1}$), while prominent spectral lines are covered in dedicated narrow windows with a spectral resolution of 62.5 kHz (or $\sim$ 0.2 km $s^{-1}$), thanks to the use of the additional high-resolution correlator units available to NOEMA. The NOEMA observations for the DR21 filament were carried out between May 17 and November 18, 2020, with a total of 10 antennas available at the time, leading to baselines between ~15 m and $\sim$ 365 m. For the bandpass calibration, the quasars 3C345 and 3C273 were used, for the flux calibration MWC349 and 2010+723, while for gain calibration 2005+403, 2120+445, 2050+363 and 2013+370 were used. For the calibration and imaging of the data, the CLIC and MAPPING

software of the GILDAS package[1] were used.

Complementary single-dish observations, providing the missing short spacing information, were carried out with the IRAM 30 m telescope between February and July 2020. These observations are presented in detail in Christensen et al. (2024). To better cover the high-velocity material of the protostellar outflows,I reduced the spectral resolution of the combined NOEMA and IRAM 30m telescope from the best possible resolution of 0.8 km s$^{-1}$ to 2 km s$^{-1}$, allowing us to create datacubes that cover extended velocity ranges with higher sensitivity. For this work, the emission of $HCO^+$, $H^{13}CO^+$ and SiO is used. The resulting single channel $\sigma_{\rm rms}$ noise, for a channel width of 2 km s$^{-1}$, and beam sizes for the three targeted lines are shown in Table 3.1.

### 3.2.1 Continuum observations

From the full frequency range of the NOEMA observations, omitting spectral lines, the 3mm continuum emission was constructed.. In order to provide short-spacings information for the continuum, additional observations using the Green Bank Telescope's (GBT) MUSTANG-2 instrument were performed. MUSTANG-2 offers a 4.2′ field-of-view (FOV), using an array of 215 feedhorn-coupled TES bolometers (Dicker et al., 2014), and has a 30 GHz bandpass, with an effective center close to 90 GHz (Ginsburg et al., 2020). The GBT observations where carried out between February 2 and March 14 2022, as part of the GBT22A-280 project. Data calibration and reduction was done using the MUSTANG IDL Data Analysis System (MIDAS; Romero et al., 2020). The MUSTANG-2 observations where then combined with the upper side band data from NOEMA, which are also centered around 90 GHz. For the combination of the two datasets, the uv_short task from the GILDAS software package was used. The final synthesized beam of the combined data is $3.32'' \times 2.66''$, and the noise is $\sigma_{\rm rms} = 0.07$ mJy beam$^{-1}$. The GBT observations along with the combination process are described in more detail in Kim et al. (2025). The final continuum image for the entire DR21 filament is shown in Figure 3.1. Note though that the strong artifacts caused by the presence of the powerful continuum

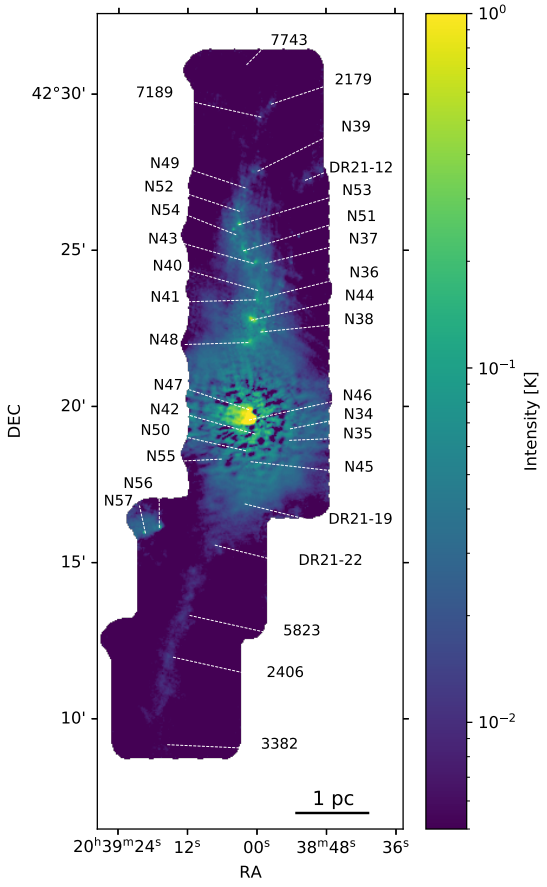


Figure 3.1: Combined NOEMA and GBT 3.6 mm continuum map of the DR21 filament region. Marked are the location of all dense clumps associated with the region (see Section 3.2.2).

[1] https://www.iram.fr/IRAMFR/GILDAS/

source DR21 Main influence a big part of the map. Since emission at 3.6mm can have also string free-free contributions these observations are not ideal for the identification of cores, still they can be used to assist in identifying the locations of the driving sources of protostellar outflows.

### 3.2.2 Dense molecular clumps in the CASCADE field

The Cygnus-X region, and especially the DR21 filament, is a very active high-mass star-forming region, which has already been covered by multiple continuum surveys and there are multiple clump catalogs available in the literature. For this work, I make use of the Motte, Bontemps, Schilke et al. (2007), Cao, Qiu, Q. Zhang, Y. Wang, Hu et al. (2019), and Cao, Qiu, Q. Zhang, Y. Wang and Xiao (2021) catalogs, in order to create the most complete sample of clumps and cores in the area of the DR21 filament, covered by the CASCADE observations.

I primarily follow the naming conventions from Motte, Bontemps, Schilke et al. (2007), with sources named as N followed by a number (e.g., 'N51'). For sources that appear in the Cao, Qiu, Q. Zhang, Y. Wang, Hu et al. (2019) catalog and have no corresponding clumps in Motte, Bontemps, Schilke et al. (2007), I adopt the name from the former publication, which consists of the larger structure name followed by an increasing number (e.g., 'DR21-12'). Finally, for cores that only appear in the Cao, Qiu, Q. Zhang, Y. Wang and Xiao (2021) catalog, the four digit number assigned on the core is used (e.g., '5823').

The Motte, Bontemps, Schilke et al. (2007) catalog is based on continuum observations at 1.2 mm, with a resolution of $11''$, and using the MAMBO camera of the IRAM 30m telescope. Their masses are then calculated as:

$$M_{1.2\,\mathrm{mm}} \approx 5.3 M_{\odot} \times \left(\frac{S^{\mathrm{int}}_{1.2\,\mathrm{mm}}}{100\mathrm{mJy}}\right)\left(\frac{d}{1.7\mathrm{kpc}}\right)^{2} \times \left(\frac{\kappa_{1.2\,\mathrm{mm}}}{0.01\mathrm{cm}^{2}\mathrm{g}^{-1}}\right)^{-1}\left(\frac{T_{\mathrm{dust}}}{20\mathrm{K}}\right)^{-1} \tag{3.1}$$

where $S^{\mathrm{int}}_{1.2\,\mathrm{mm}}$ is the integrated flux at 1.2 mm, $d$ is the assumed distance, $\kappa_{1.2\,\mathrm{mm}}$ is the dust opacity at 1.2 mm, and $T_{\mathrm{dust}}$ is the dust temperature. Volume averaged densities are then calculated as:

$$< n_{\mathrm{H_2}} >= \frac{M_{1.2\,\mathrm{mm}}}{\frac{4}{3}\pi \times FWHM^{3}} \tag{3.2}$$

where $FWHM$ is the full width at half maximum, determined by Gaussian fits. For more details on the source catalog I refer to the original publication by Motte, Bontemps, Schilke et al. (2007).

The Cao, Qiu, Q. Zhang, Y. Wang, Hu et al. (2019) catalog makes use of *Herschel* PACS (70 and 160 $\mu$m with resolutions of $9.2''$ and $12.6''$ respectively), SPIRE (250, 350, and 500 $\mu$m with resolutions of $18.4''$, $25.2''$, and $36.7''$ respectively), and JCMT SCUBA-2 (450 and 850 $\mu$m with resolutions of $7.9''$ and $13''$ respectively) in addition the the aforementioned IRAM 30m (1.2 mm) continuum observations. Sources are then extracted using the *getsources* (Men'shchikov et al., 2012; Men'shchikov, 2017). Four additional criteria where applied to ensure the robustness of the detected cores: i) Having fluxes in at least three bands, ii) having SEDs that can be fitted to

obtain masses and temperatures, iii) having a relative mass error in the SED fitting of $\frac{\Delta M}{M} < 0.8$, and iv) having a relative temperature error of $\frac{\Delta T}{T} < 0.5$. Masses and dust temperatures for the sources in Cao, Qiu, Q. Zhang, Y. Wang, Hu et al. (2019) are estimated from the SED fitting. In addition, the far-IR luminosity, column density, and volume density are also calculated as:

$$L_{\rm FIR} = 4\pi D^2 \int_0^{+\infty} F_\nu {\rm d}\nu \tag{3.3}$$

$$N_{\rm H_2} = \frac{4}{\pi} \frac{M}{\mu_{\rm H_2} m_{\rm H} FWHM^2} \tag{3.4}$$

$$n_{\rm H_2} = \frac{6}{\pi} \frac{M}{\mu_{\rm H_2} m_{\rm H} FWHM^3} \tag{3.5}$$

where $FWHM$ is the deconvolved FWHM size at 160 $\mu$m. As Cao, Qiu, Q. Zhang, Y. Wang, Hu et al. (2019) focused on massive dense cores, only sources with $M > 40 M_\odot$ are included in their catalog.

The core sample from Cao, Qiu, Q. Zhang, Y. Wang and Xiao (2021) was derived by applying the $getsources$ algorithm on the $N_{\rm H_2}$ map, constructed from the SED fits presented in Cao, Qiu, Q. Zhang, Y. Wang, Hu et al. (2019). To improve the robustness of the algorithm results, the following criteria where used: i) $M_{\rm core} > 0.07 M_\odot$, ii) relative core mass uncertainty, as given by $getsources$ $\frac{\Delta M}{M} \leq 1$, iii) core $FWHM \leq 0.6$ pc, and iv) distance from edge of field $\geq 50''$ in order to avoid artifacts.

For the core sample used in this work, I included all sources from the Motte, Bontemps, Schilke et al. (2007) catalog, subsequently adding those from the Cao, Qiu, Q. Zhang, Y. Wang, Hu et al. (2019) and Cao, Qiu, Q. Zhang, Y. Wang and Xiao (2021) catalogs, with no equivalent source reported in Motte, Bontemps, Schilke et al. (2007). A summary of all unique cores in the three catalogs, that will be studied in this work, along with their properties, are given in Table 3.2. In addition, the location of all cores is marked in Figure 3.1.

Table 3.2: Core properties for sources in the CASCADE field

| Name | RA | DEC | $FWHM$ [$''$] | $M$ [$M_\odot$] | $<n_{H_2}>$ [$10^5$ cm$^{-3}$] | $T$ [K] | $N_{H_2}$ [$10^{22}$cm$^{-2}$] | $L_{FIR}$ [$L_\odot$] | Classification |
|---|---|---|---|---|---|---|---|---|---|
| | | | | **DR21** | | | | | |
| N36 | 20:38:58.49 | 42:23:30.12 | 0.19 | 11 | 120000 | – | – | – | – |
| N38/DR21-13 | 20:38:59.40 | 42:22:23.16 | 0.18 / 0.054 | 138/ 85.3 | 2.7 / 131 | 20.7 | 152.7 | 643 | IR-quiet |
| N39/DR21-15 | 20:38:59.90 | 42:27:32.04 | 0.16 / 0.18 | 10 / 51.1 | 0.3 / 2.1 | 14.2 | 8.1 | 40.1 | starless |
| N41 | 20:39:00.19 | 42:23:25.08 | 0.03 | 10 | 19 | – | – | – | – |
| N42/DR21-17 | 20:39:00.29 | 42:19:06.96 | 0.05/0.206 | 5/47.6 | 4.5/1.3 | 20.6 | 5.8 | 348 | IR-quiet |
| N45/DR21-16 | 20:39:01.10 | 42:18:14.04 | 0.13/0.159 | 16/50.6 | 0.64/3 | 15.9 | 10.3 | 79.9 | IR-quiet |
| N47 | 20:39:01.39 | 42:19:54.12 | 0.08 | 19 | – | – | – | – | – |
| N48/DR21-3 | 20:39:01.49 | 42:22:03 | 0.17/0.177 | 197/261 | 3.5/11.1 | 22.6 | 42.8 | 3353 | IR-bright |
| N49/DR21-14 | 20:39:01.99 | 42:27:00 | 0.15/(0.086) | 8/72.6 | 1.2/≥32.1 | 12.6 | ≥56.4 | 27.6 | IR-quiet |
| N50/DR21-6 | 20:39:01.90 | 42:18:34.92 | 0.24/(0.086) | 12/121 | 1.0/≥53.6 | 15.4 | ≥94.3 | 153 | IR-quiet |
| /DR21-20 | – | – | 0.119 | 37.9 | 5.4 | 14.6 | 13.8 | 35.9 | IR-quiet |
| N52/DR21-21 | 20:39:03.00 | 42:26:15 | 0.16/0.175 | 33/37.2 | 0.49/1.6 | 16.2 | 6.3 | 64.8 | IR-quiet |
| N53/DR21-7 | 20:39:03.19 | 42:25:49.08 | 0.14/0.053 | 85/115 | 2.2/186.2 | 17.0 | 213.1 | 267 | IR-quiet |
| N54 | 20:39:03.60 | 42:25:30 | 0.18 | 24 | 0.6 | – | – | – | – |
| N37 | 20:38:58.61 | 42:24:34.92 | 0.03 | 4 | 8.7 | – | – | – | – |
| N40/DR21-8 | 20:38:59.81 | 42:23:43.08 | 0.33/0.159 | 106/114 | 1.1/6.7 | 19.8 | 23.2 | 672 | IR-quiet |
| N43/DR21-23 | 20:39:00.60 | 42:24:34.92 | 0.19/0.106 | 66/35.1 | 1.1/7 | 34.7 | 16.1 | 5865 | IR-bright |
| N51/DR21-4 | 20:39:02.40 | 42:24:59.04 | 0.19/0.078 | 125/153 | 2.0/77.8 | 19.7 | 131.3 | 853 | IR-bright |
| N56/DR21-9 | 20:39:16.90 | 42:16:06.96 | 0.12/0.053 | 32/94.9 | 1.4/152.6 | 14.6 | 175.2 | 89.7 | IR-quiet |
| N46/DR21-1 | 20:39:01.39 | 42:19:33.96 | 0.19/0.195 | 949/1355 | 9.1/43.3 | 20.6 | 183.5 | 10095 | IR-bright |
| N44/DR21-2 | 20:39:01.01 | 42:22:45.84 | 0.14/0.134 | 446/1048 | 10.0/103.7 | 21.0 | 301.7 | 8600 | IR-quiet |
| N55/DR21-11 | 20:39:06.10 | 42:18:19.08 | 0.15/(0.086) | 11/89.9 | 0.8/≥39.7 | 14 | ≥69.8 | 66.3 | starless |
| N57/DR21-10 | 20:39:19.30 | 42:15:56.16 | 0.09/0.06 | 11/94.1 | 1.5/105.1 | 10.3 | 136.3 | 10.6 | IR-quiet |
| N34/DR21-5 | 20:38:54.29 | 42:19:17.04 | 0.19/0.226 | 23/125 | 0.61/2.6 | 17.5 | 12.6 | 351 | IR-quiet |
| N35 | 20:38:54.41 | 42:18:55.08 | 0.13 | 8 | 1.5 | – | – | – | – |
| DR21-19 | 20:39:02.12 | 42:16:53 | 0.169 | 39.6 | 1.9 | 16.2 | 7.1 | 68.6 | IR-quiet |
| DR21-12 | 20:38:51.65 | 42:27:14.50 | (0.086) | 88.5 | ≥39.1 | 13.0 | ≥68.7 | 41.7 | IR-quiet |
| DR21-22 | 20:39:07.30 | 42:15:33.90 | 0.202 | 36.5 | 1 | 17.8 | 4.6 | 111 | IR-quiet |
| 2179 | 20:38:57.567 | 42:29:40.78 | 0.272 | 27.95 | – | 17.4 | – | – | – |
| 2406 | 20:39:14.526 | 42:11:58.52 | 0.559 | 39.097 | – | 19.33 | – | – | – |
| 3382 | 20:39:15.503 | 42:09:10.29 | 0.438 | 15.946 | – | 19.74 | – | – | – |
| 5823 | 20:39:11.660 | 42:13:18.73 | 0.528 | 34.512 | – | 19.56 | – | – | – |
| 7189 | 20:38:59.247 | 42:29:16.02 | 0.136 | 2.602 | – | 17.52 | – | – | – |
| 7743 | 20:39:01.818 | 42:30:56.49 | 0.296 | 9.722 | – | 18.5 | – | – | – |

**Notes:** Sources following the "NXX" naming convention are taken from Motte, Bontemps, Schilke et al. (2007), those with "DR21-XX" are taken from Cao, Qiu, Q. Zhang, Y. Wang, Hu et al. (2019) and "XXXX" sources are from Cao, Qiu, Q. Zhang, Y. Wang and Xiao (2021). Where two values are presented, separated by "/", the source was detected in both Motte, Bontemps, Schilke et al. (2007) and Cao, Qiu, Q. Zhang, Y. Wang, Hu et al. (2019). The first value given is from Motte, Bontemps, Schilke et al. (2007) and the second from Cao, Qiu, Q. Zhang, Y. Wang, Hu et al. (2019). (a) Values taken from the catalog where the source was initially reported if available. (b) Values only available for sources in the Cao, Qiu, Q. Zhang, Y. Wang, Hu et al. (2019) and Cao, Qiu, Q. Zhang, Y. Wang and Xiao (2021) catalogs . (c) Information only available for sources in the Cao, Qiu, Q. Zhang, Y. Wang, Hu et al. (2019) catalog. (1) Both DR21-6 and DR21-20 fall within the FWHM of N50.

## 3.3 Results

### 3.3.1 Core-averaged spectra

I extracted $HCO^+$ and $H^{13}CO^+$ spectra at the location of all sources listed in Table 3.2. The spectra are averaged over the area covered by the FWHM of the corresponding source. There are several notable features appearing on spectra of various sources. Some examples of spectra, displaying these features, are shown in Figure 3.2. The spectra for all remaining sources are shown in Appendix A.1.

The most common characteristics of the $HCO^+$ spectra are extended line wings, suggesting the presence of molecular outflows (see e.g., N47, N53, and N44, Figure 3.2). Depending on the source, the wings extend from ~few km $s^{-1}$ all the way up to ~70 km $s^{-1}$ from the source velocity (indicated by vertical black lines in Figure 3.2). In addition, line wings do not always appear to be symmetrical, with some sources, showing a dominant wing (e.g., N47 and N53). Some sources also show signs of absorption at the source velocity that leads to double peaked spectra (e.g., N44 and N53). Since the short spacing information from the IRAM 30m single-dish observations is included in the data, this effect cannot be attributed to spatial filtering effects introduced from the interferometric observations. Instead, the double peaked profiles are most likely a result of high optical depth and self-absorption of $HCO^+$.

Two additional velocity components are commonly seen in my sources, apart from the main velocity component of the DR21 filament at –3 km $s^{-1}$. The first such component is the known 9 km $s^{-1}$ component, believed to be originating from material associated with W75N and extends to the South in front of the DR21 ridge (J. R. Dickel, H. R. Dickel and W. J. Wilson, 1978; Schneider, Csengeri et al., 2010). This velocity component is seen in multiple sources along the DR21 ridge, both in absorption (e.g., N47) or emission (e.g., 5823) depending on the level of background emission. The second velocity component appears at ~18 km $s^{-1}$ and is seen in sources towards the southern end of the DR21 ridge (e.g., 5823). Since this velocity matches well the main velocity component of N56 and N57, it is attributed to extended and diffuse material associated with the structure containing the two sources and located to the East of the DR21 ridge. Channel maps of the $HCO^+$ emission for the three velocity components are shown in Figure 3.3. In addition, certain sources,show a 'shelf'-like emission feature between ~0 and ~10 km $s^{-1}$ (e.g., N55). This is likely the result of the aforementioned 9 km $s^{-1}$ component, shifting to slightly lower velocities, and merging with the emission from the main velocity component.

### 3.3.2 $HCO^+$ outflow maps

As mentioned in Section 3.3.1, a large number of sources in the sample show substantial wing features in their core-averaged spectra. Such wings are often signs of ongoing outflow activity, originating from the protostars within the cores. Identifying protostellar outflows in regions such as the DR21 filament is not a trivial process. The high density of star formation in the region means that multiple outflows can appear in close proximity, creating confusion regarding the exact origin of each individual high velocity component. Adding to the complexity are outflows from more evolved sources than the ones examined in this work, as well as large scale flows along the filament that can appear as either blue- or red-shifted. In an effort to verify which cores

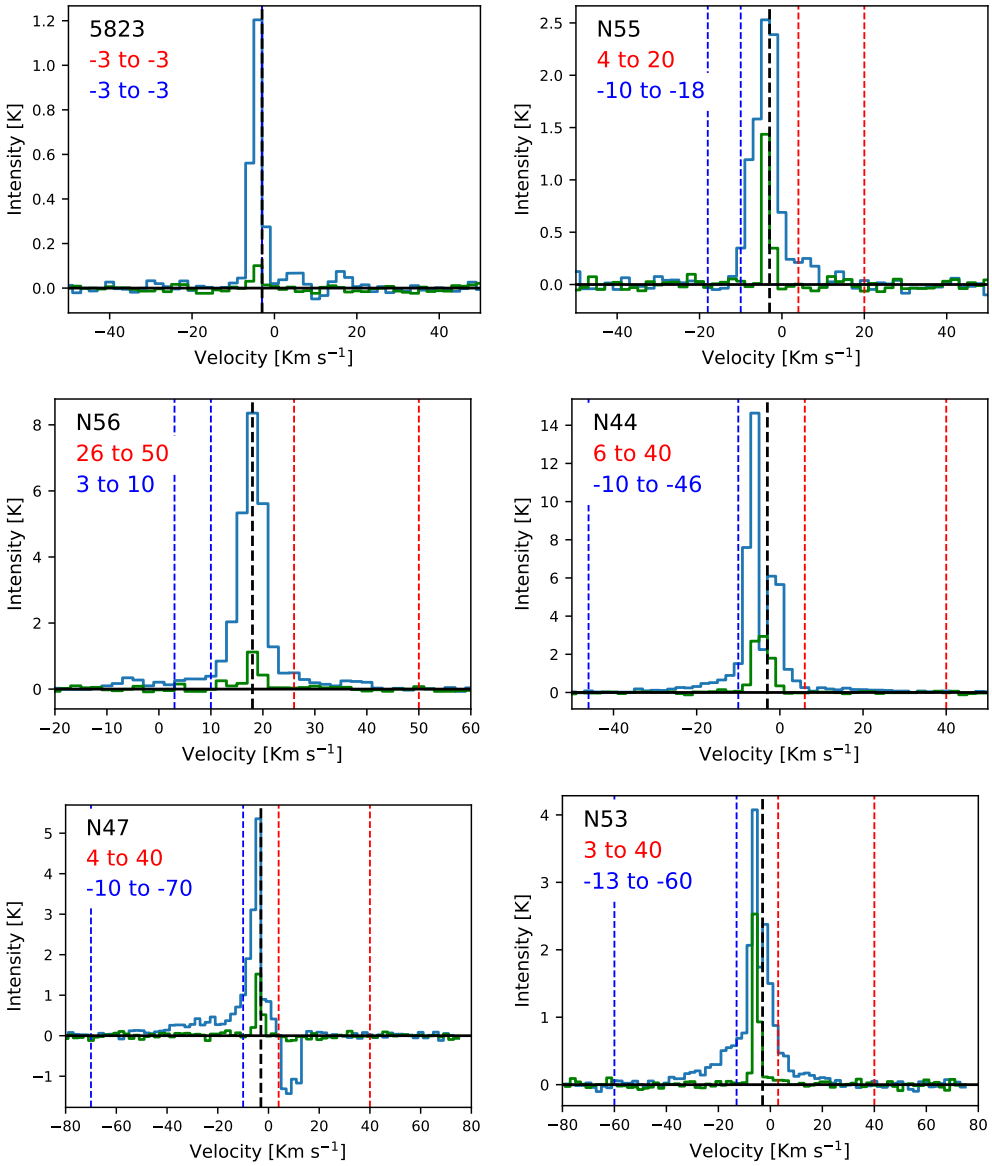


Figure 3.2: Spectra of $HCO^+$ $J$=1-0 (blue) and $H^{13}CO^+$ $J$=1-0 (green) for clumps along DR21 Ridge: 5823, N55, N56, N44, N47 and N53. The spectra were averaged over the FWHM of the corresponding clumps (Table 3.2). Red and blue dashed lines mark the velocity range associated with outflow wing emission. The black dashed line marks the source velocity, $v_{\rm source}$ = -3 km s$^{-1}$ for all sources except N56, which is located in a separate structure east of DR21, where $V_{\rm source}$ = 18 km s$^{-1}$.

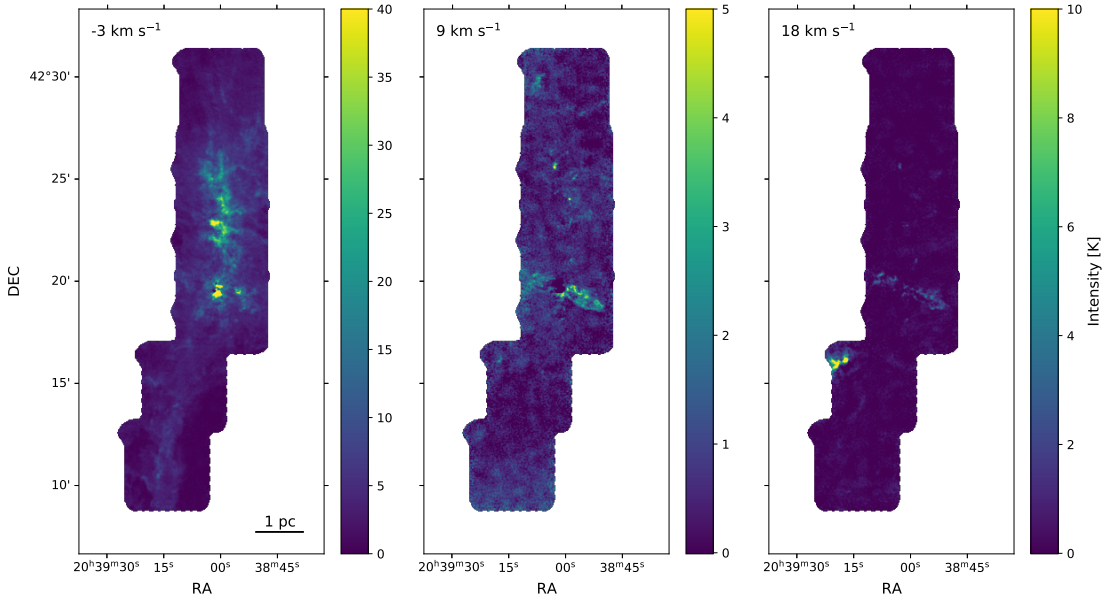


Figure 3.3: $HCO^+$ channel maps of the 3 different velocity components detected in the DR21 filament. The main component at -3 km s$^{-1}$ is shown on the left panel, the 9 km s$^{-1}$ component is shown in the middle, while the 18 km s$^{-1}$ component is on the right. The velocity width of the channels is 2.0 km s$^{-1}$.

actually contain outflow driving sources I examined in detail integrated intensity maps of the high-velocity $HCO^+$ emission as well as channel maps of the same tracer. In addition, I used the 3 mm CASCADE continuum, along with available literature information, in order to connect the detected high velocity $HCO^+$ component to either a continuum driving source, or to a previously reported molecular outflow. Figures 3.4, and 3.5 show the $HCO^+$ outflow emission for the sources I was able to confirm their outflows. Maps for the remaining sources with velocity wings or other notable features seen in their spectra, such as emission in additional velocity components or a 'shelf'-like emission feature (see Section 3.3.1), but no clear outflow, are shown in Figure A.6. The velocity ranges used for the contours in each source were selected by comparing the $HCO^+$ spectrum with that of the usually optically thin $H^{13}CO^+$ isotopologue. The velocity ranges used for each source are noted on the corresponding spectrum are shown in table 3.3. For sources in the DR21 ridge, the channel at 9 km s$^{-1}$ is not included in the integration in order to avoid contamination from the foreground component. Below I discuss each outflow source in more detail.

**N37:** No clear continuum peak, associated with N37, can be seen in the 3.6 mm emission map. Nevertheless, I report the tentative presence of a bipolar outflow, extending along the E-W direction. The red lobe appears brighter, and extending to higher velocities compared to the blue lobe. Interestingly, the red lobe appears clearly detached from the N37 core. This, combined with the presence of SiO emission at the forward edge of the red lobe, suggests that the HCO+ emission is likely tracing compressed, entrained gas at the front of the outflow. The relative weakness of

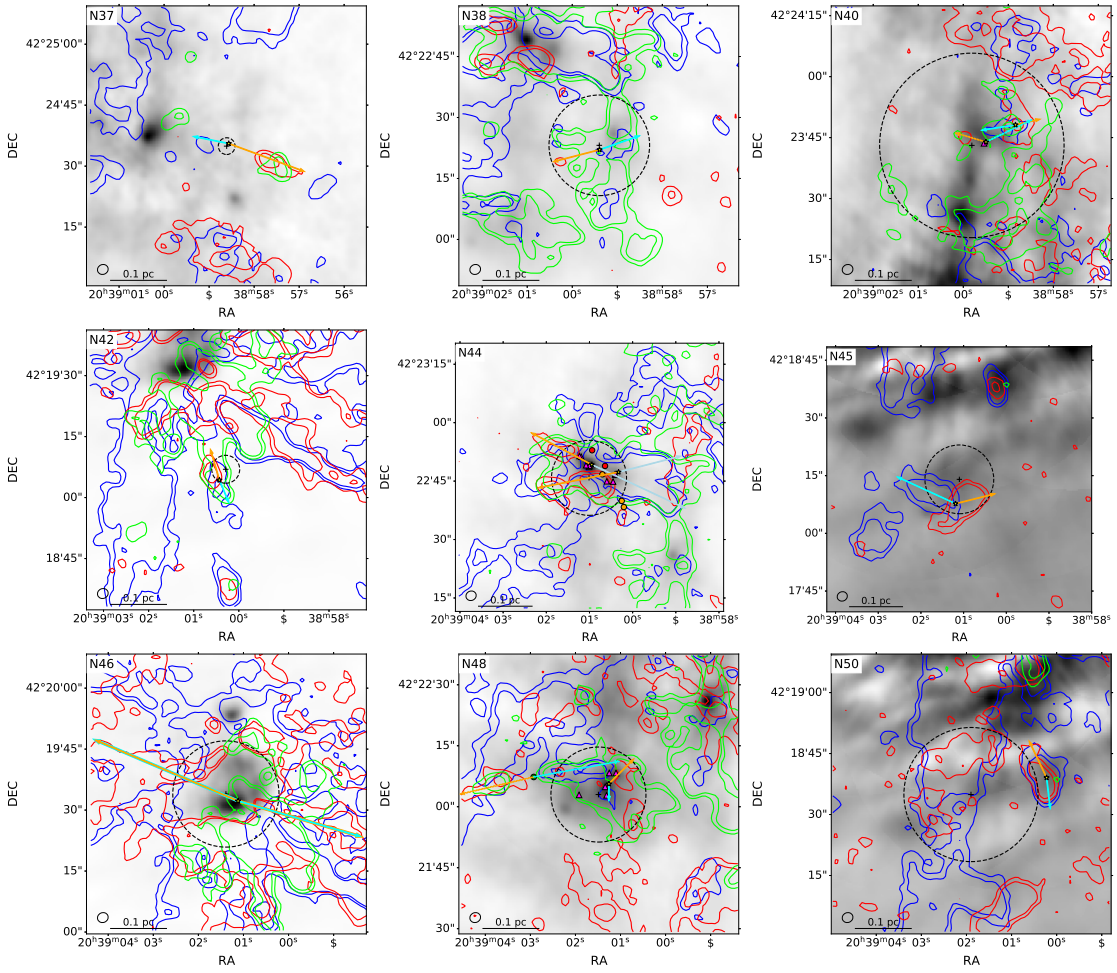


Figure 3.4: Velocity-integrated maps of the red-shifted (red contours) and blue-shifted (blue contours) $HCO^+$ emission. Velocity ranges used for each source are given in table 3.3. Green contours show the integrated SiO intensity. The black cross and dashed circle indicate the location and size of the corresponding core (see Table 3.2). Orange and cyan arrows mark the most likely direction of the outflow, and the yellow star indicates the outflow origin. Finally, the grayscale background shows the 3.6 mm continuum from NOEMA and GBT.

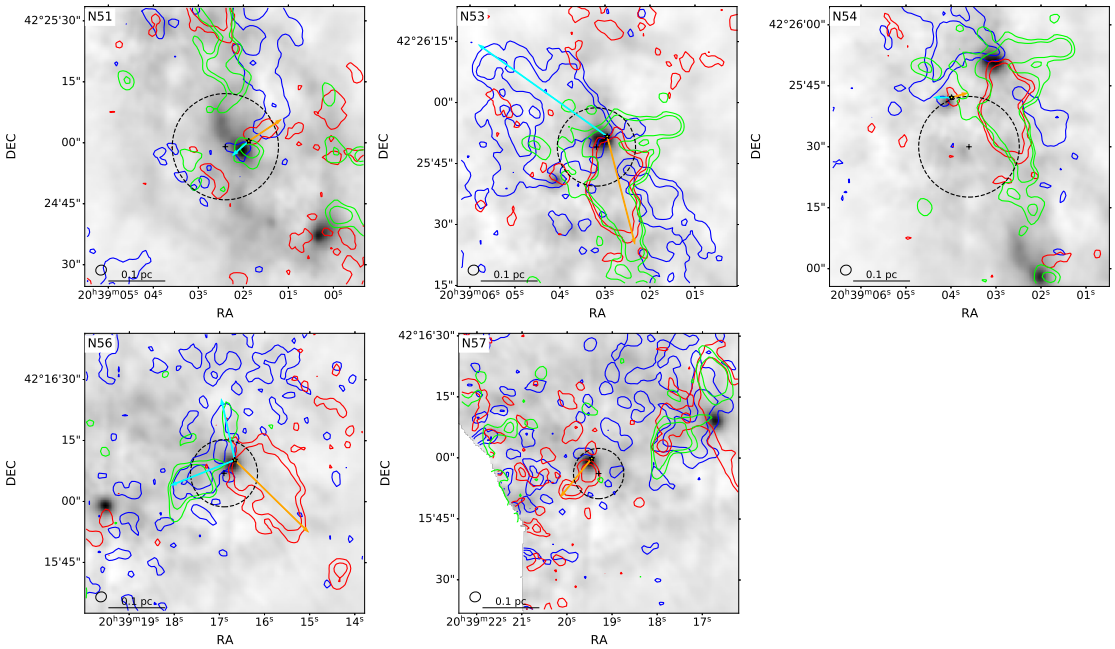


Figure 3.5: Same as in Figure 3.4

the blue lobe might arise from the characteristics of the environment surrounding N37. Namely, the blue lobe extends towards the dense material associated with N43, which is likely to rapidly slow down the outflowing material. Another possibility is that higher column densities around N43 lead to the attenuation of the blue-shifted emission.

**N38:** There is a tentative detection of an $HCO^+$ outflow, extending in the E-W direction. The outflow appears to be relatively weak, especially in the case of the red lobe, which is barely detected, and significantly detached from the most likely origin point of the outflow. Even so, the proposed orientation of the outflow, shown in Figure 3.4, closely matches that of the CO outflow reported by Ching et al. (2018), leading us to believe that the $HCO^+$ emission seen is indeed part of a molecular outflow. An additional CO outflow, not seen in $HCO^+$, was reported in Skretas and Kristensen (2022). This second outflow, extends in a North-South direction and appears to match well the SiO outflow previously reported in Ching et al. (2018) and Yang, Qiu and Pan (2024).

**N40:** Two possible outflow configurations are marked in the case of N40. The first configuration, consists of the stronger detections in both red- and blue-shifted emission (solid arrows, Figure 3.4). An additional outflow configuration though, extends on the East - West direction, sharing the same blueshifted lobe as the first outflow candidate (dotted arrows, Figure 3.4). This configuration matches the outflow seen in SiO emission both in this work but also in Duarte-Cabral, Bontemps, Motte, Hennemann et al. (2013). However, no $HCO^+$ outflow is seen at the location of the small scale CO outflow, reported in Duarte-Cabral, Bontemps, Motte, Hennemann et al. (2013). In addition, an extended red-shifted, and a less extended blue shifted structures are seen at the north

edge of the FWHM of N40. The origin of these structures is unclear, but they do not seem to be associated with continuum emission from the N40 core. As a result, they are not taken into consideration in the analysis of molecular outflows associated with dense cores.

Table 3.3: Outflow velocity ranges

| Name | Blue | | Red | |
|---|---|---|---|---|
| | $v_{in}$ | $v_{out}$ | $v_{in}$ | $v_{out}$ |
| N38 | -13 | -25 | 13 | 25 |
| N42 | -16 | -24 | 12 | 22 |
| N45 | -17 | -35 | 10 | 30 |
| N48 | -12 | -25 | 2 | 10 |
| N50 | -8 | -50 | 4 | 24 |
| N53 | -13 | -60 | 3 | 40 |
| N54 | -22 | -55 | 4 | 40 |
| N37 | -10 | -20 | 12 | 30 |
| N40 | -10 | -22 | 6 | 25 |
| N51 | -18 | -30 | 4 | 26 |
| N56 | 3 | 10 | 26 | 50 |
| N44 | -10 | -46 | 6 | 40 |
| N57 | – | – | 23 | 30 |

**Notes:** Values in km $s^{-1}$

**N42:** The area North of N42 is dominated by emission from the DR21 Main outflow. To the East of N42, the known blue-shifted structure, extending from DR21 Main towards the South can also be seen. Between these two large scale structures, a bipolar outflow extending mostly in the N-S direction, is detected. This structure could potentially be part of the extended DR21 Main outflow, but given that both the blue and red lobes appear to peak over the area associated with N42, it is most likely that the origin of the emission comes from within N42. To the South of N42, the outflow associated with N50 is also visible.

**N44:** N44 corresponds to DR21(OH), the second most prominent continuum source in the DR21 ridge, after DR21 Main. Two prominent continuum peaks can be seen within the FWHM of N44, which fragment into multiple peaks at higher resolution observations (Zapata, Loinard et al., 2012). The $HCO^+$ emission closely follows that of the CO emission (Zapata, Loinard et al., 2012). The presence of multiple continuum peaks, as well as the separation seen predominantly in the red-shifted lobes, supports the scenario of two separate outflows in N44, as was proposed by Zapata, Loinard et al. (2012). At the same time, however, I cannot rule out the scenario that the $HCO^+$ emission is tracing the cavity walls of a large-scale outflow. A large scale methanol outflow, with opposite orientation from that of the CO and $HCO^+$ outflows, has been reported by Araya et al. (2009). A significant blue-shifted structure, seen at the eastern edge of N44 could potentially be associated with this outflow, but no corresponding red-shifted emission is detected. For the purposes of this work, only the outflow structure that matches the CO outflows from the literature will be considered.

**N45:** A bipolar outflow, extending in the E-W direction is clearly seen towards the southern half of the FWHM of N45. An additional blue-shifted structure is visible to the SW of N45. At lower velocities this structure appears to be loosely connected to the blue-shifted emission that extends southwards from DR21 Main. The outflow associated with N50 is also visible North of N45.

**N46 & N47:** The cores of N46 and N47 are part of the DR21 Main region. The powerful outflow of DR21 Main is clearly seen in $HCO^+$ emission, and has been discussed in detail in Skretas, Karska, Wyrowski et al. (2023). As a uniform size of 0.5×0.5 pc was used for all the outflow maps presented in this work, the outflow of DR21 Main extends outside the limits of the presented

field in both the East and West directions. Given the more central location, the closest association with SiO emission, the stronger and more extended continuum emission, the outflow of DR21 Main is most likely originating from N46. A possible scenario for the formation of the DR21 Main outflow is that it actually consists of multiple different outflows, all aligned in the same direction. In such a scenario, given the complexity of the emission in the region, I cannot rule out the presence of an outflow originating from N47. For the remainder of this work though, it will be assumed that the outflow of DR21 Main is driven by N46.

**N48:** There is a tentative detection of a blue and red outflow lobes close to the continuum peak of N48. While the $HCO^+$ detection is not very clear, with emission seen mostly at lower velocities, its orientation appears to match that of the CO outflow (Duarte-Cabral, Bontemps, Motte, Hennemann et al., 2013; Ching et al., 2018; Skretas and Kristensen, 2022), suggesting that the emission indeed originates from the bipolar outflow. An additional red-shifted structure is seen at the South-West part of the FWHM of N48. This structure is considered as an additional red-shifted outflow in Ching et al. (2018), but it does not appear connected to any of the continuum fragments (Bontemps, Motte et al., 2010), and also lacks a blue-shifted counterpart. As a result, I excluded it from further analysis in this work. The location of the infrared source IS-1, a more evolved source detected with IRAC at 3.6 and 4.5 $\mu$m is marked with a green circle. The bipolar outflow of IS-1, reported in Duarte-Cabral, Bontemps, Motte, Hennemann et al. (2013) and Duarte-Cabral, Bontemps, Motte, Gusdorf et al. (2014), is also clearly visible. SiO emission appears to cover most of the extent of the FWHM of N48, covering both the proposed N48 outflow, the additional red-shifted lobe to the south and the blue-shifted lobe of IS-1.

**N50:** $HCO^+$ emission in N50 is dominated by blue-shifted material extending southwards from DR21 Main. Even so, a clear bipolar outflow can be seen at the western edge of the FWHM of N50. Given the significant overlap of the two lobes, it is likely that the outflow extends along the line of sight. As the continuum emission in the region is strongly affected from sidelobes arising from DR21 Main, it is not possible to confirm the location of the driving source of the N50 outflow.

**N51:** High velocity $HCO^+$ emission reveals a bipolar outflow, matching the location and direction of the CO outflow (Skretas and Kristensen, 2022). Additional fragmented red- and blue-shifted emission is seen at the Southeast part of N51. Given its fragmented nature, and the lack of close connection with any prominent continuum peaks in N51, this emission is not considered to be part of an outflow. Finally, an extended, filamentary, blue-shifted structure can be seen, extending from the top of N51 toward the North. This structure was previously seen in CO emission by Schneider, Csengeri et al. (2010). The lack of a red-shifted counterpart and of a close association with any of the reported cores, suggest that this structure is not part of a protostellar outflow.

**N53 & N54:** A prominent bipolar outflow is evident in $HCO^+$, matching the orientation of the CO outflow from Skretas and Kristensen (2022). An additional blue-shifted structure is detected, which extends towards the South. This structure matches the one seen North of N51, and as discussed previously, does not appear to be part of an outflow. A secondary continuum peak,

associated with N54, can be seen at the Southeast edge of N53. Similar to the CO maps (Skretas and Kristensen, 2022), a small-scale bipolar outflow is originating from N54. In the velocity range adopted to create the map of N53, the blue-shifted emission of N54 is blended with the more widespread blue lobe coming from N53. To avoid including the N54 outflow in the calculation of outflow properties of N53, I use a higher inner velocity limit for the blue-shifted outflow, thus restricting its extent to the point that the two outflows can be separated. In turn this might lead to a slight underestimate of the outflow properties of the N53 outflow. The velocity range in the map of N54 has been adjusted to higher velocities in order to more clearly separate to two outflow lobes.

**N55:** N55 is one of the sources displaying the 'shelf'-like emission feature. The integrated intensity map reveals that this component is widespread and fragmented, and does not form part of a coherent structure. Combined with the complete lack of any blue-shifted emission, this suggest that the red-shifted emission seen in N55 is not part of any outflow, but is rather associated with widespread foreground material.

**N56 & N57:** The cores N56 and N57 are located in a structure located $\sim 1''$ East of the DR21 ridge. This structure is seen at a velocity of $\sim$18 km s$^{-1}$ and is likely the origin of the third velocity component detected in some of the DR21 cores discussed in Section 3.3.1. The $HCO^+$ map of N56 reveals a clear bipolar outflow. The red lobe of the outflow is very well defined, but the blue emission appears more fragmented and noisy. The most likely reasons are the proximity of the sources at the edge of the FOV of the CASCADE coverage, but also blending of the blue-shifted outflow wing with the other velocity components (at -3 and 9 km s$^{-1}$) seen in DR21). Regardless, two possible directions can be seen for the blue-shifted lobes, hinting at the possibility of multiple outflows being driven from N56. Finally, SiO emission is detected over both sides of the blue-shifted emission, but not over the red-shifted lobe. The strongest SiO emission is associated with the blue-shifted lobe extending towards the east, and thus this direction will be adopted for the calculation of relevant outflow parameters, such as outflow extent and dynamical time. In the case of N57, there is a tentative detection of a red-lobe, which lacks any clear blue-shifted counter part. In addition, due to the even closer proximity of N57 to the edge of the field observed in CASCADE, the emission is dominated by noise, making the identification of an outflow impossible.

Overall, my analysis of the $HCO^+$ emission in the vicinity of all 34 dense molecular clumps reported in the DR21 filament revealed 14 molecular outflows, for a detection rate of $\sim$40 %. In the vast majority of sources, both outflow lobes are detected, with only a single sources displaying only red-shifted emission. Constraining the outflow emission enables us advance further my analysis, by constraining their energetic properties.

### 3.3.3 Outflow properties

The $HCO^+$ observations of CASCADE, allow for the calculation of the typical outflow properties such as, the outflow force, $F$, the outflow mass, $M$, and the kinetic energy, $E_{\rm kin}$ for all the detected

outflows discussed in Section 3.3.2. For the calculation I follow the same approach as in Skretas, Karska, Wyrowski et al. (2023), where the properties of the outflow of DR21 Main were estimated.

In brief, the outflow force is determined using the Separation method presented in van der Marel et al. (2013). In this method, the outflow force for a single outflow lobe is given by

$$F_{\mathrm{HCO^+}} = c_3 \times \frac{K\left(\sum_{\mathrm{j}}\left[\int_{v_{\mathrm{in}}}^{v_{\mathrm{out,j}}} T(v')v'\mathrm{d}v'\right]_{\mathrm{j}}\right)v_{\mathrm{max}}}{R_{\mathrm{lobe}}}. \tag{3.6}$$

Here, $c_3$ is a correction factor depending on the inclination angle of the outflow (Table 3.4), $K$ is a conversion factor between the line integrated intensity and the molecular gas mass, and the integral $\int_{v_{\mathrm{in}}}^{v_{\mathrm{out,j}}} T(v')v'\mathrm{d}v'$ is the velocity weighted integrated intensity. In addition, $v_{\mathrm{max}}$ corresponds to the maximum line-of-sight velocity in the outflow lobe, and $R_{\mathrm{lobe}}$ is the length of the outflow lobe, while the sum runs over all pixels (j) that are part of the outflow. In turn, the line intensity-to-mass conversion factor $K$ is given by

$$K = \mu m_{\mathrm{H}} A \frac{8\pi k_{\mathrm{B}} \nu^2}{hc^3 A_{\mathrm{ul}}} \left[\frac{\mathrm{H_2}}{\mathrm{HCO^+}}\right] \frac{Q(T_{\mathrm{exc}})}{g_{\mathrm{u}}} \mathrm{e}^{E_{\mathrm{u}}/T_{\mathrm{exc}}} \tag{3.7}$$

where $\mu$ is the mean molecular weight, $m_{\mathrm{H}}$ is the hydrogen mass, $A$ is the observed area of the outflow, $[\mathrm{H_2/HCO^+}]$ is the abundance ratio between $\mathrm{H_2}$ and $\mathrm{HCO^+}$, $Q(T_{\mathrm{exc}})$ is the partition function at a specific excitation temperature $T_{\mathrm{exc}}$, $g_{\mathrm{u}}$ is the degeneracy of the upper level of the observed transition, $E_{\mathrm{u}}$ is the upper level energy in Kelvins, and $\nu$ is the frequency of the observed transition in Hz. Additionally, $c$ is the speed of light, $k_{\mathrm{B}}$ is Boltzmann's constant, $h$ is Planck's constant and $A_{\mathrm{ul}}$ is Einstein A coefficient for the transition in $\mathrm{s^{-1}}$. A more detailed description of the conversion factor is presented in Appendix C of van der Marel et al. (2013). In this work, I assume a single excitation temperature of 40 K for all sources, which was calculated for DR21 Main (R. P. Garden, Hayashi et al., 1991). The abundance ratio of $\mathrm{H_2}$ over $\mathrm{HCO^+}$ in high-mass star-forming regions has been found to range between $2 \times 10^9$ down to $3 \times 10^7$ (Godard, Falgarone et al., 2010; Gerner et al., 2014). Here, I adopt the abundance ratio of $\mathrm{H_2}$ over $\mathrm{HCO^+}$ of $1.6 \times 10^8$ estimated for DR21 Main (R. P. Garden and Carlstrom, 1992), similar to what was used in Skretas, Karska, Wyrowski et al. (2023). The corresponding value of the partition function and the remaining molecular data are taken from the CDMS line database (Müller et al., 2001).

Table 3.4: Inclination correction factors for the calculation of outflow forces using the Separation method

| $i$ (°) | 10 | 30 | 50 | 70 |
|---|---|---|---|---|
| $c_3$ | 0.6 | 1.3 | 2.4 | 3.8 |

**Notes:** (a) $i$ is measured from the line of sight. (b) Values are interpolated from Table 6 of T. P. Downes and Cabrit (2007), where $\alpha = 90 - i$.

For the remaining outflow properties, the total gas mass carried by the outflow is calculated as:

$$M = K \left( \sum_{\mathrm{j}} \left[ \int_{v_{\mathrm{in}}}^{v_{\mathrm{out,j}}} T(v') \mathrm{d}v' \right]_{\mathrm{j}} \right), \tag{3.8}$$

while, the time-averaged kinetic energy of the outflow is calculated as:

$$E_{\mathrm{kin}} = \frac{1}{2} M \langle v \rangle^2, \tag{3.9}$$

and the momentum as:

$$P = K \left( \sum_{\mathrm{j}} \left[ \int_{v_{\mathrm{in}}}^{v_{\mathrm{out,j}}} T(v') v' \mathrm{d}v' \right]_{\mathrm{j}} \right). \tag{3.10}$$

The dynamical time, representing a rough estimate of the age of each outflow, can be calculated as:

$$t_{\mathrm{dyn}} = \frac{R_{\mathrm{lobe}}}{v_{\mathrm{max}}}, \tag{3.11}$$

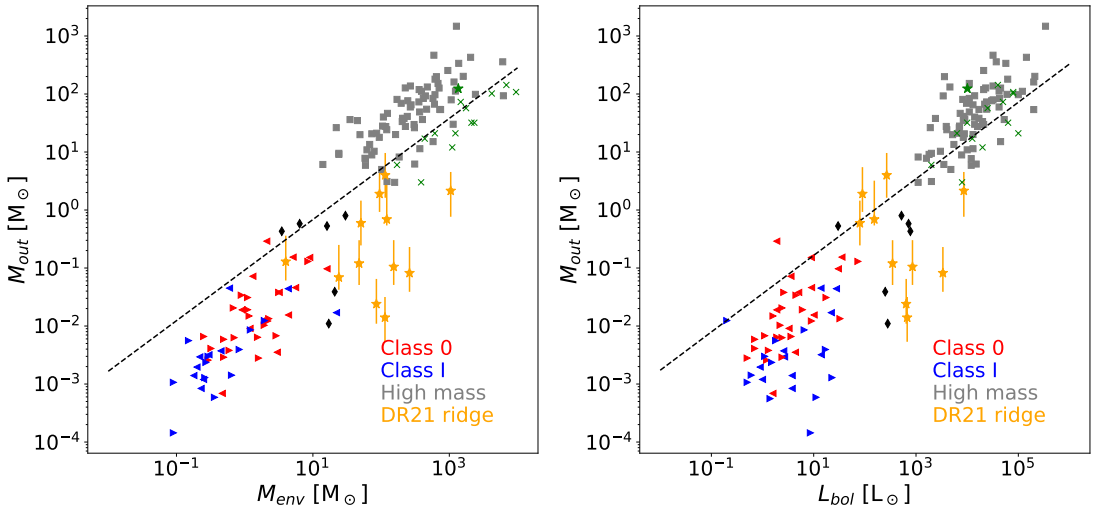


Figure 3.6: Outflow mass over the envelope mass (left) and the bolometric luminosity (right) of the driving protostellar sources. Right facing triangles represent low-mass sources from Mottram et al. (2017), left facing triangles mark sources taken from Yıldız et al. (2015) and upwards are from van der Marel et al. (2013) while in blue are the Class I sources and in red the Class 0. Black diamonds mark intermediate mass sources (van Kempen, Hogerheijde et al., 2016), gray squares mark high-mass sources from Maud et al. (2015), green "×" mark high-mass sources from Beuther, Schilke et al. (2002), and orange stars mark the sources in the DR21 ridge (this work). The green star represents the DR21 Main outflow from Skretas, Karska, Wyrowski et al. (2023) and the dashed, black line shows the best fit to the outflow force - envelope mass correlation for all sources. The errorbars mark the possible variation of the outflow mass estimate due to the inclination correction factor.

allowing, in turn, the calculation of the mass loss rate:

$$\dot{M} = \frac{M}{t_{\rm dyn}}, \tag{3.12}$$

and the kinetic power of the outflows:

$$L_{\rm kin} = \frac{E_{\rm kin}}{t_{\rm dyn}}. \tag{3.13}$$

The outflow properties are determined separately for the blue- and red-shifted outflow lobes, and the resulting properties are listed in Table 3.5. Overall, the derived outflow properties are comparable to those of other high-mass sources (e.g., Beuther, Schilke et al., 2002; Maud et al., 2015).

To determine the outflow properties, I adopted a number of assumption as follows. Firstly, in order for the conversion factor $K$ to be accurate, optically thin emission is required. While the ridge displays some very high column densities, the optically thin assumption is in general believed to hold for the higher velocities in protostellar outflows. This is found to be true even in the massive outflow of DR21 Main (R. P. Garden and Carlstrom, 1992; Skretas, Karska, Wyrowski et al., 2023), located in the densest region along the ridge. To avoid including material from the dense ridge in the calculation, I excluded channels with velocities close to that of the main filament (-3 km s$^{-1}$). This has the potential to lead to an underestimate of the measured mass, with Offner, E. J. Lee et al. (2011) suggesting, based on simulation, that integrating over velocities >2 km s$^{-1}$ can lead to an underestimate of the outflow mass by a factor of 5–10. The impact on $F$ or $E_{\rm kin}$ is not as significant due to the dependence of those parameters on $v^2$, and thus to the higher velocity material. Secondly, the correction factor of inclination angle, $c_3$, has been calculated only for the inclination angles of 10°, 30°, 50°, and 70° (Table 3.4). As the inclination of the outflows is not trivial to estimate, in this work the outflow properties were estimated using all four different factors and the average values are provided in Table 3.5. Depending on the true inclination, the true values can differ from the assumed average by a factor of up to ~6. Finally, a uniform excitation temperature of 40 K was assumed for all outflows along the ridge. While this might not be very accurate it has been shown that changes in excitation temperatures of an order of a few have small impacts on the resulting outflow properties (e.g. Skretas and Kristensen, 2022, where an increase of the excitation temperature from 50 K to 100 K was found to lead to an increase of the outflow force by a factor of 1.4). As the scatter observed in the outflow - source properties correlations is typically larger than an order of magnitude, I do not believe that the above uncertainties will drastically affect the subsequent discussions.

To sum up, using $HCO^+$ observations I estimated the outflow properties for all outflows associated with dense molecular clumps within the DR21 filament. The resulting values are in line with those of other protostellar outflows of high- and intermediate mass sources in the literature. A more detailed comparison, in the light of the established correlations between outflow and source properties is presented in Section 3.4.1.

Table 3.5: Outflow properties

| Name | | $R_{\rm lobe}$ [pc] | $t_{\rm dyn}$ [yr] | $M$ [$\times 10^{-2}$ $M_\odot$] | $P$ [$M_\odot$ km s$^{-1}$] | $E_{\rm kin}$ [$\times 10^{43}$ erg] | $\dot{M}$ [$\times 10^{-5}$ $M_\odot$ yr$^{-1}$] | $F$ [$\times 10^{-4}$ $M_\odot$ km yr$^{-1}$ s$^{-1}$] | $L_{\rm kin}$ [$\times 10^{40}$ erg yr$^{-1}$] |
|---|---|---|---|---|---|---|---|---|---|
| N38 | Blue | 0.06 | 1000 | 1.4 | 0.25 | 3.3 | 2.2 | 3.7 | 5.0 |
| | Red | 0.07 | 920 | 1.0 | 0.19 | 4.5 | 1.7 | 3.2 | 7.4 |
| | Total | – | – | 2.4 | 0.44 | 7.8 | 3.8 | 6.9 | 12.0 |
| N42 | Blue | 0.07 | 950 | 2.6 | 0.54 | 14.0 | 4.2 | 8.6 | 23.0 |
| | Red | 0.05 | 580 | 9.4 | 1.63 | 42.0 | 24.2 | 42.1 | 110.0 |
| | Total | – | – | 12.0 | 2.17 | 56.0 | 28.4 | 50.7 | 133.0 |
| N45 | Blue | 0.10 | 700 | 20.8 | 4.75 | 150.0 | 44.7 | 102.0 | 330.0 |
| | Red | 0.06 | 470 | 38.6 | 8.37 | 180.0 | 123.8 | 268.7 | 57.0 |
| | Total | – | – | 59.4 | 13.12 | 330.0 | 168.5 | 370.7 | 387.0 |
| N48 | Blue | 0.02 | 410 | 0.2 | 0.02 | 0.3 | 0.6 | 0.9 | 1.2 |
| | Red | 0.04 | 820 | 8.0 | 0.45 | 7.4 | 14.8 | 8.4 | 14.0 |
| | Total | – | – | 8.2 | 0.47 | 7.7 | 15.4 | 9.3 | 15.2 |
| N50 | Blue | 0.04 | 380 | 36.5 | 5.57 | 210.0 | 143.3 | 218.5 | 810.0 |
| | Red | 0.06 | 880 | 32.6 | 3.05 | 90.0 | 55.5 | 52.1 | 150.0 |
| | Total | – | – | 69.1 | 8.72 | 300.0 | 198.8 | 270.6 | 960.0 |
| N53 | Blue | 0.25 | 1520 | 171.6 | 37.62 | 1300.0 | 170.7 | 374.1 | 1300.0 |
| | Red | 0.17 | 1070 | 227.3 | 33.94 | 1500.0 | 320.1 | 478.1 | 2100.0 |
| | Total | – | – | 398.9 | 71.56 | 2800.0 | 490.8 | 852.2 | 3400.0 |
| N54 | Blue | 0.02 | 210 | 3.5 | 0.93 | 30.0 | 25.1 | 67.4 | 220.0 |
| | Red | 0.02 | 340 | 3.4 | 0.29 | 5.5 | 15.1 | 12.8 | 24.0 |
| | Total | – | – | 6.9 | 1.22 | 35.5 | 40.2 | 80.2 | 244.0 |
| N37 | Blue | 0.05 | 970 | 0.5 | 0.07 | 1.2 | 0.8 | 1.0 | 1.8 |
| | Red | 0.13 | 1170 | 12.4 | 2.42 | 59.0 | 16.1 | 31.3 | 76.0 |
| | Total | – | – | 12.9 | 2.49 | 60.2 | 16.9 | 32.3 | 77.8 |
| N40 | Blue | 0.08 | 1650 | 0.4 | 0.05 | 1.0 | 0.4 | 0.5 | 0.9 |
| | Red | 0.05 | 670 | 1.0 | 0.12 | 1.0 | 2.2 | 2.6 | 2.2 |
| | Total | – | – | 1.4 | 0.17 | 2.0 | 2.6 | 3.1 | 3.1 |
| N51 | Blue | 0.03 | 350 | 0.3 | 0.07 | 1.7 | 1.5 | 3.2 | 7.2 |
| | Red | 0.06 | 780 | 10.2 | 0.93 | 19.0 | 19.7 | 17.9 | 38.0 |
| | Total | – | – | 10.5 | 1.00 | 20.7 | 21.2 | 21.1 | 45.2 |
| N56 | Blue | 0.11 | 940 | 21.0 | 3.76 | 100.0 | 33.7 | 60.4 | 160.0 |
| | Red | 0.16 | 1310 | 168.9 | 23.04 | 580.0 | 194.7 | 265.6 | 660.0 |
| | Total | – | – | 189.9 | 26.80 | 680.0 | 228.4 | 326.0 | 820.0 |
| N44 | Blue | 0.17 | 980 | 137.0 | 31.55 | 930.0 | 211.9 | 487.9 | 1400.0 |
| | Red | 0.11 | 610 | 77.6 | 13.68 | 240.0 | 193.2 | 340.4 | 590.0 |
| | Total | – | – | 214.6 | 45.23 | 1170.0 | 405.1 | 828.3 | 1990.0 |
| N57 | Blue | – | – | – | – | – | – | – | – |
| | Red | 0.07 | 1440 | 9.7 | 0.74 | 9.7 | 10.1 | 7.8 | 10.0 |
| | Total | – | – | – | – | – | – | – | – |

## 3.4 Discussion

### 3.4.1 Correlation of outflow and source properties

The presence of correlations connecting the properties of protostellar outflows with the properties of their driving sources has been well established over the years for both the low- (e.g., Bontemps, Andre et al., 1996) and high-mass regime (e.g., Beuther, Schilke et al., 2002). These correlations allow us to better put into context the outflow properties measured for the outflows in the DR21 ridge by comparing them to previous measurements from the literature.

Figures 3.6 - 3.11 show the correlation between all the outflow properties with both the envelope masses ($M_{\rm env}$) and bolometric luminosity ($L_{\rm bol}$) for the outflows of the DR21 ridge, along with an extended sample of sources from the literature (Beuther, Schilke et al., 2002; van Kempen, Hogerheijde et al., 2016; van der Marel et al., 2013; Yıldız et al., 2015; Maud et al., 2015; Mottram et al., 2017). The values for $M_{\rm env}$ and $L_{\rm bol}$ are taken from Cao, Qiu, Q. Zhang, Y. Wang, Hu et al. (2019).

N37 and N54 have no counterparts in Cao, Qiu, Q. Zhang, Y. Wang, Hu et al. (2019), therefore $M_{\rm env}$ values for these sources are taken from Motte, Bontemps, Schilke et al. (2007). As Motte, Bontemps, Schilke et al. (2007) does not provide $L_{\rm bol}$ measurements, N37 and N54 are not included in the associated correlations. In addition note that, Cao, Qiu, Q. Zhang, Y. Wang, Hu et al. (2019) provides values for $L_{\rm FIR}$, therefore $L_{\rm bol}$ values are likely underestimated.

The sources of the DR21 filament cover a range of $\sim 2$ orders of magnitude in both the $M_{\rm env}$ and $L_{\rm bol}$ space, with $M_{\rm env} \approx 10 - 10^3$ M$_\odot$ and $L_{\rm bol} \approx 10^2 - 10^4$ L$_\odot$. This places the DR21 filament sources in the intermediate to high-mass regime, where so far only few measurements of outflow properties have been reported in the literature. Within that range of source parameters, the outflows of the DR21 filament display significant variation in all of their outflow parameter values, often spanning several orders of magnitude. Such scatter is similar to that observed in the

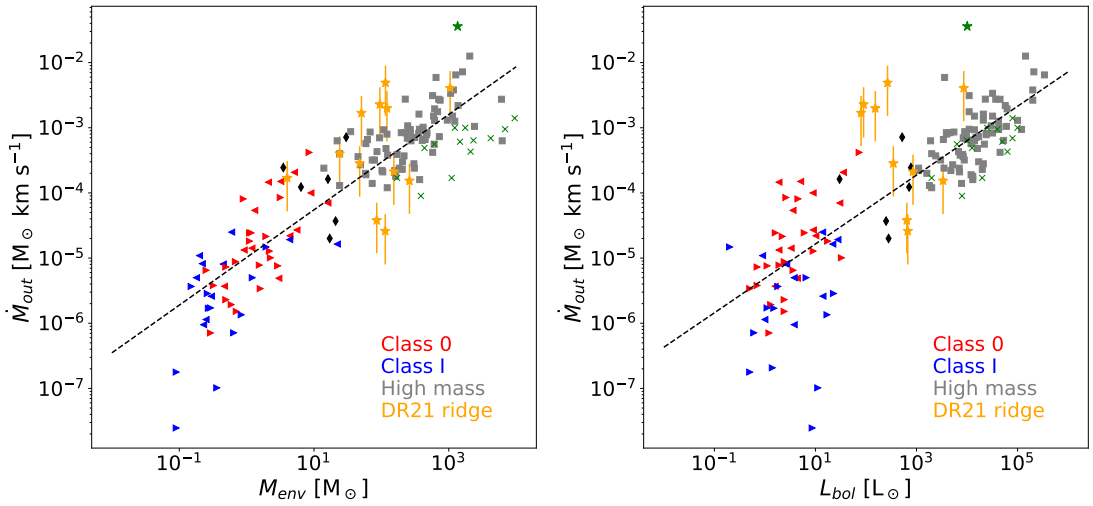


Figure 3.7: Outflow mass rate versus envelope mass (left) and bolometric luminosity (right). The labels are the same as in Figure 3.6.

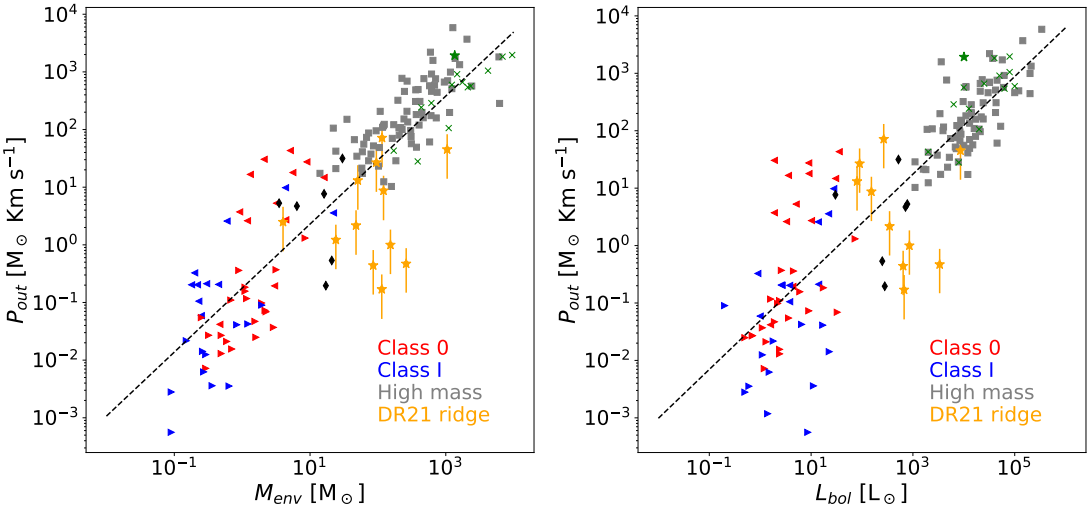


Figure 3.8: Outflow momentum versus envelope mass (left) and bolometric luminosity (right). The labels are the same as in Figure 3.6.

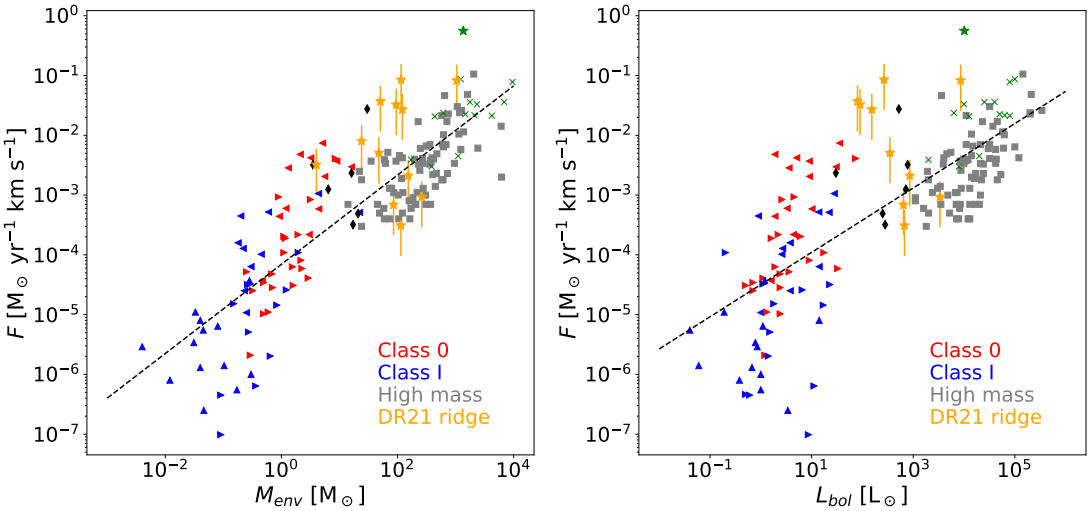


Figure 3.9: Outflow force versus envelope mass (left) and bolometric luminosity (right). The labels are the same as in Figure 3.6.

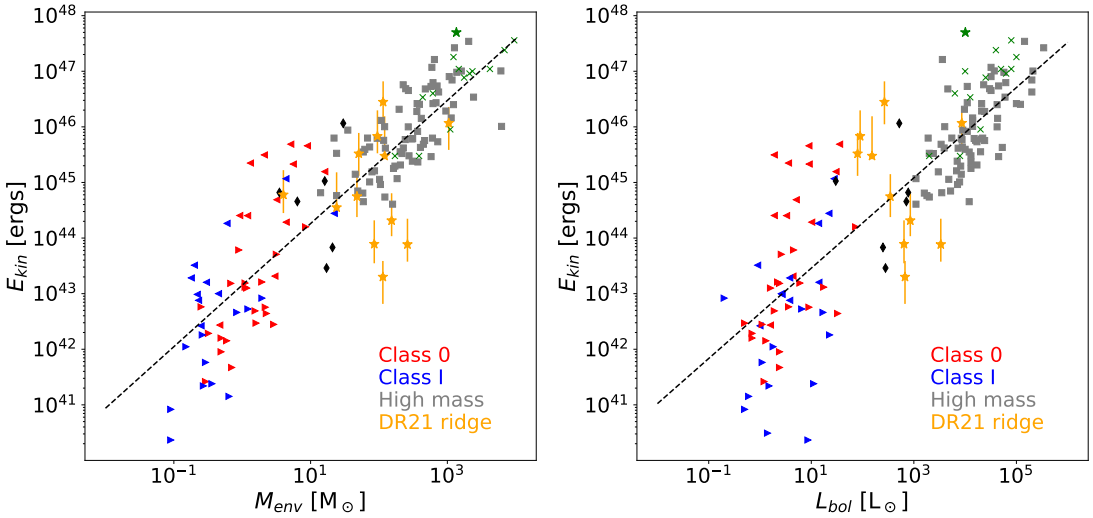


Figure 3.10: Outflow kinetic energy versus envelope mass (left) and bolometric luminosity (right). The labels are the same as in Figure 3.6.

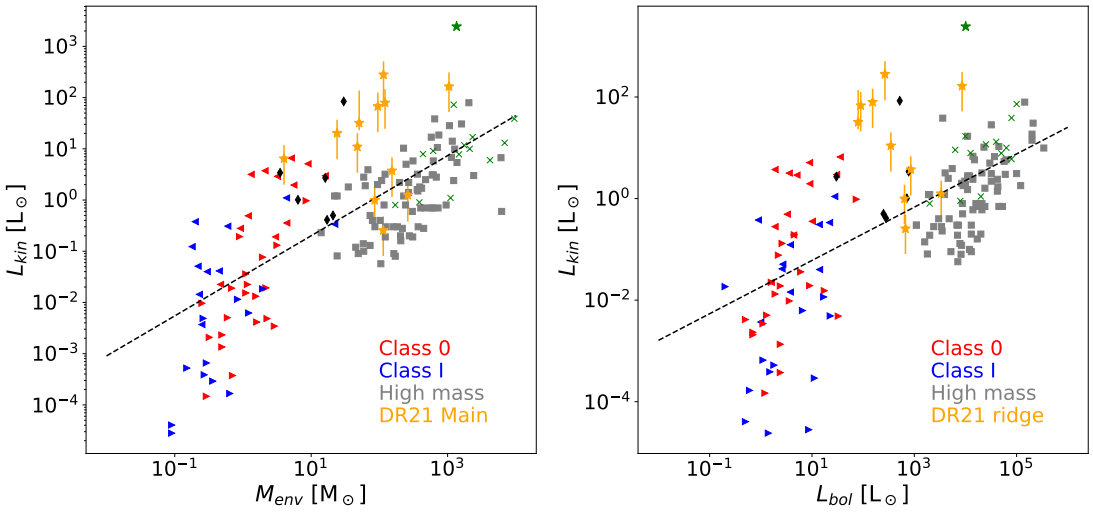


Figure 3.11: Outflow kinetic luminosity versus envelope mass (left) and bolometric luminosity (right). The labels are the same as in Figure 3.6.

low-mass sources, but is not seen in the high mass sample. Given that the DR21 filament sources are closer to the high-mass regime, this indicates that the large scatter of the correlation seen in the low-mass regime, is likely to actually extend into the high-mass regime. The lack of scatter seen so far in the high-mass samples can potentially be attributed to their, on average, larger distances. More precisely, due to these larger distances the available spatial resolution, especially of single dish telescopes, is severely restricted. As a result, disentangling the outflow emission, and accurately identifying the outflow lobes becomes significantly more challenging. In addition, the higher distances would lead to a drop in observed fluxes, potentially causing emission from weaker outflows to drop below sensitivity limits. As a result, it is possible that in past surveys of high mass protostellar outflows, the measured properties are biased, covering only the upper limit of high mass outflows that were easier to detect at the time. Unbiased observations of high mass star forming regions at high enough spatial resolution and sensitivity will potentially reveal whether the lack of scatter in the high mass regime is indeed due to observational biases.

Protostellar outflows are closely connected to the accretion process, and by extension to the whole of star formation. Therefore, outflow properties can serve as an easily accessible way to investigate the impact of environmental factors onto the star formation process itself. The case of the DR21 filament presents a unique case, since it represents the most extreme part, of an already intense high-mass star-forming region Cygnus-X. The close agreement of the DR21 sources with the literature sample seen in Figs. 3.6 - 3.11 suggests that even in this extreme case, the impact of the environment on the outflows and by extension the accretion process, is minimal. A similar argument was made by Beuther, Kuiper and Tafalla (2025), based on studies of multiplicity and the initial mass function (IMF) at different star forming regions. For a more concrete comparison between the DR21 sample and the literature sources, I performed a statistical comparison between the two i.e., the 'Energy-distance' test. For this test, first the metric $D^2(F, G)$ is calculated as:

$$D^2(F, G) = 2E\|(X - Y)\| - E\|(X - X')\| - E\|(Y - Y')\|, \tag{3.14}$$

where $F$ and $G$ are two sets of two-dimensional data points, $X$ and $Y$ represent elements of $F$ and $G$, respectively, and $E$ stands for the expected value. This value is then compared to the distribution of $D^2$-values estimated by randomly distributing all points from both sets, into new sets with the same sizes as the original and re-calculating the metric. A $p$-value can then be estimated, representing the possibility of $D^2$-values greater than the one corresponding to the initial sets being measured.

The results of the 'Energy-distance' test for all outflow parameters collected from the literature sample and calculated for the DR21 sources are presented in Tables 3.6 and 3.7. I find $p$-values $> 0.05$ indicating that there is no statistically significant difference between the two samples. Note, however, that the sample size of the DR21 sources is comparatively small, when contrasted to the sample of literature sources, and therefore small differences in the sample distributions might not be as noticeable in the statistical comparison. In addition, due to the substantial inherent scatter seen in the outflow-source correlations, a small variation in the correlation for a small number of sources can be particularly hard to detect. With that in mind, the good agreement of the DR21 sources to the broad literature sample suggests that protostellar outflows, and by extension the accretion and star-formation process, remains largely unaffected even when taking place in extreme and clustered environments, such as the DR21 filament.

Table 3.6: Energy distances ($E_{\rm dist}$) and corresponding p-values for energy distance tests of the distributions of outflow parameters with respect to the source envelope mass

| | $E_{\rm dist}$ | $p-$value |
|---|---|---|
| Mass | 77.06 | 0.29 |
| Mass rate | 71.99 | 0.31 |
| Momentum | 122.36 | 0.17 |
| Force | 71.99 | 0.31 |
| Kinetic energy | $4.10\times10^{45}$ | 0.24 |
| Kinetic luminosity | 71 | 0.3160 |

**Notes:** In the cases where p-value > 0.05, the samples cannot be differentiated statistically.

The logarithms of outflow properties have been found to scale linearly with those of the source properties (e.g. Beuther, Schilke et al., 2002; van der Marel et al., 2013; Skretas and Kristensen, 2022). With the addition of the DR21 filament sources, I carried out new linear fits for all outflow properties correlations with both $M_{\rm env}$ and $L_{\rm bol}$ providing updated values for the scaling relations. The resulting best-fit parameters are shown in Tables A.1-A.6, Appendix A.3. The fits are carried out separately for low-, intermediate- and high-mass sources, but also for the combined sample. Among the individual samples, the tighter correlations (higher Pearson's $r$ coefficients) are found for the low-mass sample. In contrast, the intermediate-mass sample display the lowest $r$ coefficients, likely due to the limited sample size. Notably, in same cases the intermediate mass sources display negative $r$ values, suggesting an anti-correlation with the outflow properties, but again, due to the limited sample size and the inherent scatter of the overall corelation this result cannot be trusted. When the entire sample of protostellar outflows are considered together, a tight, positive linear correlations is always found with Pearson's coefficients $\geq 0.6$. The existence of this tight correlation across such an extended range of source properties (fiver orders of magnitude in $M_{\rm env}$ and 6 in $L_{\rm bol}$), supports the existence of a common formation mechanism for both low- and high-mass stars.

Summarizing the findings of this section, the comparison of the outflow and source properties correlations reveals that the outflows of the DR21 filament occupy mainly the intermediate to high-mass range. In addition, they display a significant scatter, similar to that of low-mass sources, suggesting that this scatter extends into the high mass regime, where it was not clearly seen previously. Finally, the outflow properties of the DR21 sample appear statistically similar to those of the extended sample, suggesting that even the extreme environment of DR21 has no noticeable impact on the star formation process.

### 3.4.2 Distribution of outflow sources along the ridge

The impact of the general environment (e.g. strong UV fields from nearby OB stars, clustered versus isolated formation, physical conditions of the star-forming molecular cloud) onto the process of star formation is still a matter of debate (e.g., Beuther, Kuiper and Tafalla, 2025). In this section, I discuss my results regarding the outflows of sources along the DR21 ridge in the context of the large scale properties of the filament in an effort to constrain whether they are

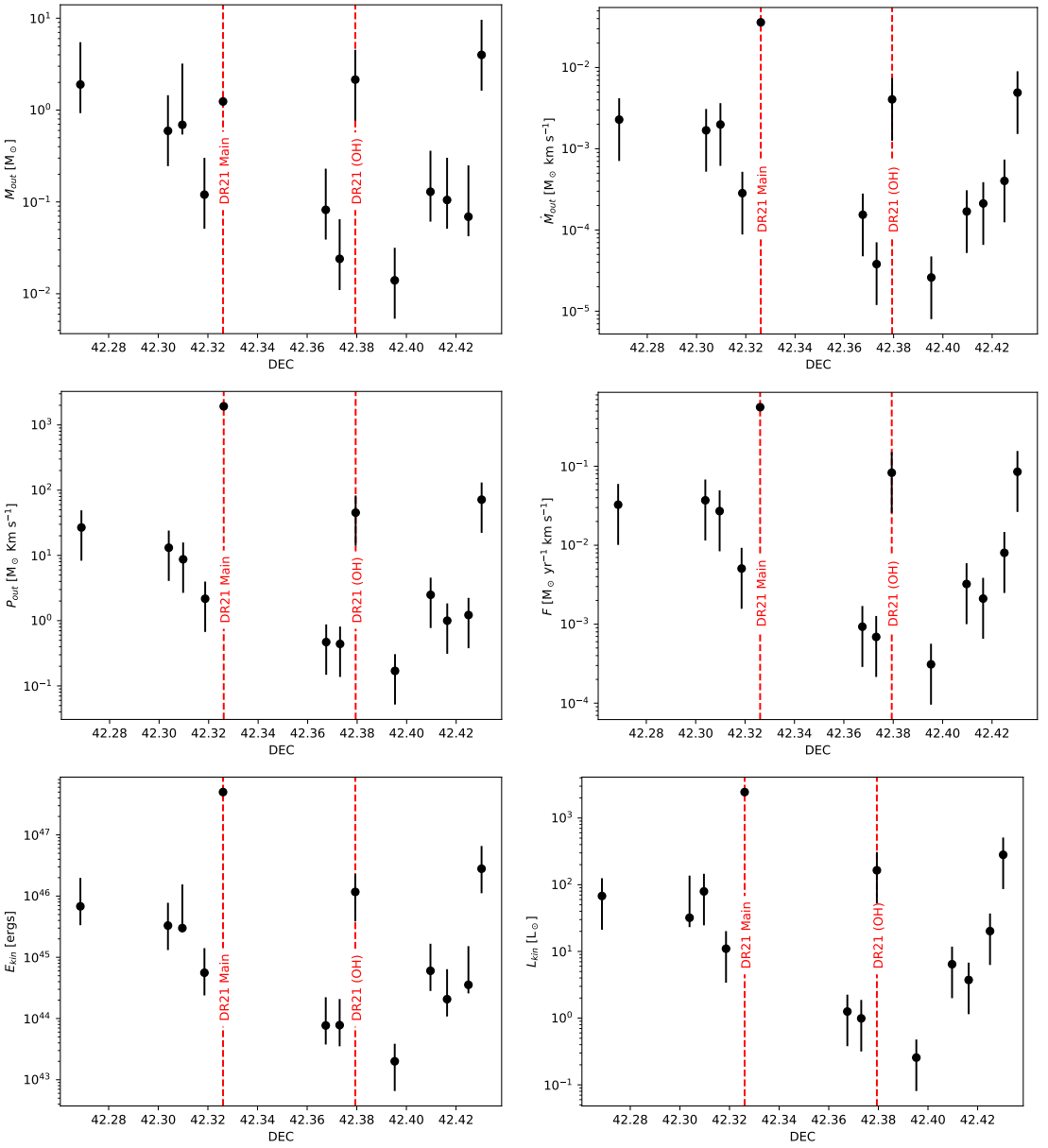


Figure 3.12: Outflow properties over source declination for all outflow sources in the sample. From top to bottom the outflow properties shown are: outflow mass (left) and outflow mass rate (right), outflow momentum (left) and outflow force (right), and outflow kinetic energy (left) and luminosity (right). Dashed lines mark the location of DR21 Main and DR21 (OH). The green square corresponds to the outflow of N56, which is located in a separate structure from the DR21 ridge. The errorbars mark the possible variation of the corresponding value due to the inclination correction factor.

Table 3.7: Energy distances ($E_{\rm dist}$) and corresponding p-values for energy distance tests of the distributions of outflow parameters with respect to the source bolometric luminosity

| | $E_{\rm dist}$ | $p-$value |
|---|---|---|
| Mass | 6550.41621 | 0.09 |
| Mass rate | 6550.39 | 0.09 |
| Momentum | 6551.94 | 0.09 |
| Force | 6550.39 | 0.09 |
| Kinetic energy | $3.72\times10^{45}$ | 0.38 |
| Kinetic luminosity | 6548.04 | 0.10 |

**Notes:** In the cases where p-value > 0.05, the samples cannot be differentiated statistically.

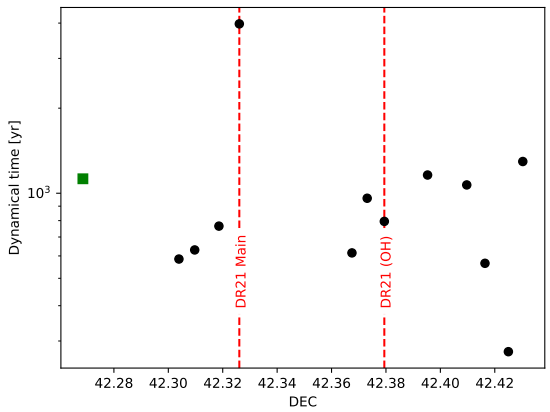


Figure 3.13: Dynamical time over source declination for all outflows sources in the sample. The dynamical time shown here is the average between the dynamical times estimated for the two outflow lobes. Dashed lines mark the location of DR21 Main and DR21 (OH). The green square corresponds to the outflow of N56, which is located in a separate structure from the DR21 ridge.

impacted in any way from the broader environment.

Previous *Herschel* observations of the DR21 ridge revealed the presence of a gradient in the evolutionary stage of the various dense clumps located along the filament. Hennemann et al. (2012) found that both the 70 $\mu$m luminosity and the dust temperature of the dense clumps along the DR21 filament decrease moving from the South to the North end of the filament. I investigate here whether this evolutionary trend along the DR21 ridge has a noticeable impact on the protostellar outflows. Figure 3.12 shows the distribution of outflow properties along the DR21 filament revealing a lack of any obvious trends. Three sources appear to stand apart from the majority in terms of their outflow properties, DR21 Main-N46, DR21 (OH)-N44 and N53. These three sources are relatively equally spaced along the DR21 ridge, with DR21 Main on the south end, DR21 (OH) in the middle, and N53 towards the northern edge. When not taking these exceptional case into account, a decrease in outflow properties can be noted between Dec $\sim$ 42.3° and $\sim$ 42.4°; however, outflow properties seem to increase again as one moves further North. The strong correlation of the outflow properties with those of the driving source (see Section 3.4.1) is

potentially overshadowing any trend arising from the evolutionary stage of the clumps along the ridge. Looking at the dynamical times of the outflows along the ridge, as a more direct estimate of the outflow age (Figure 3.13), I again find no sign that the outflows along the ridge follow the reported evolutionary trend. Interestingly, sources in the south end of the ridge, associated with relatively higher outflow properties have relatively low dynamical times, while on the other hand, DR21 Main and N53 the two sources with consistently highest outflow properties also have the highest dynamical ages. There does not seem to be a direct connection between the dynamical time and the outflow properties. Note though that the dynamical time of an outflow is a highly inaccurate measure of its actual age, due to the impact the inclination angle has on its calculation. Still, I overall find no indication that the North to South evolutionary trend of the DR21 ridge has any impact on the protostellar outflows themselves.

Another interesting characteristic of the DR21 ridge is that it appears to still be accreting mass, through multiple filaments connecting to it (Schneider, Csengeri et al., 2010; Hennemann et al., 2012). The intersection of such filaments has often been proposed as the location of high-mass star formation (e.g., Balsara, Ward-Thompson and Crutcher, 2001; Banerjee, Pudritz and Anderson, 2006; R. J. Smith et al., 2011; Motte, Bontemps and Louvet, 2018; Hacar et al., 2025) Indeed, in the case of DR21, it has been shown that the F3 filament connects to DR21 (OH) (Csengeri, Bontemps et al., 2011), while the southern filaments S and SW are associated with DR21 Main (Hennemann et al., 2012). This can also be seen in Figure 3.14 where the location of the filaments reported in Hennemann et al. (2012) is shown over the column density map of the DR21 ridge from Marsh et al. (2017). In addition, Figure 3.14 shows that the massive clump N53 is located close to the position where the two northern filaments F1 and N would intersect. While a more detailed analysis of the filaments is required to confirm the connection between the filaments and the clumps, based on the spatial distribution of the clumps and previous studies (Csengeri, Bontemps et al., 2011; Hennemann et al., 2012) all three most outstanding outflow sources along the ridge appear closely associated with filaments accreting material.

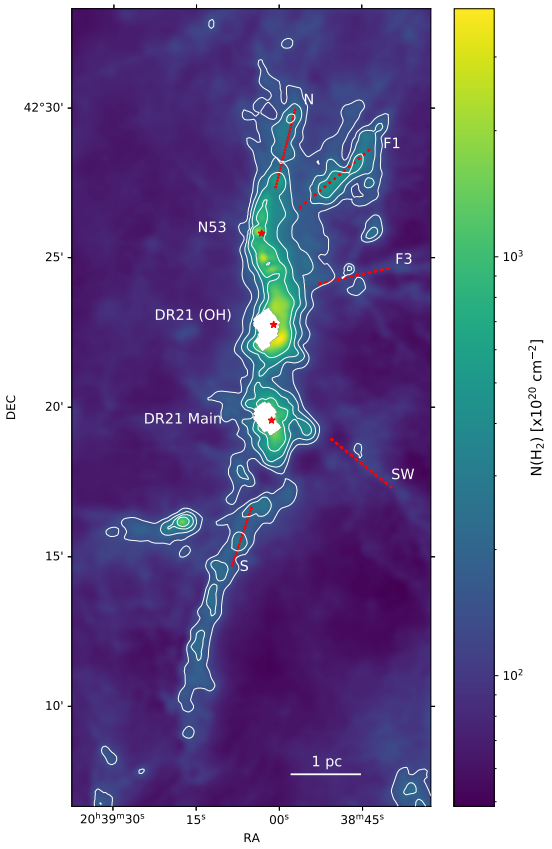


Figure 3.14: $H_2$ column density map of the entire DR21 ridge from Marsh et al. (2017). Contour levels correspond to 2,3,5, and 10 $\sigma_{\rm rms}$ of the column density. Red stars mark the location of the most prominent outflow sources DR21 Main - N46, DR21 (OH)- N44, and N53. Red dotted lines mark the location of the accreting filaments, as identified by Hennemann et al. (2012). The saturated regions around DR21 Main and DR21 (OH) have been masked.

The strongly skewed morphology of the

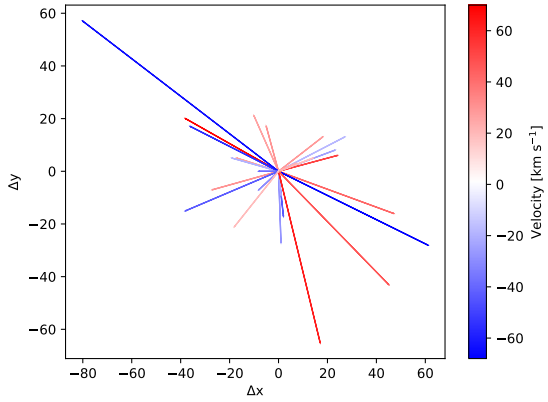


Figure 3.15: Orientation and extent of outflow lobes in the DR21 ridge. The colorscale of the lines corresponds to the maximum/minimum velocity measured for red and blueshifted lobes respectively.

DR21 filament could potentially lead to a preferential rotation direction for the cores forming within it, dictated by the large scale flows along its length. Since, the orientation of protostellar outflows is in principle determined by the original rotation of the collapsing core and subsequent accretion disk, the direction of protostellar outflows along the ridge could shed some light on whether core rotation is influenced by the large scale cloud morphology and kinematics or are instead dictated by more local dynamics. Figure 3.15 shows that outflows along the DR21 filament show no preferential direction, but appear more randomly distributed suggesting the lack of a preferred core rotation direction. An argument can be made that some of the shorter outflows could actually be closer to the line-of-sight direction, instead of north-south and thus support a preference of outflows to extend perpendicular to the filament, instead of along it. In that case, one would expect such outflows to display higher velocities, since the projection effect would be less significant. Figure 3.15 shows that most of the shorter outflows also have lower velocities indicating that this is not the case. While the sample is limited to a single cloud, my results suggest that there is no strong connection between the orientation of the large scale filamentary structure and the rotation of the dense cores forming within it.

In brief, the comparison of outflow properties between the sources along the DR21 filament showed that the established evolutionary trend along the filament has no noticeable impact on the current protostellar outflows. In contrast, the three sources located at the intersection of the DR21 filament with the various accretion filaments, display consistently higher outflow properties, supporting the proposed connection of hub filament systems as regions of high mass star formation. Finally, despite the strongly skewed large scale morphology of the DR21 filament, there appears to be no preferential rotation direction passed down to the core scales, as the outflow directions appear to uniformly spread towards all directions.

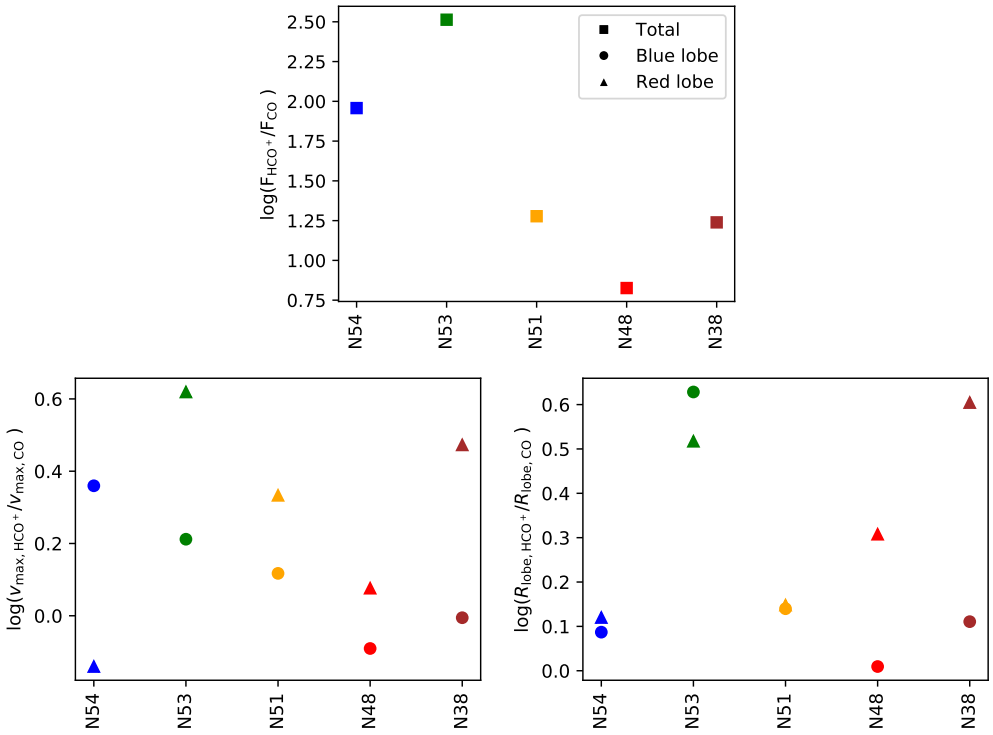


Figure 3.16: Comparison of different outflow properties measured using the CASCADE $HCO^+$ observations (this work) and CO $J$ =3-2 observations taken with the SMA (Skretas and Kristensen, 2022). [Top]: Comparison between the outflow forces ($F$). [Left]: Maximum velocity ($v_{max}$) in each lobe. [Right]: Radius of outflow lobes ($R_{lobe}$). Square points, in top panel, represent values for the whole outflow, while circles and triangles, in the second and third panels correspond to the values of the blue- and red-shifted outflow lobes respectively.

### 3.4.3 Comparison of CO and $HCO^+$ outflows

The outflow properties in this work are estimated using $HCO^+$ $J = 1 - 0$, whereas all previous detections of outflows in DR21 ridge used low-$J$ transitions of $^{12}CO$ (Section 3.4.1). Due to a relatively high critical density of $HCO^+$ with respect to $^{12}CO$, it is possible that these two molecular species do not trace the same outflow components. Indeed, H. G. Arce and Sargent (2006) suggested that $HCO^+$ might be more closely associated with the outflow cavity walls than the bulk of the molecular outflows. To verify the comparisons of Section 3.4.1, it is therefore crucial to investigate the impact of the choice of molecular tracer on the outflow properties.

To that end, I compare the outflow properties obtained with $HCO^+$ with those observed as part of the PILS-Cygnus survey (van der Walt et al., 2021; Skretas and Kristensen, 2022). Figure 3.16 shows the ratio between the outflow forces, maximum outflow velocities, and outflow extents measured using $HCO^+$ $J = 1 - 0$ (this work) and CO $J = 3 - 2$ (Skretas and Kristensen, 2022) for the common sources in the two samples (N54, N53, N51, N48, and N38). I find that the values for the outflow forces calculated here are ∼1 - 2 orders of magnitude higher than those from Skretas

and Kristensen (2022). This difference is likely due to the lack of short spacing observations in the PILS-Cygnus survey leading to significant filtering of the extended outflow emission. While not to the same extent, I also see differences in the $v_{\rm max}$ and $R_{\rm lobe}$ values measured in the two studies, with $HCO^+$ measured values being usually higher by a factor of a few. The usually larger values for $R_{\rm lobe}$ measured in the $HCO^+$ outflows supports the argument that spatial filtering effects are affecting the CO measurements.

In fact, comparisons of outflow properties using CO and $HCO^+$ in the literature provided contradictory results. For example, Walker-Smith et al. (2014) found outflow properties of low-mass protostars of about an order of magnitude lower using $HCO^+$ $J = 4 - 3$ than those from a previous study that used $^{12}$CO $J = 3 - 2$ (Curtis et al., 2010). In contrast, D.-J. Liu et al. (2021) reported that outflow properties measured using $HCO^+$ 1-0 are higher by approximately an order of magnitude than those measured with $^{12}$CO for a sample of high-mass sources. The use of different transitions of the two molecules can have a significant impact on the resulting outflow properties, as the critical densities of each transition, even for the same molecule, are different and therefore can probe different parts of the outflows. As a result, the reported changes in outflow properties can also be at least partially attributed to these effects.

It becomes apparent that, additional and more consistent in term of observations, comparisons between the two outflow tracers are required in order to accurately constrain the relation between them. To that end, the NASCENT-stars project (Csengeri, Bouscasse et al., 2024) can potentially allow for a significantly more accurate and thorough comparison of properties between CO and $HCO^+$ outflows, by providing CO observations toward the regions covered by CASCADE. Despite this uncertainty, due to the large scatter inherent in the correlations of outflow and source properties, the conclusions of Section 3.4.1 would remain largely unaffected even if the outflow properties where to shift by an order of magnitude in either direction.

## 3.5 Summary and Conclusions

In this work, I presented $HCO^+$ $J = 1 - 0$, $H^{13}CO^+$ $J = 1 - 0$, and SiO $J = 2 - 1$ observations covering the entire DR21 filament. The observations were taken as part of the CASCADE project, using both the NOEMA interferometer and the IRAM 30m telescope. I took advantage of the extended coverage and great spatial resolution of the CASCADE observations to investigate the $HCO^+$ emission associated with all dense molecular cores along the filament for signs of molecular outflows. Subsequently, I compared the outflow activity inside the ridge both with the large scale properties of the filament as well as with extended outflow samples from the literature to assess the impact of environment onto the outflow properties and by extension the star formation process. M conclusions are as follows:

- Based on the spectral emission and moment 0 maps, $HCO^+$ outflows are detected in 14 out of 34 dense molecular cores in the DR21 filament. The outflows appear bipolar in all but one cases.
- Outflow properties (Mass, Momentum, Kinetic energy and the related rates) are calculated for all detected outflows. The "Separation method" (van der Marel et al., 2013) is used for the calculation.

- The outflow properties of the sources in DR21 filament are found not to be statistically different from those of an extended literature sample, suggesting that the extreme and clustered environment of the DR21 filament has no significant impact on the outflow properties. The close connection of outflow activity with accretion, suggests that the star formation process is not strongly afflicted by the broader environment.
- The DR21 sample extends the currently available sample in the intermediate-mass regime, assisting in bridging the apparent gap between high- and low-mass sources in the Outflow - source properties correlations.
- No signs of a correlation between the outflow properties and the declination of the source are found, suggesting the the reported evolutionary stage gradient along the DR21 filament (Hennemann et al., 2012) does not affect significantly the ongoing star formation.
- No preferential direction of the bipolar outflows along the DR21 filament is seen, suggesting that the large scale morphology does not strongly impact the core scales that dictate the outflow launch direction.
- An likely association between the three most extreme outflows along the DR21 ridge (Those of DR21 Main - N46, DR21 (OH) - N44, and N53) and the connection points of accretion filaments is found.

Overall, the results indicate that the star formation process, even in extreme and clustered environments such as the DR21 filament, remains largely unaffected by the broader environment and is rather dictated by local processes. In addition, the results support the presence of a single, common correlation between outflow and source properties across all $M_{\rm env}$ and $L_{\rm bol}$ ranges. Additional and more consistent in term of tracers, resolution, and sensitivity observations of protostellar outflows are required to solidify this result. The existence of a common correlation across the entire $M_{\rm env}$ regime would strongly suggest a single formation mechanism for star of all masses.

CHAPTER 4

# UV-irradiated outflows from low-mass protostars in Ophiuchus with JWST/MIRI

*This chapter contains a summary of the second published article associated with this thesis, titled:*

"**UV-irradiated outflows from low-mass protostars in Ophiuchus with JWST/MIRI**"

I. M. Skretas, A. Karska, L. Francis, W. R. M. Rocha, M. L. van Gelder, Ł. Tychoniec, M. Figueira, M. Sewiło, F. Wyrowski, and P. Schilke
Astronomy & Astrophysics, Volume 703, id.A139.

*The full article can be found in Appendix C.*

*Author contributions: IMS performed the scientific analysis and wrote the manuscript with the supervision of AK and comments from co-authors. The data reduction and some of the scripts used in the analysis were prepared by the co-authors LF, WRMR, MLG, and LT. The figure of the UV field in Ophiuchus was provided by MF.*

## 4.1 Context

As discussed previously in this thesis, the process of star formation is connected with the launch of bipolar outflows and collimated jets. Apart from the millimeter regime, these outflows are bright in the IR wavelength range, through the emission of shock excited $H_2$ as well as various atomic and ionic transitions (see also Section 1.3.4). Previous studies have revealed that UV irradiation can play a significant role in setting the molecular abundances within protostellar outflows (e.g., Karska, Kristensen et al., 2014). The advent of JWST, offering observations of unprecedented sensitivity and spatial resolution, in combination with the development of shock models to cover broad ranges of gas physical conditions and UV fields (e.g., Godard, Pineau des Forêts et al., 2019; Kristensen, Godard et al., 2023) have now opened the path for detailed studies of shocks within protostellar outflows. The nearby low-mass star forming region of Ophiuchus offers a unique opportunity, for such studies thanks to its close distance and high levels of UV irradiation.

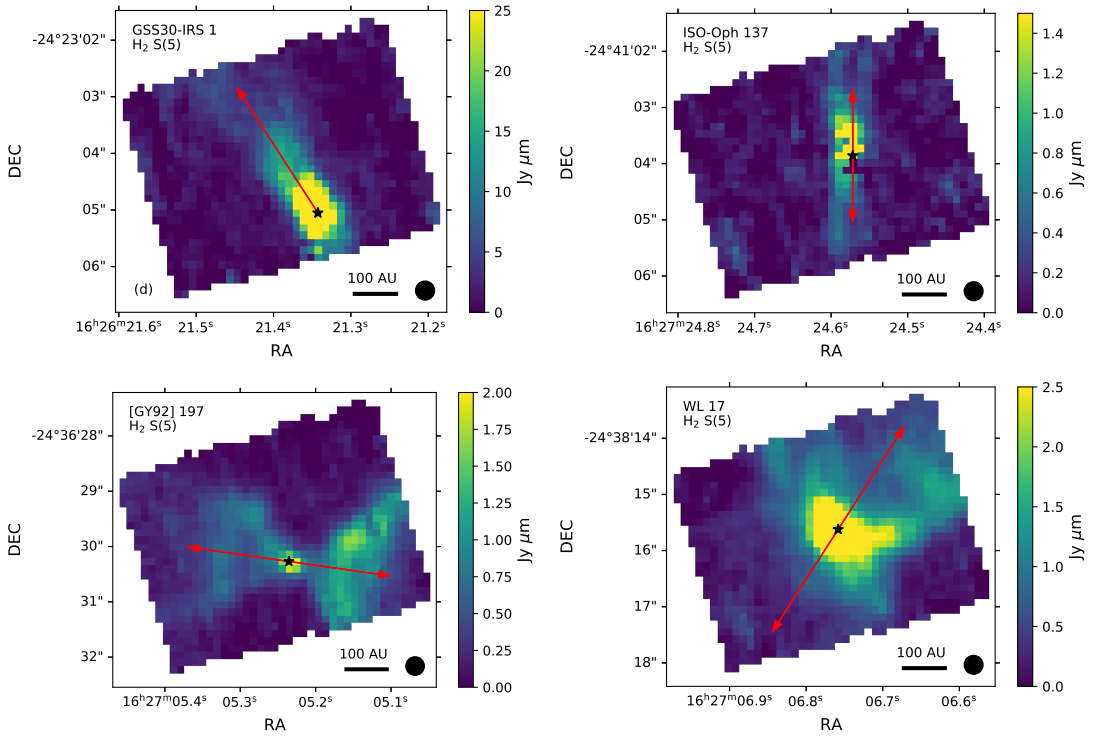


Figure 4.1: Integrated emission of $H_2$ S(5) line at 6.91 $\mu$m toward GSS30-IRS 1, ISO-Oph 137, [GY92] 197, and WL 17. The positions of the protostars, measured from the line-free region at 6.9 $\mu$m, are shown with black stars. The red arrows shows the apparent outflow direction based on the $H_2$ emission. The black filled circle marks the spatial resolution of MIRI at $\lambda$ = 6.9 $\mu$m ($\sim 0.2''$). Figure from Skretas, Karska, Francis et al., 2025.

## 4.2 Aims

The primary aim of this project was to resolve and study the $H_2$, atomic and ionic emission within low-mass protostellar outflows. In particular, to investigate the morphology of the different components, their physical conditions, along with their potential origin in connection with shocks. In addition, I also investigated the potential impact that the external UV radiation field can have on shocks and the subsequent excitation of outflow material.

## 4.3 Methods

In order to address the aforementioned goals, I used observations of five low-mass protostars in the Ophiuchus molecular cloud, taken with the MIRI/MRS on board the JWST. The MIRI/MRS observations allowed for the creation of integrated line intensity maps, enabling the study of the outflow and jet morphology in the various molecular, atomic, and ionic transitions covered within its wavelength range. Thanks to the multiple rotational transitions of $H_2$ that are covered within that range, the construction of rotational diagrams is also possible, allowing in turn an accurate

characterization of the gas properties within protostellar outflows. Finally, the comparison with available shock model predictions covering a vast range of parameters enables to constrain shock conditions and in particular the level of UV irradiation required to reproduced observed line ratios through shocks.

## 4.4 Results

Integrated intensity maps of the different $H_2$ transitions within the MIRI range (S(1) - S(8)) revealed the presence of outflows in four out of the five sources in my sample. Interestingly, the detected outflows display two distinct morphologies, with two sources showing narrow, well collimated outflows and the other two wide angled flows, with well defined cavities (see Figure 4.1). In turn, the ionic transitions, and especially those of [Fe II], reveal collimated jets in 3 of the outflow sources. WL 17 is the only outflow source with no detected jet, instead the only extended emission detected comes from widespread [Ne II] within the outflow cavity.

The creation of rotational diagrams, using the $H_2$ transitions, allowed us to probe the physical conditions of the outflowing gas (e.g., see Figure 4.2). In order to fit the curvature of the rotational diagram, two separate gas components where needed in all cases, a warm component with temperatures of $\sim$ 520 K and a hot component with temperatures upwards of 1000 K. The resulting temperatures are in line with those found for other $H_2$ outflows studied with JWST (e.g., Tychoniec, van Gelder et al., 2024; Francis et al., 2025). Comparison with temperature estimates from *Herschel* high-$J$ CO observations (Karska, Kaufman et al., 2018) showed that the $H_2$ temperatures are consistently higher, suggesting that the two tracers probe slighty different parts of the outflows (Figure 4.3).

Comparison of the observed $H_2$ line ratios, with those produced in UV irradiated shock models (Kristensen, Godard et al., 2023) resulted in two possible families of possible solutions (Figure

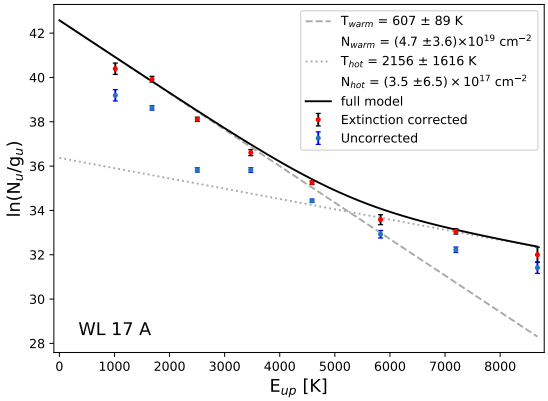


Figure 4.2: Example of $H_2$ rotational diagram for the outflow of WL 17. The extinction-corrected values are shown in red, and the ones before the correction in blue. The dashed and dotted lines mark the fits to the two gas components of the outflow (warm and hot respectively), while the black line marks the combined fit. Figure adapted from Skretas, Karska, Francis et al., 2025.

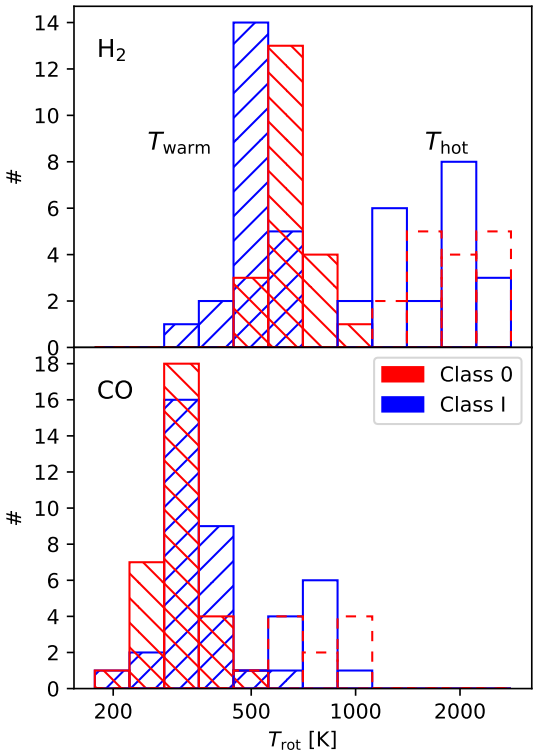


Figure 4.3: Distribution of the rotational temperatures of $H_2$ (top) and high-$J$ CO (bottom) in low-mass protostars. Temperatures in Class 0 protostars are shown in red, and in Class I sources in blue. The warm gas components is shown in stripped bins, and the hot one in clear bins. $H_2$ results for Class 0 protostars are adopted from Francis et al., 2025, and CO results for both Class 0 and I are from Karska, Kaufman et al., 2018. Figure taken from Skretas, Karska, Francis et al., 2025.

4.4). The first possible kind of shocks are low-density ($n_H \leq 10^3$ cm$^{-3}$), slow-moving ($v_{sh} \leq 20$ km s$^{-1}$) $J$-type shocks. For higher densities ($n_H \geq 10^4$ cm$^{-3}$), $C$-type shocks are seen to better match the $H_2$ line ratios even for velocities above 20 km s$^{-1}$. In both cases, however, the presence of an external UV radiation field of the order of 10-100 $G_0$ seems to be the one best reproducing the observed line ratios. In addition, synthetic rotational diagrams, reproduced from the shock model results in Kristensen, Godard et al., 2023 show that $J$ shocks are better at reproducing the curvature of the observed rotational diagrams, but underestimate the column densities by one to two orders of magnitude, while $C$ shocks match the column densities but are better represented by a single temperature component.

Finally, I estimated the UV field at the locations of my sources using two separate methods, firstly based on the dust continuum emission and secondly by summing all the UV emission from all nearby massive stars. These two approaches both showed a substantial variation of the UV field strength between the locations of the sources. Despite that, I found that the outflow properties of all sources appear relatively uniform, suggesting that the UV radiation from the broader environment is not impacting the outflow shocks. A possible explanation then for

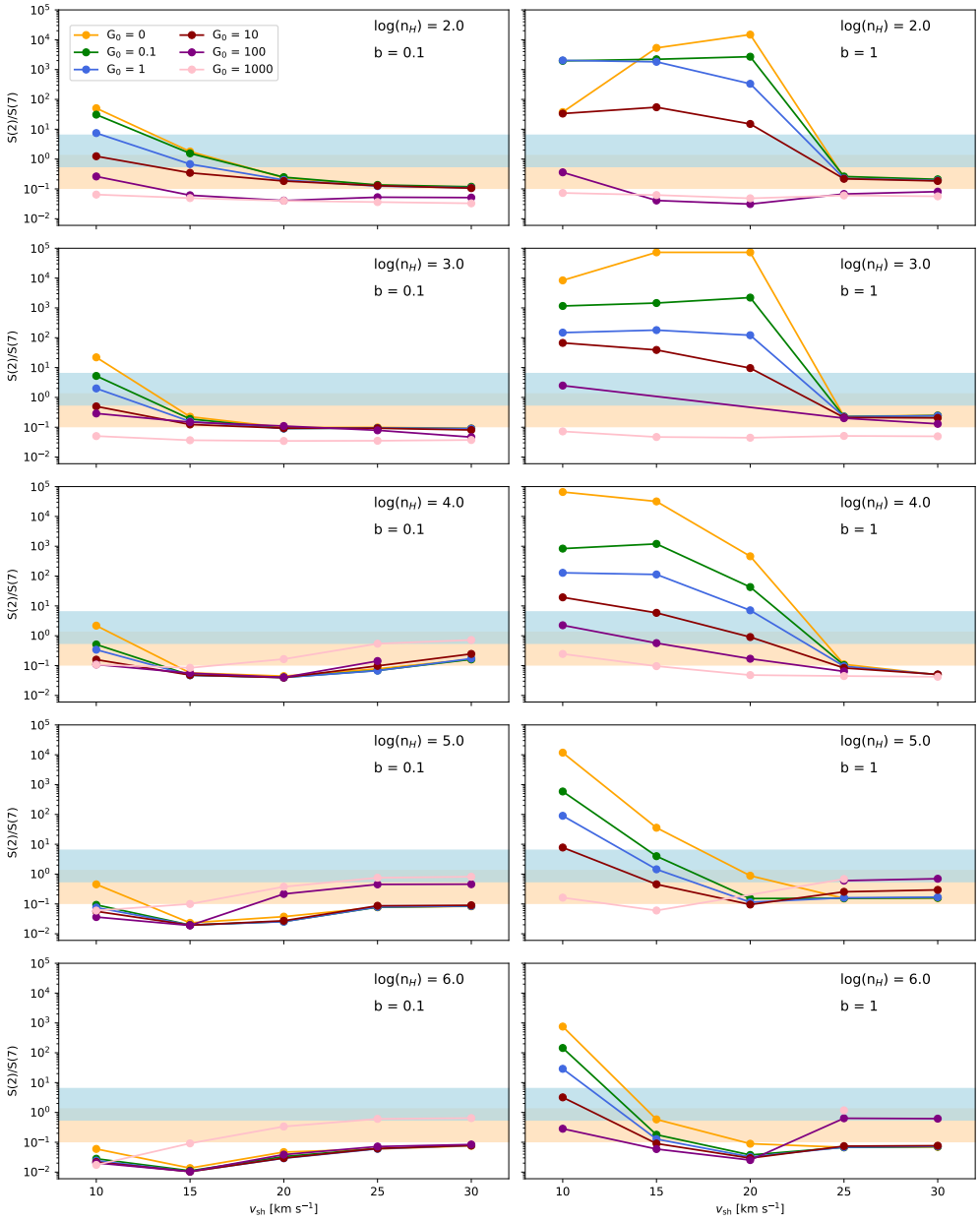


Figure 4.4: Ratio of the S(2) over the S(7) transition of $H_2$ against the shock velocity for different UV field strengths. The log($n_H$) ranges from 2 to 6 from top to bottom, while magnetic field strength is b = 0.1 for the left column and 1 for the right. For all panels $\zeta = 10^{-17}$ s$^{-1}$, and X(PAH)= $10^{-7}$ are used. The blue shaded region marks the observed range of S(2)/S(7) ratios for the sources in Ophiuchus, while the beige region marks the range for Class 0 sources from Francis et al., 2025. Note that line intensities from Kristensen, Godard et al., 2023 are not available for all combinations of model parameters covered in the figure. Figure taken from Skretas, Karska, Francis et al., 2025.

the origin of the UV irradiation within the outflows is that it arises from other shocks within the outflow or accretion shocks onto the central protostar, that then escapes within the outflow cavity.

## 4.5 Conclusions

This work showcased in great detail the morphology of four protostellar outflows, as they appear at the vicinity of protostars, and highlighted their differences. At the same time, it showed that physical conditions within those outflows remain relatively consistent despite morphological and environmental differences. Finally, this work highlights the important role that UV irradiation plays in shocks within protostellar outflows, indicating that the origin of this UV emission is localized within the sources.

CHAPTER 5

# Summary and outlook

## 5.1 Summary

Throughout this thesis, I studied several different aspects of protostellar outflows, in an effort to further our understanding of this key ingredient of star formation. Taking advantage of the CASCADE observations, which cover the Cygnus-X high-mass star-forming region in the 3 millimeter window (Beuther, Wyrowski et al., 2022), I started by looking into one of the most extreme cases of protostellar outflows, that of the outflow of DR21 Main. I studied its morphological, kinematic and energetic properties in detail, eventually aiming to understand the true nature of this remarkable outflow, as it has been proposed to be an explosive outflow (Zapata, Schmid-Burgk, Pérez-Goytia et al., 2013), a new class of outflows associated with the disintegration of protostellar systems (Bally and Zinnecker, 2005; Zapata, Schmid-Burgk, Ho et al., 2009). Subsequently, I expanded the study of outflows covering the entirety of the DR21 filament. Making use of existing catalogs of dense molecular clumps (Motte, Bontemps, Schilke et al., 2007; Cao, Qiu, Q. Zhang, Y. Wang, Hu et al., 2019; Cao, Qiu, Q. Zhang, Y. Wang and Xiao, 2021), the location of high-mass star formation, along with observations from CASCADE, I aimed to identify all the outflow activity taking place along the filament. Armed with such a coherent sample of outflows I investigated which, if any, environmental factors impact the star formation process both through comparison of the sources along the filament, but also by comparing the entire DR21 sample with literature-drawn samples of outflows from other, less active, star-forming regions. Finally, I shifted the focus from the cold, entrained, outflows probed in the millimeter regime, to the warm inner parts of outflows that are bright in the IR, and from the regions of high-mass star-formation to those of their low-mass counterparts. More precisely, using JWST observations of five low-mass protostars in the nearby Ophiuchus molecular cloud I had the opportunity to probe the hot $H_2$ molecular parts of protostellar outflows as well as the atomic/ionic jet components. In my analysis, I aimed to investigate the origin of the hot $H_2$ emission in shocks along with the role UV radiation plays in its excitation. In the following, I briefly summarize the results of the different projects presented in this thesis.

### Part I: A detailed kinematic analysis of the DR21 Main outflow

- The analysis of integrated intensity maps for all the different molecular species covered in the range of the CASCADE observations showed that they can broadly be separated in three distinct categories, depending on the morphology. The first is strongly associated with the bipolar outflow, showing high velocity emission and tracing the two outflow lobes (e.g., $HCO^+$), the second traces colder and denser material, and is best associated with the dense DR21 ridge in the North-South direction (e.g., $N_2H^+$), while the third shows centrally concentrated emission near the location of DR21 Main (e.g., SiO).

- High-velocity $HCO^+$ emission in DR21 Main revealed two well defined lobes extending in a northeast - southwest direction. The shape of the two lobes, along with their collimation at higher distances is resembles more that of a typical bipolar outflow. Additionally, the blue and red-shifted components are found to overlap almost completely across both lobes.

- Looking into local maxima of the $HCO^+$ emission at different velocity steps, I was unable to detect any velocity coherent filamentary structures, like those seen in the prototypical explosive outflow Orion KL. As these structures are believed to be a key characteristic of explosive outflows, my observations suggest that the outflow of DR21 Main is more akin to a typical bipolar outflow instead of an explosive one.

- I estimated the energetic properties of the DR21 Main outflow (i.e., the mass, momentum, kinetic energy, and the associated rates) using the commonly used estimation methods (e.g., van der Marel et al., 2013) and compared them with those of an extended sample of literature sources. Based on the correlation between outflow and driving source properties, I found that the outflow of DR21 Main has energetic properties consistently higher than those of other sources with similar envelope mass and bolometric luminosity, cementing DR21 Main as one of the most powerful known outflows in the Galaxy.

- My analysis also revealed that the western outflow lobe is actively interacting with a dense molecular structure. The dense structure itself was seen in $N_2H^+$ emission, while the $HCO^+$ emission from the outflow was seen peaking right in front of it. The detection of $H_2CO$ and SiO emission along the interface between $N_2H^+$ and $HCO^+$ indicated the presence of shocks, likely caused by the interaction.

### Part II: Overview of the molecular outflows along the DR21 ridge

- Analysis of the $HCO^+$ emission from CASCADE, revealed outflows in 14 out of the 34 dense molecular clumps along the DR21 filament. In all but one case the detected outflows were bipolar.

- Outflow properties for all detected outflows, were calculated using the separation method (van der Marel et al., 2013), adapted for use with $HCO^+$ observations.

- Next, I compared the outflow properties of the DR21 filament sources with those of an extended literature sample and found no statistically significant difference between the two

samples. This result indicates that the highly clustered, active, and irradiated environment of the DR21 filament, has minimal impact on the protostellar outflows.

- The DR21 sample also appears to successfully fill the gap of intermediate mass sources in the correlations of outflow and source properties, connecting the low- and high-mass sources. The existence of a uniform distribution of outflow and source properties across the entire mass spectrum suggests a shared formation mechanism regardless of mass.

- I detected no clear trends between the outflow properties and their declination, suggesting that the reported age gradient running from north to south along the filament (Hennemann et al., 2012) has no impact on outflow properties.

- In addition, I found that the orientation of outflows along the filament is mostly random, despite the tight North-South direction of the DR21 ridge. This result suggests that core-scale rotation, which dictates outflow orientation, is independent of the large scale filaments that make up star-forming regions.

- Lastly, I identified an apparent connection between the three most prominent outflow sources in the DR21 ridge (DR21 Main, DR21 (OH), and N53), and the locations where accretion filaments intersect with the main DR21 ridge. This results reinforces the proposed hub-filament systems as prime locations of high-mass star formation theory.

**Part III: UV-irradiated outflows from low-mass protostars in Ophiuchus with JWST/MIRI**

- I detected $H_2$ outflows in four out of five sources in the sample. Creating integrated intensity maps of the emission, I found that, despite all sources sharing the same evolutionary stage (Class I), two of them had narrow and well collimated outflows while the other two showed broad outflows with well defined cavities.

- I also detected ionic jets in three out of four outflow sources. These jets were primarily seen in the transitions of [Fe II]. The only ionic emission seen in the final source was extended [Ne II] emission, which was seen filling the outflow cavity.

- Multiple rotational transitions of $H_2$, were detected within the outflows, allowing the creation of rotational diagrams. In all cases, I found that a two-temperature model with warm component temperatures of ~500-600 K and hot component temperature exceeding ~1000 K reproduces well the observed rotational diagrams. These results are similar to those found in other JWST studies, but consistently higher than those measured earlier in the high-$J$ CO transitions with *Herschel*, suggesting that the $H_2$ and high-$J$ CO gas trace somewhat different outflow components.

- To constrain the origin of the $H_2$ emission to shock excitation, I carried out comparisons with state-of-the-art shock models. The results showed two possible types of solutions capable of reproducing the observed line ratios. The first are low-density ($n_H \leq 10^3$ cm$^{-3}$), slow moving ($v_{sh} \leq 20$ km s$^{-1}$), $J$-type shocks, while the other is higher density ($n_H \geq 10^4$

cm$^{-3}$) *C*-type shocks. In both cases, I found that the presence of a substantial external UV field of the order of 10-100 $G_0$ is required to best match the observations. Interestingly, *J*-type shocks are better reproducing the curvature of the observed rotational diagrams but underestimate the column densities, while the opposite is true for *C*-type models.

- In order to determine the origin of the UV emission that is required to reproduce the observed $H_2$ excitation, I constrained the UV radiation at the location of my sources using two independent methods, one based on the dust continuum emission and the other based on the radiation from nearby stars. Both approaches showed that the UV field strength varies by approximately an order of magnitude between the sources. Given that the observed excitation of the sources varies much less, the results suggest that the external UV field does not have significant impact on the protostellar outflows. The possible origin of the UV radiation within the outflows is therefore either other shocks taking place along the protostellar jet and outflow, or accretion shocks onto the surface of the protostar itself, with the radiation escaping along the outflow cavity.

Through the various individual results of the projects that make up this thesis, a common narrative emerged regarding the lack of a strong connection between the protostellar outflow activity and the environment within which these outflows are formed. More precisely, the results of this thesis have shown, for a variety of protostellar sources and for a variety of environments, that the majority of environmental factors (density of star formation in the region, evolutionary trends of the host molecular cloud, orientation of large scale filaments, UV radiation field) have minimal impact on the presence and properties of protostellar outflows. The link between the outflow activity and the accretion onto protostars, allows to extrapolate this conclusion, and to propose that the star formation process as a whole is largely independent of the environment, but is rather dictated by processes taking place at the smaller, core scales.

## 5.2 Outlook and future steps

The results presented in this thesis represent significant steps in furthering our understanding of multiple aspects of protostellar outflow activity and the star formation process. As such, those results serve as a stepping stone for future research, required to constrain the details of these complex processes.

### The outflow of DR21 Main and other explosive outflows

On the topic of explosive outflows, the results concerning the outflow of DR21 Main, one of the few candidate explosive outflows reported (Zapata, Schmid-Burgk, Pérez-Goytia et al., 2013), showed little signs of the telltale signs of explosive outflows. This result has already led to follow-up studies of the source, with Guzmán Ccolque, Fernández López et al., 2024, using new ALMA observations of CO, proposing a dual-nature scenario for DR21 Main, with an initial bipolar outflow followed by an explosive outflow seen centrally. More and more new candidate explosive outflows are nowadays being reported (e.g., Zapata, Fernández-López et al., 2023; Issac

et al., 2025), but the results of this thesis highlight that substantial scrutiny is required before confirming the explosive nature of protostellar outflows.

In addition, this thesis showed that DR21 Main, along with other explosive outflows, demonstrate particularly elevated values of their energetic properties, in comparison to sources of bipolar outflows with similar source properties ($M_{\rm env}$ and $L_{\rm bol}$). Particularly in the case of DR21 Main this result was also later confirmed by far-IR observations (Karska, Figueira et al., 2025). While restricted by the limited sample size examined so far, this results offers a unique way to identify in the future additional explosive outflow candidates, based solely on their energetic properties, without the need to resolve the small scale filament-like structures that require high-resolution interferometric observations. Since the study of explosive outflows is still in its early steps, with only a small number of proposed sources currently existing, a way to easily identify new candidate sources is of great importance.

Apart from focusing into expanding the available sample of explosive outflow sources, which will allow for more statistically supported conclusions on their details to be drawn, additional questions remain important to address. On the observational side, it is of great interest to analyze the composition of the filament-like structures that make up explosive outflows. So far, those have only been reported in the low rotational transitions of CO (e.g., Zapata, Schmid-Burgk, Pérez-Goytia et al., 2013; Zapata, Schmid-Burgk, Rodríguez et al., 2017; Guzmán Ccolque, Fernández López et al., 2024) and were not seen in other tracers, such us the $HCO^+$ emission used in this work (Skretas, Karska, Wyrowski et al., 2023). In-depth spectroscopic observations targeting the locations of the reported filament-like structures of known explosive outflows are a necessary next step, in order to shed light into the inner structure of these filaments and constrain their formation mechanism. To that end, efforts on modeling explosive outflows, with primary focus on constraining their formation mechanisms have already started (e.g., Rivera-Ortiz et al., 2025).

### The outflows of Cygnus-X North - expanding the analysis of the CASCADE observations

The CASCADE observations cover all the densest parts of the Cygnus-X North region. This includes several additional molecular clouds in addition to DR21. In the future, I aim to expand the search of protostellar outflows so that it covers the entire region of CASCADE, significantly expanding the sample of outflows in Cygnus-X. All these clouds are also covered in the molecular clump catalogs of Motte, Bontemps, Schilke et al., 2007; Cao, Qiu, Q. Zhang, Y. Wang, Hu et al., 2019; Cao, Qiu, Q. Zhang, Y. Wang and Xiao, 2021, therefore the necessary information to expand the analysis carried out over the DR21 filament (see Chapter 3) to the other regions is already available. This expansion will more than triple the total number of dense molecular clumps covered, representing a significant expansion to the number of sources studied so far thus giving a much stronger statistical significance to the results presented in this thesis.

In addition, as many of the sources reported in Motte, Bontemps, Schilke et al., 2007; Cao, Qiu, Q. Zhang, Y. Wang, Hu et al., 2019; Cao, Qiu, Q. Zhang, Y. Wang and Xiao, 2021 fall in the intermediate mass range, constraining the properties of their outflows will expand substantially the sample of protostellar outflows in the mass range of the apparent gap in the outflow - source

properties correlations (e.g., Skretas and Kristensen, 2022). Obtaining a robust sample of intermediate mass sources with well constrained outflow properties will then allow the unification of the low and high mass regimes, solidifying the presence of a unified formation mechanism across the entire protostellar mass range. Collecting such a coherent sample of protostellar outflows, with well studied source properties will allow us also to investigate the connection between the outflow activity and the properties of the sources. More precisely the limits, if any, in source properties above or below which outflows are no longer detected can be probed. Determining whether such limits are real or sensitivity based is crucial in understanding the edge cases of star formation. As all clouds in the Cygnus-X North share the same large scale environment (e.g., UV field), comparisons between sources located within the different clouds of Cygnus-X can reveal the impact of the cloud scale environmental properties (e.g., star formation density, cloud column density) on the star formation process, thus expanding on the results from Chapter 3.

Finally, of particular interest is the apparent disconnect between outflow orientation and the orientation of the host filament of DR21 (see Figure 3.15), that my preliminary results indicate. This result challenges the belief that the large scale filaments, which carry most of the mass infalling toward the protostelar cores, also dictate their rotation. Building upon this result would initially require further analysis, in particular regarding a more accurate representation of the orientation of the host filament at small scales surrounding the individual star-forming cores. A more detailed orientation of the filaments can be achieved through the use of filament finding algorithms on the CASCADE observations, or alternatively from previous literature studies that performed a similar analysis (e.g., Cao, Qiu, Q. Zhang and Li, 2022). Subsequently, further confirmation of this promising result can be achieved through the study of additional star forming filaments. Constraining the connection between the orientation of outflows and the direction of the host filaments, is a crucial factor in the development of more accurate models describing the overall evolution of molecular clouds.

### The future of IR outflow studies - the origin of shock excited $H_2$ emission

The JWST has the resolving power and sensitivity to revolutionize the studies of protostellar outflows. Early results, including those shown in Chapter 4, show MIRI observations have the power to resolve the protostellar jets and outflows down to distances of a few hundreds of AUs. In addition, they provide access to the rotational transitions of $H_2$, thus allowing the estimation of gas physical properties and comparisons with shock models to constrain its origin (e.g., Caratti o Garatti et al., 2024; Tychoniec, van Gelder et al., 2024). Similarly, NIRSpec studies has also shown a wealth of ionic jets from protostars (e.g., Federman et al., 2024), while NIRCam has proved ideal in imaging the complex structures of outflow lobes (e.g., Ray et al., 2023). The main restriction for all these studies so far have been limitation in sample sizes, as observations of protostars with JWST have been quite limited. This is now changing, with some JWST large programs targeting protostars and their outflows having been completed over the past two years. For example, the JWST Observations of Young protoStars (JOYS; van Dishoeck, Tychoniec et al., 2025) targeted multiple low- and high-mass protostars and their outflows, while the High Angular Resolution observations of Stellar Emergence in Filamentary Environments (HEFE; Megeath et al., 2024) targeted the integral shape filament in Orion. The large samples of protostellar

outflows offer ample opportunity to expand the analysis presented in Chapter 4.

In addition, the large coverage of the integral shape filament with NIRCam in HEFE opens additional opportunities to study the complex morphologies of protostellar outflow lobes as they interact with the surrounding ISM. These morphologies hold the key to understanding the interaction between outflows are their surroundings, and potentially quantifying their impact. As the HEFE project also contains narrow band filters covering the shock excited $H_2$ emission, the HEFE field can be used for the identification of shock knots along protostellar jets and outflow cavity walls. Follow-up observations with MIRI of such shock locations will enable the study of shock properties relative to the their location within the protostellar outflows potentially revealing the origin of the UV irradiation identified in Chapter 4 of this work.

Overall, while these are still the early days of outflow studies with JWST, the initial results already show significant promise. With the addition of the newly available data from the different observing programs, the required statistics for constraining the outflow and shock properties in the IR regime are also becoming available.

In total, it is apparent that, despite all the work that has been done on protostellar outflows over the years, there are still a lot of open question remaining. With the results presented in this thesis suggesting that large scale environmental factors do not significantly impact the process of star formation, the question of which factor are then really dictating star formation is naturally raised. While my results indicate the existence of a uniform driving mechanism for all protostellar outflows, the details of such a mechanism remain unclear. Lastly, despite demonstrating the internal origin of the UV irradiation that influences the shock excitation of $H_2$ in outflows, the mechanism behind the extended $H_2$ emission within those outflows is still a mystery. Still, thanks to the ever increasing capabilities of modern observing facilities, enabling among other, the execution of large scale surveys covering entire star forming regions, like CASCADE and HEFE, I remain optimistic that more answers will be uncovered in the future.

# Bibliography


Ahmadi, A. et al. (2023), *Kinematics and stability of high-mass protostellar disk candidates at sub-arcsecond resolution. Insights from the IRAM NOEMA large programme CORE*, A&A **677**, A171 A171, arXiv: 2305.00020 [astro-ph.GA].

Andre, P., J. Martin-Pintado, D. Despois and T. Montmerle (1990), *Discovery of a remarkable bipolar flow and exciting source in the rho Ophiuchi cloud core.*, A&A **236** 180.

Andre, P., D. Ward-Thompson and M. Barsony (1993), *Submillimeter Continuum Observations of rho Ophiuchi A: The Candidate Protostar VLA 1623 and Prestellar Clumps*, ApJ **406** 122.

Andrews, S. M. et al. (2018), *The Disk Substructures at High Angular Resolution Project (DSHARP). I. Motivation, Sample, Calibration, and Overview*, ApJ **869**, L41 L41, arXiv: 1812.04040 [astro-ph.SR].

Araya, E. D., S. Kurtz, P. Hofner and H. Linz (2009), *Radio Continuum and Methanol Observations of DR21(OH)*, ApJ **698** 1321, arXiv: 0904.4086 [astro-ph.GA].

Arce, H. G., D. Shepherd et al. (2007), "Molecular Outflows in Low- and High-Mass Star-forming Regions", *Protostars and Planets V*, ed. by B. Reipurth, D. Jewitt and K. Keil 245, arXiv: astro-ph/0603071 [astro-ph].

Arce, H. G. and A. I. Sargent (2006), *The Evolution of Outflow-Envelope Interactions in Low-Mass Protostars*, ApJ **646** 1070, arXiv: astro-ph/0605139 [astro-ph].

Argyriou, I. et al. (2023), *JWST MIRI flight performance: The Medium-Resolution Spectrometer*, A&A **675**, A111 A111, arXiv: 2303.13469 [astro-ph.IM].

Bachiller, R. (1996), *Bipolar Molecular Outflows from Young Stars and Protostars*, ARA&A **34** 111.

Bally, J. and C. J. Lada (1983), *The high-velocity molecular flows near young stellar objects*, ApJ **265** 824.

Bally, J. (2016), *Protostellar Outflows*, ARA&A **54** 491.

Bally, J., N. J. Cunningham et al. (2011), *Explosive Outflows Powered by the Decay of Non-hierarchical Multiple Systems of Massive Stars: Orion BN/KL*, ApJ **727**, 113 113, arXiv: 1011.5512 [astro-ph.GA].

Bally, J., A. Ginsburg, H. Arce et al. (2017), *The ALMA View of the OMC1 Explosion in Orion*, ApJ **837**, 60 60, arXiv: 1701.01906 [astro-ph.SR].

Bally, J., A. Ginsburg, D. Silvia and A. Youngblood (2015), *The Orion fingers: Near-IR adaptive optics imaging of an explosive protostellar outflow*, A&A **579**, A130 A130, arXiv: 1502.04711 [astro-ph.GA].

Bally, J. and H. Zinnecker (2005), *The Birth of High-Mass Stars: Accretion and/or Mergers?*, AJ **129** 2281, arXiv: astro-ph/0502485 [astro-ph].

Balsara, D., D. Ward-Thompson and R. M. Crutcher (2001), *A turbulent MHD model for molecular clouds and a new method of accretion on to star-forming cores*, MNRAS **327** 715, arXiv: astro-ph/0105327 [astro-ph].

Banerjee, R., R. E. Pudritz and D. W. Anderson (2006), *Supersonic turbulence, filamentary accretion and the rapid assembly of massive stars and discs*, MNRAS **373** 1091, arXiv: astro-ph/0609428 [astro-ph].

Barnard, E. E. (1907), *On a nebulous groundwork in the constellation Taurus.*, ApJ **25** 218.

– (1909), *On the colors of some of the stars in the globular cluster M13 Herculis.*, ApJ **29** 72.

Beerer, I. M. et al. (2010), *A Spitzer View of Star Formation in the Cygnus X North Complex*, ApJ **720** 679, arXiv: 1007.2112 [astro-ph.SR].

Beltrán, M. T. and W. J. de Wit (2016), *Accretion disks in luminous young stellar objects*, A&A Rev. **24**, 6 6, arXiv: 1509.08335 [astro-ph.GA].

Beuther, H., R. Kuiper and M. Tafalla (2025), *Star Formation from Low to High Mass: A Comparative View*, ARA&A **63** 1, arXiv: 2501.16866 [astro-ph.GA].

Beuther, H., P. Schilke et al. (2002), *Massive molecular outflows*, A&A **383** 892, arXiv: astro-ph/0110372 [astro-ph].

Beuther, H., F. Wyrowski et al. (2022), *The Cygnus Allscale Survey of Chemistry and Dynamical Environments: CASCADE. Overview and first results toward DR20 from the Max Planck IRAM Observatory program (MIOP)*, A&A **665**, A63 A63, arXiv: 2207.10964 [astro-ph.GA].

Beuther, H. and D. Shepherd (2005), "Precursors of UchII Regions and the Evolution of Massive Outflows", *Astrophysics and Space Science Library*, ed. by M. S. N. Kumar, M. Tafalla and P. Caselli, vol. 324, Astrophysics and Space Science Library 105, arXiv: astro-ph/0502214 [astro-ph].

Bhandare, A. et al. (2018), *First core properties: from low- to high-mass star formation*, A&A **618**, A95 A95, arXiv: 1807.06597 [astro-ph.SR].

Bjerkeli, P., M. H. D. van der Wiel, D. Harsono, J. P. Ramsey and J. K. Jørgensen (2016), *Resolved images of a protostellar outflow driven by an extended disk wind*, Nature **540** 406, arXiv: 1612.05148 [astro-ph.SR].

Blandford, R. D. and D. G. Payne (1982), *Hydromagnetic flows from accretion disks and the production of radio jets.*, MNRAS **199** 883.

Böker, T. et al. (2023), *In-orbit Performance of the Near-infrared Spectrograph NIRSpec on the James Webb Space Telescope*, PASP **135**, 038001 038001, arXiv: 2301.13766 [astro-ph.IM].

Bonnell, I. A., R. B. Larson and H. Zinnecker (2007), "The Origin of the Initial Mass Function", *Protostars and Planets V*, ed. by B. Reipurth, D. Jewitt and K. Keil 149, arXiv: astro-ph/0603447 [astro-ph].

Bonnell, I. A., M. R. Bate and H. Zinnecker (1998), *On the formation of massive stars*, MNRAS **298** 93, arXiv: astro-ph/9802332 [astro-ph].

Bonnell, I. A., S. G. Vine and M. R. Bate (2004), *Massive star formation: nurture, not nature*, MNRAS **349** 735, arXiv: astro-ph/0401059 [astro-ph].

Bontemps, S., P. Andre, S. Terebey and S. Cabrit (1996), *Evolution of outflow activity around low-mass embedded young stellar objects*, A&A **311** 858.

Bontemps, S., F. Motte, T. Csengeri and N. Schneider (2010), *Fragmentation and mass segregation in the massive dense cores of Cygnus X*, A&A **524**, A18 A18, arXiv: 0909.2315 [astro-ph.GA].

Cabrit, S. and C. Bertout (1992), *CO line formation in bipolar flows. III. The energetics of molecular flows and ionized winds.*, A&A **261** 274.

Canto, J. and L. F. Rodriguez (1980), *A stellar-wind focusing mecanism as an explanation for Herbig-Haro objects.*, ApJ **239** 982.

Cao, Y., K. Qiu, Q. Zhang and G.-X. Li (2022), *The DR21(OH) Trident-Resolving the Massive Ridge into Three Entangled Fibers as the Initial Condition of Cluster Formation*, ApJ **927**, 106 106, arXiv: 2112.14080 [astro-ph.GA].

Cao, Y., K. Qiu, Q. Zhang, Y. Wang, B. Hu et al. (2019), *Surveys of Clumps, Cores, and Condensations in Cygnus X. I. A New Catalog of ~0.1 pc Massive Dense Cores*, ApJS **241**, 1 1, arXiv: 1901.06475 [astro-ph.GA].

Cao, Y., K. Qiu, Q. Zhang, Y. Wang and Y. Xiao (2021), *Core Mass Function of a Single Giant Molecular Cloud Complex with 10,000 Cores*, ApJ **918**, L4 L4, arXiv: 2108.01313 [astro-ph.GA].

Caratti o Garatti, A. et al. (2024), *JWST Observations of Young protoStars (JOYS): HH211: Textbook case of a protostellar jet and outflow*, A&A **691**, A134 A134, arXiv: 2409.16061 [astro-ph.SR].

Chandrasekhar, S. (1931), *The Maximum Mass of Ideal White Dwarfs*, ApJ **74** 81.

Charnley, S. B. (1997), *Sulfuretted Molecules in Hot Cores*, ApJ **481** 396.

Chen, H., P. C. Myers, E. F. Ladd and D. O. S. Wood (1995), *Bolometric Temperature and Young Stars in the Taurus and Ophiuchus Complexes*, ApJ **445** 377.

Ching, T.-C. et al. (2018), *Interactions Between Gas Dynamics and Magnetic Fields in the Massive Dense Cores of the DR21 Filament*, ApJ **865**, 110 110, arXiv: 1808.03459 [astro-ph.GA].

Christensen, I. B. et al. (2024), *The Cygnus Allscale Survey of Chemistry and Dynamical Environments: CASCADE. III. The large scale distribution of $DCO^+$, DNC, and DCN in the DR21 filament*, A&A **688**, A215 A215, arXiv: 2406.09145 [astro-ph.GA].

Csengeri, T., S. Bontemps et al. (2011), *Convergent Flows and Low-velocity Shocks in DR21(OH)*, ApJ **740**, L5 L5, arXiv: 1108.4451 [astro-ph.GA].

Csengeri, T., L. Bouscasse et al. (2024), "NASCENT-stars large program: origin of molecular complexity towards emerging high-mass protostars", *The Promises and Challenges of the ALMA Wideband Sensitivity Upgrade* 10.

Curtis, E. I., J. S. Richer, J. J. Swift and J. P. Williams (2010), *A submillimetre survey of the kinematics of the Perseus molecular cloud - II. Molecular outflows*, MNRAS **408** 1516, arXiv: 1006.3218 [astro-ph.GA].

Cyganowski, C. J., M. J. Reid, V. L. Fish and P. T. P. Ho (2003), *Dual Cometary H II Regions in DR 21: Bow Shocks or Champagne Flows?*, ApJ **596** 344, arXiv: astro-ph/0307502 [astro-ph].

Dame, T. M., D. Hartmann and P. Thaddeus (2001), *The Milky Way in Molecular Clouds: A New Complete CO Survey*, ApJ **547** 792, arXiv: astro-ph/0009217 [astro-ph].

Dannhauer, S. M. et al. (2025), *The Diamond Ring in Cygnus X: Advanced stage of an expanding bubble of ionised carbon*, arXiv e-prints, arXiv:2509.22427 arXiv:2509.22427, arXiv: 2509.22427 [astro-ph.GA].

Davis, C. J. et al. (2007), *WFCAM, Spitzer/IRAC and SCUBA observations of the massive star-forming region DR21/W75 - I. The collimated molecular jets*, MNRAS **374** 29, arXiv: astro-ph/0610186 [astro-ph].

Delabrosse, V. et al. (2024), *JWST study of the DG Tau B disk-wind candidate. I. Overview and nested $H_2$-CO outflows*, A&A **688**, A173 A173, arXiv: 2403.19400 [astro-ph.SR].

Dickel, J. R., H. R. Dickel and W. J. Wilson (1978), *The detailed structure of CO in molecular cloud complexes. II. The W75-DR21 region.*, ApJ **223** 840.

Dicker, S. R. et al. (2014), *MUSTANG 2: A Large Focal Plane Array for the 100 m Green Bank Telescope*, Journal of Low Temperature Physics **176** 808.

Downes, D. and R. Rinehart (1966), *Microwave Observations of the Cygnus X Region*, ApJ **144** 937.

Downes, T. P. and S. Cabrit (2007), *Jet-driven molecular outflows from class 0 sources: younger and stronger than they seem?*, A&A **471** 873.

Draine, B. T. (1980), *Interstellar shock waves with magnetic precursors*, ApJ **241** 1021.

Draine, B. T., W. G. Roberge and A. Dalgarno (1983), *Magnetohydrodynamic shock waves in molecular clouds.*, ApJ **264** 485.

Draine, B. T. (2011), *Physics of the Interstellar and Intergalactic Medium*.

Duarte-Cabral, A., S. Bontemps, F. Motte, A. Gusdorf et al. (2014), *SiO emission from low- and high-velocity shocks in Cygnus-X massive dense clumps*, A&A **570**, A1 A1, arXiv: 1407.6400 [astro-ph.GA].

Duarte-Cabral, A., S. Bontemps, F. Motte, M. Hennemann et al. (2013), *CO outflows from high-mass Class 0 protostars in Cygnus-X*, A&A **558**, A125 A125, arXiv: 1308.6490 [astro-ph.GA].

Dunham, M. M., A. M. Stutz et al. (2014), "The Evolution of Protostars: Insights from Ten Years of Infrared Surveys with Spitzer and Herschel", *Protostars and Planets VI*, ed. by H. Beuther, R. S. Klessen, C. P. Dullemond and T. Henning 195, arXiv: 1401.1809 [astro-ph.GA].

Dunham, M. M., H. G. Arce et al. (2014), *Molecular Outflows Driven by Low-mass Protostars. I. Correcting for Underestimates When Measuring Outflow Masses and Dynamical Properties*, ApJ **783**, 29 29, arXiv: 1401.2391 [astro-ph.GA].

Dutrey, A. et al. (2014), "Physical and Chemical Structure of Planet-Forming Disks Probed by Millimeter Observations and Modeling", *Protostars and Planets VI*, ed. by H. Beuther, R. S. Klessen, C. P. Dullemond and T. Henning 317, arXiv: 1402.3503 [astro-ph.GA].

Ellerbroek, L. E. et al. (2013), *The outflow history of two Herbig-Haro jets in RCW 36: HH 1042 and HH 1043*, A&A **551**, A5 A5, arXiv: 1212.4144 [astro-ph.SR].

Evans II, N. J. et al. (2009), *The Spitzer c2d Legacy Results: Star-Formation Rates and Efficiencies; Evolution and Lifetimes*, ApJS **181** 321, arXiv: 0811.1059 [astro-ph].

Fall, S. M., M. R. Krumholz and C. D. Matzner (2010), *Stellar Feedback in Molecular Clouds and its Influence on the Mass Function of Young Star Clusters*, ApJ **710** L142, arXiv: 0910.2238 [astro-ph.SR].

Federman, S. A. et al. (2024), *Investigating Protostellar Accretion-driven Outflows across the Mass Spectrum: JWST NIRSpec Integral Field Unit 3–5 μm Spectral Mapping of Five Young Protostars*, ApJ **966**, 41 41, arXiv: 2310.03803 [astro-ph.SR].

Ferrière, K. M. (2001), *The interstellar environment of our galaxy*, Reviews of Modern Physics **73** 1031, arXiv: astro-ph/0106359 [astro-ph].

Flower, D. R. and G. Pineau Des Forêts (2010), *Excitation and emission of H2, CO and H2O molecules in interstellar shock waves*, MNRAS **406** 1745.

Flower, D. R. and G. Pineau des Forêts (2012), *Time-dependent modelling of the molecular line emission from shock waves in outflow sources*, MNRAS **421** 2786.

Flower, D. R., G. Pineau des Forets and T. W. Hartquist (1985), *Theoretical studies of interstellar molecular shocks. I - General formulation and effects of the ion-molecule chemistry*, MNRAS **216** 775.

Francis, L. et al. (2025), *JOYS: The [D/H] abundance derived from protostellar outflows across the Galactic disk measured with JWST*, A&A **694**, A174 A174, arXiv: 2501.02085 [astro-ph.GA].

Frank, A. et al. (2014), "Jets and Outflows from Star to Cloud: Observations Confront Theory", *Protostars and Planets VI*, ed. by H. Beuther, R. S. Klessen, C. P. Dullemond and T. Henning 451, arXiv: 1402.3553 [astro-ph.SR].

Furlan, E. et al. (2008), *Spitzer IRS Spectra and Envelope Models of Class I Protostars in Taurus*, ApJS **176** 184, arXiv: 0711.4038 [astro-ph].

Gagné, M., S. L. Skinner and K. J. Daniel (2004), *Simultaneous Chandra and Very Large Array Observations of Young Stars and Protostars in ρ Ophiuchus Cloud Core A*, ApJ **613** 393, arXiv: astro-ph/0405467 [astro-ph].

Garden, R. P., M. Hayashi, I. Gatley, T. Hasegawa and N. Kaifu (1991), *A Spectroscopic Study of the DR 21 Outflow Source. III. The CO Line Emission*, ApJ **374** 540.

Garden, R., T. R. Geballe, I. Gatley and D. Nadeau (1986), *An extremely luminous bipolar H2 flow in the DR 21 star-forming region.*, MNRAS **220** 203.

Garden, R. P. and J. E. Carlstrom (1992), *High-Velocity HCO + Emission Associated with the DR 21 Molecular Outflow*, ApJ **392** 602.

Garrod, R. T., S. L. Widicus Weaver and E. Herbst (2008), *Complex Chemistry in Star-forming Regions: An Expanded Gas-Grain Warm-up Chemical Model*, ApJ **682** 283, arXiv: 0803.1214 [astro-ph].

Genzel, R. (1991), "Physical Conditions and Heating/Cooling Processes in High Mass Star Formation Regions", *The Physics of Star Formation and Early Stellar Evolution*, ed. by C. J. Lada and N. D. Kylafis, vol. 342, NATO Advanced Study Institute (ASI) Series C 155.

Gerner, T. et al. (2014), *Chemical evolution in the early phases of massive star formation. I*, A&A **563**, A97 A97, arXiv: 1401.6382 [astro-ph.SR].

Ginsburg, A. et al. (2020), *The MUSTANG Galactic Plane Survey (MGPS90) Pilot*, ApJS **248**, 24 24, arXiv: 2004.09555 [astro-ph.GA].

Godard, B., E. Falgarone, M. Gerin, P. Hily-Blant and M. de Luca (2010), *Molecular absorption lines toward star-forming regions: a comparative study of $HCO^+$, HNC, HCN, and CN*, A&A **520**, A20 A20, arXiv: 1006.0582 [astro-ph.GA].

Godard, B., G. Pineau des Forêts et al. (2019), *Models of irradiated molecular shocks*, A&A **622**, A100 A100, arXiv: 1901.04273 [astro-ph.GA].

Gómez, M., D. P. Stark, B. A. Whitney and E. Churchwell (2003), *Jets and Herbig-Haro Objects in the ρ Ophiuchi Embedded Cluster*, AJ **126** 863.

Guzmán Ccolque, E., M. Fernández López, L. A. Zapata, J. Bally and P. R. Rivera-Ortiz (2024), *Confirming the explosive dispersal outflow in DR21 with ALMA*, A&A **689**, A339 A339, arXiv: 2406.03564 [astro-ph.GA].

Guzmán Ccolque, E., M. Fernández-López, L. A. Zapata and T. Baug (2022), *Possible Explosive Dispersal Outflow in IRAS 16076-5134 Revealed with ALMA*, ApJ **937**, 51 51, arXiv: 2208.12317 [astro-ph.GA].

Hacar, A. et al. (2025), *Emergence of high-mass stars in complex fiber networks (EMERGE): V. From filaments to spheroids: the origin of the hub-filament systems*, A&A **694**, A69 A69, arXiv: 2411.05613 [astro-ph.GA].

Haro, G. (1952), *Herbig's Nebulous Objects Near NGC 1999.*, ApJ **115** 572.

Hatchell, J., S. Terebey et al. (2012), *The Spitzer Survey of Interstellar Clouds in the Gould Belt. V. Ophiuchus North Observed with IRAC and MIPS*, ApJ **754**, 104 104, arXiv: 1206.5422 [astro-ph.GA].

Hatchell, J., M. A. Thompson, T. J. Millar and G. H. MacDonald (1998), *Sulphur chemistry and evolution in hot cores*, A&A **338** 713.

Hennemann, M. et al. (2012), *The spine of the swan: a Herschel study of the DR21 ridge and filaments in Cygnus X*, A&A **543**, L3 L3, arXiv: 1206.1243 [astro-ph.GA].

Herbig, G. H. (1951), *The Spectra of Two Nebulous Objects Near NGC 1999.*, ApJ **113** 697.

Hirano, N. et al. (2010), *Extreme Active Molecular Jets in L1448C*, ApJ **717** 58, arXiv: 1005.0703 [astro-ph.SR].

Hollenbach, D. (1997), "The Physics of Molecular Shocks in YSO Outflows", *Herbig-Haro Flows and the Birth of Stars*, ed. by B. Reipurth and C. Bertout, vol. 182, IAU Symposium 181.

Hollenbach, D. and C. F. McKee (1989), *Molecule Formation and Infrared Emission in Fast Interstellar Shocks. III. Results for J Shocks in Molecular Clouds*, ApJ **342** 306.

Hubble, E. (1929), *A Relation between Distance and Radial Velocity among Extra-Galactic Nebulae*, Proceedings of the National Academy of Science **15** 168.

Immer, K., C. Cyganowski, M. J. Reid and K. M. Menten (2014), *The cometary H II regions of DR 21: Bow shocks or champagne flows or both?*, A&A **563**, A39 A39, arXiv: 1401.1343 [astro-ph.GA].

Issac, N. et al. (2025), *Detection of an Explosive Outflow in G34.26+0.15*, AJ **169**, 324 324, arXiv: 2504.15748 [astro-ph.SR].

Jeans, J. H. (1928), *Astronomy and cosmogony*.

Kahn, F. D. (1974), *Cocoons around early-type stars.*, A&A **37** 149.

Karska, A., M. Figueira et al. (2025), *SOFIA FIFI-LS spectroscopy of DR21 Main: Energetics of the spatially resolved outflow from a high-mass protostar*, A&A **697**, A186 A186, arXiv: 2503.15059 [astro-ph.GA].

Karska, A., G. J. Herczeg et al. (2013), *Water in star-forming regions with Herschel (WISH). III. Far-infrared cooling lines in low-mass young stellar objects*, A&A **552**, A141 A141, arXiv: 1301.4821 [astro-ph.SR].

Karska, A., L. E. Kristensen et al. (2014), *Shockingly low water abundances in Herschel/PACS observations of low-mass protostars in Perseus*, A&A **572**, A9 A9, arXiv: 1409.4658 [astro-ph.SR].

Karska, A., M. J. Kaufman et al. (2018), *The Herschel-PACS Legacy of Low-mass Protostars: The Properties of Warm and Hot Gas Components and Their Origin in Far-UV Illuminated Shocks*, ApJS **235**, 30 30, arXiv: 1802.03379 [astro-ph.SR].

Kaufman, M. J. and D. A. Neufeld (1996), *Far-Infrared Water Emission from Magnetohydrodynamic Shock Waves*, ApJ **456** 611.

Kessler, M. F. et al. (1996), *The Infrared Space Observatory (ISO) mission.*, A&A **315** L27.

Kim, W.-J. et al. (2025), *The Cygnus Allscale Survey of Chemistry and Dynamical Environments: CASCADE: IV. Unveiling the hidden structures in DR18*, A&A **694**, A30 A30, arXiv: 2501.04518 [astro-ph.GA].

Klessen, R. S. and S. C. O. Glover (2016), *Physical Processes in the Interstellar Medium*, Saas-Fee Advanced Course **43** 85, arXiv: 1412.5182 [astro-ph.GA].

Knödlseder, J. (2000), *Cygnus OB2 - a young globular cluster in the Milky Way*, A&A **360** 539, arXiv: astro-ph/0007442 [astro-ph].

Kong, S. et al. (2019), *Widespread Molecular Outflows in the Infrared Dark Cloud G28.37+0.07: Indications of Orthogonal Outflow-filament Alignment*, ApJ **874**, 104 104, arXiv: 1903.05273 [astro-ph.GA].

König, C. et al. (2017), *ATLASGAL-selected massive clumps in the inner Galaxy. III. Dust continuum characterization of an evolutionary sample*, A&A **599**, A139 A139, arXiv: 1610.09055 [astro-ph.GA].

Kristensen, L. E., B. Godard, P. Guillard, A. Gusdorf and G. Pineau des Forêts (2023), *Shock excitation of $H_2$ in the James Webb Space Telescope era*, A&A **675**, A86 A86, arXiv: 2307.04178 [astro-ph.GA].

Kristensen, L. E., T. L. Ravkilde, D. Field, J. L. Lemaire and G. Pineau Des Forêts (2007), *Excitation conditions in the Orion molecular cloud obtained from observations of ortho- and para-lines of H {2}*, A&A **469** 561.

Kristensen, L. E., T. L. Ravkilde, G. Pineau Des Forêts et al. (2008), *Observational 2D model of $H_2$ emission from a bow shock in the Orion Molecular Cloud*, A&A **477** 203.

Kristensen, L. E., E. F. van Dishoeck, E. A. Bergin et al. (2012), *Water in star-forming regions with Herschel (WISH). II. Evolution of 557 GHz $1_{10}$-$1_{01}$ emission in low-mass protostars*, A&A **542**, A8 A8, arXiv: 1204.0009 [astro-ph.SR].

Kristensen, L. E., E. F. van Dishoeck, J. C. Mottram et al. (2017), *Origin of warm and hot gas emission from low-mass protostars: Herschel-HIFI observations of CO J = 16-15. I. Line profiles, physical conditions, and $H_2O$ abundance*, A&A **605**, A93 A93, arXiv: 1705.10269 [astro-ph.GA].

Kroupa, P. (2002), *The Initial Mass Function of Stars: Evidence for Uniformity in Variable Systems*, Science **295** 82, arXiv: astro-ph/0201098 [astro-ph].

Kurtz, S., R. Cesaroni, E. Churchwell, P. Hofner and C. M. Walmsley (2000), "Hot Molecular Cores and the Earliest Phases of High-Mass Star Formation", *Protostars and Planets IV*, ed. by V. Mannings, A. P. Boss and S. S. Russell 299.

Lacy, J. H., R. Knacke, T. R. Geballe and A. T. Tokunaga (1994), *Detection of Absorption by H 2 in Molecular Clouds: A Direct Measurement of the H 2:CO Ratio*, ApJ **428** L69.

Lada, C. J. and B. A. Wilking (1984), *The nature of the embedded population in the rho Ophiuchi dark cloud : mid-infrared observations.*, ApJ **287** 610.

Larson, R. B. (1969), *Numerical calculations of the dynamics of collapsing proto-star*, MNRAS **145** 271.

Launhardt, R., D. Nutter et al. (2010), *Looking Into the Hearts of Bok Globules: Millimeter and Submillimeter Continuum Images of Isolated Star-forming Cores*, ApJS **188** 139, arXiv: 1004.0869 [astro-ph.GA].

Launhardt, R., Y. N. Pavlyuchenkov et al. (2023), *A resolved rotating disk wind from a young T Tauri star in the Bok globule CB 26*, A&A **678**, A135 A135, arXiv: 2309.01629 [astro-ph.SR].

Lee, C.-F. et al. (2017), *A rotating protostellar jet launched from the innermost disk of HH 212*, Nature Astronomy **1**, 0152 0152, arXiv: 1706.06343 [astro-ph.GA].

Leung, H. O. and P. Thaddeus (1992), *A Complete CO Survey of the Cygnus X Region*, ApJS **81** 267.

Levenson, N. A., J. R. Graham, L. D. Keller and M. J. Richter (1998), *Panoramic Views of the Cygnus Loop*, ApJS **118** 541, arXiv: astro-ph/9805008 [astro-ph].

Liseau, R. et al. (1999), *Looking at the bright side of the rho Ophiuchi dark cloud. Far infrared spectrophotometric observations of the rho Oph cloud with the ISO*, A&A **344** 342.

Liu, D.-J. et al. (2021), *High-sensitivity Millimeter Imaging of Molecular Outflows in Nine Nearby High-mass Star-forming Regions*, ApJS **253**, 15 15, arXiv: 2012.03226 [astro-ph.GA].

Loinard, L., R. M. Torres, A. J. Mioduszewski and L. F. Rodríguez (2008), *A Preliminary VLBA Distance to the Core of Ophiuchus, with an Accuracy of 4%*, ApJ **675** L29, arXiv: 0801.2192 [astro-ph].

López-Vázquez, J. A., L. A. Zapata, S. Lizano and J. Cantó (2020), *ALMA Observations and Modeling of the Rotating Outflow in Orion Source I*, ApJ **904**, 158 158, arXiv: 2010.00132 [astro-ph.SR].

Loren, R. B. (1989a), *The Cobwebs of Ophiuchus. I. Strands of 13CO: The Mass Distribution*, ApJ **338** 902.

– (1989b), *The Cobwebs of Ophiuchus. II. 13CO Filament Kinematics*, ApJ **338** 925.

Lovas, F. J. (2004), *NIST Recommended Rest Frequencies for Observed Interstellar Molecular Microwave Transitions-2002 Revision*, Journal of Physical and Chemical Reference Data **33** 177.

Lynds, B. T. (1962), *Catalogue of Dark Nebulae.*, ApJS **7** 1.

Mangum, J. G., A. Wootten and L. G. Mundy (1992), *Synthesis Imaging of the DR 21 (OH) Cluster. II. Thermal Ammonia and Water Maser Emission*, ApJ **388** 467.

Maret, S. et al. (2009), *Spitzer Mapping of Molecular Hydrogen Pure Rotational Lines in NGC 1333: A Detailed Study of Feedback in Star Formation*, ApJ **698** 1244, arXiv: 0904.0603 [astro-ph.SR].

Marsh, K. A. et al. (2017), *Multitemperature mapping of dust structures throughout the Galactic Plane using the PPMAP tool with Herschel Hi-GAL data*, MNRAS **471** 2730, arXiv: 1707.03808 [astro-ph.GA].

Maud, L. T. et al. (2015), *A distance-limited sample of massive molecular outflows*, MNRAS **453** 645, arXiv: 1509.00199 [astro-ph.SR].

McClure, M. (2009), *Observational 5-20 μm Interstellar Extinction Curves Toward Star-Forming Regions Derived From Spitzer IRS Spectra*, ApJ **693** L81, arXiv: 0810.4561 [astro-ph].

McKee, C. F. and E. C. Ostriker (2007), *Theory of Star Formation*, ARA&A **45** 565, arXiv: 0707.3514 [astro-ph].

McKee, C. F. and J. C. Tan (2002), *Massive star formation in 100,000 years from turbulent and pressurized molecular clouds*, Nature **416** 59, arXiv: astro-ph/0203071 [astro-ph].

– (2003), *The Formation of Massive Stars from Turbulent Cores*, ApJ **585** 850, arXiv: astro-ph/0206037 [astro-ph].

McLean, I. S. et al. (1998), "Design and development of NIRSPEC: a near-infrared echelle spectrograph for the Keck II telescope", *Infrared Astronomical Instrumentation*, ed. by A. M. Fowler, vol. 3354, Society of Photo-Optical Instrumentation Engineers (SPIE) Conference Series 566.

Megeath, T. et al. (2024), *HEFE: High Angular Resolution observations of Stellar Emergence in Filamentary Environments*, JWST Proposal. Cycle 3, ID. #5804.

Men'shchikov, A. (2017), *Background derivation and image flattening: getimages*, A&A **607**, A64 A64, arXiv: 1707.09574 [astro-ph.IM].

Men'shchikov, A. et al. (2012), *A multi-scale, multi-wavelength source extraction method: getsources*, A&A **542**, A81 A81, arXiv: 1204.4508 [astro-ph.IM].

Mezger, P. G. et al. (1992), *Dust emission from star-forming regions*, A&A **265** 743.

Minkowski, R. (1958), *Cygnus Loop and Some Related Nebulosities*, Reviews of Modern Physics **30** 1048.

Motte, F., S. Bontemps, P. Schilke et al. (2007), *The earliest phases of high-mass star formation: a 3 square degree millimeter continuum mapping of Cygnus X*, A&A **476** 1243, arXiv: 0708.2774 [astro-ph].

Motte, F., S. Bontemps and F. Louvet (2018), *High-Mass Star and Massive Cluster Formation in the Milky Way*, ARA&A **56** 41, arXiv: 1706.00118 [astro-ph.GA].

Mottram, J. C. et al. (2017), *Outflows, infall and evolution of a sample of embedded low-mass protostars. The William Herschel Line Legacy (WILL) survey*, A&A **600**, A99 A99, arXiv: 1701.04647 [astro-ph.SR].

Movsessian, T. A., T. Y. Magakian, B. Reipurth and H. R. Andreasyan (2024), *New Herbig-Haro objects associated with embedded sources*, MNRAS **530** 2068, arXiv: 2404.02891 [astro-ph.SR].

Müller, H. S. P., S. Thorwirth, D. A. Roth and G. Winnewisser (2001), *The Cologne Database for Molecular Spectroscopy, CDMS*, A&A **370** L49.

Myers, P. C. and E. F. Ladd (1993), *Bolometric Temperatures of Young Stellar Objects*, ApJ **413** L47.

Narang, M. et al. (2024), *Discovery of a Collimated Jet from the Low-luminosity Protostar IRAS 16253-2429 in a Quiescent Accretion Phase with the JWST*, ApJ **962**, L16 L16, arXiv: 2310.14061 [astro-ph.SR].

Neufeld, D. A., G. J. Melnick and M. Harwit (1998), *Infrared Space Observatory Observations of Molecular Hydrogen in HH 54:Measurement of a Nonequilibrium Ratio of Ortho- to Para-$H_2$*, ApJ **506** L75.

Nisini, B., S. Antoniucci et al. (2018), *Connection between jets, winds and accretion in T Tauri stars. The X-shooter view*, A&A **609**, A87 A87, arXiv: 1710.05587 [astro-ph.SR].

Nisini, B., G. Santangelo et al. (2015), *[O I] 63 μm Jets in Class 0 Sources Detected By Herschel*, ApJ **801**, 121 121, arXiv: 1501.03681 [astro-ph.SR].

Nutter, D., D. Ward-Thompson and P. André (2006), *A SCUBA survey of L1689 - the dog that didn't bark*, MNRAS **368** 1833, arXiv: astro-ph/0603203 [astro-ph].

Offner, S. S. R., M. Moe et al. (2023), "The Origin and Evolution of Multiple Star Systems", *Protostars and Planets VII*, ed. by S. Inutsuka, Y. Aikawa, T. Muto, K. Tomida and M. Tamura, vol. 534, Astronomical Society of the Pacific Conference Series 275, arXiv: 2203.10066 [astro-ph.SR].

Offner, S. S. R., E. J. Lee, A. A. Goodman and H. Arce (2011), *Radiation-hydrodynamic Simulations of Protostellar Outflows: Synthetic Observations and Data Comparisons*, ApJ **743**, 91 91, arXiv: 1110.5640 [astro-ph.SR].

Oliva, A. and R. Kuiper (2023), *Modeling disks and magnetic outflows around a forming massive star. II. Dynamics of jets from massive protostars*, A&A **669**, A81 A81, arXiv: 2210.01492 [astro-ph.SR].

Omura, M., K. Tokuda and M. N. Machida (2024), *Revealing Multiple Nested Molecular Outflows with Rotating Signatures in HH270mms1-A with ALMA*, ApJ **963**, 72 72, arXiv: 2401.03086 [astro-ph.GA].

Ortiz-León, G. N. et al. (2017), *The Gould's Belt Distances Survey (GOBELINS). I. Trigonometric Parallax Distances and Depth of the Ophiuchus Complex*, ApJ **834**, 141 141, arXiv: 1611.06466 [astro-ph.SR].

Palla, F. and S. W. Stahler (1993), *The Pre-Main-Sequence Evolution of Intermediate-Mass Stars*, ApJ **418** 414.

Persson, M. V. (2014), *Current view of protostellar evolution (ENG)*, URL: https://figshare.com/articles/figure/Current_view_of_protostellar_evolution/654555.

Piddington, J. H. and H. C. Minnett (1952), *Radio-Frequency Radiation from the Constellation of Cygnus*, Australian Journal of Scientific Research A Physical Sciences **5** 17.

Pilbratt, G. L. et al. (2010), *Herschel Space Observatory. An ESA facility for far-infrared and submillimetre astronomy*, A&A **518**, L1 L1, arXiv: 1005.5331 [astro-ph.IM].

Pillitteri, I., S. J. Wolk, A. Goodman and S. Sciortino (2014), *Smooth X-ray variability from ρ Ophiuchi A+B. A strongly magnetized primary B2 star?*, A&A **567**, L4 L4, arXiv: 1406.5049 [astro-ph.SR].

Pineda, J. E. et al. (2023), "From Bubbles and Filaments to Cores and Disks: Gas Gathering and Growth of Structure Leading to the Formation of Stellar Systems", *Protostars and Planets VII*, ed. by S. Inutsuka, Y. Aikawa, T. Muto, K. Tomida and M. Tamura, vol. 534, Astronomical Society of the Pacific Conference Series 233, arXiv: 2205.03935 [astro-ph.GA].

Plambeck, R. L. and K. M. Menten (1990), *95 GHz Methanol Masers near DR 21 and DR 21(OH)*, ApJ **364** 555.

Pontoppidan, K. M., N. Evans, J. Bergner and Y.-L. Yang (2024), *A Constrained Dust Opacity for Models of Dense Clouds and Protostellar Envelopes*, Research Notes of the American Astronomical Society **8**, 68 68.

Pudritz, R. E. and C. A. Norman (1983), *Centrifugally driven winds from contracting molecular disks*, ApJ **274** 677.

– (1986), *Bipolar Hydromagnetic Winds from Disks around Protostellar Objects*, ApJ **301** 571.

Pudritz, R. E., R. Ouyed, C. Fendt and A. Brandenburg (2007), "Disk Winds, Jets, and Outflows: Theoretical and Computational Foundations", *Protostars and Planets V*, ed. by B. Reipurth, D. Jewitt and K. Keil 277, arXiv: astro-ph/0603592 [astro-ph].

Ray, T. P. et al. (2023), *Outflows from the youngest stars are mostly molecular*, Nature **622** 48.

Reber, G. (1944), *Cosmic Static.*, ApJ **100** 279.

Rivera-Ortiz, P. R. et al. (2025), *Gravitationally Induced Explosive Outflows*, ApJ **986**, 71 71, arXiv: 2504.11252 [astro-ph.SR].

Romero, C. E. et al. (2020), *Pressure Profiles and Mass Estimates Using High-resolution Sunyaev-Zel'dovich Effect Observations of Zwicky 3146 with MUSTANG-2*, ApJ **891**, 90 90, arXiv: 1908.09200 [astro-ph.CO].

Rosenthal, D., F. Bertoldi and S. Drapatz (2000), *ISO-SWS observations of OMC-1: H_2 and fine structure lines*, A&A **356** 705, arXiv: astro-ph/0002456 [astro-ph].

Rota, A. A. et al. (2025), *A correlation between accretion and outflow rates for class II young stellar objects with full and transition disks*, A&A **700**, A32 A32, arXiv: 2505.16586 [astro-ph.EP].

Roueff, E. et al. (2019), *The full infrared spectrum of molecular hydrogen*, A&A **630**, A58 A58, arXiv: 1909.11585 [physics.atom-ph].

Rygl, K. L. J. et al. (2012), *Parallaxes and proper motions of interstellar masers toward the Cygnus X star-forming complex. I. Membership of the Cygnus X region*, A&A **539**, A79 A79, arXiv: 1111.7023 [astro-ph.GA].

Schneider, N., S. Bontemps et al. (2006), *A new view of the Cygnus X region. KOSMA $^{13}$CO 2 to 1, 3 to 2, and $^{12}$CO 3 to 2 imaging*, A&A **458** 855.

Schneider, N., T. Csengeri et al. (2010), *Dynamic star formation in the massive DR21 filament*, A&A **520**, A49 A49, arXiv: 1003.4198 [astro-ph.GA].

Schneider, N., R. Simon, C. Kramer, J. Stutzki and S. Bontemps (2002), *A multiwavelength study of the S106 region. I. Structure and dynamics of the molecular gas*, A&A **384** 225.

Shang, H., R. Krasnopolsky and C.-F. Liu (2023), *A Unified Model for Bipolar Outflows from Young Stars: Apparent Magnetic Jet Acceleration*, ApJ **945**, L1 L1, arXiv: 2301.08512 [astro-ph.SR].

Shepherd, D. S. and E. Churchwell (1996), *Bipolar Molecular Outflows in Massive Star Formation Regions*, ApJ **472** 225.

Shepherd, D. S., S. E. Kurtz and L. Testi (2004), *The Nature of the Massive Young Stars in W75 N*, ApJ **601** 952, arXiv: astro-ph/0310418 [astro-ph].

Shu, F. H. (1977), *Self-similar collapse of isothermal spheres and star formation.*, ApJ **214** 488.

Shu, F. H., J. R. Najita, H. Shang and Z. .-.-Y. Li (2000), "X-Winds Theory and Observations", *Protostars and Planets IV*, ed. by V. Mannings, A. P. Boss and S. S. Russell 789.

Shu, F. H., F. C. Adams and S. Lizano (1987), *Star formation in molecular clouds: observation and theory.*, ARA&A **25** 23.

Shu, F. et al. (1994), *Magnetocentrifugally Driven Flows from Young Stars and Disks. I. A Generalized Model*, ApJ **429** 781.

Skretas, I. M., A. Karska, L. Francis et al. (2025), *UV-irradiated outflows from low-mass protostars in Ophiuchus with JWST/MIRI*, arXiv e-prints, arXiv:2509.10256 arXiv:2509.10256, arXiv: 2509.10256 [astro-ph.GA].

Skretas, I. M., A. Karska, F. Wyrowski et al. (2023), *The Cygnus Allscale Survey of Chemistry and Dynamical Environments: CASCADE. II. A detailed kinematic analysis of the DR21 Main outflow*, A&A **679**, A66 A66, arXiv: 2309.09687 [astro-ph.GA].

Skretas, I. M. and L. E. Kristensen (2022), *Connecting Galactic and extragalactic outflows: From the Cygnus-X cluster to active galaxies*, A&A **660**, A39 A39, arXiv: 2202.04676 [astro-ph.GA].

Smith, M. D., J. Eisloffel and C. J. Davis (1998), *ISO observations of molecular hydrogen in the DR21 bipolar outflow*, MNRAS **297** 687.

Smith, R. J., S. C. O. Glover, I. A. Bonnell, P. C. Clark and R. S. Klessen (2011), *A quantification of the non-spherical geometry and accretion of collapsing cores*, MNRAS **411** 1354, arXiv: 1009.5395 [astro-ph.GA].

Snell, R. L., R. B. Loren and R. L. Plambeck (1980), *Observations of CO in L 1551 : evidence for stellar wind driven shocks.*, ApJ **239** L17.

Speckert, M., T. Rector and L. Prato (2025), "High-Sensitivity Detections of New Herbig Haro Objects in the Ophiuchus Star Forming Region", *American Astronomical Society Meeting Abstracts #245*, vol. 245, American Astronomical Society Meeting Abstracts 357.05.

Tokunaga, A. T., S. J. Bus, M. S. Connelley and J. T. Rayner (2015), "The NASA Infrared Telescope Facility (IRTF): New Observational Capabilities", *AAS/Division for Planetary Sciences Meeting Abstracts #47*, vol. 47, AAS/Division for Planetary Sciences Meeting Abstracts 312.20.

Trumpler, R. J. (1930), *Preliminary results on the distances, dimensions and space distribution of open star clusters*, Lick Observatory Bulletin **420** 154.

Tychoniec, Ł., C. F. Manara et al. (2020), *Dust masses of young disks: constraining the initial solid reservoir for planet formation*, A&A **640**, A19 A19, arXiv: 2006.02812 [astro-ph.EP].

Tychoniec, Ł., E. F. van Dishoeck et al. (2021), *Which molecule traces what: Chemical diagnostics of protostellar sources*, A&A **655**, A65 A65, arXiv: 2107.03696 [astro-ph.SR].

Tychoniec, Ł., M. L. van Gelder et al. (2024), *JWST Observations of Young protoStars (JOYS). Linked accretion and ejection in a Class I protobinary system*, A&A **687**, A36 A36, arXiv: 2402.04343 [astro-ph.SR].

Urquhart, J. S. (2024), "Evolutionary Trends in Star Formation", *Cosmic Masers: Proper Motion Toward the Next-Generation Large Projects*, ed. by T. Hirota, H. Imai, K. Menten and Y. Pihlström, vol. 380, IAU Symposium 135.

Uyaniker, B., E. Fürst, W. Reich, B. Aschenbach and R. Wielebinski (2001), *The Cygnus superbubble revisited*, A&A **371** 675.

Vaidya, B., C. Fendt, H. Beuther and O. Porth (2011), *Jet Formation from Massive Young Stars: Magnetohydrodynamics versus Radiation Pressure*, ApJ **742**, 56 56, arXiv: 1108.4924 [astro-ph.SR].

van der Marel, N. et al. (2013), *Outflow forces of low-mass embedded objects in Ophiuchus: a quantitative comparison of analysis methods*, A&A **556**, A76 A76, arXiv: 1305.6453 [astro-ph.SR].

van der Tak, F. F. S., E. F. van Dishoeck, N. J. Evans II, E. J. Bakker and G. A. Blake (1999), *The Impact of the Massive Young Star GL 2591 on Its Circumstellar Material: Temperature, Density, and Velocity Structure*, ApJ **522** 991, arXiv: astro-ph/9905035 [astro-ph].

van der Walt, S. J. et al. (2021), *Protostellar Interferometric Line Survey of the Cygnus X region (PILS-Cygnus). First results: Observations of CygX-N30*, A&A **655**, A86 A86, arXiv: 2109.03640 [astro-ph.SR].

van Dishoeck, E. F. and J. H. Black (1986), *Comprehensive Models of Diffuse Interstellar Clouds: Physical Conditions and Molecular Abundances*, ApJS **62** 109.

van Dishoeck, E. F., L. E. Kristensen et al. (2021), *Water in star-forming regions: physics and chemistry from clouds to disks as probed by Herschel spectroscopy*, A&A **648**, A24 A24, arXiv: 2102.02225 [astro-ph.GA].

van Dishoeck, E. F., Ł. Tychoniec et al. (2025), *JWST Observations of Young protoStars (JOYS): Overview of program and early results*, A&A **699**, A361 A361, arXiv: 2505.08002 [astro-ph.GA].

van Dishoeck, E. F. and G. A. Blake (1998), *Chemical Evolution of Star-Forming Regions*, ARA&A **36** 317.

van Kempen, T. A., M. R. Hogerheijde et al. (2016), *Outflow forces in intermediate-mass star formation*, A&A **587**, A17 A17, arXiv: 1507.01937 [astro-ph.SR].

van Kempen, T. A., E. F. van Dishoeck et al. (2009), *The nature of the Class I population in Ophiuchus as revealed through gas and dust mapping*, A&A **498** 167, arXiv: 0902.4005 [astro-ph.GA].

Walker-Smith, S. L., J. S. Richer, J. V. Buckle, J. Hatchell and E. Drabek-Maunder (2014), *The James Clerk Maxwell Telescope dense gas survey of the Perseus molecular cloud*, MNRAS **440** 3568, arXiv: 1403.3051 [astro-ph.GA].

Warren, S. J. et al. (2007), *The UKIRT Infrared Deep Sky Survey Second Data Release*, arXiv e-prints, astro-ph/0703037 astro, arXiv: astro-ph/0703037 [astro-ph].

Wendker, H. J., L. A. Higgs and T. L. Landecker (1991), *The Cygnus X region. XVIII. A detailed investigation of radio-continuum structure on large and small scales.*, A&A **241** 551.

Werner, M. W. et al. (2004), *The Spitzer Space Telescope Mission*, ApJS **154** 1, arXiv: astro-ph/0406223 [astro-ph].

Wilking, B. A., M. Gagné and L. E. Allen (2008), "Star Formation in the $\rho$ Ophiuchi Molecular Cloud", *Handbook of Star Forming Regions, Volume II*, ed. by B. Reipurth, vol. 5 351.

Wilking, B. A., R. D. Schwartz, T. M. Fanetti and E. D. Friel (1997), *Herbig-Haro Objects in the Ophiuchi Cloud*, PASP **109** 549.

Wilking, B. A., M. R. Meyer, J. G. Robinson and T. P. Greene (2005), *Optical Spectroscopy of the Surface Population of the $\rho$ Ophiuchi Molecular Cloud: The First Wave of Star Formation*, AJ **130** 1733, arXiv: astro-ph/0506251 [astro-ph].

Wilson, R. W., K. B. Jefferts and A. A. Penzias (1970), *Carbon Monoxide in the Orion Nebula*, ApJ **161** L43.

Winnewisser, G., S. P. Belov, T. Klaus and R. Schieder (1997), *Sub-Doppler Measurements on the Rotational Transitions of Carbon Monoxide*, Journal of Molecular Spectroscopy **184** 468.

Wright, G. S. et al. (2023), *The Mid-infrared Instrument for JWST and Its In-flight Performance*, PASP **135**, 048003 048003.

Wright, N. J., J. J. Drake, J. E. Drew and J. S. Vink (2010), *The Massive Star-Forming Region Cygnus OB2. II. Integrated Stellar Properties and the Star Formation History*, ApJ **713** 871, arXiv: 1003.2463 [astro-ph.SR].

Wu, J., M. Wang, J. Yang, L. Deng and J. Chen (2002), *Herbig-Haro Objects in the Off-Core Regions of the ρ Ophiuchi Dark Cloud*, AJ **123** 1986.

Yang, K., K. Qiu and X. Pan (2024), *Surveys of clumps, cores, and condensations in Cygnus-X. SMA observations of SiO (5−4)*, A&A **684**, A140 A140, arXiv: 2312.04880 [astro-ph.GA].

Yıldız, U. A. et al. (2015), *APEX-CHAMP$^+$ high-J CO observations of low-mass young stellar objects. IV. Mechanical and radiative feedback*, A&A **576**, A109 A109, arXiv: 1501.03259 [astro-ph.SR].

Zapata, L. A., M. Fernández-López et al. (2023), *One, Two, Three ... An Explosive Outflow in IRAS 12326-6245 Revealed by ALMA*, ApJ **956**, L35 L35, arXiv: 2309.11386 [astro-ph.GA].

Zapata, L. A., P. T. P. Ho et al. (2020), *Confirming the Explosive Outflow in G5.89 with ALMA*, ApJ **902**, L47 L47, arXiv: 2010.13835 [astro-ph.GA].

Zapata, L. A., L. Loinard et al. (2012), *Millimeter Multiplicity in DR21(OH): Outflows, Molecular Cores, and Envelopes*, ApJ **744**, 86 86, arXiv: 1109.3153 [astro-ph.GA].

Zapata, L. A., J. Schmid-Burgk, P. T. P. Ho, L. F. Rodríguez and K. M. Menten (2009), *Explosive Disintegration of a Massive Young Stellar System in Orion*, ApJ **704** L45, arXiv: 0907.3945 [astro-ph.GA].

Zapata, L. A., J. Schmid-Burgk, N. Pérez-Goytia et al. (2013), *A 10,000 Year Old Explosion in DR21*, ApJ **765**, L29 L29, arXiv: 1302.0208 [astro-ph.GA].

Zapata, L. A., J. Schmid-Burgk, L. F. Rodríguez, A. Palau and L. Loinard (2017), *Molecular Outflows: Explosive versus Protostellar*, ApJ **836**, 133 133, arXiv: 1701.07113 [astro-ph.SR].

Zhang, M. and H. Wang (2009), *Outflows in ρ Ophiuchi as Seen with the Spitzer Infrared Array Camera*, AJ **138** 1830, arXiv: 0910.0540 [astro-ph.SR].

Zinnecker, H. and H. W. Yorke (2007), *Toward Understanding Massive Star Formation*, ARA&A **45** 481, arXiv: 0707.1279 [astro-ph].

# APPENDIX A

# CASCADE: Overview of the molecular outflows along the DR21 ridge

## A.1 Spectra

The average spectra of the $HCO^+$ $J = 1 - 0$ and $H^{13}CO^+$ $J = 1 - 0$ emission for the remaining sources in the DR21 ridge are shown in Figures A.1 - A.5.

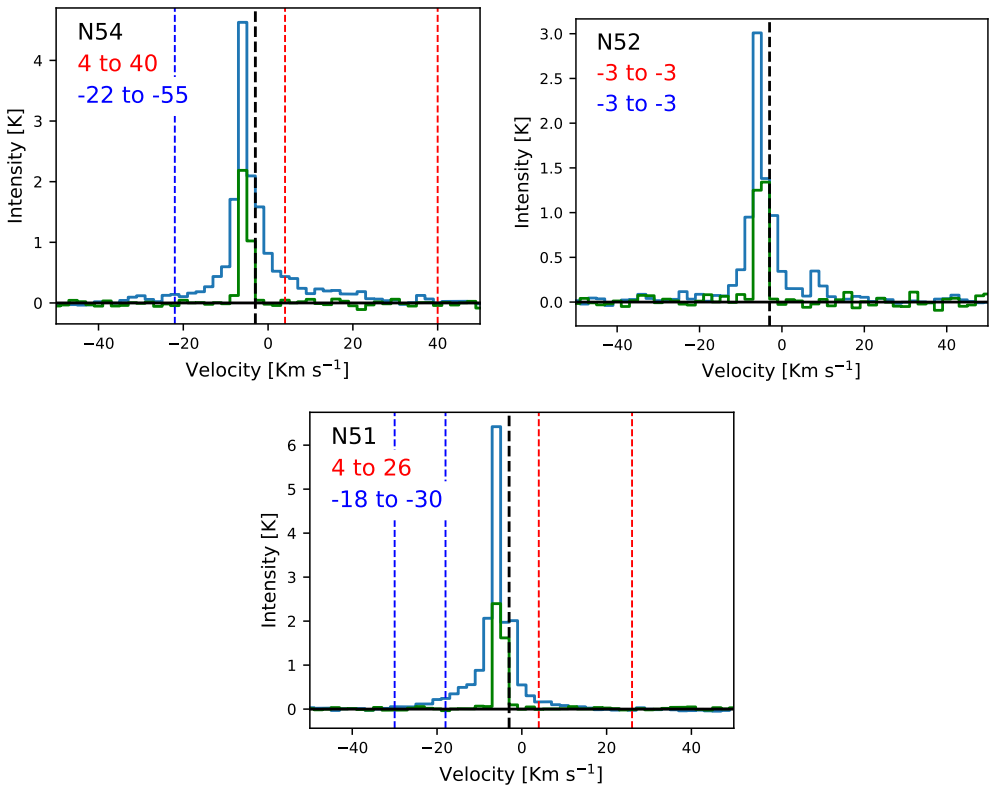


Figure A.1: Spectra of $HCO^+$ $J = 1 - 0$ (blue) and $H^{13}CO^+$ $J = 1 - 0$ (green) for clumps N54, N52, and N51. The spectra were averaged over the FWHM of the corresponding clumps (Table 3.2). Red and blue dashed lines mark the velocity range associated with outflow wing emission. The black dashed line marks the source velocity, $v_{source}$ = -3 km s$^{-1}$ for all sources.

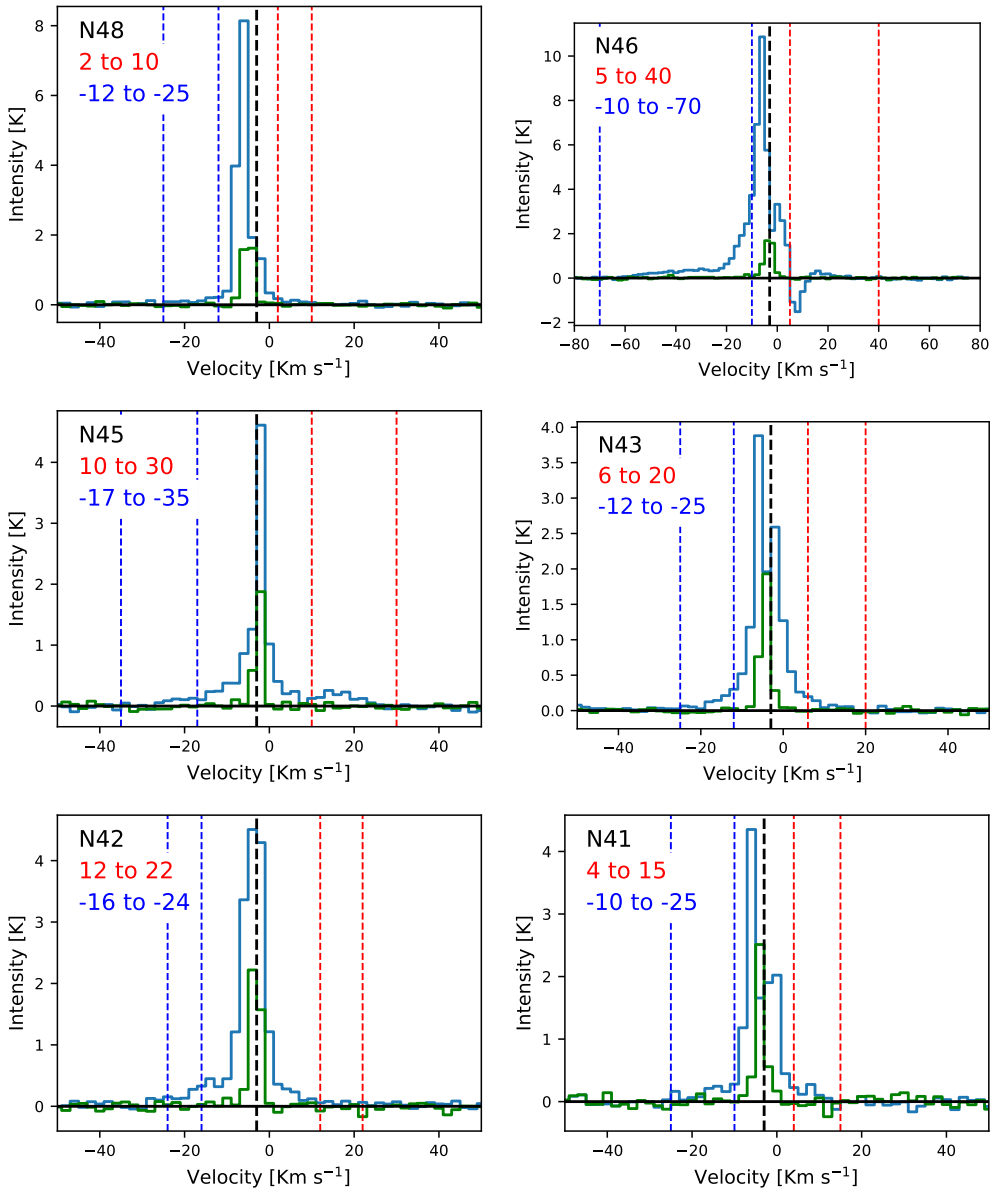


Figure A.2: Spectra of $HCO^+$ $J = 1 - 0$ (blue) and $H^{13}CO^+$ $J = 1 - 0$ (green) for clumps N48, N46, N45, N43, N42, and N41. The spectra were averaged over the FWHM of the corresponding clumps (Table 3.2). Red and blue dashed lines mark the velocity range associated with outflow wing emission. The black dashed line marks the source velocity, $v_{\rm source}$ = -3 km s$^{-1}$.

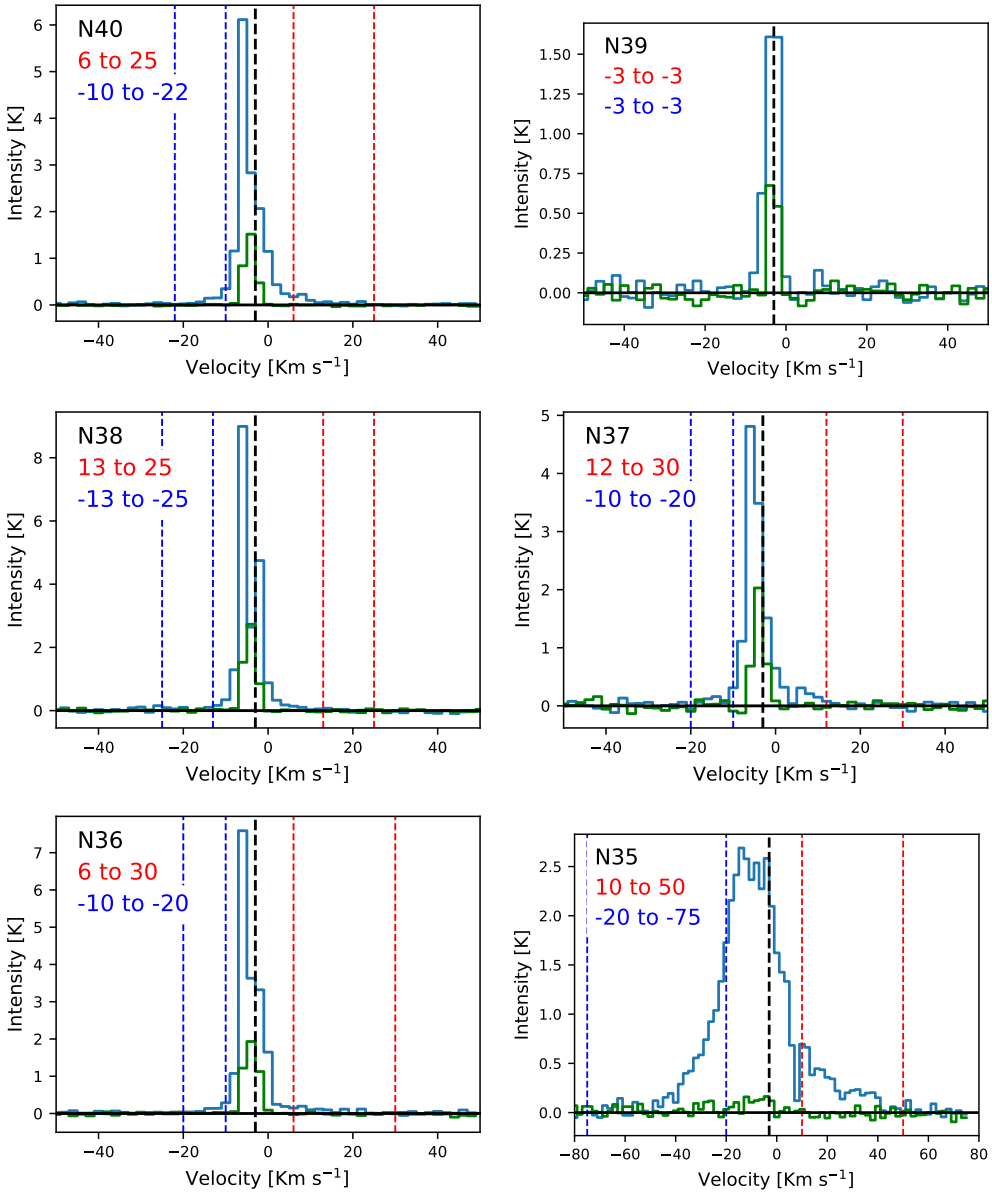


Figure A.3: Spectra of $HCO^+$ $J = 1 - 0$ (blue) and $H^{13}CO^+$ $J = 1 - 0$ (green) for clumps N40, N39, N38, N37, N36, and N35. The spectra were averaged over the FWHM of the corresponding clumps (Table 3.2). Red and blue dashed lines mark the velocity range associated with outflow wing emission. The black dashed line marks the source velocity, $v_{\rm source}$ = -3 km s$^{-1}$.

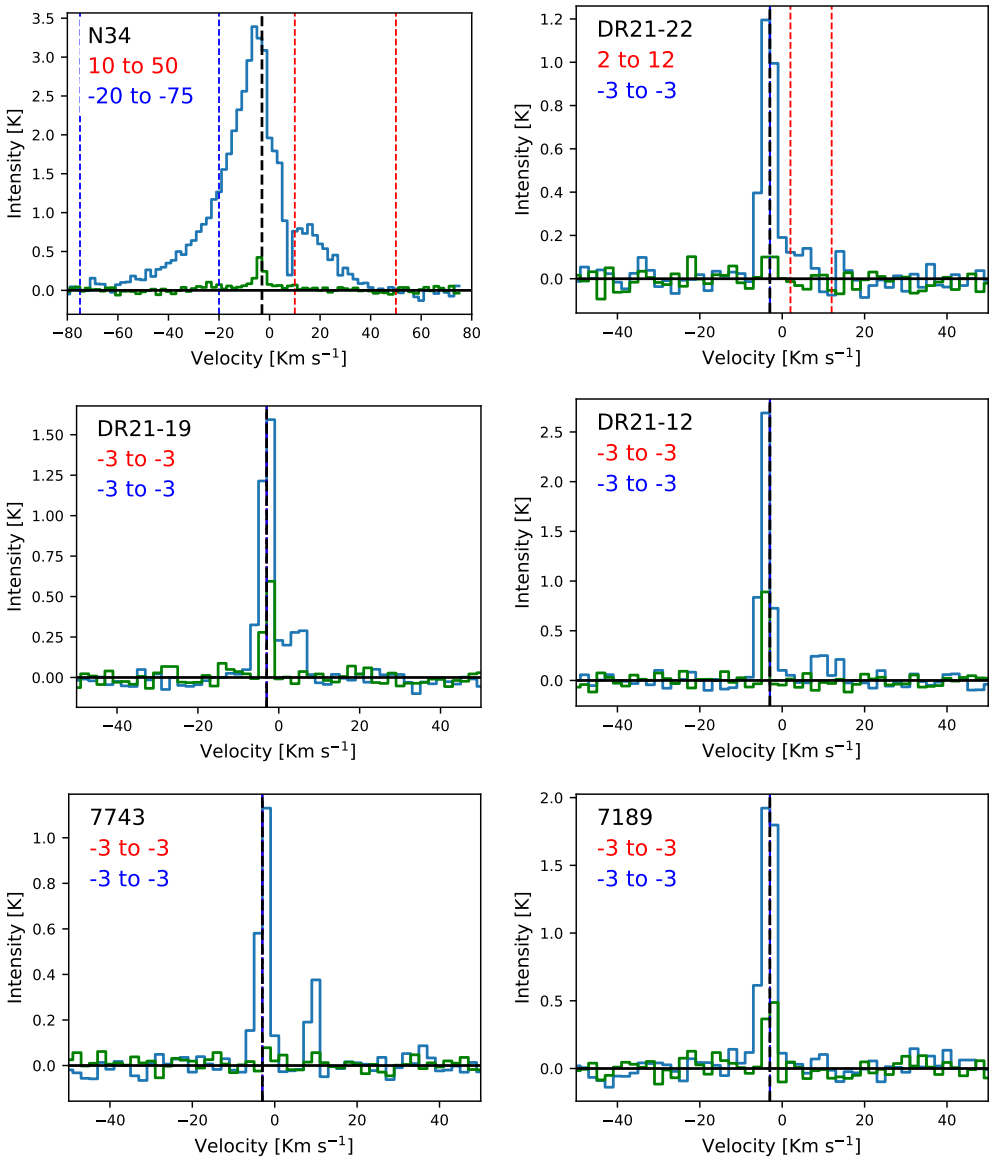


Figure A.4: Spectra of $HCO^+$ $J = 1 - 0$ (blue) and $H^{13}CO^+$ $J = 1 - 0$ (green) for clumps N34, DR21-22, DR21-19, DR21-12, 7743, and 7189. The spectra were averaged over the FWHM of the corresponding clumps (Table 3.2). Red and blue dashed lines mark the velocity range associated with outflow wing emission. The black dashed line marks the source velocity, $v_{\rm source}$ = -3 km s$^{-1}$.

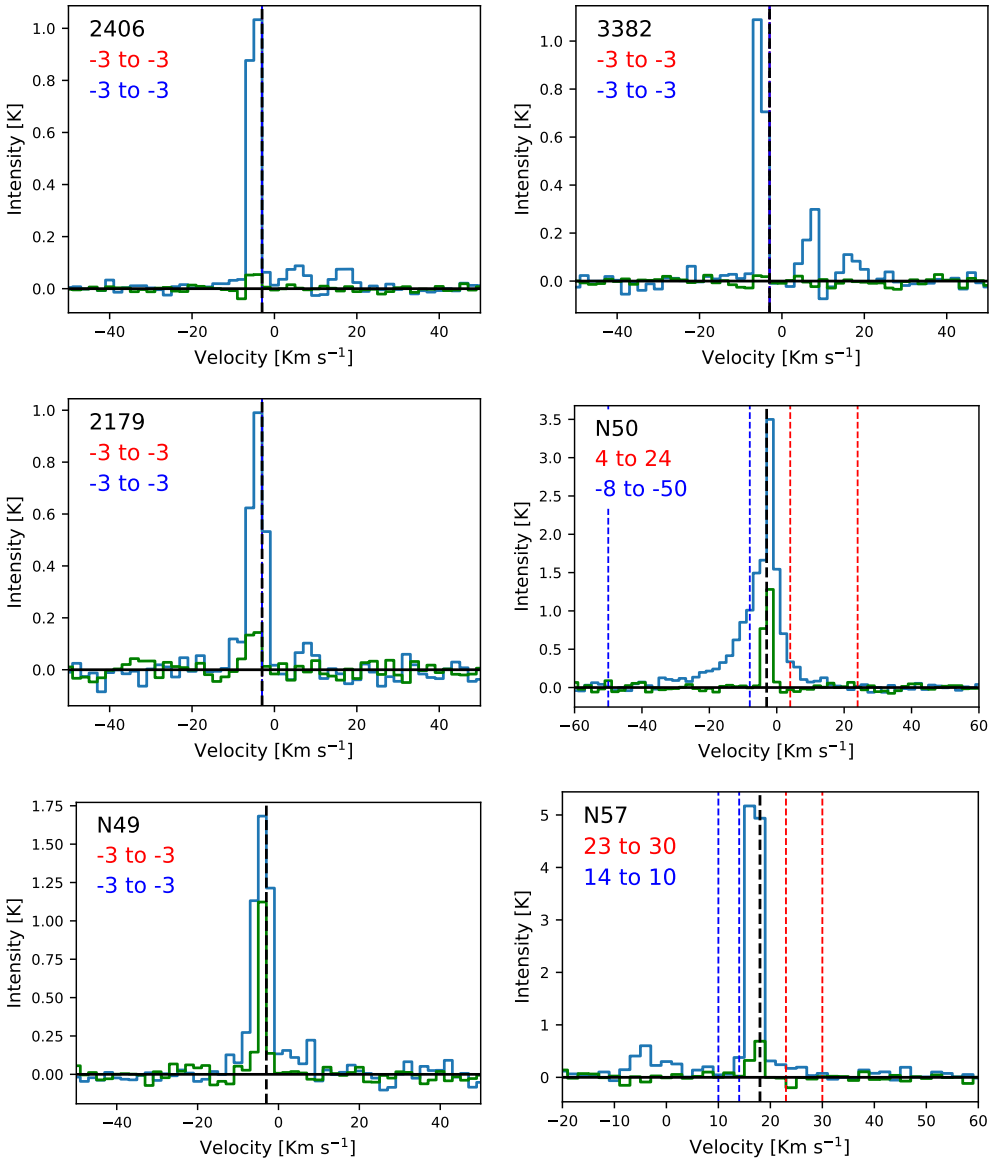


Figure A.5: Spectra of $HCO^+$ $J = 1 - 0$ (blue) and $H^{13}CO^+$ $J = 1 - 0$ (green) for clumps 2406, 3382, 2179, N50, N49, and N57. The spectra were averaged over the FWHM of the corresponding clumps (Table 3.2). Red and blue dashed lines mark the velocity range associated with outflow wing emission. The black dashed line marks the source velocity, $v_{\rm source}$ = -3 km s$^{-1}$ except N57, which is located in a separate structure east of DR21, where $V_{\rm source}$ = 18 km s$^{-1}$.

## A.2 Additional Contour maps

I provide here a short description for sources that displayed wings or other notable features in their spectra (see Section 3.3.1), but where found not to drive any molecular outflows. Figure A.6 shows the corresponding integrated intensity maps.

**DR21-22:** DR21-22 is a prime example of sources whose spectrum displayed the 'shelf'-like structure (Section 3.3.1), and extending between 0 and 10 km $s^{-1}$. The integrated intensity map, covering the velocity range of the 'shelf', reveals no coherent structures. This suggests that it is not part of an outflow, but it is rather associated with foreground material, possibly from the 9 km $s^{-1}$ component. The lack of blue-shifted emission in DR21-22 is in agreement with the absence of any outflow.

**N34 & N35:** The cores N34 and N35 are located in a dense structure West of DR21 Main, first detected by Plambeck and Menten, 1990. This structure appears to be actively interacting with the outflow of DR21 Main (Skretas, Karska, Wyrowski et al., 2023; Karska, Figueira et al., 2025). N34 and N35 lie in the path of the DR21 Main outflow, which is also dominating their integrated intensity maps , as a result, I cannot determine the presence of any additional outflows, originating from within N34 or N35. The lack of any clear outflow activity from these cores, even though their respective spectra show impressive line wings, highlights the danger of relying solely on spectral information for the identification of molecular outflows. This is especially true in clustered regions, like Cygnus-X, where multiple cores are located in a relatively small area.

**N36:** The continuum emission in the field of N36 is dominated by emission from N44, barely visible at the left bottom of the field. As a result, the weaker continuum emission associated with N36 is not clearly seen. The $HCO^+$ integrated intensity contours show fragmented red parts, corresponding to the broad but weak red-shifted component seen in the spectrum. The lack of a clearly defined lobe, and of a blue-shifted counterpart, suggests that there is no outflow associated with N36. In contrast, the outflow of N40 can be seen North of N36, directly outside the FWHM radius. Interesting to note is the presence of extended SiO emission over the core. The origin of this SiO is unclear, but is likely associated with N41, located to the East of N36.

**N41:** While there is some blue- and red-shifted emission near the location of N41, as seen also in the corresponding spectrum (see A.2), channel maps analysis shows that the blue-shifted emission appears significant only for velocities close to the source velocities, while the red-shifted emission is likely part of the extended red-shifted structures extending on the N - S direction. Therefore, it appears that N41 drives no significant $HCO^+$ outflow. Interestingly, significant SiO emission, at low velocities, can be seen, associated with the location of N41. This is the SiO emission that extends also over N36.

**N43:** In the case of N43, a bipolar outflow has been reported using CO $J = 3 - 2$ emission (Ching et al., 2018).In addition, $H_2O$ maser emission, often associated with outflowing material, has been reported near the continuum peak of N43. Some high-velocity $HCO^+$ components

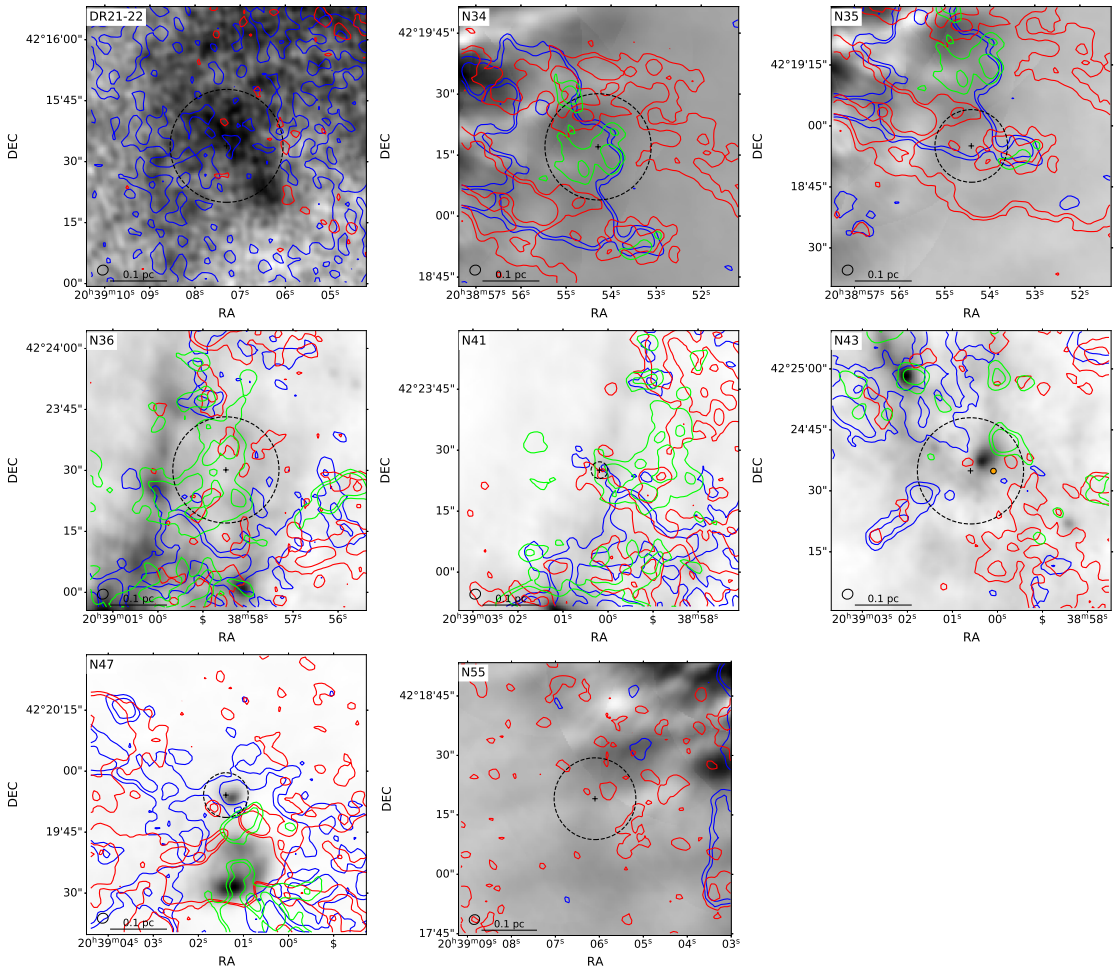


Figure A.6: Same as in Fig. 3.4 but for sources with no clear outflow detection.

appear in the vicinity of N43. The extended blue-shifted emission, at the north of N43 matches the direction of the blue-shifted CO lobe in Ching et al., 2018, but the structure is not consistent, at higher velocities, with the origin from N43. An additional blue-shifted component, located at the Eastern edge of the FWHM of N43, does not match the CO emission, and is significantly disconnected from the continuum peak. At the same time, there is only a marginal detection of the red-shifted emission coinciding with the FWHM of N43. Therefore, it appears that there is no clear HCO+ counterpart to the CO outflow in N43. Finally, significant SiO emission is detected near the continuum peak of N43. This emission appears at source velocity, and while it is relatively narrow in velocity space, it is likely to be originating in shocks related to the CO outflow.

## A.3 Outflow properties correlation fits

I carried out linear fits on the outflow - source properties correlations both separately for each component (low, intermediate, and high mass sources) as well as for the entire combined sample. The resulting best-fit parameters for cases are shown in Tables A.1 - A.6.

Table A.1: Outflow force correlations best-fit results

| | Sample | slope ($\alpha$) | intercept ($\beta$) | r |
|---|---|---|---|---|
| $F - M_{\rm env}$ | High mass | 0.733 ± 0.001 | -4.258 ± 0.002 | 0.699 |
| | Inter. mass | 0.428 ± 0.008 | -3.054 ± 0.077 | 0.337 |
| | Low mass | 1.189 ± 0.001 | -4.013 ± 0.001 | 0.756 |
| | All sources | 0.743 ± 0.001 | -4.221 ± 0.001 | 0.871 |
| $F - L_{\rm bol}$ | High mass | 0.266 ± 0.001 | -3.450 ± 0.018 | 0.288 |
| | Inter. mass | -0.116 ± 0.02168 | -2.052 ± 1.11491 | -0.081 |
| | Low mass | 0.891 ± 0.00156 | -4.745 ± 0.00055 | 0.486 |
| | All sources | 0.544 ± 0.001 | -4.581 ± 0.001 | 0.774 |

Table A.2: Outflow mass correlations best-fit results

| | Sample | slope ($\alpha$) | intercept ($\beta$) | r |
|---|---|---|---|---|
| $M_{\rm out} - M_{\rm env}$ | High mass | 0.057 ± 0.001 | 1.525 ± 0.001 | 0.123 |
| | Inter. mass | 0.226 ± 0.009 | -1.145 ± 0.200 | 0.180 |
| | Low mass | 0.943 ± 0.000 | -2.070 ± 0.001 | 0.758 |
| | All sources | 0.872 ± 0.000 | -1.036 ± 0.001 | 0.673 |
| $M_{\rm out} - L_{\rm bol}$ | High mass | -0.130 ± 0.001 | 2.202 ± 0.001 | -0.315 |
| | Inter. mass | -0.147 ± 0.015 | -0.239 ± 0.789 | -0.111 |
| | Low mass | 0.508 ± 0.001 | -2.404 ± 0.001 | 0.401 |
| | All sources | 0.660 ± 0.001 | -1.442 ± 0.001 | 0.657 |

Table A.3: Outflow mass rate correlations best-fit results

| | Sample | slope ($\alpha$) | intercept ($\beta$) | r |
|---|---|---|---|---|
| $\dot{M}_{\rm out} - M_{\rm env}$ | High mass | 0.368 ± 0.001 | -4.086 ± 0.001 | 0.479 |
| | Inter. mass | 0.457 ± 0.005 | -4.288 ± 0.048 | 0.396 |
| | Low mass | 1.044 ± 0.001 | -5.093 ± 0.001 | 0.716 |
| | All sources | 0.732 ± 0.001 | -4.991 ± 0.001 | 0.860 |
| $\dot{M}_{\rm out} - L_{\rm bol}$ | High mass | 0.267 ± 0.001 | -4.252 ± 0.004 | 0.398 |
| | Inter. mass | -0.055 ± 0.015 | -3.384 ± 0.779 | -0.042 |
| | Low mass | 0.506 ± 0.001 | -5.437 ± 0.001 | 0.338 |
| | All sources | 0.528 ± 0.001 | -5.311 ± 0.001 | 0.812 |

Table A.4: Outflow momentum correlations best-fit results

| | Sample | slope ($\alpha$) | intercept ($\beta$) | r |
|---|---|---|---|---|
| $P_{out} - M_{env}$ | High mass | 0.944 ± 0.001 | -0.241 ± 0.004 | 0.686 |
| | Inter. mass | 0.176 ± 0.010 | 0.218 ± 0.094 | 0.139 |
| | Low mass | 1.444 ± 0.002 | -0.736 ± 0.001 | 0.692 |
| | All sources | 1.110 ± 0.001 | -0.750 ± 0.001 | 0.875 |
| $P_{out} - L_{bol}$ | High mass | 0.852 ± 0.001 | -1.321 ± 0.011 | 0.738 |
| | Inter. mass | -0.216 ± 0.021 | 1.106 ± 1.056 | -0.151 |
| | Low mass | 0.963 ± 0.005 | -1.360 ± 0.002 | 0.451 |
| | All sources | 0.850 ± 0.001 | -1.307 ± 0.001 | 0.890 |

Table A.5: Outflow kinetic energy correlations best-fit results

| | Sample | slope ($\alpha$) | intercept ($\beta$) | r |
|---|---|---|---|---|
| $E_{kin} - M_{env}$ | High mass | 0.992 ± 0.001 | 43.463 ± 0.004 | 0.715 |
| | Inter. mass | 0.283 ± 0.016 | 44.348 ± 0.156 | 0.195 |
| | Low mass | 1.631 ± 0.003 | 43.173 ± 0.001 | 0.710 |
| | All sources | 1.107 ± 0.001 | 43.153 ± 0.001 | 0.874 |
| $E_{kin} - L_{bol}$ | High mass | 0.766 ± 0.001 | 42.837 ± 0.022 | 0.640 |
| | Inter. mass | -0.243 ± 0.037 | 45.469 ± 1.882 | -0.147 |
| | Low mass | 1.091 ± 0.007 | 42.463 ± 0.003 | 0.461 |
| | All sources | 0.812 ± 0.001 | 42.646 ± 0.001 | 0.837 |

Table A.6: Outflow kinetic luminosity correlations best-fit results

| | Sample | slope ($\alpha$) | intercept ($\beta$) | r |
|---|---|---|---|---|
| $L_{kin} - M_{env}$ | High mass | 0.519 ± 0.001 | -0.971 ± 0.010 | 0.390 |
| | Inter. mass | 0.519 ± 0.015 | -0.004 ± 0.142 | 0.350 |
| | Low mass | 1.663 ± 0.004 | -1.552 ± 0.001 | 0.679 |
| | All sources | 0.782 ± 0.001 | -1.480 ± 0.001 | 0.713 |
| $L_{kin} - L_{bol}$ | High mass | 0.156 ± 0.001 | -0.342 ± 0.054 | 0.134 |
| | Inter. mass | -0.105 ± 0.041 | 1.101 ± 2.086 | -0.062 |
| | Low mass | 1.141 ± 0.010 | -2.298 ± 0.004 | 0.449 |
| | All sources | 0.524 ± 0.001 | -1.743 ± 0.001 | 0.626 |

APPENDIX B

# The Cygnus Allscale Survey of Chemistry and Dynamical Environments: CASCADE. II. A detailed kinematic analysis of the DR21 Main outflow

A&A, 679, A66 (2023)
https://doi.org/10.1051/0004-6361/202346825
© The Authors 2023

Astronomy & Astrophysics

# The Cygnus Allscale Survey of Chemistry and Dynamical Environments: CASCADE

## II. A detailed kinematic analysis of the DR21 Main outflow

I. M. Skretas[1], A. Karska[1,2,3], F. Wyrowski[1], K. M. Menten[1], H. Beuther[4], A. Ginsburg[5], A. Hernández-Gómez[6,1], C. Gieser[7], S. Li[4], W.-J. Kim[8], D. A. Semenov[4], L. Bouscasse[9], I. B. Christensen[1], J. M. Winters[9], and A. Hacar[10]

[1] Max-Planck-Institut für Radioastronomie, Auf dem Hügel 69, 53121 Bonn, Germany
e-mail: iskretas@mpifr-bonn.mpg.de
[2] Argelander-Institut für Astronomie, Universität Bonn, Auf dem Hügel 71, 53121 Bonn, Germany
[3] Institute of Astronomy, Faculty of Physics, Astronomy and Informatics, Nicolaus Copernicus University, ul. Grudziądzka 5, 87-100 Toruń, Poland
[4] Max Planck Insitute for Astronomy, Königstuhl 17, 69117 Heidelberg, Germany
[5] Department of Astronomy, University of Florida, PO Box 112055, Gainesville, FL 32611-2055, USA
[6] Tecnologico de Monterrey, Escuela de Ingeniería y Ciencias, Avenida Eugenio Garza Sada 2501, Monterrey 64849, Mexico
[7] Max-Planck-Institut für extraterrestrische Physik, Giessenbachstrasse 1, 85748 Garching, Germany
[8] I. Physikalisches Institut, Universität zu Köln, Zülpicher Str. 77, 50937 Köln, Germany
[9] IRAM, 300 rue de la Piscine, Domaine Universitaire de Grenoble, 38406 St.-Martin-d'Hères, France
[10] Department of Astrophysics, University of Vienna, Turkenschanzstrasse 17, 1180 Vienna, Austria

Received 5 May 2023 / Accepted 17 September 2023

**ABSTRACT**

*Context.* Molecular outflows are believed to be a key ingredient in the process of star formation. The molecular outflow associated with DR21 Main in Cygnus-X is one of the most extreme molecular outflows in the Milky Way in terms of mass and size. The outflow is suggested to belong to a rare class of explosive outflows formed by the disintegration of protostellar systems.
*Aims.* We aim to explore the morphology, kinematics, and energetics of the DR21 Main outflow, and to compare those properties to confirmed explosive outflows in order to unravel the underlying driving mechanism behind DR21.
*Methods.* We studied line and continuum emission at a wavelength of 3.6 mm with IRAM 30 m and NOEMA telescopes as part of the Cygnus Allscale Survey of Chemistry and Dynamical Environments (CASCADE) program. The spectra include ($J$ = 1–0) transitions of $HCO^+$, HCN, HNC, $N_2H^+$, $H_2CO$, and CCH, which trace different temperature and density regimes of the outflowing gas at high velocity resolution (~0.8 km s$^{-1}$). The map encompasses the entire DR21 Main outflow and covers all spatial scales down to a resolution of 3″ (~0.02 pc).
*Results.* Integrated intensity maps of the $HCO^+$ emission reveal a strongly collimated bipolar outflow with significant overlap of the blueshifted and redshifted emission. The opening angles of both outflow lobes decrease with velocity, from ~80 to 20° for the velocity range from 5 to 45 km s$^{-1}$ relative to the source velocity. No evidence is found for the presence of elongated, "filament-like" structures expected in explosive outflows. $N_2H^+$ emission near the western outflow lobe reveals the presence of a dense molecular structure, which appears to be interacting with the DR21 Main outflow.
*Conclusions.* The overall morphology as well as the detailed kinematics of the DR21 Main outflow are more consistent with a typical bipolar outflow than with an explosive counterpart.

**Key words.** stars: protostars – stars: winds, outflows – stars: formation – ISM: jets and outflows – ISM: kinematics and dynamics – ISM: molecules

## 1. Introduction

Molecular outflows are a ubiquitous part of star formation arising from both high- and low-mass protostars (Arce et al. 2007; Frank et al. 2014; Bally 2016). A new type of outflow, formed by the disintegration of protostellar systems due to a merging event, has been proposed and linked to regions of high-mass star formation (Bally & Zinnecker 2005; Zapata et al. 2009). The massive outflow of DR21 Main is one of the proposed candidates for this type of explosive outflow (Zapata et al. 2013). The large angular extent of the DR21 Main outflow allows a detailed analysis of its structure and properties, with a view to compare these to the same attributes of other explosive outflow candidates.

Molecular protostellar outflows range from highly collimated molecular jets, such as HH211 (Gueth & Guilloteau 1999), all the way to wide-angled outflows from high-mass sources (Beuther & Shepherd 2005a). In general, outflows tend to appear "narrower" at higher velocities (Bachiller & Tafalla 1999), and become less collimated as they evolve (Beuther & Shepherd 2005b; Arce & Sargent 2006; Offner et al. 2011; Hsieh et al. 2023). They can vary significantly in size and energetics, with sizes from 0.1 pc up to parsec scales and momentum rates of between $10^{-5}$ and $10^{-2}$ $M_\odot$ km s$^{-1}$ yr$^{-1}$ for low-mass sources and some O type stars, respectively (e.g., Maud et al. 2015). Some outflow properties, such as their mass, force, and mechanical luminosity, correlate well with the intrinsic parameters of their driving



Open Access article, published by EDP Sciences, under the terms of the Creative Commons Attribution License (https://creativecommons.org/licenses/by/4.0), which permits unrestricted use, distribution, and reproduction in any medium, provided the original work is properly cited.
This article is published in open access under the Subscribe to Open model. Open access funding provided by Max Planck Society.

sources, such as the bolometric luminosity (Bally & Lada 1983; Cabrit & Bertout 1992; Wu et al. 2004) and the mass of the molecular gas envelope of their driving source (Bontemps et al. 1996; Beuther et al. 2002), suggesting a common driving mechanism in both the low- and high-mass sources. Clearly, molecular outflows play a critical role in regulating star formation by removing excess angular momentum and thus facilitating the further growth in mass of a protostellar system (Blandford & Payne 1982; Machida 2014), and also play a part in dispersing the surrounding envelope, reducing the available mass reservoir (Arce & Sargent 2006).

Due to their large size and the energy they carry, molecular outflows can have a significant impact on the surrounding interstellar medium (ISM) over different spatial scales. First, at envelope scales ($10^3$–$10^4$ AU), powerful young outflows entrain and clear out dense material giving rise to bipolar cavities (e.g., Gueth et al. 1997; Velusamy & Langer 1998; Arce & Sargent 2004, 2005). At core scales (0.1–0.3 pc), outflows are considered a significant contributor to turbulence (Myers et al. 1988; Zhang et al. 2005). In addition, outflows from high-mass young stellar objects (YSOs) might impact the morphology of the host molecular cloud and may even break it apart (Fuente et al. 1998; Benedettini et al. 2004). Finally, the propagation of outflows through the surrounding dense material leads to the formation of shocks, which locally compress and heat the gas, and drive chemical processes enriching the ISM (e.g., Kaufman & Neufeld 1996; Flower & Pineau Des Forêts 2010; Burkhardt et al. 2019).

A newly proposed type of molecular outflow is the so-called explosive dispersal outflow, whose origin appears to be linked to the disintegration of young stellar systems (Bally et al. 2017; Rivera-Ortiz et al. 2021) or to protostellar mergers (Bally & Zinnecker 2005). The interpretation is limited due to the small sample of explosive-outflow candidates: Orion-KL (Zapata et al. 2009), DR21 Main (Zapata et al. 2013), G5.89 (Zapata et al. 2019), and IRAS 16076-5134 (Guzmán Ccolque et al. 2022). Nevertheless, these explosive outflows share the following characteristics (Zapata et al. 2009, 2017): (i) they consist of multiple straight, narrow, and relatively isotropically distributed filament-like structures; (ii) these filament-like structures should all point towards the point of origin of the explosive outflow and show an increase in velocity with distance from the point of origin akin to a Hubble flow; (iii) have a significant overlap of their blueshifted and redshifted emission components. The filament-like structures of explosive outflows form because all material is simultaneously accelerated in the explosion. As a result, faster-moving material has traveled further away from the source and is trailed by the slower parts of the outflow. Overall, the properties of these outflows have mostly been studied using low-$J$ CO transitions at high angular resolution (e.g., Zapata et al. 2009, 2013, 2019). Observations of the inner parts of these explosive molecular outflows reveal multiple filament-like structures. At the same time, the lack of similar observations in other molecular tracers limits our understanding of their chemistry and the various physical gas components.

The DR21 Main outflow is a particularly interesting explosive outflow candidate (Zapata et al. 2013), as it is one of the most massive ($M_{\rm out} > 3000\,M_\odot$) and energetic ($E_{\rm kin} > 2 \times 10^{48}$ erg) outflows detected in our Galaxy (Garden et al. 1986, 1991b), first in the vibrationally excited 2.12 μm line of shock-excited molecular hydrogen ($H_2$). DR21 Main itself is a compact HII region prominent at radio wavelengths. It is located in the Cygnus-X high-mass star-forming region–molecular cloud complex (Leung & Thaddeus 1992), at the southern end of the DR21 molecular ridge (Dickel et al. 1978), and at a distance of 1.5 kpc (Rygl et al. 2012). The outflow appears bipolar, with the outflow lobes extending from east to west (Garden et al. 1986, 1991a; Garden & Carlstrom 1992; Schneider et al. 2010). High-velocity low-$J$ CO emission has also been reported in the north–south direction (Garden et al. 1991b). The blueshifted and redshifted parts of the outflow overlap significantly, suggesting that it extends very close to the plane of the sky (Cruz-González et al. 2007). It was initially suggested that the DR21 Main outflow is driven by a massive protostar, with $L_{\rm bol}$ of $\sim 10^5$–$10^6\,L_\odot$ (Garden et al. 1991b; Garden & Carlstrom 1992), but no such source has yet been identified (Cruz-González et al. 2007). The absence of a clearly detected driving source, along with the detection of some filament-like structures in CO (1–0) emission, led Zapata et al. (2013) to suggest a possible explosive nature for the DR21 Main outflow.

In this work, we aim to study the morphology, kinematics, and energetics of the DR21 Main outflow using observations in multiple molecular lines, which are sensitive to a range of physical conditions. We also aim to determine whether the characteristics of the DR21 Main outflow are consistent with those expected for explosive outflows or rather with those of typical protostellar outflows.

This work is part of the Max Planck IRAM Observatory Program (MIOP) "Cygnus Allscale Survey of Chemistry and Dynamical Environments (CASCADE)" (Beuther et al. 2022). CASCADE is designed to map significant parts of the Cygnus-X molecular cloud complex at high angular resolution and with a broad bandpass using the Northern Extended Array for Millimeter Astronomy (NOEMA) and the 30 m telescope, both operated by the Institut de Radioastronomie Millimètrique (IRAM). The combination of velocity-resolved single-dish and interferometric observations offers the high resolution necessary to resolve the outflow structure without losing information on extended emission. CASCADE aims to take advantage of these high-quality observations to connect the transition of gas all the way from the large scales of molecular clouds down to the small scales of cores; to look for signs of collapse or feedback; to investigate the impact of star-forming cores on their surroundings; and to search for possible trends with evolutionary stage and more. The scope and goals of CASCADE are discussed in detail by Beuther et al. (2022).

The paper is organized as follows. Section 2 describes the observations from CASCADE. Section 3 presents line detections and maps of the DR21 Main outflow in several molecular transitions, and provides the analysis of outflow properties. In Sect. 4, the results are discussed and scenarios for the origin of the DR21 Main outflow are explored along with its interactions with the surrounding molecular cloud. Finally, in Sect. 5 we present a summary and conclusions.

## 2. Observations

A detailed overview of the CASCADE program is given in Beuther et al. (2022). Briefly, CASCADE covers all high-column-density areas in the Cygnus-X molecular cloud complex using 40 mosaics, each covering 16 arcmin$^2$. Each of the mosaics corresponds to 78 NOEMA pointings and was observed in both the C and D configurations. The observations have a total bandwidth of 16 GHz, 8 in each sideband, at the 3.6 mm window. The full bandwidth is covered with a spectral resolution of 2.0 MHz, but selected parts surrounding the most important lines are also covered by additional high-resolution correlator units providing a spectral resolution of 62.5 kHz. The DR21 Main outflow is

**Table 1.** Continuum and spectral line parameters for all lines covered by the CASCADE observations.

| Species | Transition | Frequency (GHz) | $\sigma_{\rm rms}$ $\left(\frac{\rm mJy}{\rm beam}\right)$ | Beam (arcsec) | $E_{\rm up}$ (K) | Log($A_{ij}$) ($s^{-1}$) |
|---|---|---|---|---|---|---|
| Continuum | – | 82.028 | 0.05 | $2.80 \times 2.54$ | – | – |
| $DCO^+$ | (1–0) | 72.039 | 15 | $3.57 \times 3.19$ | 3.46 | –4.16 |
| CCD | (1–0) | 72.108 | 15 | $3.57 \times 3.19$ | 3.46 | –6.06 |
| DCN | (1–0) | 72.415 | 16 | $3.56 \times 3.18$ | 3.47 | –4.88 |
| $SO_2$ | ($6_{0,6}$–$5_{1,5}$) | 72.758 | 14 | $3.54 \times 3.16$ | 19.15 | –5.56 |
| HCCCN | (8–7) | 72.784 | 14 | $3.54 \times 3.16$ | 15.72 | –4.53 |
| $H_2CO$ | ($1_{0,1}$–$0_{0,0}$) | 72.838 | 16 | $3.90 \times 3.28$ | 3.50 | –5.09 |
| $CH_3CN$ | ($4_k$–$3_k$) | 73.590 | 12 | $3.51 \times 3.13$ | 8.83 | –4.66 |
| DNC | (1–0) | 76.306 | 10 | $3.24 \times 2.90$ | 3.66 | –4.79 |
| $CH_3OH$ | ($5_{0,5}$–$4_{1,3}$)E | 76.510 | 10 | $3.24 \times 2.89$ | 47.93 | –6.05 |
| $NH_2D$ | ($1_{1,1}$–$1_{0,1}$) | 85.926 | 10 | $2.77 \times 2.51$ | 20.68 | –5.71 |
| $H^{13}CN$ | (1–0) | 86.340 | 9 | $2.75 \times 2.50$ | 4.14 | –4.65 |
| $H^{13}CO^+$ | (1–0) | 86.754 | 7 | $2.74 \times 2.49$ | 4.16 | –4.41 |
| SiO | (2–1) | 86.847 | 11 | $3.25 \times 2.70$ | 6.25 | –4.53 |
| $HN^{13}C$ | (1–0) | 87.091 | 9 | $2.73 \times 2.48$ | 4.18 | –4.73 |
| CCH | (1–0) | 87.329 | 10 | $2.72 \times 2.47$ | 4.19 | –5.90 |
| HNCO | ($4_{0,4}$–$3_{0,3}$) | 87.925 | 8 | $2.71 \times 2.45$ | 10.55 | –5.06 |
| HCN | (1–0) | 88.632 | 13 | $3.18\times 2.64$ | 4.25 | –4.62 |
| $HCO^+$ | (1–0) | 89.189 | 10 | $3.29 \times 2.74$ | 4.28 | –4.38 |
| HNC | (1–0) | 90.664 | 11 | $3.12 \times 2.57$ | 4.35 | –4.57 |
| HCCCN | (10–9) | 90.979 | 9 | $2.64 \times 2.39$ | 24.01 | –4.24 |
| $CH_3CN$ | ($5_k$–$4_k$) | 91.987 | 9 | $2.61 \times 2.36$ | 13.24 | –4.85 |
| H41$\alpha$ | – | 92.034 | 6 | $2.60 \times 2.36$ | – | – |
| $^{13}CS$ | (2–1) | 92.494 | 10 | $2.59 \times 2.35$ | 6.66 | –4.85 |
| $N_2H^+$ | (1–0) | 93.174 | 11 | $2.58 \times 2.33$ | 4.47 | –4.44 |

**Notes.** The rms noise level, $\sigma_{\rm rms}$, is calculated for channels of 0.8 km $s^{-1}$ except for the case of H41$\alpha$ for which the channel width is 3.0 km $s^{-1}$. Rest frequencies are from NIST recommended rest frequencies (Lovas 2004) and the Cologne Database for Molecular Spectroscopy (CDMS, Müller et al. 2001), while $E_{\rm up}$ and $A_{ij}$ are taken from CDMS. The conversion factor from Jy beam$^{-1}$ to K in the Rayleigh-Jeans limit is ∼23.75 for a frequency of 89.189 GHz.

covered by two of the NOEMA mosaics, which were observed between 2020 May 29 and November 6. During that time, the array consisted of ten antennas, yielding baselines between 15 m and 365 m. The strong quasars 3C345 and 3C273 were used as bandpass calibrators, MWC349 and 2010+723 were used for flux calibration, and 2005+403, 2120+445, 2050+363 and 2013+370 were used for gain calibration. Complementary single-dish observations were carried out with the IRAM 30m telescope between 2020 February and July, in order to provide the missing short spacing information. These observations will be presented in detail in an upcoming paper by Christensen et al. (in prep.).

The calibration and imaging of the data was done using CLIC and MAPPING software, which are part of the GILDAS package[1]). The NOEMA observations are combined with the IRAM 30m data using the UV_SHORT task. The resulting single-channel $\sigma_{\rm rms}$ noise – for a channel width of 0.8 km $s^{-1}$ – and beam sizes for all observed lines are summarized in Table 1.

## 3. Results and analysis

We present the CASCADE observations for an area surrounding DR21 Main that covers the entirety of its outflow. Our data allow us to analyze the kinematics, morphology, and energetics of the DR21 Main outflow and to contribute to a discussion about its nature.

[1] https://www.iram.fr/IRAMFR/GILDAS/

### 3.1. Molecular detections

Several molecular lines are detected in the CASCADE observations of the DR21 Main (see Table 2). The spatial distribution of the emission can be divided into three cases: (i) tracing the outflow (extended emission in the W–E direction), (ii) tracing the DR21 ridge (extended emission in the N–S direction), and (iii) sporadic (compact emission that appears in multiple locations) or compact emission (see Fig. 1). The different tracers can therefore be used to examine the morphology of the various gas components in DR21 Main. Integrated intensity contour maps for all the emission lines are shown in Appendix A.

The contour map of the $HCO^+$ integrated intensity (Fig. 1, left panel) shows that most of the emission arises from the area of the outflow lobes and also appears to be in close agreement with the $H_2$ emission at 2.2 μm (see also Garden et al. 1986; Davis et al. 2007) associated with outflowing shocked gas. Interestingly, the $HCO^+$ (1–0) contours also reveal the presence of hollowed-out cavities in both outflow lobes lacking line emission, which is similar to early findings by Garden & Carlstrom (1992). The cavities are more prominent in the eastern outflow lobe, which appears entirely separated from the center of the DR21 Main area. Therefore, while $HCO^+$ is well associated with the outflowing material, it most accurately traces the outer parts of the outflow cavities. In a similar fashion, line emission in HCN (1–0) is also associated with the outflow, but shows a more compact pattern in the direction of the peaks of $HCO^+$ emission (see Fig. A.1).

**Table 2.** Molecular line detections (at 5$\sigma$ level) in the area of the DR21 Main outflow.

| Location | Species |
|---|---|
| Outflow (E–W) | $HCO^+$, HCN |
| DR21 ridge – Dense gas (N–S) | $^{13}CS$, CCH, $H_2CO$, $H^{13}CO^+$, HCCCN, HNC, $N_2H^+$, $H^{13}CN$, $HN^{13}C$ |
| Sporadic or compact emission | $CH_3CN$[(a)], $CH_3OH$, DCN, $DCO^+$, DNC, H41$\alpha$, $NH_2D$, SiO |
| Nondetections | CCD, HNCO, $SO_2$ |

**Notes.** [(a)]Only a 3$\sigma$ detection.

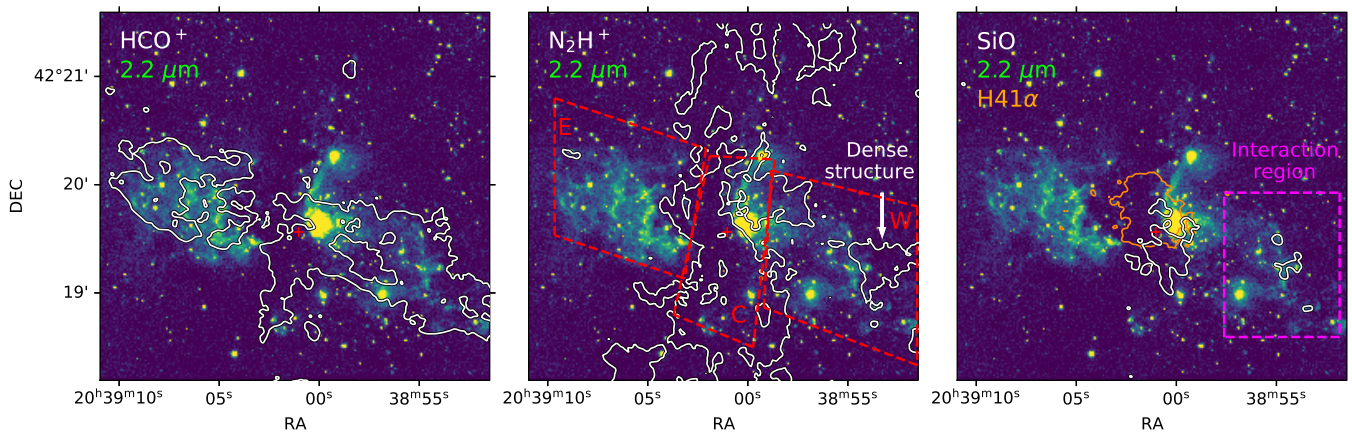


**Fig. 1.** United Kingdom Infra-Red Telescope (UKIRT) Wide Field Camera (WFCAM) continuum image of the DR21 Main region at 2.2 μm (Warren et al. 2007) and the line emission in key gas tracers observed as part of CASCADE. Shock-excited $H_2$ emission makes a significant contribution to the 2.2 μm image, in particular to the lobes off the central region. White contours mark the 5$\sigma$ $HCO^+$ (left), $N_2H^+$ (middle), and SiO (right) emission. Intensities are integrated between –50 and 50, –20 and 10, and –20 and 20 km s$^{-1}$ for the $HCO^+$, $N_2H^+$, and SiO emission, respectively. The adopted point of origin of the outflow is marked in all cases with a red cross. Red dashed lines (middle) mark the three separate areas of the DR21 Main region used to extract the spectra in Fig. 2, with "E" marking the eastern outflow lobe, "C" the central area, and "W" the western outflow lobe. The magenta dashed box (right) marks the location of the interaction region shown in Fig. 11. Finally orange contours (right) show the 5$\sigma$ integrated intensity of H41$\alpha$ from –30 to 30 km s$^{-1}$.

In contrast, the $N_2H^+$ emission appears to trace the DR21 ridge along the N–S direction (the middle panel of Fig. 1, Wilson & Mauersberger 1990; Motte et al. 2007). This is expected as $N_2H^+$ is known to trace dense, cold, CO-depleted gas (Caselli et al. 2002; Jørgensen et al. 2004). In addition to the ridge, $N_2H^+$ also reveals the presence of a molecular structure near the western lobe. This structure was previously detected in CS (2–1) by Plambeck & Menten (1990) who also reported the detection of a collisionally excited class I methanol maser in its interaction region with the outflow traced by $H_2$ emission. Other molecules that are often associated with dense gas, such as CCH (1–0), HCCCN (both the (10–9) and (8–7) transitions), $^{13}CS$ (1–0), and HNC (1–0), show a distribution similar to that of $N_2H^+$ (1–0) (see Figs. A.1, A.2 and A.3).

Finally, SiO is detected close to the center of the outflow, but also shows very localized emission in an area of the western outflow lobe (Fig. 1, right panel). Although SiO typically traces shocks in the ISM (e.g., Martin-Pintado et al. 1992; Schilke et al. 1997; Gusdorf et al. 2008), its emission peak in the center of DR21 might also originate from photo-evaporating ice mantles in the dusty envelope of a driving source(s) (e.g., Walmsley et al. 1999; Schilke et al. 2001). On the other hand, the SiO emission detected near the western lobe could result from the interaction of the outflow and the dense structure seen, for example, in $N_2H^+$, located there. This scenario is discussed in more detail in Sect. 4.3.

Figure 2 shows the profiles of the strongest lines averaged over the eastern outflow lobe, the central area of DR21 Main, and the western outflow lobe (Fig. 1). Similar spectra for the rest of the lines are presented in Appendix B. The peak of the line emission lies at a velocity of –3 km s$^{-1}$, which corresponds to the velocity of the DR21 ridge (Dickel et al. 1978). The 9 km s$^{-1}$ feature, caused by more diffuse foreground material in the so-called extended W75 cloud (Dickel et al. 1978; Nyman 1983) can also be seen in some of the lines, but is most prominent in $HCO^+$ and HCN. The profiles of both the $HCO^+$ and HCN lines display extended line wings and strong emission in both outflow lobes, confirming their association with the outflowing material. In contrast, emission from molecules associated with the denser gas and the bulk of the DR21 ridge, such as $N_2H^+$ or HNC, have narrower emission lines and relatively weaker emission from the outflow lobes.

In summary, the CASCADE observations offer a clear view of the different gas components in the DR21 Main area. Most importantly, the $HCO^+$ is found to accurately trace the molecular outflow, $N_2H^+$ highlights the dense filament, and SiO emission suggests the possibility of an interaction between the outflow and the surrounding ISM, a scenario further explored in Sect. 4.3. The release of a full line list, including unidentified lines for all targets of the CASCADE survey, will be presented in a future paper of the collaboration.

### 3.2. The molecular outflow of DR21 Main

The $HCO^+$ emission is one of the best tracers of the molecular outflow in DR21 Main and its distribution closely follows that of

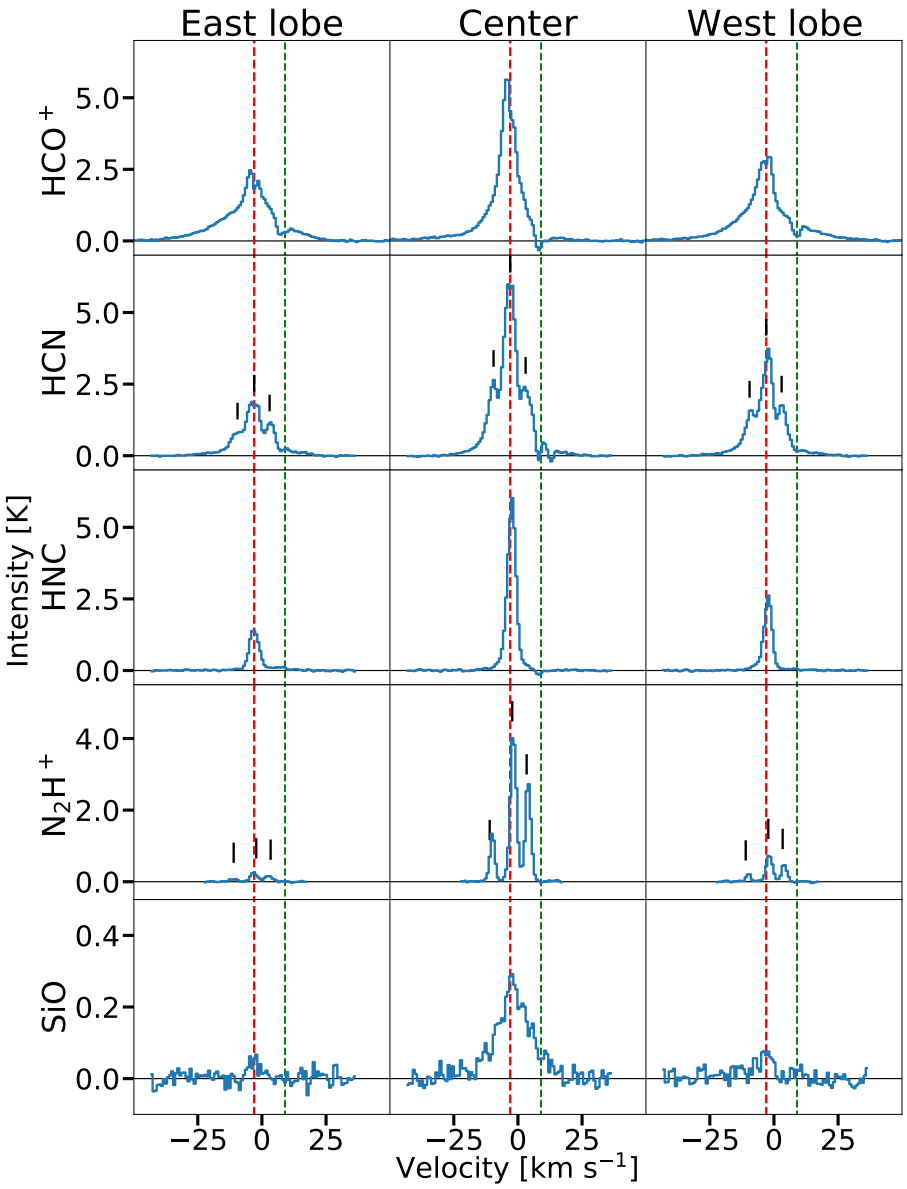


**Fig. 2.** Averaged line profiles of the (1–0) transitions of $HCO^+$, HCN, HNC, $N_2H^+$, and the (2–1) transition of SiO toward the eastern lobe, the center, and the western lobe of the DR21 Main outflow (see Fig. 1). For HCN and $N_2H^+$, the velocities corresponding to hyperfine structure components are marked with black ticks. Red dashed lines show the source velocity, $-3\,\mathrm{km\,s^{-1}}$, green dashed lines mark the location of the absorption feature at $9\,\mathrm{km\,s^{-1}}$, and the gray horizontal lines show the baselines.

the $H_2$ emission (Sect. 3.1, Fig. 1). Therefore, we use it to explore the kinematics as well as the outflow morphology at different velocities. In particular, we investigate the change of the opening angle with gas velocity.

Figure 3 shows the spatial distribution of the $HCO^+$ (1–0) emission integrated over velocity intervals of $5\,\mathrm{km\,s^{-1}}$ in the range from 5 and $45\,\mathrm{km\,s^{-1}}$ relative to the source velocity ($v_{\mathrm{source}} = -3\ \mathrm{km\,s^{-1}}$) for the redshifted emission, and from −5 to $-45\,\mathrm{km\,s^{-1}}$ for the blueshifted emission. Most of the $HCO^+$ emission is elongated in the W–E direction, tracing the outflow lobes of a bipolar outflow (Fig. 1). Some emission extends also in the N–S direction in a narrow range of velocities, suggesting that it is associated with the DR21 ridge. However, some of this emission might also originate from the outflowing gas, as suggested by CO (1–0) maps (Garden et al. 1991b).

Overall, the velocity-channel maps (Fig. 3) show a rather symmetric morphology, but some small asymmetries can be noted. Namely, the blueshifted part of the outflow appears stronger and extends to higher velocities than its redshifted counterpart. Similar behavior is also seen between the two lobes of the outflow, with the western lobe both appearing brighter and showing higher velocities than the eastern one. These small asymmetries are likely to arise because of the relative position of the outflow driving source compared to the bulk of material in the surrounding ISM. In addition, the higher-velocity $HCO^+$ emission seems to be detached from the point of origin of the outflow (see also Garden & Carlstrom 1992). Thanks to the higher angular resolution of the current observations, we find cleared-out cavities in the outflow lobes. Finally, the known overlap of the blueshifted and redshifted parts of the DR21 Main outflow, indicating that the outflow extends close to the plane of the sky, is clearly seen (see Fig. 4, and Schneider et al. 2010). However, we note that we cannot estimate the inclination of the outflow more precisely because of the complexity of the ISM surrounding DR21 Main, for example, the interaction region.

Figure 5 shows the position–velocity diagram of $HCO^+$ along the DR21 Main outflow illustrating several key outflow structures. First, the bright negative peak near the offset of 200″ indicates the location of the interaction region, where material is deflected into the line of sight. Secondly, an extended absorption feature is detected near the middle of the outflow, which corresponds to the H II region. Thirdly, the known absorption feature

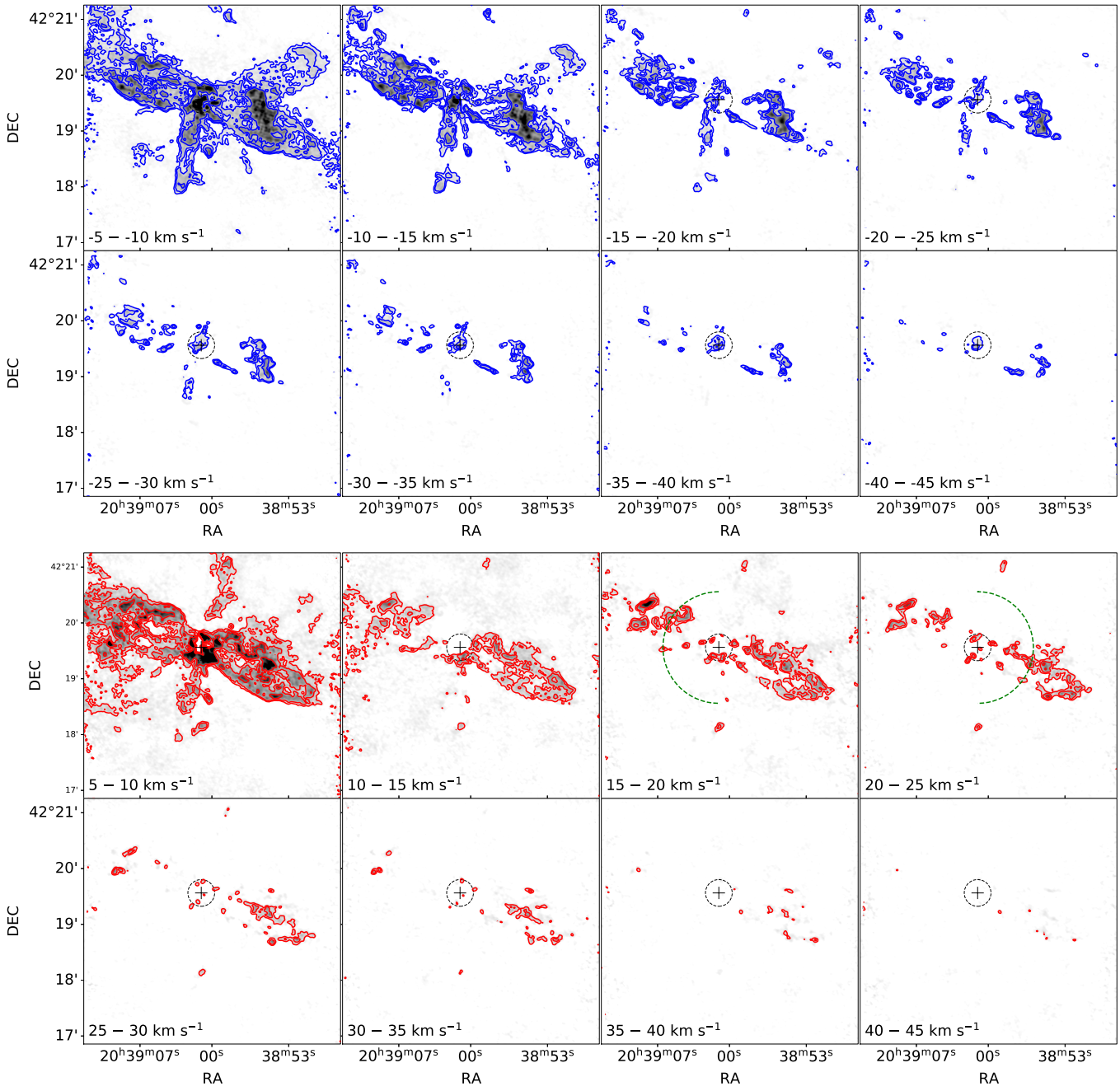


**Fig. 3.** Channel maps of the DR21 Main outflow in $HCO^+$. Contours of the blueshifted $HCO^+$ emission (in blue) and redshifted emission (in red) are integrated over velocity steps of 5 km s$^{-1}$ and are plotted over the corresponding grayscale. The full velocity range is from 5 to 45 km s$^{-1}$ relative to the source velocity (−3 km s$^{-1}$) and the contour levels correspond to 5, 10, and 20 $\sigma_{\rm rms}$. The black dashed circle shows the area of the DR21–1 core in Cao et al. (2019). The green dashed lines denote the half-circles used to derive the outflow opening angles (see Fig. 7).

at 9 km s$^{-1}$, which is caused by more diffuse foreground material associated with W75, is also detected along the entire length of the outflow (Dickel et al. 1978). Finally, several structures are detected in the less disrupted eastern lobe, which resemble a sawtooth pattern associated with the extremely high-velocity (EHV) component of the low-mass protostar IRAS 04166+2706 (Santiago-García et al. 2009). A first estimate of the maximum velocity of the structures (∼20 km s$^{-1}$) and the separation between them (∼10″) using approximate values derived from the PV diagram yields upper limits for the timescales between these knots of the order of ∼$10^3$ yr. This result corresponds to the upper limits of the timescales found between the knots in the outflows of W43–MM1 (Nony et al. 2020).

Figure 6 compares the velocities of $HCO^+$ with those of $N_2H^+$ in the direction of the DR21 ridge. $N_2H^+$ is exclusively associated with the ridge (Fig. 1) and shows three peaks corresponding to its hyperfine-splitted lines. All those components show a velocity gradient along the DR21 ridge, with velocities becoming increasingly blue-shifted North of DR21 Main. A similar gradient cannot be probed in the corresponding $HCO^+$ position–velocity diagram (Fig. 6) due to the complex line profiles. Similar to Fig. 5, a strong central absorption feature exists, associated with the H II region. In addition, the extended emission in the North–South is detected as a blue-shifted structure between offsets 50″ and 100″. The lack of corresponding red-shifted emission favors the scenario that this emission is

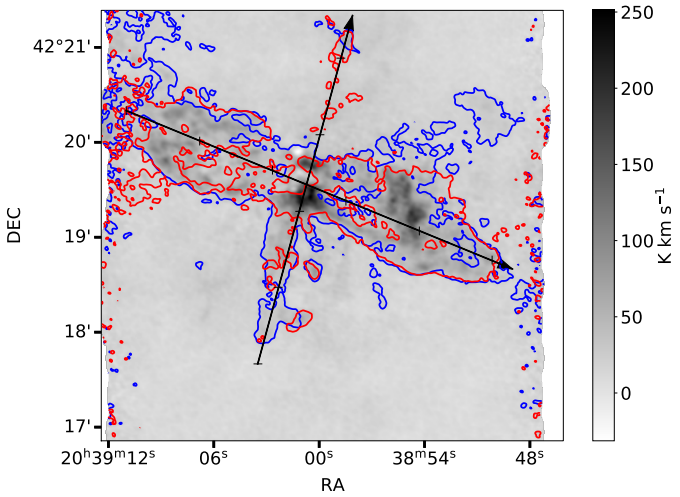


**Fig. 4.** $HCO^+$ emission integrated from –50 to 50 km s$^{-1}$. Red and blue contours mark the redshifted (5 to 45 km s$^{-1}$) and blueshifted (−5 to −45 km s$^{-1}$) $HCO^+$ emission, respectively. Contours correspond to 5 $\sigma_{\rm rms}$ emission and the velocity ranges are given relative to the source velocity (−3 km s$^{-1}$). Black arrows mark the cuts for the PV diagrams (Figs. 5 and 6) and the ticks mark distances of 50 arcsec along the arrows.

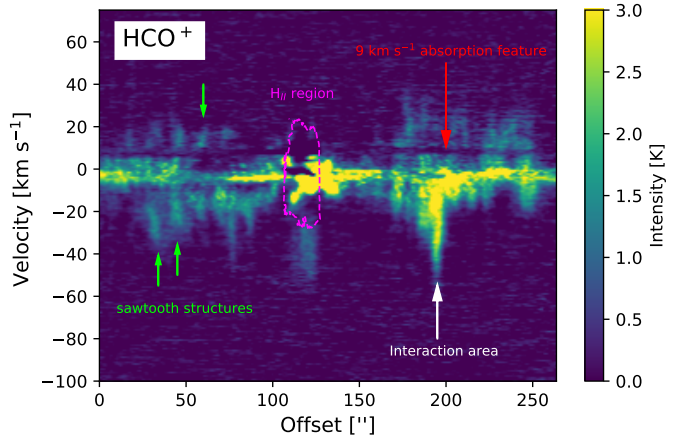


**Fig. 5.** Position–velocity diagram for $HCO^+$ emission along the DR21 Main outflow. The offset is measured from the edge of the eastern lobe towards the west. The arrow points to the 9 km s$^{-1}$ absorption feature (Dickel et al. 1978), the white arrow highlights the location of the interaction region (this work), the magenta dashed contour marks the H41$\alpha$ emission from the H II region, and the light green arrows mark examples of sawtooth pattern structures (Santiago-García et al. 2009).

associated with the ridge and not an additional outflow, extending in the N–S direction.

An important characteristic often used to describe outflows is their opening angle, a measure of how wide or collimated an outflow actually is. Here we calculated the opening angles for the DR21 Main outflow, separately for each lobe and for red- and blue-shifted emission, by examining the spectra of $HCO^+$ emission along a half-circle with radius approximately equal to half the extent of the corresponding outflow lobe (The exact location of these half-circles is shown in Fig. 3). The opening angle then corresponds to the angle between the location where the emission first becomes significant and the location where it drops further to noise level. The resulting opening angles for all different cases and for different velocities are plotted in Fig. 7 over the corresponding velocity. Interestingly, the opening angles for

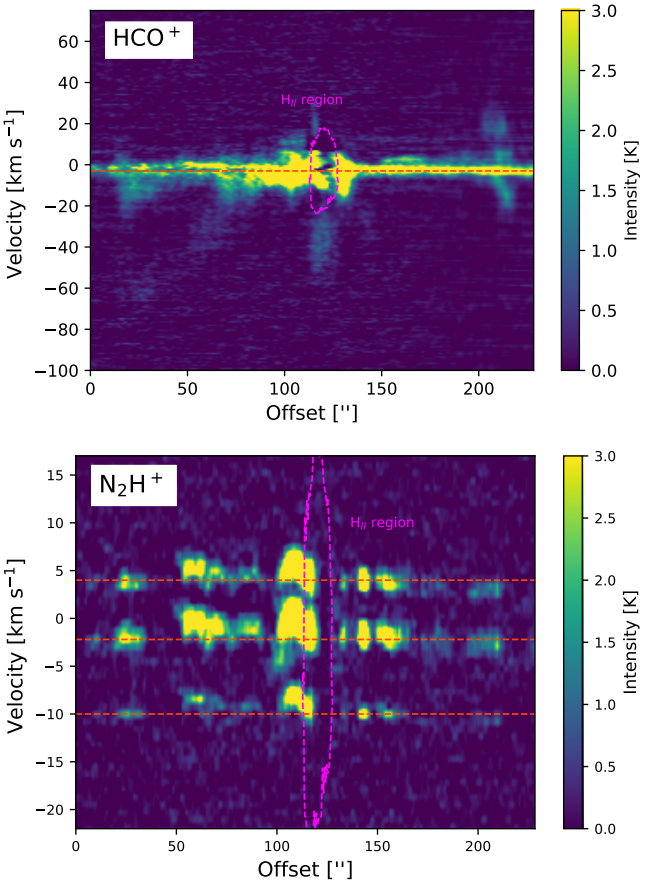


**Fig. 6.** Position–velocity diagrams for $HCO^+$ (top) and $N_2H^+$ (bottom) emission along the DR21 ridge. The offset is measured from south to north (see Fig. 4 for the exact location of the cut). The magenta dashed contour marks the H41$\alpha$ emission from the H II region while the orange dashed lines mark the source velocity (−3 km s$^{-1}$). For the $N_2H^+$ line, the velocities of the three resolved hyperfine structure components are marked at 4, −3, and −10 km s$^{-1}$, respectively.

all cases appear to be decreasing for higher velocities, a behavior that is expected in the case of a typical bipolar outflow powered by a narrow and well-collimated jet (e.g., Zhang et al. 2019; Rabenanahary et al. 2022).

### 3.3. Energetics of the outflow

The spatially- and velocity-resolved observations of the DR21 Main outflow allow us to calculate key outflow properties, such as the outflow force, $F$, the rate at which the outflow injects momentum into the surrounding ISM, the outflow mass, $M$, and its kinetic energy, $E_{\rm kin}$. For all calculations, we use the $HCO^+$ (1–0) emission, which is found to be a good tracer of the molecular outflow (Sect. 3.1).

To measure the force of the DR21 Main outflow, we use the so-called separation method introduced in van der Marel et al. (2013), where the outflow force is calculated as:

$$F_{\rm HCO^+} = c_3 \times \frac{K\left(\sum_j \left[\int_{v_{\rm in}}^{v_{{\rm out},j}} T(v')v'{\rm d}v'\right]_j\right)v_{\rm max}}{R_{\rm lobe}}. \quad (1)$$

Here, $c_3$ is a correction factor for a given inclination angle of the outflow (Table 3), $K$ is a conversion factor between the line-integrated intensity and the molecular gas mass, the integral

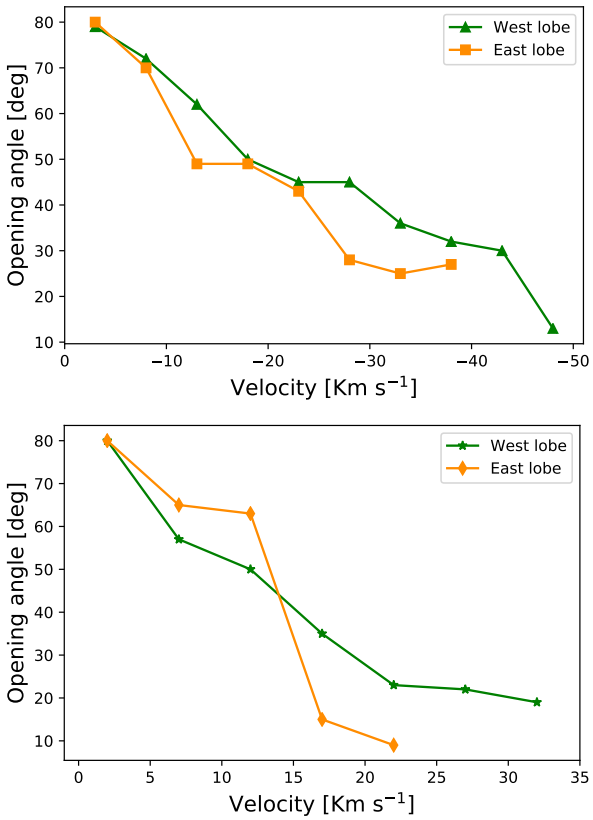


**Fig. 7.** Opening angle of the DR21 Main outflow as a function of velocity using $HCO^+$ 1–0 line profiles. The angles are calculated every 5 km s$^{-1}$ from the source velocity up to $v_{max}$ = 22, 32, −38, and −48 km s$^{-1}$ for the east-red, west-red, east-blue, and west-blue outflow lobes, respectively. *Top*: opening angles for blueshifted outflow velocities. *Bottom*: opening angles for redshifted outflow velocities.

**Table 3.** Inclination correction factors used in the different methods of outflow force calculation.

| $i^{(a)}$ (°) | 10 | 30 | 50 | 70 | Ref |
|---|---|---|---|---|---|
| $c_1$ | 0.28 | 0.45 | 0.45 | 1.1 | 1, 2 |
| $c_2$ | 1.6 | 3.6 | 6.3 | 14 | 1 |
| $c_3$ $^{(b)}$ | 0.6 | 1.3 | 2.4 | 3.8 | 3 |

**Notes.** $^{(a)}i$ is measured from the line of sight. $^{(b)}$Values are interpolated from Table 6 of Downes & Cabrit (2007), where $\alpha = 90 - i$.
**References.** (1) Cabrit & Bertout (1990); (2) Cabrit & Bertout (1992); (3) Downes & Cabrit (2007).

$\int_{v_{in}}^{v_{out,j}} T(v')v'\mathrm{d}v'$ corresponds to the velocity-weighted integrated intensity, $v_{max}$ is the maximum line-of-sight velocity in the outflow lobe, and $R_{lobe}$ is the length of the outflow lobe, while the sum runs over all pixels ($j$) that are part of the outflow. The conversion factor $K$ (see Appendix C of van der Marel et al. 2013) is given by:

$$K = \mu m_H A \frac{8\pi k_B \nu^2}{hc^3 A_{ul}} \left[\frac{H_2}{HCO^+}\right] \frac{Q(T_{exc})}{g_u} e^{E_u/T_{exc}}, \quad (2)$$

where $\mu$ is the mean molecular weight, $m_H$ is the hydrogen mass, $A$ is the observed area of the outflow, $[H_2/HCO^+]$ is the abundance ratio between $H_2$ and $HCO^+$, $Q(T_{exc})$ is the partition function at a specific excitation temperature $T_{exc}$, $g_u$ is the degeneracy of the upper level of the observed transition, $E_u$ is the upper-level energy in Kelvin, $\nu$ is the frequency of the observed transition in Hz, $c$ is the speed of light, $k_B$ is Boltzmann's constant, $h$ is Planck's constant, and $A_{ul}$ is the Einstein A coefficient for the transition in s$^{-1}$. We assume a single excitation temperature of 40 K (Garden et al. 1991b). The abundance ratio of $H_2$ over $HCO^+$ in high-mass star-forming regions has been found to range from $2 \times 10^9$ down to $3 \times 10^7$ (Godard et al. 2010; Gerner et al. 2014). In the present work, we adopt an abundance ratio of $H_2$ over $HCO^+$ of $1.6 \times 10^8$ (Garden & Carlstrom 1992), which is well within the above range and was estimated for DR21 Main. The corresponding value of the partition function and the remaining molecular data are taken from Splatalogue[2] using the CDMS catalog (Müller et al. 2001).

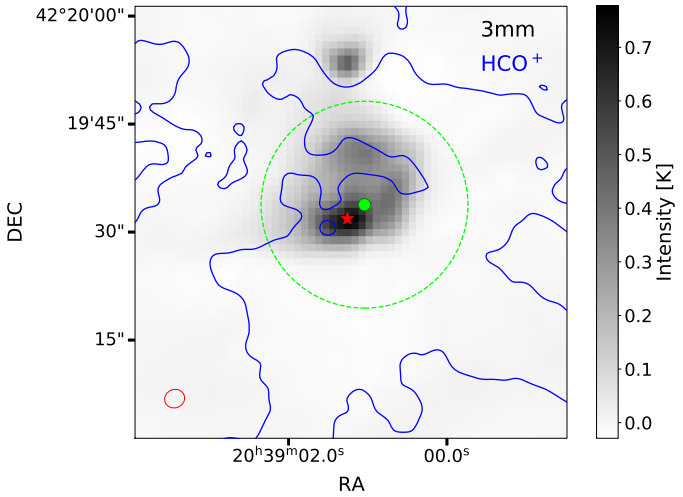


**Fig. 8.** Image showing the 3 mm continuum emission in the area of DR21 Main. The peak of the continuum emission is marked with a red star, while the green circle marks the location of the dense core DR21-1 (Cao et al. 2019), and the green dashed line the FWHM. Blue contours mark the integrated $HCO^+$ intensity (–50 to 50 km s$^{-1}$), while the beam of the continuum observations is shown with the red ellipse.

The inner velocities for the integration ($v_{in}$) are −5 and 5 km s$^{-1}$ relative to the source velocity for the blueshifted and redshifted parts of the emission, excluding the innermost 10 km s$^{-1}$ in order to avoid contamination from the cloud material.

The calculation of the length of the outflow lobe, $R_{lobe}$, requires information about the point of origin of the outflow. Here, we take this to be the position of the dense core DR21-1 from Cao et al. (2019; see also core N46 in Motte et al. 2007), which is located close to the center of the two outflow lobes and at the DR21 ridge. The location of the core also agrees well with the peak of the 3 mm continuum emission, as shown in Fig. 8. Higher-resolution observations of this area would be required to determine the exact location and nature of the driving source, which is outside of the scope of this paper.

The gas mass carried by the outflow is obtained as

$$M = K\left(\sum_j \left[\int_{v_{in}}^{v_{out,j}} T(v')\mathrm{d}v'\right]_j\right). \quad (3)$$

Subsequently, the time-averaged kinetic energy of the outflow is calculated as

$$E_{kin} = \frac{1}{2} M \langle v \rangle^2, \quad (4)$$

[2] https://splatalogue.online/advanced1.php

**Table 4.** Outflow parameters of the DR21 Main outflow.

| | $v_{max}$ (km s$^{-1}$) | $R_{lobe}$ (pc) | $t_{dyn}$ (yr) | $M$ ($M_\odot$) | $P$ ($M_\odot$ km s$^{-1}$) | $E_{kin}$ (erg) | $\dot{M}$ ($M_\odot$ yr$^{-1}$) | $F$ ($M_\odot$ km yr$^{-1}$ s$^{-1}$) | $L_{kin}$ (erg yr$^{-1}$) |
|---|---|---|---|---|---|---|---|---|---|
| East lobe: red | 38.6 | 0.74 | 4900 | 7 | 87 | $1.2 \times 10^{46}$ | 0.002 | 0.02 | $4.87 \times 10^{42}$ |
| blue | –62.2 | 0.75 | 3100 | 47 | 669 | $2.4 \times 10^{47}$ | 0.015 | 0.22 | $1.57 \times 10^{44}$ |
| West lobe: red | 52.2 | 0.88 | 4300 | 13 | 135 | $1.8 \times 10^{46}$ | 0.003 | 0.03 | $8.14 \times 10^{42}$ |
| blue | –70.2 | 0.98 | 3600 | 57 | 1037 | $2.3 \times 10^{47}$ | 0.016 | 0.29 | $1.26 \times 10^{44}$ |
| East+West: red | – | – | – | 20 | 222 | $3.0 \times 10^{46}$ | 0.005 | 0.05 | $1.30 \times 10^{43}$ |
| blue | – | – | – | 104 | 1706 | $4.7 \times 10^{47}$ | 0.031 | 0.51 | $2.83 \times 10^{44}$ |
| Entire outflow | – | – | – | 124 | 1928 | $5.0 \times 10^{47}$ | 0.036 | 0.56 | $2.96 \times 10^{44}$ |

and its momentum as

$$P = K\left(\sum_j \left[\int_{v_{in}}^{v_{out,j}} T(v')v'\,dv'\right]_j\right). \quad (5)$$

The dynamical time, which is an estimate of the lifetime of the outflow, is then taken as

$$t_{dyn} = \frac{R_{lobe}}{v_{max}}. \quad (6)$$

This, in turn, allows the calculation of the mass loss rate:

$$\dot{M} = \frac{M}{t_{dyn}}, \quad (7)$$

and the power of the outflow:

$$L_{kin} = \frac{E_{kin}}{t_{dyn}}. \quad (8)$$

The calculations are performed for the east and west outflow lobes, and for the redshifted and blueshifted emission, separately. The resulting outflow properties are presented in Table 4.

The outflow mass and kinetic energy can be compared with the results from Garden & Carlstrom (1992), where observations of the transition of $HCO^+$ (1–0) were analyzed. Here, we use the high-velocity component from Garden et al. (1991b) and scale it to the same distance as DR21, as adopted in this work. The outflow mass for the high-velocity component, of namely $\sim$120 $M_\odot$ (see Table 4), is a factor of 2–5 higher than the corresponding outflow mass in Garden & Carlstrom (1992). The outflow extent and the area covered by the observations are similar in both studies; Garden et al. (1991b) obtain an $R_{lobe}$ of $\sim$1.7 pc. Therefore, the difference is likely due to the velocity limits adopted in Garden & Carlstrom (1992), which exclude a significant part of gas mass at velocities close to the source velocity ($v_{in}$ from $-12.5$ to $-42.5$ km s$^{-1}$). Moreover, the outflow kinetic energy, which accounts for the relevant range of velocities, is fully consistent: $E_{kin}$ of $5.0\times10^{47}$ erg (Table 4) is within the range of $\sim$2.5–$5.0\times10^{47}$ erg reported in Garden & Carlstrom (1992) using $HCO^+$ and about a factor of 4 lower than the total energy measured using CO (Garden et al. 1991b). We provide a more thorough discussion of the DR21 Main outflow properties with respect to both low- and high-mass protostars in Sect. 4.2.

The calculation of the outflow parameters includes a few assumptions that need to be addressed. First, the conversion factor $K$ is accurate only when the observed emission is optically thin. In the case of DR21 Main, the $HCO^+$ emission is optically thin in the outflow lobes, but not in the central area (Garden & Carlstrom 1992). Using our $H^{13}CO^+$ observations, which appear to trace the dense ridge (Sect. 3), we estimate a $\tau$ of 12.5 for the DR21 Main center. To this end, the central region is excluded from the calculation of the outflow parameters. Similarly, gas with velocities within $\sim$5 km s$^{-1}$ of the velocity of the N–S filament is also excluded. We note that, even though a significant part of the outflow material is often found at low velocities, its impact on $F$ or $E_{kin}$ is not as significant due to the dependence of those parameters on $v^2$. Second, the correction factor of inclination angle, $c_3$, is available only for the inclination angles of 10°, 30°, 50°, and 70° (Table 3). In this work, $c_3$ of 3.8 is assumed (corresponding to 70°), but as the outflow of DR21 Main appears to be close to 90° (see Sect. 3.2), the correction is most likely underestimated by a factor of $\lesssim$2. Finally, we assume a uniform excitation temperature of the gas along the outflow, which likely differs by a factor of a few depending on the position of line emission. The increase in excitation temperature from 40 to 80 K would lead to an increase in the $K$ parameter by a factor of $\sim$1.9. The variations of $T_{ex}$ along the outflow are therefore not expected to significantly impact the results.

In summary, the parameters of the DR21 Main outflow calculated using $HCO^+$ provide a useful diagnostic of outflow energetics. The calculations are consistent with previous work by Garden & Carlstrom (1992), who used the same tracer and transition. Due to the optical thickness of the emission and the adopted velocity limits, the mass of the outflow as well as the related parameters are lower limits to the actual parameters.

## 4. Discussion

### 4.1. The nature of the DR21 Main outflow

The nature of the DR21 Main outflow is still a topic of discussion because it has been proposed to belong to the class of explosive outflows (Zapata et al. 2013). Detailed analysis of the morphology and the kinematics of the outflow using $HCO^+$ observations reveals a rather well-defined bipolar outflow structure reminiscent of that of a typical protostellar outflow (Sect. 3.2). The strong overlap of redshifted and blueshifted $HCO^+$ emission is indeed a property attributed to explosive outflows (Zapata et al. 2017); however, this can also appear in the case of a bipolar outflow that extends along the plane of the sky with the redshifted and blueshifted emission arising from the sideways expansion of the outflow lobes. Additionally, the apparent decrease in the opening angle of the DR21 Main outflow with increasing velocity (see Fig. 7) is characteristic of bipolar outflows that are

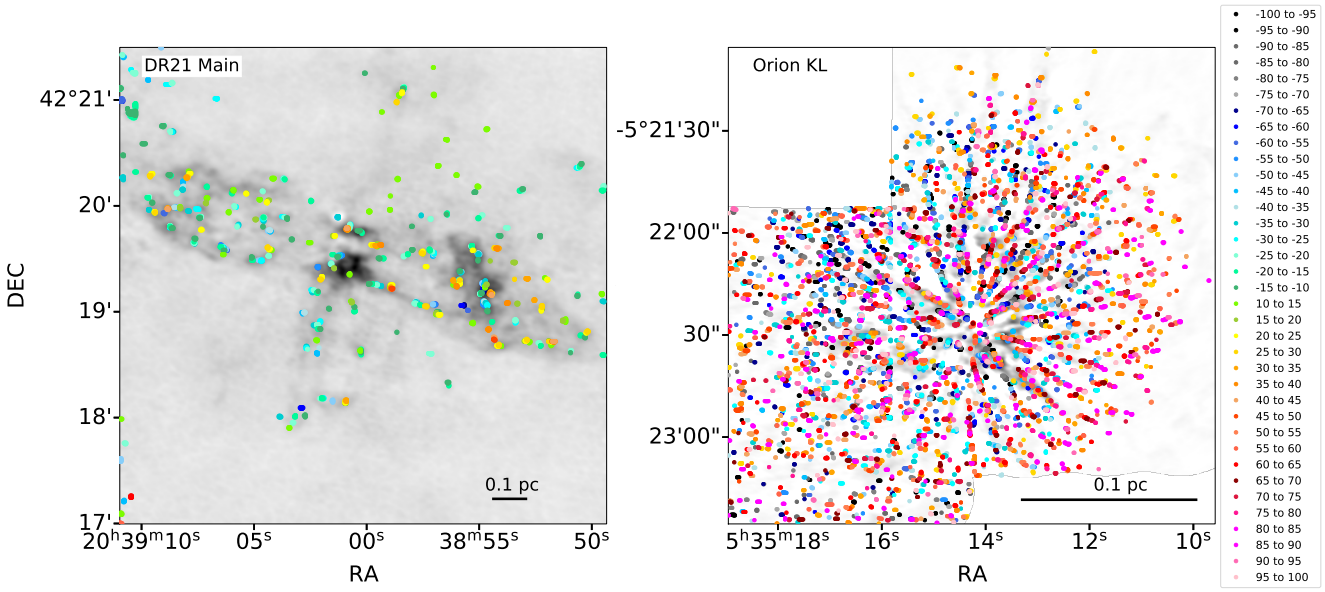


**Fig. 9.** Distribution of gas velocities associated with the outflows in DR21 (left) and Orion KL (right, Bally et al. 2017). Each point shows a local intensity peak of the $HCO^+$ emission (above 2 $\sigma$) integrated in velocity steps of 5 km s$^{-1}$. The color of the points signifies the corresponding velocity steps and is the same for the two plots. Background grayscale shows the integrated $HCO^+$ (left panel) and CO emission (right panel) over the entire velocity range of the outflows (from −70 to 70 km s$^{-1}$ for DR21 Main and −100 to 100 km s$^{-1}$ for Orion KL).

powered by a narrow collimated jet; nevertheless, this scenario seems unlikely in the case of explosive outflows.

Figure 9 shows a side-by-side comparison of local intensity peaks at multiple velocity steps between the DR21 Main outflow and the Orion KL outflow. Here, we used the $HCO^+$ data presented in this work for the DR21 Main outflow, and archival ALMA CO (2–1) data for Orion (Project ID: 2013.1.00546.S, PI: John Bally, Bally et al. (2017)). The emission in Orion (right) can be seen to consist of multiple, well-defined filament-like structures, which also display clear velocity gradients along their length with higher absolute velocities being further away from the point of origin of the outflow. This behavior is probably the most distinctive characteristic of explosive outflows and is absent in the case of the DR21 Main outflow (left). More precisely, in DR21 Main, there are very few distinct filament-like structures, and those present do not show any significant velocity gradients along their length. Moreover, the structures that do exist appear to be tracing the cavity walls of the outflow lobes, contrary to the more random distribution that the filament-like structures have in Orion. However, we note that DR21, at 1.5 kpc (Rygl et al. 2012), is located significantly further away than Orion KL, which lies at ∼400pc (Menten et al. 2007; Kounkel et al. 2017), which means that the physical scales of the two outflows in Fig. 9 are significantly different.

Taking all of the above into consideration, it appears that the outflow of DR21 Main more closely resembles a typical bipolar outflow driven by a protostar rather than an explosive outflow. However, the observations presented here do not reveal a single compact emission that could be associated with the driving source (Appendix A). Further observations are required in order to discern the protostar or protostellar system behind such an exceptionally powerful bipolar outflow.

### 4.2. Outflow energetics

Multiple correlations have been reported connecting the energetics of protostellar outflows with the properties of their driving sources. For example, the correlations of the outflow force with the envelope mass and bolometric luminosity are attributed to a connection between mass-accretion rate and outflow activity (Beuther et al. 2002; Duarte-Cabral et al. 2013; Mottram et al. 2017). The existence of such correlations allows a direct comparison of the properties of the DR21 Main outflow with those of other protostellar and explosive outflows.

Figure 10 shows the comparison of the outflow force of the DR21 Main outflow and those of low-, intermediate-, and high-mass protostars (Beuther et al. 2002; van Kempen et al. 2009; van der Marel et al. 2013; Yıldız et al. 2015; Maud et al. 2015; Mottram et al. 2017; Li et al. 2020; Skretas & Kristensen 2022). We calculate the Pearson coefficients and the corresponding significance ($\sigma$) for both correlations (see e.g., Marseille et al. 2010). The outflow forces of high-mass protostars are found to correlate strongly both with their envelope masses (6.1$\sigma$) and bolometric luminosities (6.5$\sigma$); the correlation extends also to lower masses. The source sample from Li et al. 2020 represents sources at very early stages of their evolution (70 µm dark clumps), and these are therefore expected to have a low $L_{\rm bol}/M_{\rm env}$ ratio, which would explain their relatively large envelope masses with respect to other sources of similar energetic parameters.

The outflow force of DR21 is higher than those of other high-mass protostars, including the other two explosive-outflow candidates: G5.89-0.39 ($L_{\rm bol}$ of 4.1× 10$^4$ $L_\odot$, $M_{\rm env}$ of 140 $M_\odot$, van der Tak et al. 2013; Karska et al. 2014) and Orion BN/KL ($L_{\rm bol}$ of 5× 10$^4$ $L_\odot$, $M_{\rm env}$ of 150 $M_\odot$, Downes et al. 1981; Genzel & Stutzki 1989). For DR21, we adopt $L_{\rm bol}$ of 1.0× 10$^4$ $L_\odot$ and $M_{\rm env}$ of 1355 $M_\odot$, which account for the new distance to the source and the peak of the spectral energy distribution (Cao et al. 2019).

DR21 also shows enhanced mass-outflow rate and outflow kinetic luminosity, but falls within the range of other high-mass protostars in terms of outflow mass, power, and kinetic energy (Appendix C). Those differences are therefore the largest for parameters involving the outflow dynamical time, and as such are related with $v_{\rm max}$, which in turn depends on the inclination angle. However, the inclination of DR21 on the sky could only introduce a factor of approximately four difference in the derived

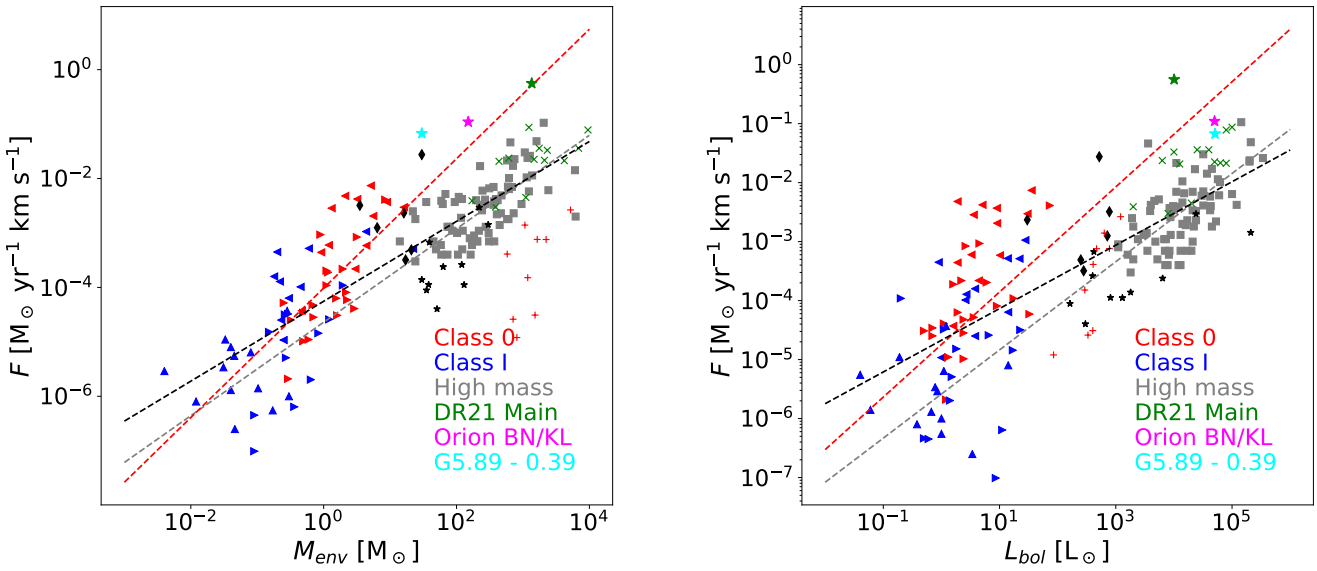


**Fig. 10.** Outflow force vs. envelope mass of the driving source for various protostellar sources. Right-facing triangles represent low-mass sources from Mottram et al. (2017), left-facing triangles mark sources taken from Yıldız et al. (2015), and upward-pointing triangles are from van der Marel et al. (2013); Class I sources are marked in blue, and Class 0 in red. Black diamonds mark intermediate-mass sources (van Kempen et al. 2009), gray squares mark high-mass sources from Maud et al. (2015), green "×" symbols mark high-mass sources from Beuther et al. (2002), and black stars mark high-mass sources in Cygnus (Skretas & Kristensen 2022). The red crosses mark a sample of high-mass 70μm dark sources (Li et al. 2020). The cyan star marks G5.89-0.39, the magenta one marks Orion KL, and the green one represents the DR21 Main outflow. The dashed black line shows the best fit to the outflow force–envelope mass correlation for all sources, while red and gray show the best fits for the low- and high-mass sources, respectively.

parameters, which is much less than the enhancement in outflow properties with respect to typical high-mass protostars.

Orion BN/KL and G5.89-0.39 also show relatively high mass-outflow rates, kinetic energies, and luminosities, which might suggest these could be common characteristics of explosive-outflow candidates. Assuming that the underlying physical mechanism for explosive outflows is different from that for typical outflows, there is presently no theoretical expectation that explosive outflows should follow the $F$–$M_{\rm env}$ and $F$–$L_{\rm bol}$ correlations (Fig. 10). However, the sample of these objects is too small for conclusions to be drawn.

The DR21 Main outflow is found to be a bipolar outflow (Sect. 4.1). Therefore, the enhanced outflow force of DR21 might indicate the presence of scatter for the high-mass sources similar to that measured in the outflow properties of low-mass YSOs (Fig. 10). In any case, the high outflow force of the DR21 Main outflow is consistent with it being one of the most powerful outflows in the Galaxy.

### 4.3. Interaction at the western outflow lobe

Outflow activity from protostars can impact the structure and chemistry of their parental and/or nearby dense cores (e.g., van Kempen et al. 2009; Lis et al. 2016; Kahle et al. 2023). The energetic outflow from DR21 Main heavily interacts with its surroundings, and creates an "interaction region" in the western outflow lobe, which has been associated with a collisionally excited Class I methanol maser (Plambeck & Menten 1990). Molecular line emission from CASCADE allows us to pin-point the detailed characteristics of the outflow-cloud interaction.

The interaction region shows various patterns of molecular line emission with HCN and $H_2CO$ peaking in its eastern part, and HNC and $N_2H^+$ emission extending to the western and outer parts of the outflow lobe (Fig. 11). The SiO emission shows a compact pattern associated most closely with $H_2CO$, suggesting the presence of shocks in the interface between for example HCN and $N_2H^+$ gas.

We investigate the line emission across the interaction regions in Figs. 12–17. $HCO^+$ emission peaks in the interaction region, and is followed by $H_2CO$ tracing warm gas and $N_2H^+$, which is sensitive to the sharp increase in cold gas density (Fig. 12). In the case of $HCO^+$, it is likely that some outflowing material is deflected into the line of sight, giving rise to the strong, high velocity, blue-shifted emission detected in this area (Fig. 3). This velocity shift is also clearly seen in the first moment of $HCO^+$, which shows that its emission in the area of the dense structure is mainly redshifted (Fig. 13). A likely explanation could be that the dense structure is located closer to the observer along the line of sight and is therefore interacting mostly with the blueshifted part of the outflow. The blueshifted emission indeed shows a high-velocity component elongated almost vertical to the outflow axis, while the redshifted emission appears almost unperturbed (Fig. 3).

The $H_2CO$ emission displays a sharp increase in the interaction area followed by a significant decrease deeper into the dense structure (also shown in Fig. 12). Such an increase is likely related to the enhanced gas temperatures in the interaction region, which lead to sputtering of $H_2CO$ from the dust grains (Benedettini et al. 2013). Alternatively, the $H_2CO$ emission could be explained by shock chemistry (e.g., Viti et al. 2011), but the commonly predicted double-peaked structure is not resolved in our observations. On the other hand, it is also possible that averaging along the interaction front leads to the blending of line emission, making this feature less apparent. A close association of $H_2CO$ with the SiO emission tracing shocks (Fig. 14) favors the scenario in which $H_2CO$ traces not only warm gas but also the location of active shocks, as was suggested by Li et al. (2022). The multiple peaks of SiO and $H_2CO$ likely arise

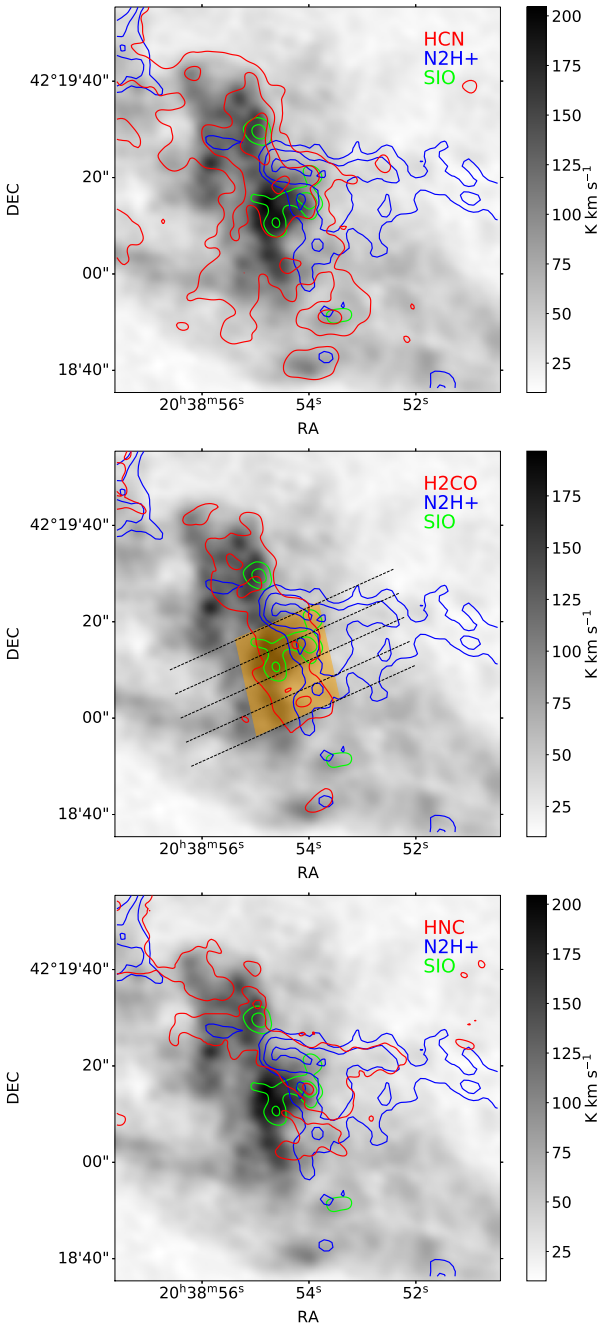


**Fig. 11.** Outflow–cloud interaction region in the western lobe of the DR21 Main outflow. The grayscale shows the integrated $HCO^+$ emission between −50 and 50 km s$^{-1}$ relative to the source velocity. Red contours show line emission of HCN (top), $H_2CO$ (middle), and HNC (bottom). Blue contours show the emission of $N_2H^+$ and green contours show the emission of SiO, in all panels. Contour levels are at 5, 10, and 20 $\sigma_{rms}$. The dashed black lines in the middle plot mark the lines used to calculate the average intensities and first moments across the interaction front presented in Figs. 12–17. The orange rectangle marks the area actively affected by the interaction as derived from these intensities.

because of averaging across the entire interaction front and the clumpy nature of SiO emission (see Fig. 11).

HCN and HNC show some differences along the interaction region (Fig. 15), which might reflect the changes in gas temperature (Hacar et al. 2020). The pattern of emission in HNC is similar to that of $N_2H^+$, whereas HCN closely follows $H_2CO$.

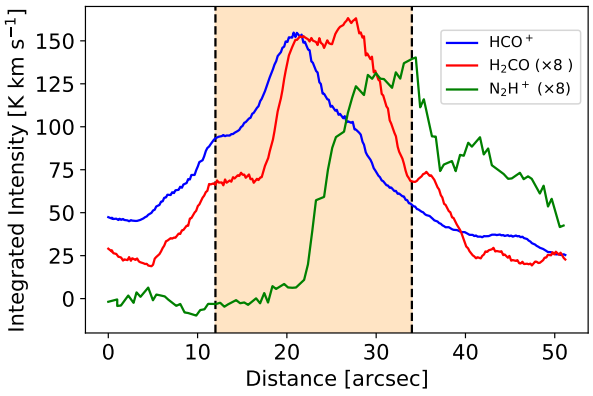


**Fig. 12.** Average integrated intensities of $HCO^+$ (in blue), $H_2CO$ (in red), and $N_2H^+$ (in green) across the interaction region in the western lobe of DR21. Intensities are integrated from −70 to 70, from −20 to 20, and from −20 to 10 km s$^{-1}$ for $HCO^+$, $H_2CO$, and $N_2H^+$, respectively. The $x$-axis shows the distance in arcseconds covering the extent of the relevant region where the outflow interacts with a dense structure (marked also in Fig. 11). The orange rectangle shows the area actively affected by the interaction. The intensities for $H_2CO$ and $N_2H^+$ are scaled up by a factor of 8 in order for their distributions to be more easily comparable.

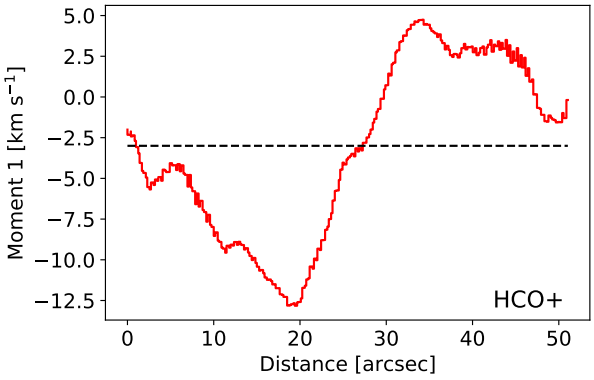


**Fig. 13.** First moment of $HCO^+$ emission across the interaction front (see Fig. 12). The black dashed line marks the DR21 cloud velocity of $v_{cloud} = -3$ km s$^{-1}$.

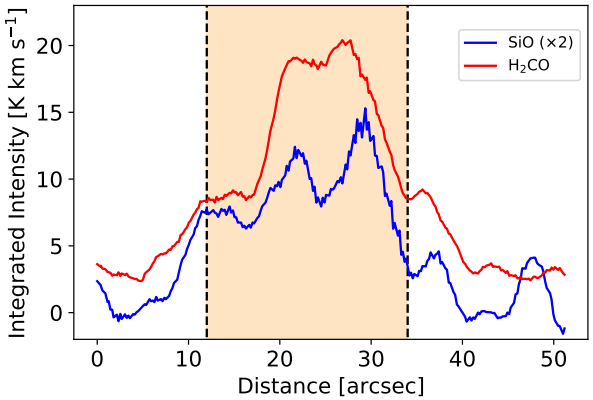


**Fig. 14.** Average integrated intensities of SiO (in blue) and $H_2CO$ (in red) across the interaction region in the western lobe of DR21. Intensities are integrated from −25 to 25 and from −20 to 20 km s$^{-1}$ for SiO and $H_2CO$, respectively. The SiO emission is scaled up by a factor of 2 for clarity.

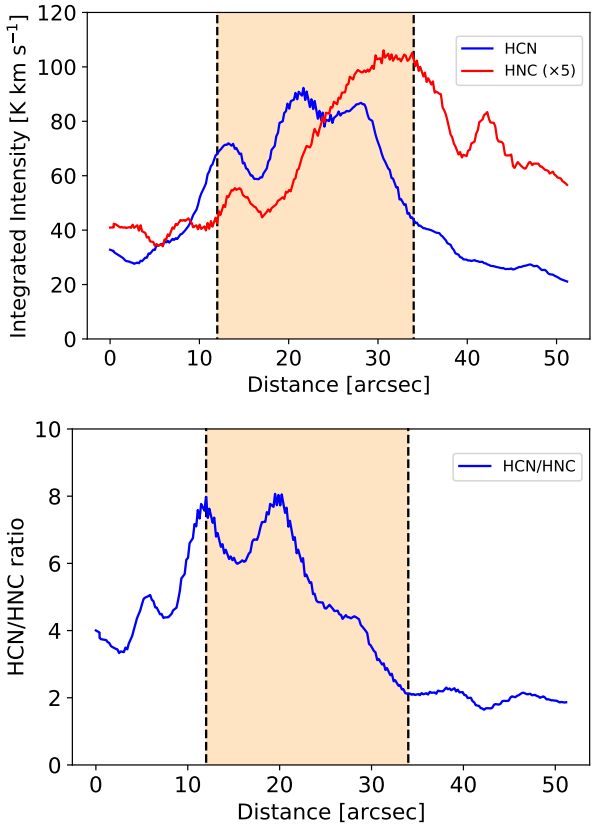


**Fig. 15.** HCN and HNC emission in the interaction region. *Top*: average integrated intensities of HCN (in blue) and HNC (in red) across the interaction region in the western lobe of DR21. Intensities are integrated from −35 to 35 and from −15 to 10 km s$^{-1}$ for HCN and HNC, respectively. The HNC emission is scaled up by a factor of 5 for clarity. *Bottom*: ratio of HCN over HNC across the interaction region.

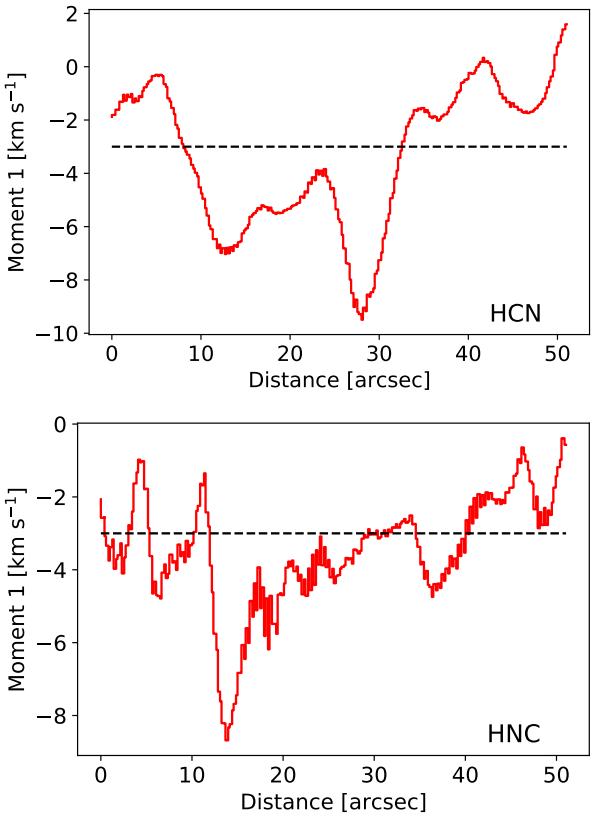


**Fig. 16.** First moment across the interaction front of the DR21 Main outflow and the dense structure located near the western outflow lobe plotted over the corresponding distance. The distance is measured from the outflow-dominated part and extends into the dense structure. The black dashed line marks the DR21 cloud velocity of $v_{\rm cloud} = -3$ km s$^{-1}$. *Top*: For HCN emission *Bottom:* for HNC emission.

We refrain from using the Hacar et al. (2020) relation to calculate gas temperatures, because the HCN over HNC line ratios partly exceed the range where the experimental relation holds. Nevertheless, the ratio of the two species suggests that the temperature increases rapidly at the front of the interaction area and then drops steadily to a relatively low value. The ratio shows two peaks that follow the peaks in HCN intensity (Fig. 15), and are found close to but not exactly at the same location as the peaks of SiO. This suggests that HCN might also be enhanced in the warm gas behind the shock front (see e.g., Mirocha et al. 2021). In addition, the velocities of the gas traced by HCN and HNC also differ (Fig. 16). HNC has velocities close to that of the cloud, especially from the middle of the interaction area and into the dense structure, where its emission becomes significant. HCN on the other hand follows $HCO^+$ and shows significant blueshifted emission, which becomes redshifted in the area dominated by the dense structure. The blueshifted peak appears deeper in the interaction area compared to that of $HCO^+$, showing that they trace different material.

HCCCN emission is detected in the area of the dense structure, as expected based on previous studies (e.g., Morris et al. 1976; Churchwell et al. 1978). The slight enhancement of HCCCN abundance in the interaction region (Fig. 17) supports the findings of Benedettini et al. (2013) that HCCCN is formed in shocks.

The intensity of CCH shows a significant increase close to the center of the interaction region, which is likely due to UV radiation originating from the shocked material in the interaction region (e.g., Gratier et al. 2017; Bouvier et al. 2020; Chahine et al. 2022).

In contrast, HNCO is not detected in the interaction region, even though it is often associated with shocks. According to Yu et al. (2018), HNCO is preferentially enhanced in slow-moving shocks, but is destroyed in high-velocity shocks, which might indeed be the case for the energetic outflow from DR21.

Finally, we note here that, because of the irregular shape of the interaction front, the simplistic average along it adopted for the above analysis suffers from significant uncertainties. Still, it can offer an interesting qualitative look into the behavior of species across such an interaction.

## 5. Summary and conclusions

This work presents the results of CASCADE observations in the area of the DR21 Main outflow covering several molecular tracers, including $HCO^+$, HCN, HNC, $N_2H^+$, $H_2CO$, and CCH at high spatial (∼3″) and spectral resolution (∼0.8 km s$^{-1}$). These molecular tracers are split into three separate categories according to their morphology, tracing the outflow ($HCO^+$ and HCN), the DR21 ridge ($^{13}CS$, CCH, $H_2CO$, $H^{13}CO^+$, HCCCN (10–9), HCCCN (8–7), HNC, $N_2H^+$), and localized emission (e.g., $CH_3CN$ ($4_k$–$3_k$), $CH_3CN$ ($5_k$–$4_k$), $CH_3OH$, DCN, $DCO^+$, DNC, H$\alpha$41, $NH_2D$, SiO).

Based on the $HCO^+$ emission, the DR21 Main outflow is found to mostly resemble a typical bipolar outflow rather than an explosive one, as its emission shows two well-structured lobes

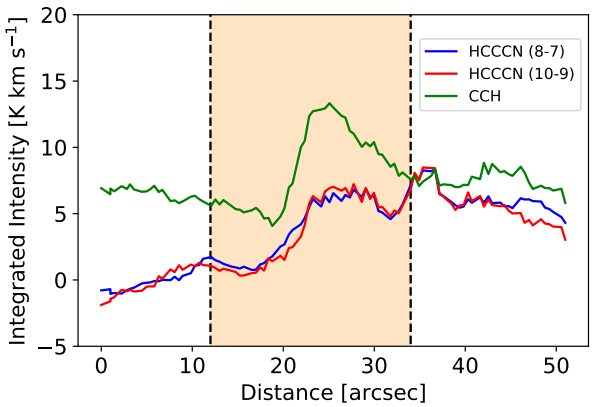


**Fig. 17.** Average integrated intensities of HCCCN $J$ = 8–7 (in blue), HCCCN $J$ = 10–9 (in red), and CCH (in green) across the interaction region in the western lobe of DR21. Intensities are integrated from –10 to 5 km s$^{-1}$ for all three lines.

that get progressively more collimated at higher velocities and lack the filament-like structures that are prevalent in established explosive outflows.

Adapting the separation method, and applying it to $HCO^+$ emission allowed us to estimate the energetic parameters (outflow force $F$ = 0.56 $M_\odot$ km yr$^{-1}$ s$^{-1}$, mass $M$ = 124 $M_\odot$, and kinetic energy $E_{\rm kin}$ = 5 $\times 10^{47}$ erg) of the outflow. Comparison with other protostellar sources showed that the outflow force of the DR21 Main outflow is about an order of magnitude higher than that of outflows originating from sources of similar envelope mass. However, it remains uncertain as to whether the outflow of DR21 Main represents an upper limit of typical protostellar outflows or is powered by a different mechanism.

Finally, a dense molecular structure was detected near the western lobe of the outflow. The detection of SiO and $H_2CO$ emission in this area shows that there is ongoing interaction between the outflow and this dense structure. We used this information to perform an analysis of the behavior of different molecular species across such an interaction and found them to be in good agreement with the results of recent modeling predictions and observations of shocked regions.

Overall, the results presented in this paper firmly establish the outflow of DR21 Main as one of the most interesting cases of bipolar, protostellar outflow, given its exceptional size and power. Additionally, the CASCADE observations offer valuable information as to the chemistry of the interaction region, but further and more detailed modeling is required in order to properly constrain the chemistry that takes place in this location.

*Acknowledgements.* The authors would like to thank the anonymous referee for his suggestions and constructive comments that improved the overall quality of the manuscript. The authors are also grateful to the staff at the NOEMA and Pico Veleta observatories for their support of these observations. We thank in particular P. Chaudet, operator at the NOEMA observatory, for his motivation and dedication in developing and testing the advanced mosaic observing procedures employed in this project. This work is based on observations carried out under project number L19MA with the IRAM NOEMA Interferometer and [145-19] with the 30 m telescope. IRAM is supported by INSU/CNRS (France), MPG (Germany) and IGN (Spain). A.K. acknowledges support from the Polish National Agency for Academic Exchange grant No. BPN/BEK/2021/1/00319/DEC/1. H.B. acknowledges support from the European Research Council under the Horizon 2020 Framework Program via the ERC Consolidator Grant CSF-648505 and from the Deutsche Forschungsgemeinschaft in the Collaborative Research Center (SFB 881) "The Milky Way System" (subproject B1). A.G. acknowledges support from NSF AAG 2008101 and NSF CAREER 2142300. D.S. acknowledges support from the European Research Council under the Horizon 2020 Framework Program via the ERC Advanced Grant No. 832428-Origins.

## References

Arce, H. G., & Sargent, A. I. 2004, ApJ, 612, 342
Arce, H. G., & Sargent, A. I. 2005, ApJ, 624, 232
Arce, H. G., & Sargent, A. I. 2006, ApJ, 646, 1070
Arce, H. G., Shepherd, D., Gueth, F., et al. 2007, in Protostars and Planets V, eds. B. Reipurth, D. Jewitt, & K. Keil, 245
Bachiller, R., & Tafalla, M. 1999, in NATO Advanced Study Institute (ASI) Series C, 540, The Origin of Stars and Planetary Systems, eds. C. J. Lada & N. D. Kylafis, 227
Bally, J. 2016, ARA&A, 54, 491
Bally, J., & Lada, C. J. 1983, ApJ, 265, 824
Bally, J., & Zinnecker, H. 2005, AJ, 129, 2281
Bally, J., Ginsburg, A., Arce, H., et al. 2017, ApJ, 837, 60
Benedettini, M., Molinari, S., Testi, L., & Noriega-Crespo, A. 2004, MNRAS, 347, 295
Benedettini, M., Viti, S., Codella, C., et al. 2013, MNRAS, 436, 179
Beuther, H., & Shepherd, D. 2005a, in Astrophysics and Space Science Library, 324, eds. M. S. N. Kumar, M. Tafalla, & P. Caselli, 105
Beuther, H., & Shepherd, D. 2005b, in Astrophysics and Space Science Library, 324, eds. M. S. N. Kumar, M. Tafalla, & P. Caselli, 105
Beuther, H., Schilke, P., Sridharan, T. K., et al. 2002, A&A, 383, 892
Beuther, H., Wyrowski, F., Menten, K. M., et al. 2022, A&A, 665, A63
Blandford, R. D., & Payne, D. G. 1982, MNRAS, 199, 883
Bontemps, S., Andre, P., Terebey, S., & Cabrit, S. 1996, A&A, 311, 858
Bouvier, M., López-Sepulcre, A., Ceccarelli, C., et al. 2020, A&A, 636, A19
Burkhardt, A. M., Shingledecker, C. N., Le Gal, R., et al. 2019, ApJ, 881, 32
Cabrit, S., & Bertout, C. 1990, ApJ, 348, 530
Cabrit, S., & Bertout, C. 1992, A&A, 261, 274
Cao, Y., Qiu, K., Zhang, Q., et al. 2019, ApJS, 241, 1
Caselli, P., Benson, P. J., Myers, P. C., & Tafalla, M. 2002, ApJ, 572, 238
Chahine, L., López-Sepulcre, A., Podio, L., et al. 2022, A&A, 667, A6
Churchwell, E., Winnewisser, G., & Walmsley, C. M. 1978, A&A, 67, 139
Cruz-González, I., Salas, L., & Hiriart, D. 2007, Rev. Mexicana Astron. Astrofis., 43, 337
Davis, C. J., Kumar, M. S. N., Sandell, G., et al. 2007, MNRAS, 374, 29
Dickel, J. R., Dickel, H. R., & Wilson, W. J. 1978, ApJ, 223, 840
Downes, T. P., & Cabrit, S. 2007, A&A, 471, 873
Downes, D., Genzel, R., Becklin, E. E., & Wynn-Williams, C. G. 1981, ApJ, 244, 869
Duarte-Cabral, A., Bontemps, S., Motte, F., et al. 2013, A&A, 558, A125
Flower, D. R., & Pineau Des Forêts, G. 2010, MNRAS, 406, 1745
Frank, A., Ray, T. P., Cabrit, S., et al. 2014, in Protostars and Planets VI, eds. H. Beuther, R. S. Klessen, C. P. Dullemond, & T. Henning, 451
Fuente, A., Martin-Pintado, J., Bachiller, R., Neri, R., & Palla, F. 1998, A&A, 334, 253
Garden, R. P., & Carlstrom, J. E. 1992, ApJ, 392, 602
Garden, R., Geballe, T. R., Gatley, I., & Nadeau, D. 1986, MNRAS, 220, 203
Garden, R. P., Geballe, T. R., Gatley, I., & Nadeau, D. 1991a, ApJ, 366, 474
Garden, R. P., Hayashi, M., Gatley, I., Hasegawa, T., & Kaifu, N. 1991b, ApJ, 374, 540
Genzel, R., & Stutzki, J. 1989, ARA&A, 27, 41
Gerner, T., Beuther, H., Semenov, D., et al. 2014, A&A, 563, A97
Godard, B., Falgarone, E., Gerin, M., Hily-Blant, P., & de Luca, M. 2010, A&A, 520, A20
Gratier, P., Bron, E., Gerin, M., et al. 2017, A&A, 599, A100
Gueth, F., & Guilloteau, S. 1999, A&A, 343, 571
Gueth, F., Guilloteau, S., Dutrey, A., & Bachiller, R. 1997, A&A, 323, 943
Gusdorf, A., Cabrit, S., Flower, D. R., & Pineau Des Forêts, G. 2008, A&A, 482, 809
Guzmán Ccolque, E., Fernández-López, M., Zapata, L. A., & Baug, T. 2022, ApJ, 937, 51
Hacar, A., Bosman, A. D., & van Dishoeck, E. F. 2020, A&A, 635, A4
Hsieh, C.-H., Arce, H. G., Li, Z.-Y., et al. 2023, ApJ, 947, 25
Jørgensen, J. K., Schöier, F. L., & van Dishoeck, E. F. 2004, A&A, 416, 603
Kahle, K. A., Hernández-Gómez, A., Wyrowski, F., & Menten, K. M. 2023, A&A, 673, A143
Karska, A., Herpin, F., Bruderer, S., et al. 2014, A&A, 562, A45
Kaufman, M. J., & Neufeld, D. A. 1996, ApJ, 456, 611
Kounkel, M., Hartmann, L., Loinard, L., et al. 2017, ApJ, 834, 142
Leung, H. O., & Thaddeus, P. 1992, ApJS, 81, 267
Li, S., Sanhueza, P., Zhang, Q., et al. 2020, ApJ, 903, 119
Li, S., Sanhueza, P., Lu, X., et al. 2022, ApJ, 939, 102
Lis, D. C., Wootten, H. A., Gerin, M., et al. 2016, ApJ, 827, 133
Lovas, F. J. 2004, J. Phys. Chem. Ref. Data, 33, 177
Machida, M. N. 2014, ApJ, 796, L17
Marseille, M. G., van der Tak, F. F. S., Herpin, F., & Jacq, T. 2010, A&A, 522, A40

Martin-Pintado, J., Bachiller, R., & Fuente, A. 1992, A&A, 254, 315
Maud, L. T., Moore, T. J. T., Lumsden, S. L., et al. 2015, MNRAS, 453, 645
Menten, K. M., Reid, M. J., Forbrich, J., & Brunthaler, A. 2007, A&A, 474, 515
Mirocha, A., Karska, A., Gronowski, M., et al. 2021, A&A, 656, A146
Morris, M., Turner, B. E., Palmer, P., & Zuckerman, B. 1976, ApJ, 205, 82
Motte, F., Bontemps, S., Schilke, P., et al. 2007, A&A, 476, 1243
Mottram, J. C., van Dishoeck, E. F., Kristensen, L. E., et al. 2017, A&A, 600, A99
Müller, H. S. P., Thorwirth, S., Roth, D. A., & Winnewisser, G. 2001, A&A, 370, L49
Myers, P. C., Heyer, M., Snell, R. L., & Goldsmith, P. F. 1988, ApJ, 324, 907
Nony, T., Motte, F., Louvet, F., et al. 2020, A&A, 636, A38
Nyman, L. A. 1983, A&A, 120, 307
Offner, S. S. R., Lee, E. J., Goodman, A. A., & Arce, H. 2011, ApJ, 743, 91
Plambeck, R. L., & Menten, K. M. 1990, ApJ, 364, 555
Rabenanahary, M., Cabrit, S., Meliani, Z., & Pineau des Forêts, G. 2022, A&A, 664, A118
Rivera-Ortiz, P. R., Rodríguez-González, A., Cantó, J., & Zapata, L. A. 2021, ApJ, 916, 56
Rygl, K. L. J., Brunthaler, A., Sanna, A., et al. 2012, A&A, 539, A79
Santiago-García, J., Tafalla, M., Johnstone, D., & Bachiller, R. 2009, A&A, 495, 169
Schilke, P., Walmsley, C. M., Pineau des Forets, G., & Flower, D. R. 1997, A&A, 321, 293
Schilke, P., Pineau des Forêts, G., Walmsley, C. M., & Martín-Pintado, J. 2001, A&A, 372, 291
Schneider, N., Csengeri, T., Bontemps, S., et al. 2010, A&A, 520, A49
Skretas, I. M., & Kristensen, L. E. 2022, A&A, 660, A39
van der Marel, N., Kristensen, L. E., Visser, R., et al. 2013, A&A, 556, A76
van der Tak, F. F. S., Chavarría, L., Herpin, F., et al. 2013, A&A, 554, A83
van Kempen, T. A., van Dishoeck, E. F., Güsten, R., et al. 2009, A&A, 507, 1425
Velusamy, T., & Langer, W. D. 1998, Nature, 392, 685
Viti, S., Jimenez-Serra, I., Yates, J. A., et al. 2011, ApJ, 740, L3
Walmsley, C. M., Pineau des Forêts, G., & Flower, D. R. 1999, A&A, 342, 542
Warren, S. J., Cross, N. J. G., Dye, S., et al. 2007, arXiv e-prints, Astro [arXiv:astro-ph/0703037]
Wilson, T. L., & Mauersberger, R. 1990, A&A, 239, 305
Wu, Y., Wei, Y., Zhao, M., et al. 2004, A&A, 426, 503
Yıldız, U. A., Kristensen, L. E., van Dishoeck, E. F., et al. 2015, A&A, 576, A109
Yu, N.-P., Xu, J.-L., & Wang, J.-J. 2018, Res. Astron. Astrophys., 18, 015
Zapata, L. A., Schmid-Burgk, J., Ho, P. T. P., Rodríguez, L. F., & Menten, K. M. 2009, ApJ, 704, L45
Zapata, L. A., Schmid-Burgk, J., Pérez-Goytia, N., et al. 2013, ApJ, 765, L29
Zapata, L. A., Schmid-Burgk, J., Rodríguez, L. F., Palau, A., & Loinard, L. 2017, ApJ, 836, 133
Zapata, L. A., Ho, P. T. P., Guzmán Ccolque, E., et al. 2019, MNRAS, 486, L15
Zhang, Q., Hunter, T. R., Brand, J., et al. 2005, ApJ, 625, 864
Zhang, Y., Arce, H. G., Mardones, D., et al. 2019, ApJ, 883, 1

## Appendix A: Integrated intensity contour maps

Figures A.1–A.6 show contour maps of the integrated intensity of all observed molecules in the area of the DR21 Main outflow. The detected molecules can broadly be separated in three categories (see Section 3.1, Table 2): (i) those tracing the outflow, (ii) those tracing the dense ridge, and (iii) those displaying localized and fragmented emission. The emission of the rare isotopologs (e.g., $H^{13}CO^+$, $H^{13}CN$, $HN^{13}C$, and $^{13}CS$) appears to trace the high-density material along the DR21 ridge. In contrast to the patterns of emission in $H^{13}CO^+$ and $H^{13}CN$, the emission in their $^{12}C$ counterparts is associated with outflowing material. The difference in behavior between the main $^{12}C$ and their $^{13}C$ isotopologs is likely due to the low abundances of rare isotopologs in the high-velocity gas.

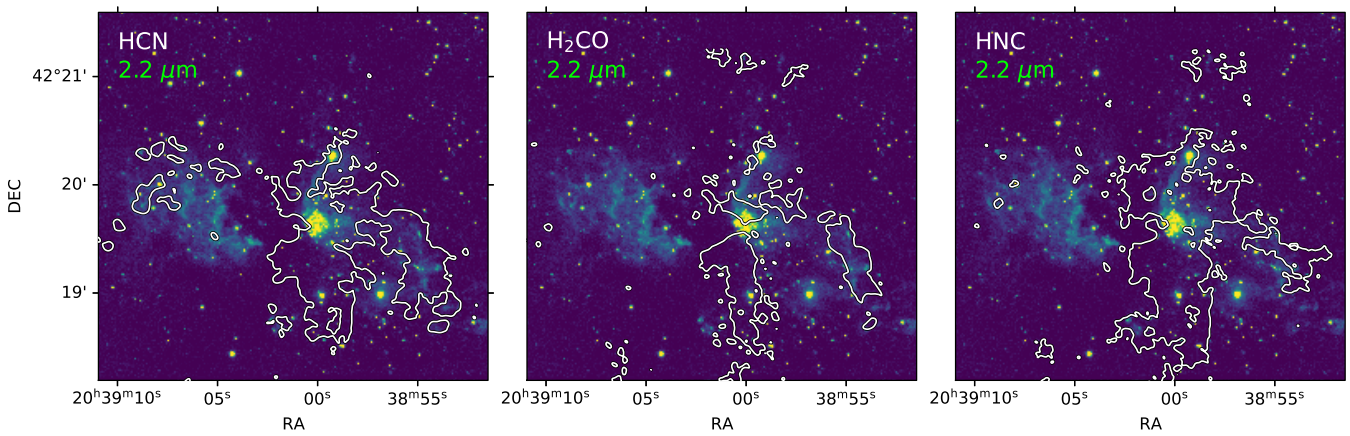


**Fig. A.1.** *UKIRT*/WFCAM continuum image of the DR21 Main region at 2.2 $\mu$m and the line emission in key gas tracers observed as part of CASCADE. White contours mark the 5$\sigma$ HCN (left), $H_2CO$ (middle), and HNC (right) emission.

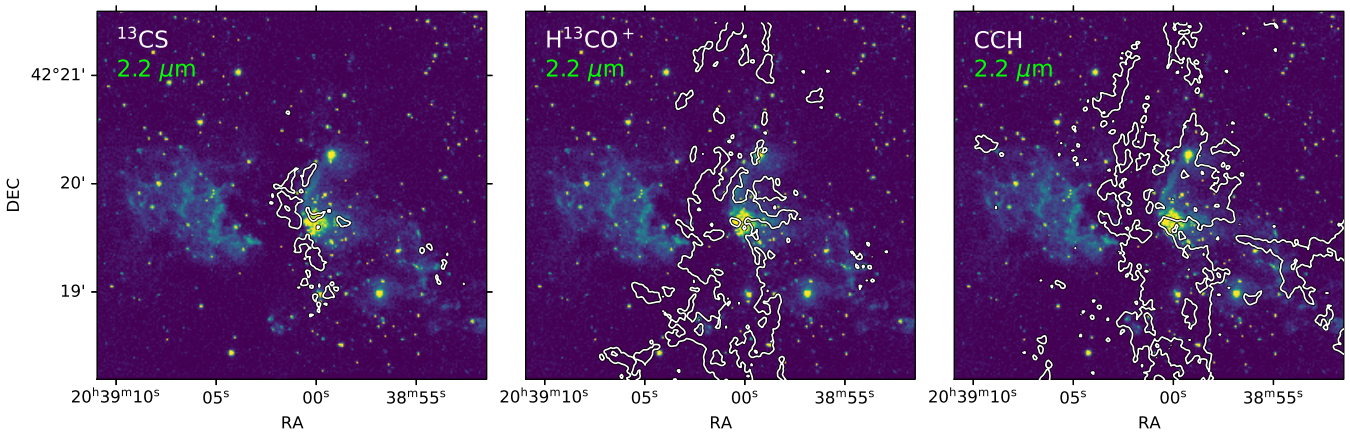


**Fig. A.2.** Similar to Fig. A.1, but for $^{13}CS$ (left), $H^{13}CO^+$ (middle) and CCH (right).

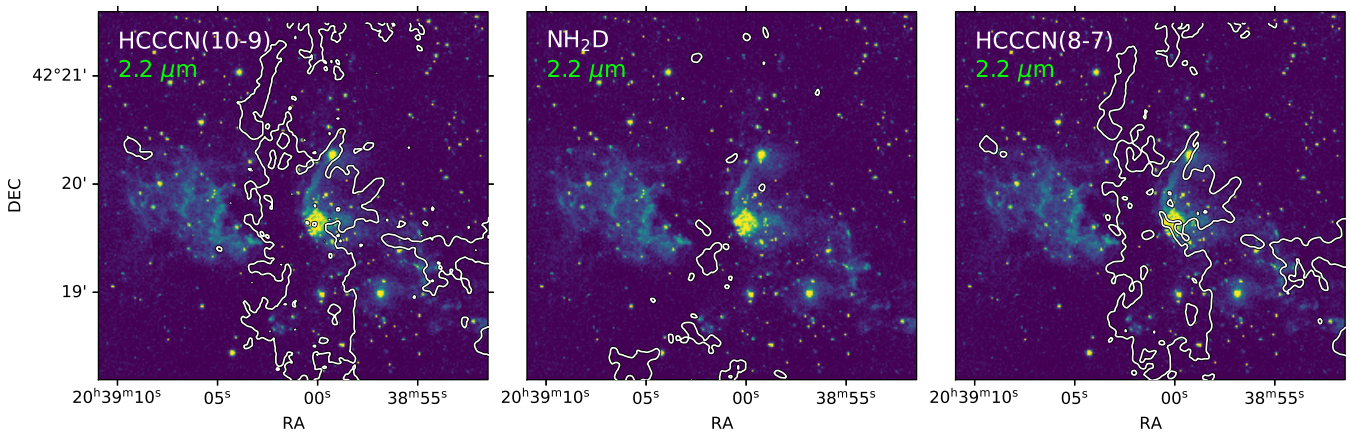


**Fig. A.3.** Similar to Fig. A.1, but for HCCCN (10-9) (left), $NH_2D$ (middle) and HCCCN (8-7) (right).

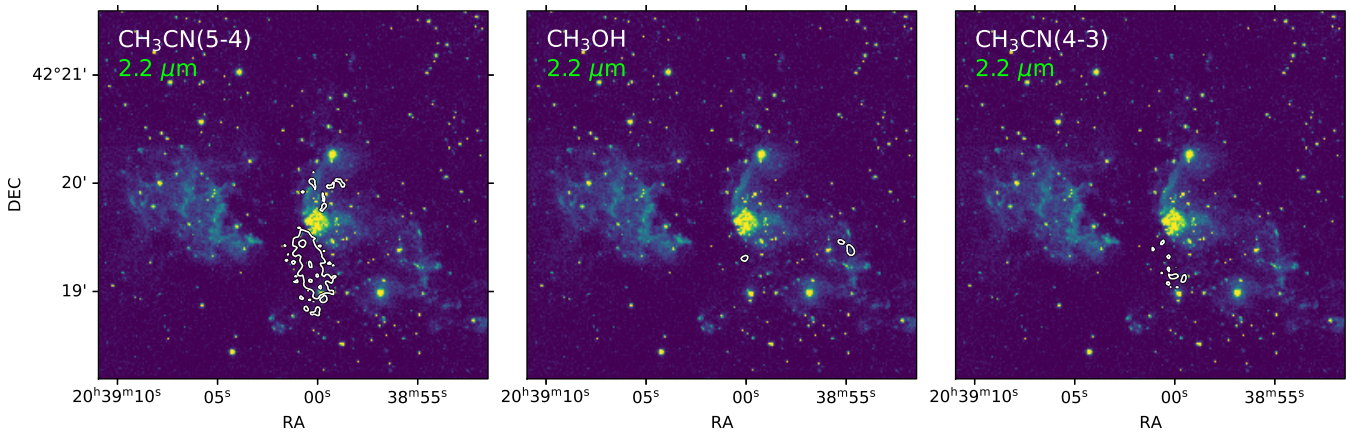


**Fig. A.4.** Similar to Fig. A.1, for $CH_3CN$ (5-4) (left), $CH_3OH$ (middle) and $CH_3CN$ (4-3) (right).

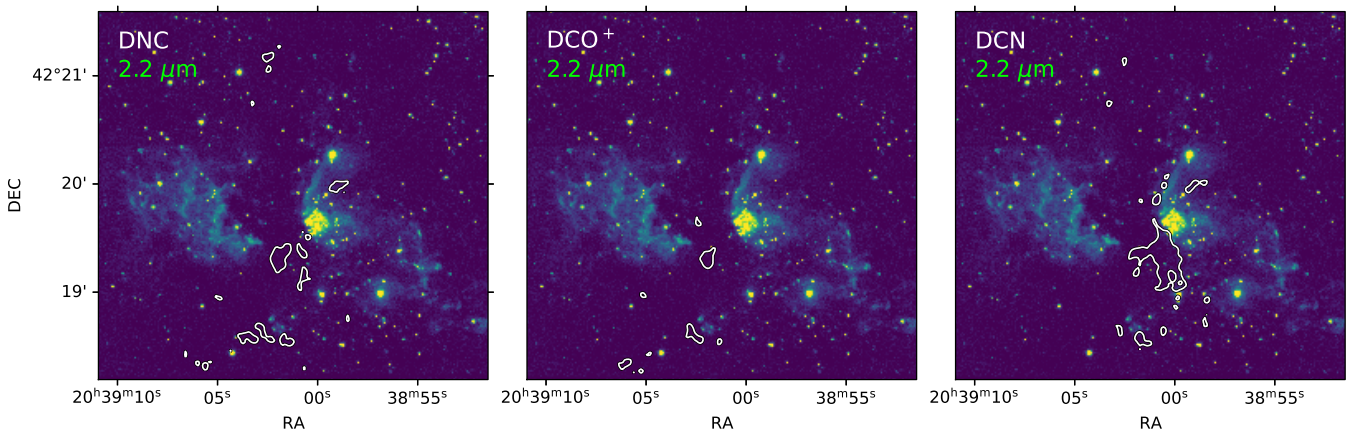


**Fig. A.5.** Similar to Fig. A.1, but for DNC (left), $DCO^+$ (middle) and DCN (8-7) (right).

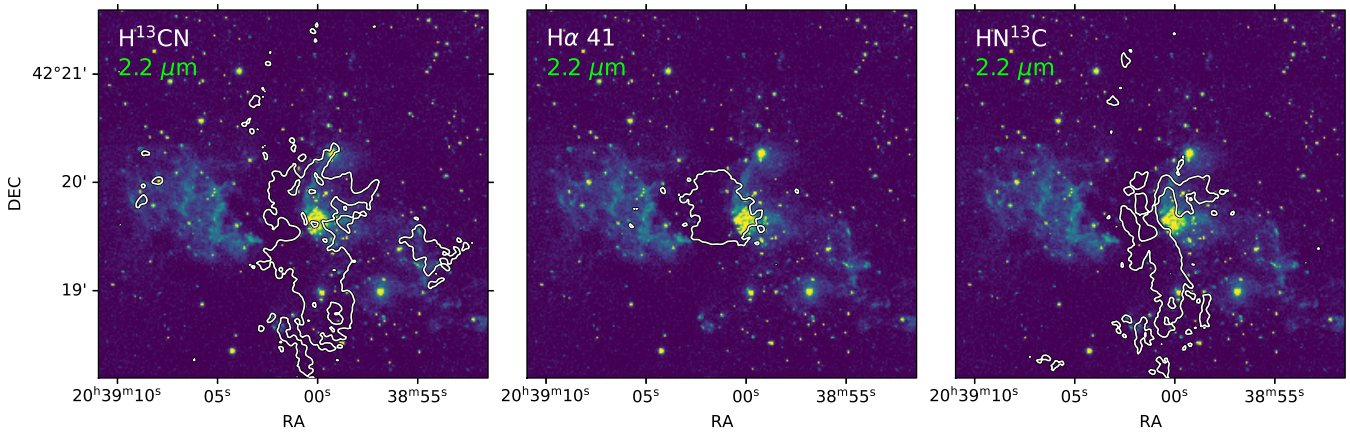


**Fig. A.6.** Similar to Fig. A.1, but for $H^{13}CN$ (left), H$\alpha$41 (middle) and $HN^{13}C$ (right).

## Appendix B: Line profiles in detected molecules

Figures B.1–B.4 show spectra of the different molecular lines observed in CASCADE. The spectra are averaged over the east lobe, the center, and the western lobe (see Fig. 1).

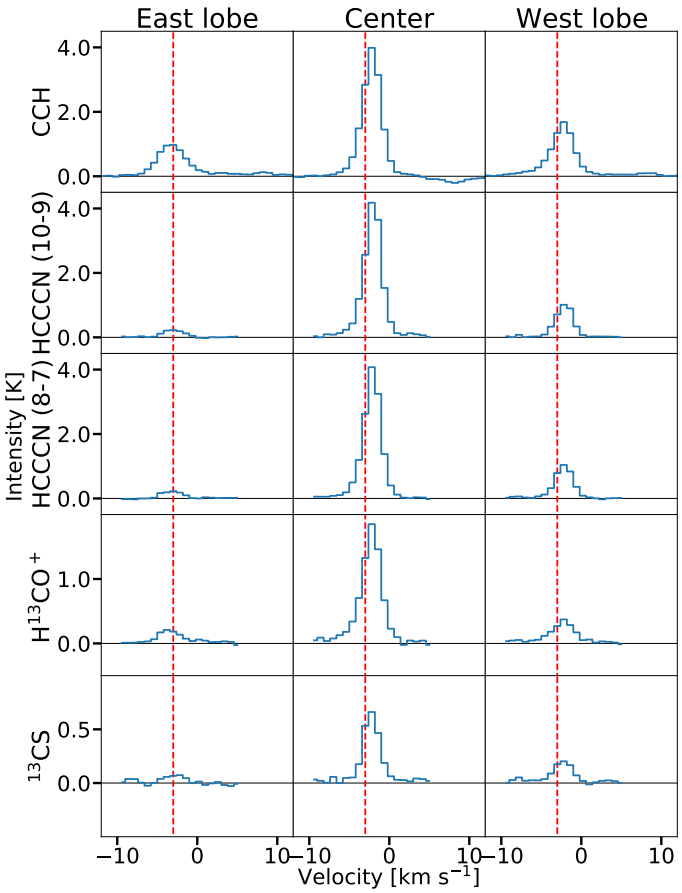


**Fig. B.1.** Similar to 2, but for CCH, HCCCN (10–9), HCCCN (8–7), $H^{13}CO$, and $^{13}CS$

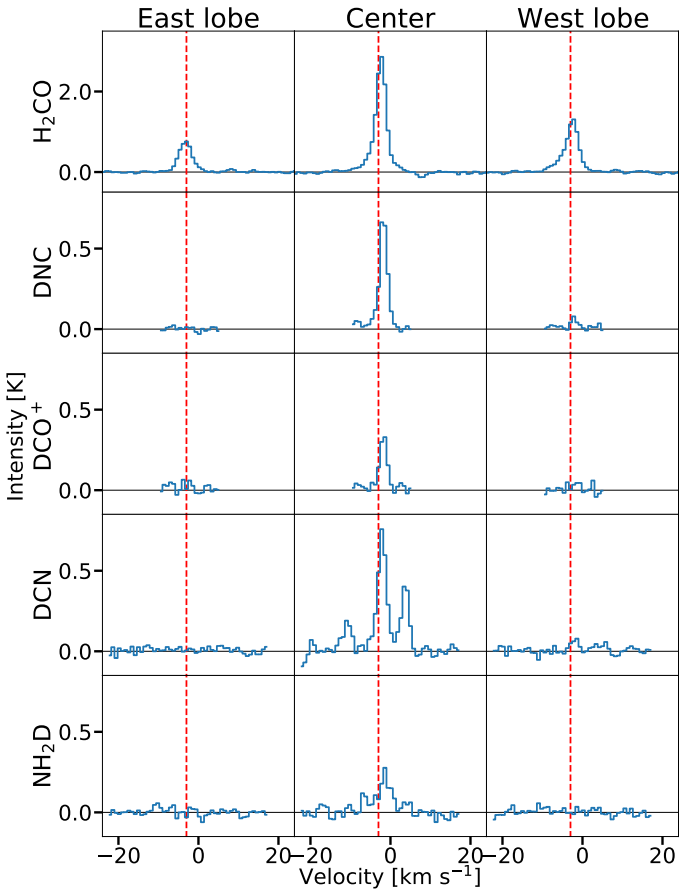


**Fig. B.2.** Similar to 2, but for H2CO, DNC, $DCO^+$, DCN, and $NH_2D$

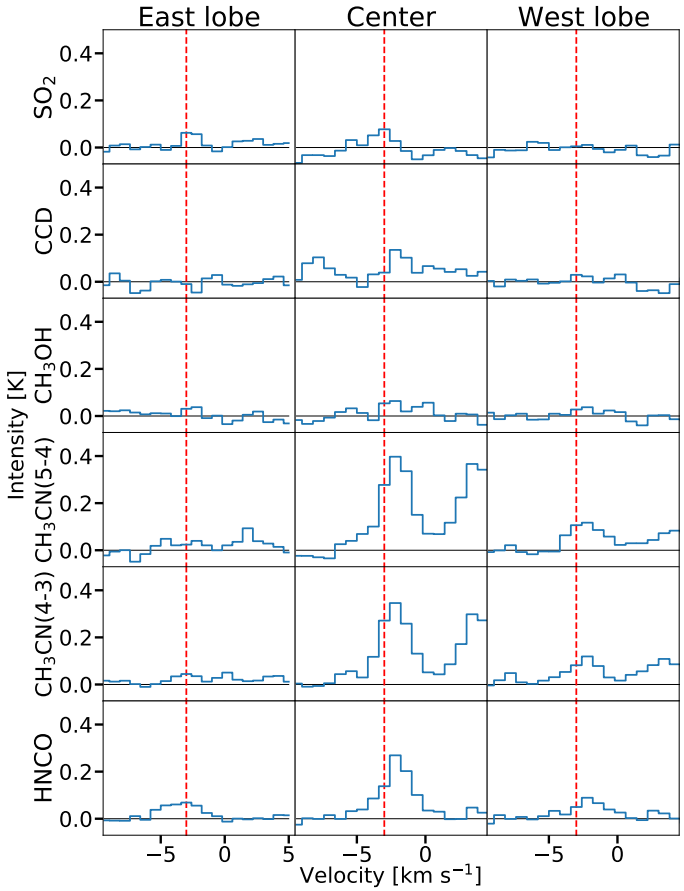


**Fig. B.3.** Same as Fig 2, but for $SO_2$, CCD, $CH_3OH$, $CH_3CN$ ($4_k$–$3_k$), $CH_3CN$ ($5_k$–$4_k$), and HNCO

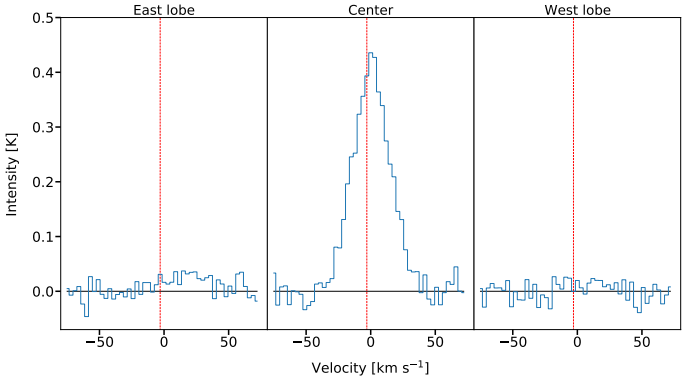


**Fig. B.4.** Same as Fig 2, but for H41$\alpha$ emission.

## Appendix C: Correlation plots

Figures C.1–C.5 show correlation plots between the different outflow parameters and the bolometric luminosity and envelope mass of their driving sources.

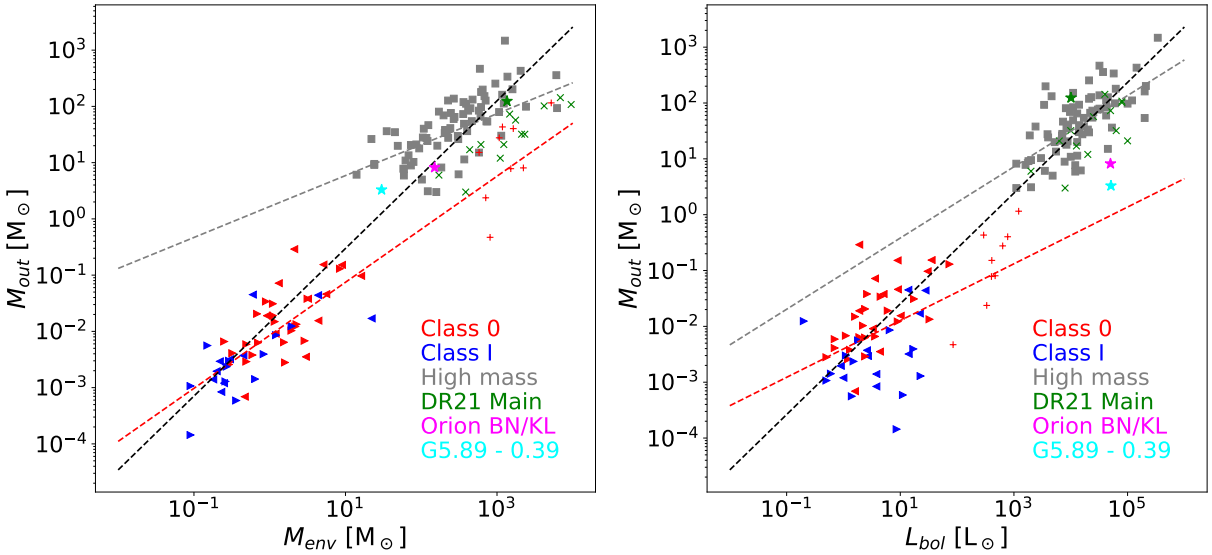


**Fig. C.1.** Outflow mass versus envelope mass and bolometric luminosity. The labels are the same as in Fig. 10.

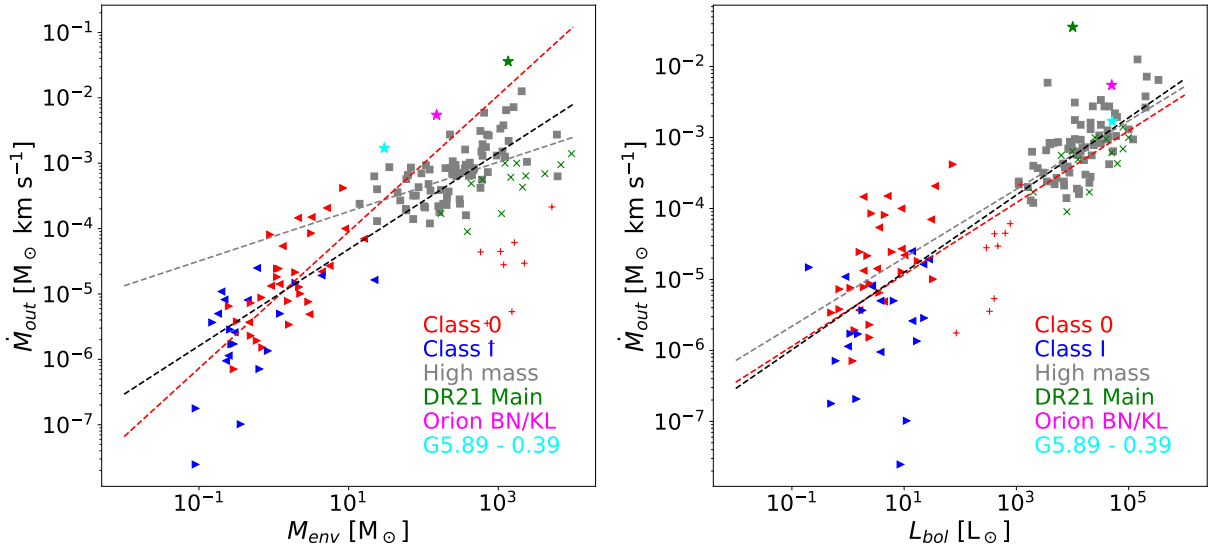


**Fig. C.2.** Outflow mass rate versus envelope mass and bolometric luminosity. The labels are the same as in Fig. 10.

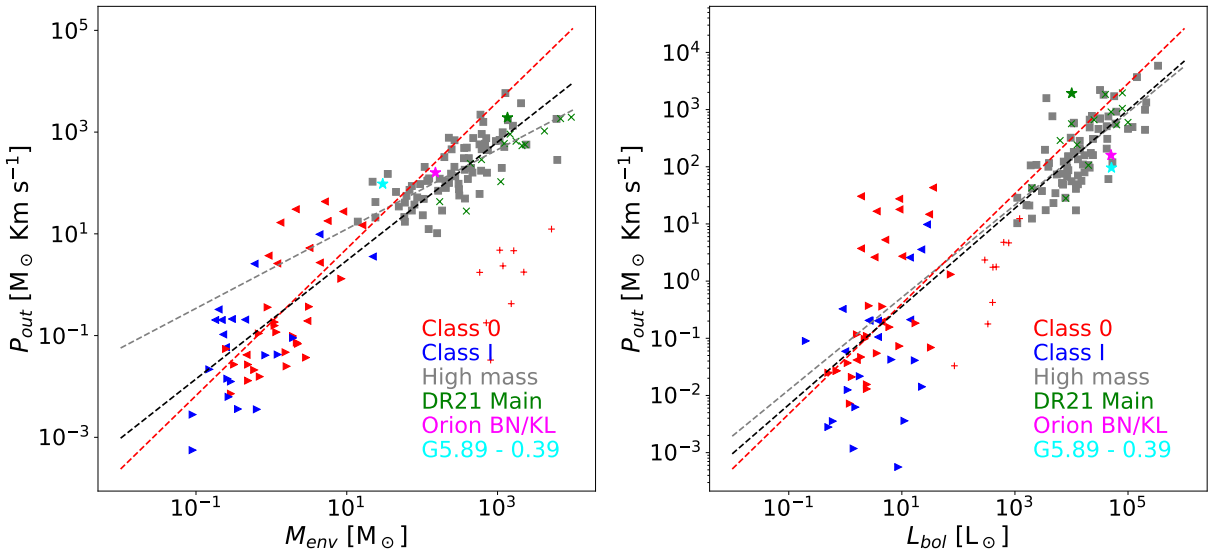


**Fig. C.3.** Outflow momentum versus envelope mass and bolometric luminosity. The labels are the same as in Fig. 10.

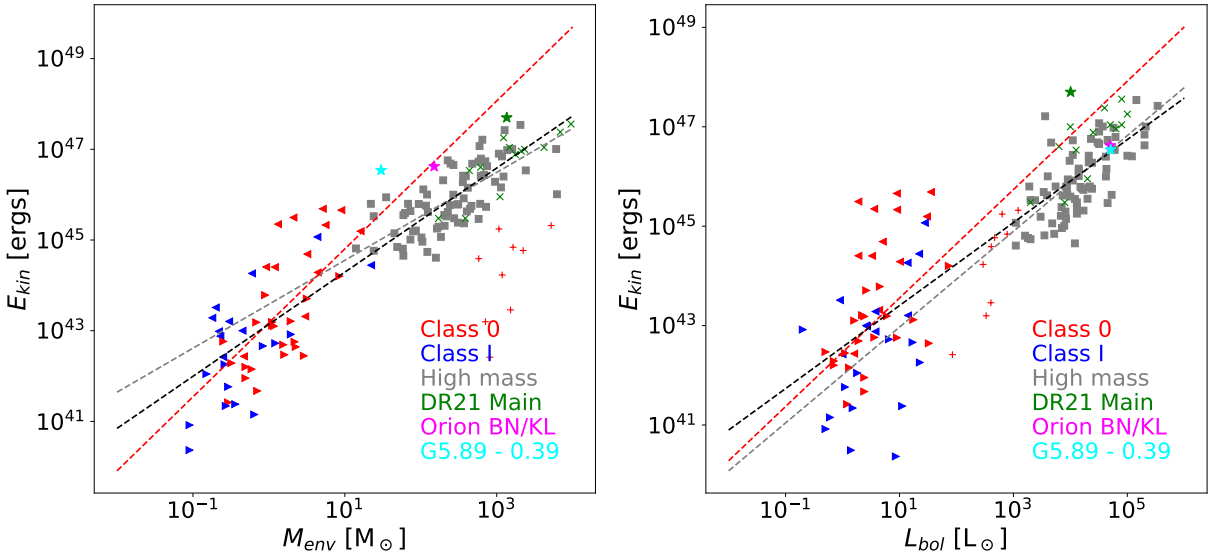


**Fig. C.4.** Outflow kinetic energy versus envelope mass and bolometric luminosity. The labels are the same as in Fig. 10.

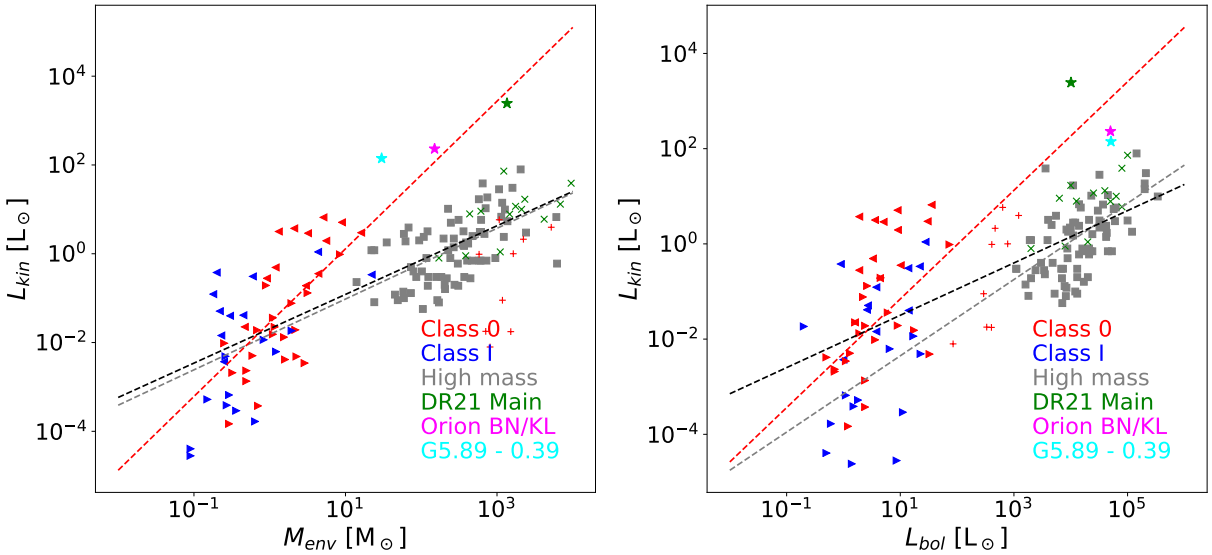


**Fig. C.5.** Outflow kinetic luminosity versus envelope mass and bolometric luminosity. The labels are the same as in Fig. 10.

APPENDIX C

# UV-irradiated outflows from low-mass protostars in Ophiuchus with JWST/MIRI

A&A, 703, A139 (2025)
https://doi.org/10.1051/0004-6361/202554977
© The Authors 2025

Astronomy & Astrophysics

# UV-irradiated outflows from low-mass protostars in Ophiuchus with JWST/MIRI

I. M. Skretas[1,⋆], A. Karska[1,2], L. Francis[3], W. R. M. Rocha[3], M. L. van Gelder[3], Ł. Tychoniec[3], M. Figueira[1,4], M. Sewiło[5,6,7], F. Wyrowski[1], and P. Schilke[8]

[1] Max-Planck-Institut für Radioastronomie, Auf dem Hügel 69, 53121 Bonn, Germany
[2] Centre for Modern Interdisciplinary Technologies, Nicolaus Copernicus University in Toruń, Wileńska 4, 87-100 Toruń, Poland
[3] Leiden Observatory, Leiden University, PO Box 9513, 2300 RA Leiden, The Netherlands
[4] National Centre for Nuclear Research, Pasteura 7, 02-093 Warszawa, Poland
[5] Exoplanets and Stellar Astrophysics Laboratory, NASA Goddard Space Flight Center, Greenbelt, MD 20771, USA
[6] Center for Research and Exploration in Space Science and Technology, NASA Goddard Space Flight Center, Greenbelt, MD 20771, USA
[7] Department of Astronomy, University of Maryland, College Park, MD 20742, USA
[8] Physikalisches Institut der Universität zu Köln, Zülpicher Str. 77, D-50937 Köln, Germany

Received 1 April 2025 / Accepted 10 September 2025

**ABSTRACT**

*Context.* The main accretion phase of protostars is characterized by the ejection of material in the form of bipolar jets and outflows. In addition, external UV irradiation can potentially have a significant impact on the excitation conditions within these outflows. High-resolution observations in the mid-infrared (mid-IR) allow us to investigate the details of those energetic processes through the emission of shock-excited $H_2$.

*Aims.* Our aim is to spatially resolve $H_2$, ionic, and atomic emission within the outflows of low-mass protostars, and investigate its origin in connection to shocks influenced by external ultraviolet irradiation.

*Methods.* We analyze spectral maps of 5 Class I protostars in the Ophiuchus molecular cloud from the James Webb Space Telescope (JWST) Medium Resolution Spectrometer (MIRI/MRS). The MIRI/MRS field of view covers an area between $\sim 3.2'' \times 3.7''$ at 6 μm and $6.6'' \times 7.7''$ at 25 μm and with a resolution of ∼0.3 to 1″, corresponding to spatial scales of a few hundred astronomical units.

*Results.* Four out of five protostars in our sample show strong $H_2$, [Ne II], and [Fe II] emission associated with outflows and jets. Pure rotational $H_2$ transitions from S(1) to S(8) are found and show two distinct temperature components on Boltzmann diagrams with rotational temperatures of ∼500–600 K and ∼1000–3000 K, respectively. Both *C*-type shocks propagating at high pre-shock densities ($n_H \geq 10^4$ cm$^{-3}$) and *J*-type shocks at low pre-shock densities ($n_H \leq 10^3$ cm$^{-3}$) reproduce the observed line ratios. However, only *C*-type shocks produce sufficiently high column densities of $H_2$, whereas predictions from a single *J*-type shock reproduce the observed rotational temperatures of the gas better. A combination of various types of shocks could play a role in protostellar outflows as long as UV irradiation is included in the models. The origin of this radiation is likely internal, since no significant differences in the excitation conditions of outflows are seen at various locations in the cloud.

*Conclusions.* Observations with MIRI offer an unprecedented view of protostellar outflows, allowing us to determine the properties of outflowing gas even at very close distances to the driving source. Further constraints on the physical conditions within outflows can be placed thanks to the possibility of direct comparisons of such observations with state-of-the-art shock models.

**Key words.** shock waves – stars: formation – stars: jets – stars: protostars – stars: winds, outflows – ISM: jets and outflows

## 1. Introduction

Bipolar outflows are the most prominent sign of ongoing star formation. They are considered an essential part of the star formation process as they remove material and excess angular momentum from the circumstellar-disk–protostar system, enabling accretion along the disk onto the protostar (Pudritz, et al. 2007; Frank et al. 2014; Bally 2016; Ray & Ferreira 2021). Furthermore, protostellar outflows might limit the star formation efficiency by injecting large amounts of energy and momentum into the surrounding interstellar medium (ISM) and dispersing the natal envelope (e.g., Fall et al. 2010; Frank et al. 2014). Since protostellar outflows transfer material from the protoplanetary disk, they also have a significant impact on the early disk evolution and planet formation (Tychoniec et al. 2020). In addition to wide-angle outflows, narrow well-collimated jets are launched at distances close to the protostar (e.g., Pudritz & Norman 1983; Ferreira 1997; Frank et al. 2014; Bai et al. 2016; Podio et al. 2021).

To investigate the origin and formation of protostellar outflows and jets, it is vital to observe them at their origin, close to the protostars. Powerful interferometers such as the Atacama Large Millimeter/submillimeter Array (ALMA) and the Northern Extended Millimeter Array (NOEMA) are well suited for studying energetic processes deep inside the dusty molecular envelopes of protostars. Low-*J* transitions of CO have often been employed to trace the large-scale protostellar outflows (e.g., Arce et al. 2013; Tychoniec et al. 2021; Skretas et al. 2023). Observations in additional tracers – for example, SiO and SO – have characterized the cold gas component of the jets (e.g., Lee 2020; Podio et al. 2021). However, as the jet and outflow

⋆ Corresponding author: iskretas@mpifr-bonn.mpg.de



Open Access article, published by EDP Sciences, under the terms of the Creative Commons Attribution License (https://creativecommons.org/licenses/by/4.0), which permits unrestricted use, distribution, and reproduction in any medium, provided the original work is properly cited.
This article is published in open access under the Subscribe to Open model. Open access funding provided by Max Planck Society.

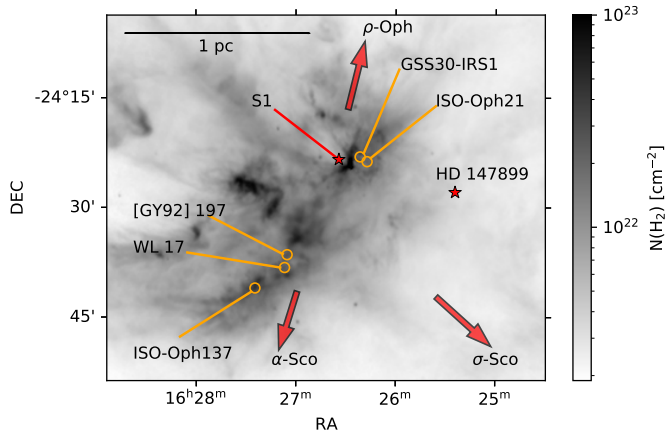


**Fig. 1.** Overview of the studied region. $H_2$ column density map from Ladjelate et al. (2020) derived from *Herschel* data. Orange circles mark the location of the targeted sources and red stars mark the nearby massive stars HD147899 and S1. The red arrows point to the direction of the surrounding massive stars $\sigma$-Sco, $\alpha$-Sco, and $\rho$-Oph, located at distances of ~4.2–4.3, ~4.3–5.2, and ~2.3–3.1 pc from the protostars, respectively.

propagate through the surrounding ISM, they compress and heat the gas, creating a significant warm gas component that is best traced in the infrared (IR) regime (Kaufman & Neufeld 1996; Flower & Pineau Des Forêts 2010).

Space observatories such as the Infrared Space Observatory (ISO), *Spitzer Space Telescope*, and *Herschel Space Observatory* detected bright emission from molecular hydrogen ($H_2$) (e.g., Nisini 2003; Maret et al. 2009; Neufeld et al. 2009) and $H_2O$ coming from shocked material in the outflows from low-mass protostars (Kristensen et al. 2012, 2017; Karska et al. 2013, 2014a; van Dishoeck et al. 2021). In addition, surprisingly bright OH emission was detected (e.g., Wampfler et al. 2013), suggesting a possible role of ultraviolet (UV) radiation in setting the abundance of $H_2O$ (Karska et al. 2014b). The inclusion of external UV irradiation of shock models by Melnick & Kaufman (2015) allowed researchers to reproduce the observed ratios of OH/$H_2O$ lines toward outflow shocks with relatively low UV fields of about 0.1–10 times the average interstellar radiation field (Karska et al. 2018). Follow-up observations of CN/HCN ratio sensitive to photodissociation suggested that even higher UV fields may be at play in clusters of low-mass protostars (Mirocha et al. 2021). The detection of irradiation tracers, such as $C_2H$ and c-$C_3H_2$ at the walls of outflow cavities further reinforces the prevalence of UV emission in protostellar outflows (Tychoniec et al. 2021; Le Gouellec et al. 2023). Shock models for a broad parameter space have recently been developed and allow us to estimate gas conditions and UV fields in various environments using, in particular, mid-IR lines of $H_2$ (Godard et al. 2019; Lehmann et al. 2020, 2022; Kristensen et al. 2023).

With the advent of James Webb Space Telescope (JWST), protostellar outflows can now be directly probed at spatial scales that reveal the origin of $H_2$ as well as atomic emission arising from shocks. Early JWST results have showcased a rich molecular emission toward the outflow of the Class 0 protostar HH 211 and a surprisingly weak atomic and ionized emission (Ray et al. 2023), while another young protostar IRAS16253 has shown a clear ionized jet in the absence of molecular gas (Narang et al. 2024). Toward the more evolved Class I protostars, TMC 1 and TMC 1A, a highly collimated, ionized jet has been detected in various [Fe II] transitions and a broader cavity has been seen in $H_2$ lines (Harsono et al. 2023; Assani et al. 2024; Tychoniec et al. 2024). The zoom-in view toward the famous outflow from HH46 presents a complicated outflow structure, including possible UV production at the location of its bow shock (Nisini et al. 2024). Finally, the detection of rotational, suprathermal OH lines toward an intermediate-mass protostar, HOPS 370, has provided evidence of the photodissociation of water by fast shocks along the jet (Neufeld et al. 2024).

In this work, we aim to study the impact of external UV irradiation on the outflows and jets of low-mass protostars and on the broader process of star formation. To that end, we investigate the morphology, physical conditions, and origin of the pure rotational emission of $H_2$ in the outflows of five protostars in Ophiuchus. All targets are classified as Class I objects (Table 1, see also van Kempen et al. 2009), which allows us to also search for possible evolutionary trends via comparisons with Class 0 objects with available JWST/MIRI data (Francis et al. 2025).

The Ophiuchus molecular complex is a nearby (distance of 137 pc; Ortiz-León et al. 2017), low-mass star-forming region (Evans et al. 2009). In addition, Ophiuchus contains a large number of prestellar cores, protostars, and more evolved young stellar objects (Wilking et al. 1989; Leous et al. 1991; Motte et al. 1998; Wilking et al. 2008; Ladjelate et al. 2020). CO observations have shown that the complex primarily consists of two molecular clouds: L1688, which is associated with intense star formation in several dense clumps (Loren et al. 1990; Motte et al. 1998; Bontemps et al. 2001), and L1689, which appears much more quiescent (e.g., Nutter et al. 2006). Both core properties and outflow activity were extensively studied using single-dish antennas by Lindberg et al. (2017) and van der Marel et al. (2013), at angular resolutions of 29″ and 15″, respectively. The protostars in Ophiuchus are under the influence of the nearby Sco OB2 association and additional B-type stars (e.g., Motte et al. 1998; Nutter et al. 2006; Wilking et al. 2008), resulting in UV fields of ~5–10 times the interstellar radiation field toward diffuse clouds (van Dishoeck & Black 1989). Thus, Ophiuchus is a unique laboratory in which to study the impact of external UV irradiation onto protostellar outflows and the star formation process.

The paper is structured as follows. In Sect. 2, we present the details of the observations analyzed in this work. In Sect. 3, we discuss the morphology of the detected $H_2$ outflows and ionic jets, as well as spectra extracted along the outflows. In Sect. 4, we show the results of the excitation analysis of the outflows emission as well as the results of comparisons with shock models. Then, in Sect. 5, we investigate the possible origin of the $H_2$ emission and compare our results with those in earlier studies. Finally, Sect. 6 contains a summary of our results and our conclusions.

## 2. Observations

This work makes use of data taken as part of the JWST project 1959 "Ice chemical complexity toward the Ophiuchus molecular cloud"[1] (PI: Will Rocha). The project consists of observations using the Medium Resolution Spectrometer (MRS) (Argyriou et al. 2023) of the Mid-Infrared Instrument (MIRI)

[1] The data used in this project may be obtained from https://doi.org/10.17909/g6cb-s335.

**Table 1.** Source properties and integration times used for the observations with MIRI/MRS

| No. | Source | R.A. (J2000) (hh:mm:ss) | Dec. (J2000) (dd:mm:ss) | $T_{bol}$ (K) | $L_{bol}$ ($L_\odot$) | Other names | Integration time (s) |
|---|---|---|---|---|---|---|---|
| | | | **$\rho$ Oph A** | | | | |
| 1 | GSS30-IRS 1 | 16:26:21.34 | -24:23:05.05 | 172 | 12.72 | Elias 21, Oph-emb 8 | 55.5 |
| 2 | ISO-Oph 21 | 16:26:17.23 | -24:23:45.98 | 490 | 0.83 | CRBR12, CRBR 2315.8-1700 | 277.5 |
| | | | **$\rho$ Oph E** | | | | |
| 3 | [GY92] 197 | 16:27:05.24 | -24:36:30.27 | 110 | 1.53 | LFAM26 | 499.5 |
| 4 | WL 17 | 16:27:06.76 | -24:38:15.62 | 310 | 0.73 | [GY92] 205 | 277.5 |
| | | | **$\rho$ Oph F** | | | | |
| 5 | ISO-Oph 137 | 16:27:24.57 | -24:41:03.86 | 191 | 1.21 | CRBR85, CRBR 2422.8-3423.8 | 222.0/455.1[a] |

**Notes.** The source coordinates are based on the peak of the 6.9 µm continuum emission from MIRI (see Fig. D.1[a]), and the source properties ($T_{bol}$, $L_{bol}$) are taken from *Herschel* (GSS30-IRS 1; Karska et al. 2018) and *Spitzer* surveys of low-mass protostars: ISO-Oph 137 from Enoch et al. (2009) and the remaining sources from Evans et al. (2009). $L_{bol}$ has been rescaled by a factor of 1.2 to account for the new estimate of the distance to Ophiuhus of 137 pc (Ortiz-León et al. 2017). [a]An integration time of 455.1 s was used only for grating B. [a]Appendix D is available online here.

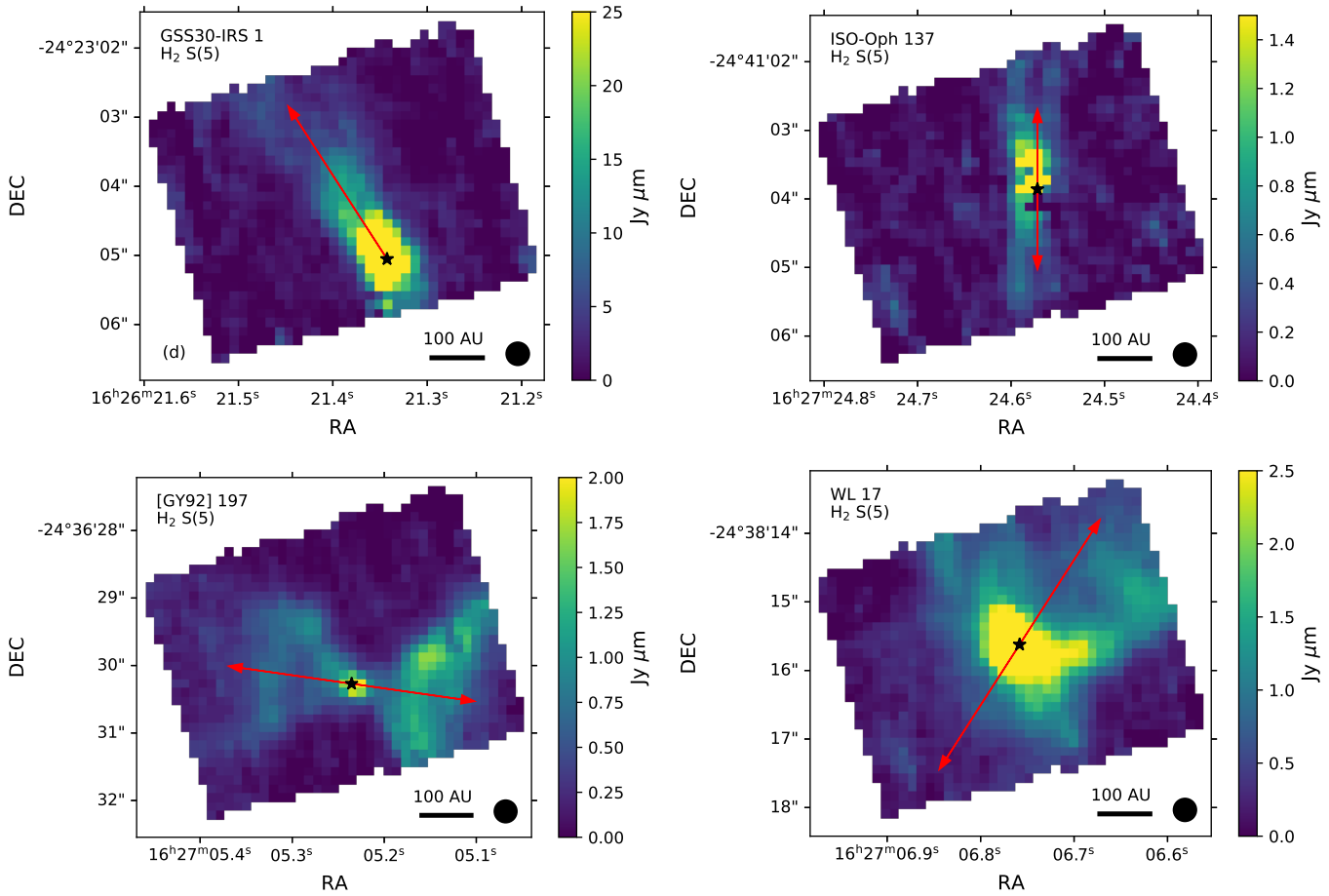


**Fig. 2.** Integrated emission of $H_2$ S(5) line at 6.91 $\mu$m toward GSS30-IRS 1, ISO-Oph 137, [GY92] 197, and WL 17. The positions of the protostars, measured from the line-free region at 6.9 $\mu$m, are shown with black stars. The red arrows shows the apparent outflow direction based on the $H_2$ emission. The filled black circle marks the spatial resolution of MIRI at $\lambda$ = 6.9 $\mu$m (~ 0.2″).

(Wright et al. 2023), targeting five Class I protostars in the Oph A, E, and F regions of the Ophiuchus molecular cloud. The sources were selected such that they have varying distances from the nearby massive stars, especially the B3 V type star S1 and the B2 V type star HD147899 (see Fig. 1). As a result, the sources are exposed to different levels of UV irradiation, enabling the study of its impact on the star-formation process. Detailed information for the targeted sources is presented in Table 1, while an overview of the region showing the observed sources as well as notable nearby massive stars is shown in Fig. 1.

The data were taken using the FASTR1 readout mode and a four-point dither pattern in the negative direction, optimized for extended sources. All three gratings (A, B, and C) were used thus covering the entire wavelength range available with MIRI

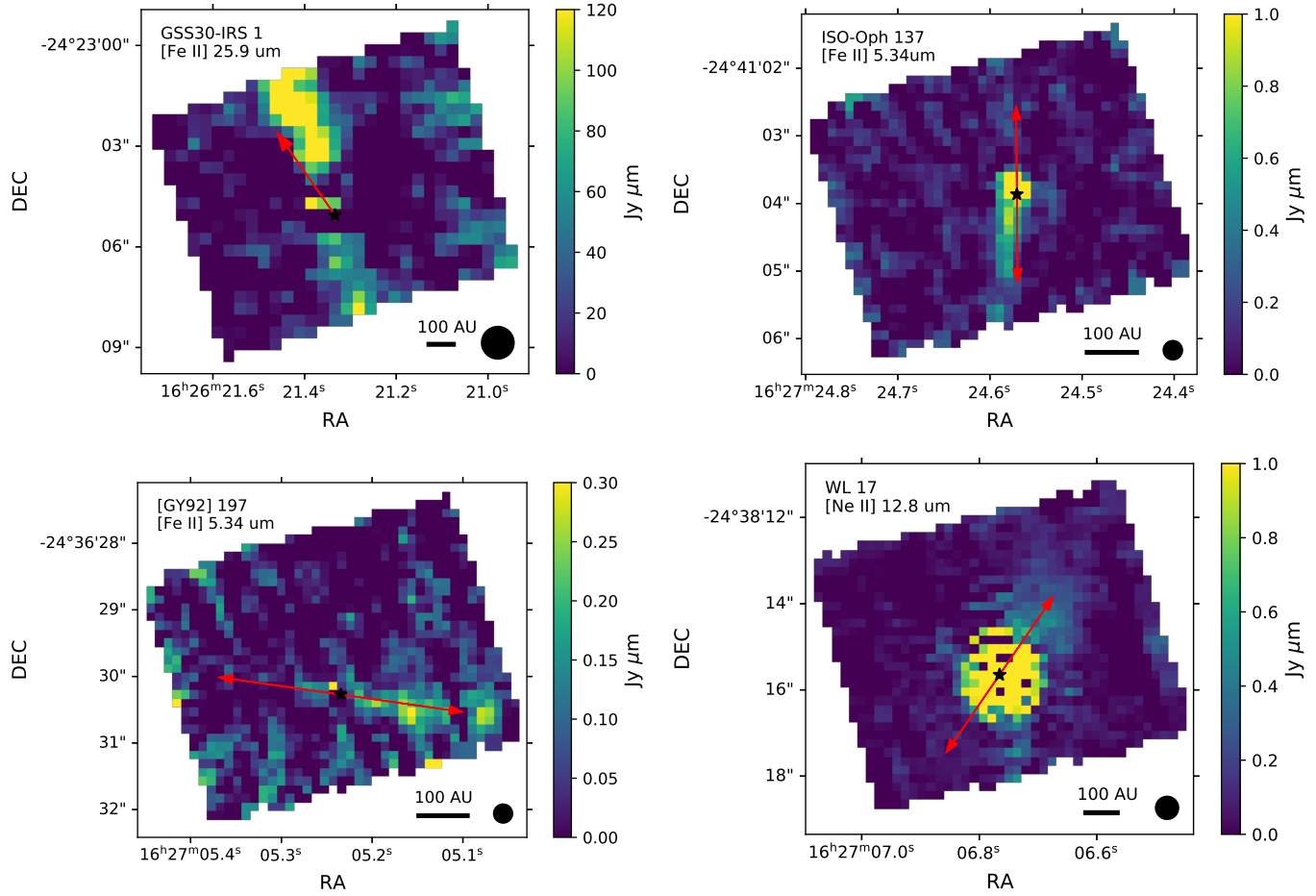


**Fig. 3.** Integrated emission of selected emission lines of ionized species: the [Fe II] line at 25.9 $\mu$m toward GSS30-IRS 1, the [Fe II] line at 5.34 $\mu$m toward ISO-Oph 137, and [GY92] 197, and – since no extended [Fe II] emission was detected – the [Ne II] line at 12.8 $\mu$m toward WL 17. The labels are the same as in Fig. 2.

(4.9–27.9 μm) with spectral resolution ranging from ~0.0015 μm at 4.9 μm to ~0.02 μm at 27.9 μm. A single pointing was used for each source targeting the corresponding source coordinates (see Table 1).The resulting field of view (FoV) depends on the MIRI Channel, and goes from 3.2″ × 3.7″ in Channel 1 (4.9–7.65 μm) up to 6.6″ × 7.7″ in Channel 4 (17.7–27.9 μm). The integration time per channel is also shown in Table 1. Two separate background observations were taken for sources in Oph A and Oph E and F, respectively.

The data were processed using the JWST pipeline (Bushouse et al. 2024) with the reference context `jwst_1188.pmap` of the JWST Calibration Reference Data System (CRDS; Greenfield & Miller 2016). The raw data were initially processed using the `Detector1Pipeline` set at default and next, the `Spec2Pipeline` was used to create the calibrated detector images. The corresponding background was then subtracted and the fringe flat as well as the residual fringe correction (Kavanagh et al. in prep.) were applied. Next, using the Vortex Imaging Processing package (Christiaens et al. 2023) an additional bad pixel map was created. The final datacubes were then created from the calibrated detector files by using the `Spec3Pipeline`, with the drizzle algorithm (Law et al. 2023), separately for each sub-band and MIRI/MRS Channel. Both the master background and the outlier rejection steps were switched off at this stage, while the wavelength calibration from Pontoppidan et al. (2024) was included in the data reduction.

## 3. Results

### 3.1. Spatial distribution of mid-IR line emission

The MIRI range covers a number of $H_2$ lines from the ground-state vibrational level, that are excellent probes of outflows from low-mass protostars (e.g., Neufeld et al. 2009; Nisini et al. 2010b; Giannini et al. 2011). The morphology of $H_2$ emission in various lines is a powerful tool to trace the interaction of the molecular jet with the surrounding envelope (e.g., Nisini et al. 2010a; Tappe et al. 2012). In this section, we compare the $H_2$ emission with those of atomic and ionic species, and discuss the results in the context of previous studies.

Figure 2 shows continuum-subtracted $H_2$ S(5) maps for four out of five sources in our sample, revealing their outflow characteristics. We detect two distinct outflow morphologies: (i) a narrow, collimated outflow structure (GSS30-IRS 1 and ISO-Oph 137), and (ii) a wide opening angle, butterfly-shaped outflow with extended outflow cavities ([GY92] 197 and WL 17). The remaining source, ISO-Oph 21, shows weak $H_2$ emission in the S(1) and S(2) lines, has no clear outflow morphology, and no other transition is detected.

Apart from $H_2$, several atoms and ions also show significantly extended line emission. Figure 3 shows the morphology of the most extended ionic emission in each source, namely that of the [Fe II] line at 5.34 μm for [GY92] 197 and ISO-Oph 137, the [Fe II] line at 25.9 μm for GSS30-IRS 1, and the [Ne II] line

at 12.8 μm for WL 17. In the latter source, [Fe II] emission is not detected. The full list of detections, for every source and location, is given in Table A.1.

The ionic emission reveals well-collimated jets in GSS30-IRS 1, ISO Oph 137, and [GY92] 197. The jet of GSS30-IRS 1 is detected in multiple transitions of [Fe II], and shows a bipolar morphology extending in the North-South direction (Fig. 3). Because of the offset of Channel 4 relative to Channels 1-3 of MIRI, the southern lobe that is not visible in $H_2$ can still be detected in the longer wavelength transitions of [Fe II]. In any case, the limited FoV of MIRI prevents the full extent of the outflow from being captured.

In ISO-Oph 137 and [GY92] 197, the [Fe II] emission tracing the jet is detected only toward one of the outflow lobes in each source (Fig. 3). Thus, the morphology differs from the emission seen in $H_2$, which shows a bipolar symmetry (Fig. 2). Emission in additional ionic tracers, in particular [Ne II] at 12.8 μm, shows a compact morphology close to the protostar position of ISO-Oph 137, but an extended pattern in [GY92] 197. In WL 17, which shows a particularly wide opening angle in the $H_2$ maps, no collimated jet is detected in atomic or ionic lines. In the following subsections, we discuss observations from MIRI/MRS in the context of previous studies of our sources from the literature.

GSS30-IRS 1: The outflow activity in GSS30-IRS 1 was identified by the detection of extended line wings of CO (Tamura et al. 1990) and its association with a bright bipolar reflection nebula (Weintraub et al. 1993). The outflow morphology was subsequently studied with single dish CO $J = 3-2$ observations with a resolution of 14″ from the James Clerk Maxwell Telescope (JCMT) (White et al. 2015). Subsequent, high-resolution (∼0.6″) CO $J = 2-1$ observations from ALMA revealed a significant overlap of the blueshifted and redshifted outflow components of GSS30-IRS 1, suggesting a large inclination angle (Friesen et al. 2018). While MIRI observations of the $H_2$ outflow are restricted to a single lobe, the spatial extent of [Fe II] confirms the N-S direction of the outflow (see Fig. 3). The disk inclination angle of $i \sim 60°$ from Michel et al. (2023) and Artur de la Villarmois et al. (2019) agrees with a scenario where the narrow collimated jet displays a well-separated bipolar morphology, and the CO emission shows a significant overlap between the outflow lobes.

ISO-Oph 137: ISO-Oph 137 is host to a well-studied protoplanetary disk (Brandner et al. 2000; Pontoppidan et al. 2005; van Kempen et al. 2009); however, a corresponding molecular outflow has not been reported. The N-S orientation of the $H_2$ outflow in the MIRI/MRS maps (see Fig. 2), along with a clear separation of the two outflow lobes, agrees with the proposed edge-on disk orientation (van Kempen et al. 2009). The collimated morphology of the outflow traces highly excited gas over a small volume, which could explain the lack of significant low-$J$ CO emission.

[GY92] 197: [GY92] 197 possesses a CO outflow that extends close to the plane of the sky in the E-W direction, revealed by low-$J$ CO single-dish observations (at a resolution of 22 and 40″, respectively) by Bussmann et al. (2007) and Nakamura et al. (2011). The atomic and ionic emission from MIRI confirms the proposed outflow orientation (see Fig. 3) and is consistent with the almost vertical and edge-on disk (Michel et al. 2023). The $H_2$ emission shows broad outflow cavities (Fig. 2), which are likely associated with the hourglass-shaped nebulosity detected in near-IR images (Duchêne et al. 2004).

WL 17: WL 17 is a confirmed embedded YSO (van Kempen et al. 2009), which drives a bipolar outflow extending in a NW-SE direction as seen in single dish CO $J = 3-2$ observations (at a resolution of 15″, van der Marel et al. 2013). High-resolution ALMA observations (∼0.03″) revealed prominent cavities in both outflow lobes (Shoshi et al. 2024). Both the direction of the outflow and the presence of cavities are also seen in the MIRI/MRS $H_2$ maps (Fig. 2). In this extended source, [Ne II] emission is seen, filling up the $H_2$ cavity (bottom right panel in Fig. 3). Given the broad shape of the emission, the Ne II does not appear to be associated with any kind of jet launched from the protostar. Scattering of [Ne II] emission from the source onto the cavity walls offers a likely explanation for the wide morphology of the emission.

ISO-Oph 21: The outflow of ISO-Oph 21 was identified via the blueshifted and redshifted line wings of CO, but the resolution was insufficient to study its morphology (White et al. 2015). The source was classified as a disk source, based on the distribution of dust continuum and dense gas emission, questioning its embedded nature (van Kempen et al. 2009). MIRI/MRS observations of ISO-Oph 21 show only very weak $H_2$ emission in the lowest rotational levels and no atomic or ionic emission. Thus, we cannot confirm the presence of an outflow from this source. The apparent lack of an outflow in ISO-Oph 21 is potentially due to its more evolved stage (Table 1). The initial detection suffered from poor angular resolution, which could lead to the confusion with prominent outflows driven by nearby sources (see Fig. 9 in White et al. 2015).

### 3.2. Spectra

We used the information about the spatial distribution of the $H_2$ emission to identify regions for the subsequent analysis. Namely, depending on the $H_2$ emission patterns, we selected 3 to 8 circular apertures for each of the sources, making sure they lie within the FoV covered by the MRS spectrometer across the full MIRI wavelength range. The exact location of the apertures for each source are shown in Fig. E.1[2]. The radius of the circular apertures is 0.5″, ensuring they cover a significant number of pixels in all four MIRI Channels. For sources with collimated outflows, we selected four (ISO-Oph 137) and three (GSS30-IRS 1) regions along the outflow direction, omitting the central region, which is strongly affected by extinction from the protostellar envelope. In case of WL 17 and [GY92] 197, characterized by the butterfly-shaped emission (Section 3.1), we selected 4 apertures in each of the outflow lobes, 8 for each object in total. In the case of ISO-Oph 21, where no clear outflow is detected, the aperture locations where selected to cover the area of the most prominent $H_2$ emission.

#### 3.2.1. Line detections across the maps

Several transitions of $H_2$ $v = 0-0$ are detected toward all targeted low-mass protostars in Ophiuchus (Table 1), except ISO-Oph 21, where only the S(1) and S(2) transitions are detected. None of the sources shows lines of $H_2$ $v = 1-1$, which were detected toward other low-mass protostars (e.g., Tychoniec et al.

[2] Appendix E is available online here.

2024). In addition, several atomic and ionic emission lines are present in the MIRI/MRS wavelength range. Among these, the most commonly detected lines are the [Fe II] lines at 5.34 μm (4 sources), the [S I] line at 25.2 μm (4 sources), and [Ne II] line at 12.8 μm (3 sources). A summary of the line emission detected in each aperture and each source is presented in Table A.1.

In GSS30-IRS 1, S(3) to S(8) $H_2$ lines are detected along the full outflow extent, whereas the S(1) and S(2) lines are only detected in its outermost parts (Fig. 2). The reason for the non-detection of lowest-excited lines is due to an increase in the noise level in the spectra, likely resulting from the imperfect fringe correction due to the bright continuum emission toward the protostar's position. It is worth noting that the [Ne II] line at 12.8 μm line is not detected toward GSS30-IRS 1, and the [S I] line at 25.2 μm is detected only in the outflow positions (B and C).

In ISO-Oph 137, S(1) to S(7) $H_2$ lines are detected in all apertures, and the most highly excited S(8) line is also detected toward the B and D positions – at the tip of the outflow imaged with MIRI/MRS (Fig. 2). The non-detection of the S(8) line close to the protostar is most likely due to blending with the $H_2O$ and CO lines present in absorption toward the protostar position (Rocha et al., in prep.). Additionally, the [Fe II] lines are detected toward all positions except position A. The [Ne II] line at 12.8 μm and [S I] line at 25.2 μm are detected along the entire outflow.

In [GY92] 197, $H_2$ lines up to S(8) are detected in the western outflow lobe, which shows a brighter $H_2$ emission in general (Fig. 2). The lack of highly excited $H_2$ lines in the bulk of the eastern outflow lobe, except the position closest to the protostar, is likely due to sensitivity limits of the observations. While [GY92] 197 is characterized by the largest number of detections of atomic and ionic species among all sources (Table A.1), such emission is absent in the eastern outflow lobe, except the [Ne II] line at 12.8 μm.

In WL 17, $H_2$ lines up to S(8) are detected across all apertures. From the ionic and atomic emission lines, the [Ne II] line at 12.8 microns is the most prominent, being detected in all positions except position D. In contrast, [Fe II] is only seen in aperture E, close to the location of the protostar.

In ISO-Oph 21, the lack of emission from $H_2$ transitions above S(2) is consistent with the lack of a clear outflow morphology (Section 3.1). It also lacks any emission from atomic and ionic lines due to the absence of a jet.

### 3.2.2. Gas kinematics

Jets from protostars are often characterized by gas velocities exceeding 100 km s$^{-1}$, primarily seen in atomic and ionic lines (Frank et al. 2014; Bally 2016). Observations with MIRI, with a velocity resolution from ~85 (in MIRI/MRS Channel 1) to ~200 km s$^{-1}$ (in Channel 4), may provide some information about the gas kinematics. For instance, a fast-moving jet resulting in velocity shifts of molecular and atomic mid-IR lines was reported in HH46 (Nisini et al. 2024).

We investigated the line profiles of molecular and ionic lines to search for possible velocity shifts across the maps. We focused on apertures corresponding to the location of $H_2$ jets (Fig. 2) to maximize the chance to detect any velocity gradients.

Figure 4 shows the results obtained for WL 17, the only source in the sample where velocity shifts can be noticed in the [Ne II] line at 12.8 μm. However, similar shifts are not as clear in the $H_2$ lines toward this source. It is worth noting that WL 17 does not possess a collimated $H_2$ jet, and is characterized by a wide opening angle in molecular emission, and a rather compact

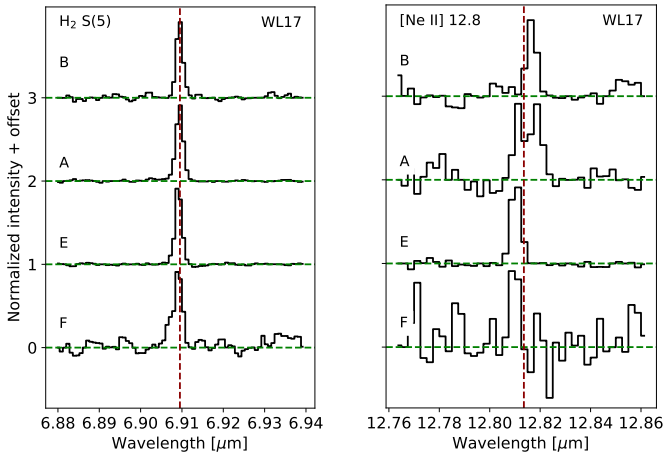


**Fig. 4.** Continuum-subtracted spectra of $H_2$ S(5) (left) and [Ne II] 12.8 μm (right) toward WL 17. An offset is added to the spectra at various positions on the maps for better visualization. The dashed lines show the laboratory wavelengths of the respective transitions.

pattern of ionic emission (Figs. 2, 3). We note here that the one sided detection of ionic emission in ISO-Oph 137 and [GY92] 197 restricts our ability to compare the velocities between the two lobes of the jet, where differences in velocity would be most prominent. Additionally, the incomplete coverage of the GSS30-IRS 1 outflow, where only one lobe is covered in all wavelengths makes such a comparison impossible in its case.

We also estimated gas velocities of the different $H_2$ transitions, using Gaussian fits to the spectra of each source and from each aperture. This approach, when applied to sufficiently strong lines, enables us to estimate velocity shifts at a resolution better than the instrumental MIRI/MRS resolution. Table 2 shows the resulting velocities for a warm gas component, estimated as the average velocity of the S(2) and S(3) transitions, and the velocity of the only the S(7) transition for a hot component. The presence of two separate gas components, warm and hot, respectively, is established through the rotational diagram analysis in Sect. 4. Here, we selected these transitions as they represent the best detected lines associated with the warm and hot components, respectively. In most cases, despite the similar spatial distribution of the two components, the hot component displays somewhat higher velocities than the warm component, potentially indicating that the hot component has a stronger connection to the fast moving jet. Similar to the direct spectral comparison, the hot component of WL 17 is the only case in which a noticeable velocity shift between the two lobes can be seen. We detect redshifted emission in the northern lobe and blueshifted toward the south, matching the orientation of the entrained CO outflow (Shoshi et al. 2024). Still, velocities for all $H_2$ lines lie within a single spectral channel of MIRI/MRS indicating that the molecular gas component of the protostellar ejections is associated with material moving at lower velocities than the dominant atomic and ionized gas components (Harsono et al. 2023; Tychoniec et al. 2024).

## 4. Analysis

MIRI/MRS imaging of $H_2$ emission on 100 AU scales allows us to associate molecular gas with the outflows from Class I protostars. Detection of multiple $H_2$ lines can constrain both the gas excitation as well as the shock properties responsible for the emission. However, external UV radiation in the Ophiuchus

**Table 2.** Gaussian fitting velocity estimates for the warm and hot $H_2$ gas components.

| Pos. | $v_{warm}$ $(km\ s^{-1})$ | $v_{hot}$ $(km\ s^{-1})$ |
|---|---|---|
| GSS30-IRS 1 | | |
| A | $-12.4 \pm 5.9$ | $-9.8 \pm 2.0$ |
| B | $-9.9 \pm 2.7$ | $-14.7 \pm 2.3$ |
| C | $-16.7 \pm 1.3$ | $-28.8 \pm 6.9$ |
| [GY92] 197 | | |
| A | $-9.0 \pm 1.3$ | $-17.4 \pm 1.7$ |
| B | $-5.4 \pm 1.4$ | $-11.4 \pm 4.3$ |
| C | $-8.0 \pm 0.5$ | $-15.8 \pm 2.6$ |
| D | $-8.9 \pm 0.9$ | $-12.0 \pm 1.4$ |
| E | $-5.1 \pm 1.4$ | $-12.5 \pm 2.4$ |
| F | $-8.5 \pm 1.2$ | $-13.1 \pm 5.4$ |
| G | $-7.0 \pm 0.8$ | $-7.6 \pm 3.5$ |
| H | $-5.1 \pm 1.9$ | $-11.4 \pm 10.7$ |
| WL 17 | | |
| A | $-2.4 \pm 0.5$ | $1.6 \pm 1.7$ |
| B | $-4.4 \pm 1.6$ | $3.8 \pm 2.1$ |
| C | $-0.2 \pm 0.2$ | $3.8 \pm 1.0$ |
| D | $1.7 \pm 1.0$ | $11.4 \pm 1.5$ |
| E | $-10.0 \pm 0.9$ | $-20.1 \pm 1.5$ |
| F | $-4.5 \pm 1.4$ | $-23.9 \pm 9.9$ |
| G | $-9.9 \pm 1.1$ | $-19.0 \pm 1.1$ |
| H | $-7.0 \pm 0.8$ | $-15.8 \pm 3.0$ |
| ISO-Oph 137 | | |
| A | $-10.8 \pm 7.4$ | $-1.6 \pm 5.9$ |
| B | $-10.4 \pm 1.0$ | $7.1 \pm 3.3$ |
| C | $-1.8 \pm 0.1$ | $-8.7 \pm 11.9$ |
| D | $-8.7 \pm 1.3$ | $-38.1 \pm 18.7$ |

region likely also influences the shock structure and its observational signatures. In the following sections, the gas excitation toward four protostars in Ophiuchus and its spatial variation are discussed (Section 4.1), and the ratios of selected $H_2$ lines are compared with the predictions of shock models including the effects of external UV radiation (Section 4.2).

### 4.1. Rotational diagrams of $H_2$

Rotational diagrams are commonly used to estimate gas physical conditions and column densities of molecules along outflows from low-mass protostars (e.g., Neufeld et al. 2009; Herczeg et al. 2012; Karska et al. 2013; Green et al. 2016; Manoj et al. 2013; Yang et al. 2018). The detection of multiple $H_2$ lines with MIRI/MRS (Section 3.2) allows the determination of the gas rotational temperatures and the corresponding $H_2$ column densities across the maps of protostars in Ophiuchus.

For optically thin, thermalized lines, the natural logarithm of the column density of the upper level, $N_u$, of a given transition over its degeneracy, $g_u$, is related linearly to the energy, $E_u$, of that level (Mangum & Shirley 2015):

$$\ln\left(\frac{N_u}{g_u}\right) = \ln\left(\frac{N_{tot}}{Q(T_{rot})}\right) - \frac{E_u}{T_{rot}}, \quad (1)$$

where $Q(T_{rot})$ is the rotational partition function at a temperature, $T_{rot}$, for a given molecule and $N_{tot}$ is the total column density.

The level-specific column density, $N_u$, was calculated from the measured line intensities, $I_{ul}$:

$$N_u = \left(\frac{4\pi I_{ul}}{A_{ul} g_u h\nu}\right), \quad (2)$$

where $A_{ul}$ the Einstein emission coefficient, $h$ the Planck constant, and $\nu$ the frequency of the line. The line intensities, following the approach presented in Francis et al. (2025), were calculated using the integrated fluxes ($F_{ul}$; shown in Table B.1) as $I_{ul} = F_{ul}/\Omega$, where $\Omega$ is the opening angle for an aperture with a diameter of 1″ at the distance of Ophiuchus (137 pc; Ortiz-León et al. 2017).

Due to significant dust content in the envelopes of low-mass protostars, mid-IR lines of $H_2$ have to be corrected for extinction. We followed the procedure described in detail in Francis et al. (2025), in which the wavelength-dependent correction factor was determined from the fit to the rotational diagram using uncorrected intensities. Due to the positive curvature of our $H_2$ rotational diagrams, we fit the natural logarithm of the column densities obtained from observations (Eq. (2)) over the level degeneracy, $g_u$, with a two-temperature component fit and an additional term for the ortho-to-para ratio (OPR) correction:

$$y = \ln\left[\left(N_{warm}\frac{\exp(-E_u/T_{warm})}{Q(T_{warm})} + N_{hot}\frac{\exp(-E_u/T_{hot})}{Q(T_{hot})}\right) 10^{\frac{-A_\lambda}{2.5}}\right] + z(J), \quad (3)$$

where $A_\lambda$ is taken from the KP5 extinctions curve (Pontoppidan et al. 2024), and with

$$z(J) = \begin{cases} \ln\left(\frac{OPR}{3}\right) & \text{odd } J \\ 0, & \text{even } J \end{cases},$$

where OPR is the ortho-to-para ratio. This way, we obtained the $H_2$ column densities and temperatures of two gas components, as well as the value of the local extinction. In the two-component fit, the low and high temperature components are primarily constrained by the S(1)-S(4) and S(5)-S(8) transitions, respectively.

Figure 5 shows example rotational diagrams for each source in our sample, except ISO-Oph 21 (see Section 3), and for the aperture in which the number of $H_2$ line detections was the largest. Table 3 shows the temperatures and column densities obtained for all sources and apertures.

The $H_2$ rotational diagrams are described well by the two components model with distinct temperatures, corresponding to $T_{warm}$ of ~500–600 K, and $T_{hot}$ of ~1000–3000 K (Fig. 5). The warm component temperatures show a relatively narrow range considering also other apertures, whereas the range of the hot component values spans thousands of K (Table 3). It is worth noting that a small number of line detections corresponding to the hot component results in significant uncertainties of the fit. Similarly, the warm component of GSS30-IRS 1 in apertures A and B is also less constrained, and likely overestimated, due to the lack of detections of S(1)-S(2) lines caused by the strong continuum emission in the region (see Section 3.2). We find OPR = 2–3 for most cases, consistent the results of previous studies on the OPR within protostellar outflows (e.g., Neufeld et al. 2006). For GSS30-IRS 1 we adopt the equilibrium OPR ratio of 3 due to the non-detection of S(1) and S(2) lines, where the effects of deviation from the OPR = 3 are most prominent.

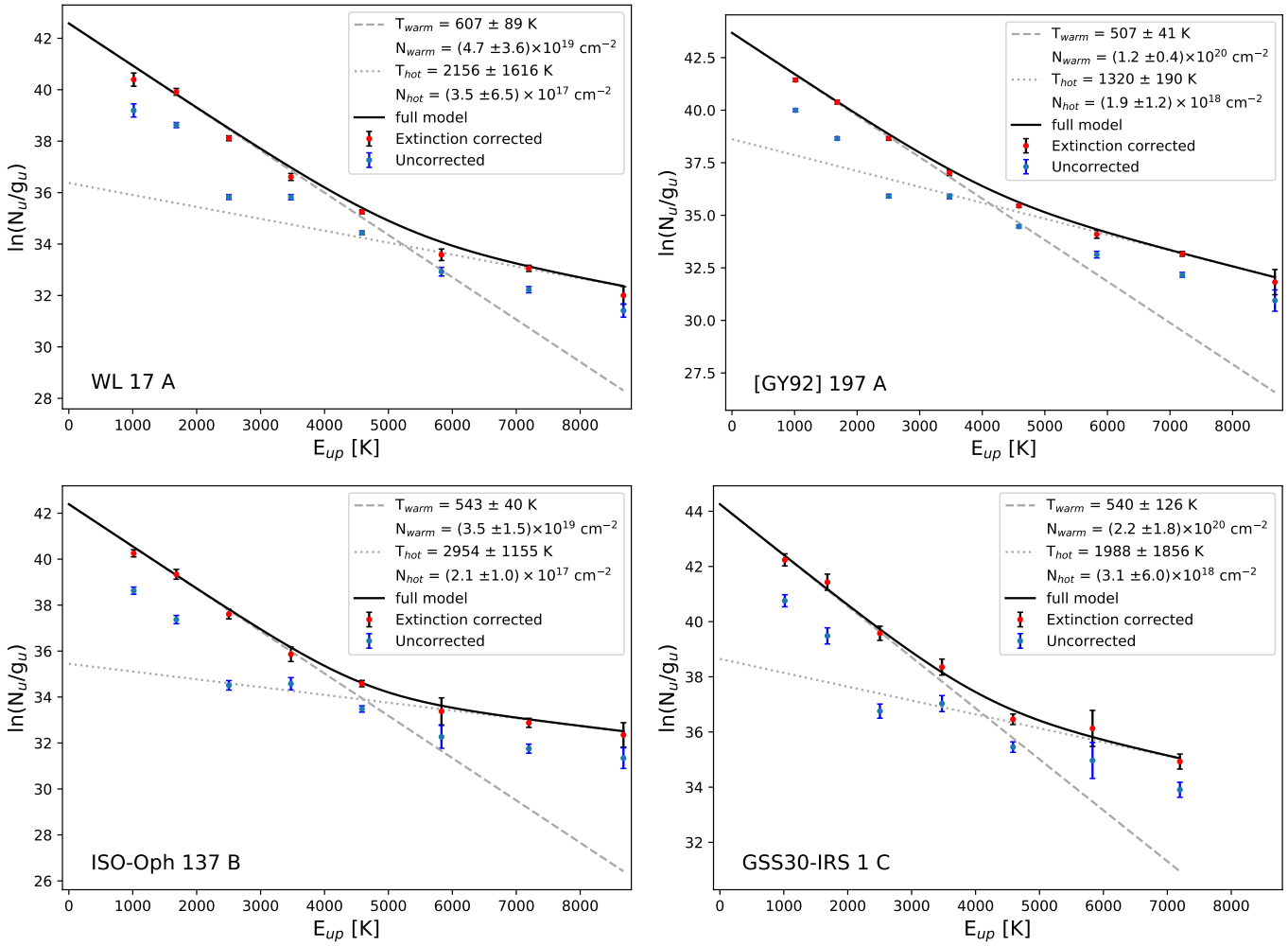


**Fig. 5.** $H_2$ rotational diagrams for the outflow positions in WL 17, [GY92] 197, ISO-Oph 137, and GSS30-IRS 1 with the largest number of line detections. The natural logarithm of the column density from a level $u$, $N_u$, divided by the degeneracy of the level, $g_u$, is written on the Y axis. The extinction-corrected values are shown in red, and the ones before the correction in blue. The two-component fits cover the transitions below and above $E_u$~4000 K for the "warm" (dashed line) and "hot" (dotted line) component (see text). The combined fit is shown as a black line. Finally, letters next to source name mark the aperture where the $H_2$ were measured.

The spatial variations in the rotational temperatures toward two sources with distinct morphologies are presented in Fig. 6. ISO-Oph 137 is a source with a bipolar collimated outflow that shows a clear increase in the gas temperatures toward the map edges – a trend that is confirmed by the detections of S(8) lines only toward the outermost apertures (Table A.1). Such a morphology is consistent with the presence of "shock spots" tracing the interaction of the jet and/or outflow with the surroundings, seen for example in L1157 (Nisini et al. 2010a). [GY92] 197, on the other hand, drives an outflow with a wide opening angle, and shows significantly less variation in the gas temperatures (Fig. 6). The western outflow lobe, which shows brighter $H_2$ emission, seems to be associated with warmer gas than the eastern outflow lobe. Generally, the highest temperatures correspond well with the positions along the outflow cavity rather than the ionic jet. This is seen also in the eastern outflow lobe, where one of the positions is associated with especially high hot component (aperture H). The higher rotational temperatures found along the edges of the outflow cavity suggest that the $H_2$ is heated by shocks produced at the cavity walls instead of along the central jet. Such shocks likely arise from the interaction between the outflowing gas and the surrounding cold envelope.

The variation in gas excitation at different positions along the outflows is further explored in Fig. 7. Here, we calculate the ratio of two $H_2$ transitions that are detected toward most of our sources: the S(2) line from the warm gas component and the S(7) line from the hot gas component (see also Section 4.2). The median ratio for our sources is ~1.0. The highest values of the ratio correspond to the central positions of the ISO-Oph 137, which show significantly lower excitation than the outermost parts of the outflow (see Fig. 6). Overall, the S(2)/S(7) ratio for the Ophiuchus protostars, constituting only Class I protostars, is about a factor of 3 higher than the same ratio calculated for other low-mass protostars using the literature data (Tychoniec et al. 2024; Francis et al. 2025). We discuss a possible impact of evolutionary trends on the $H_2$ excitation in Section 5.

To summarize, the analysis of $H_2$ lines confirms the presence of highly excited molecular gas with properties showing some changes depending on the exact origin of the emission; for example, along the outflow cavities or jet. The differences between sources in our sample are not significant, suggesting that neither the source properties nor environmental conditions play a strong role in the $H_2$ excitation.

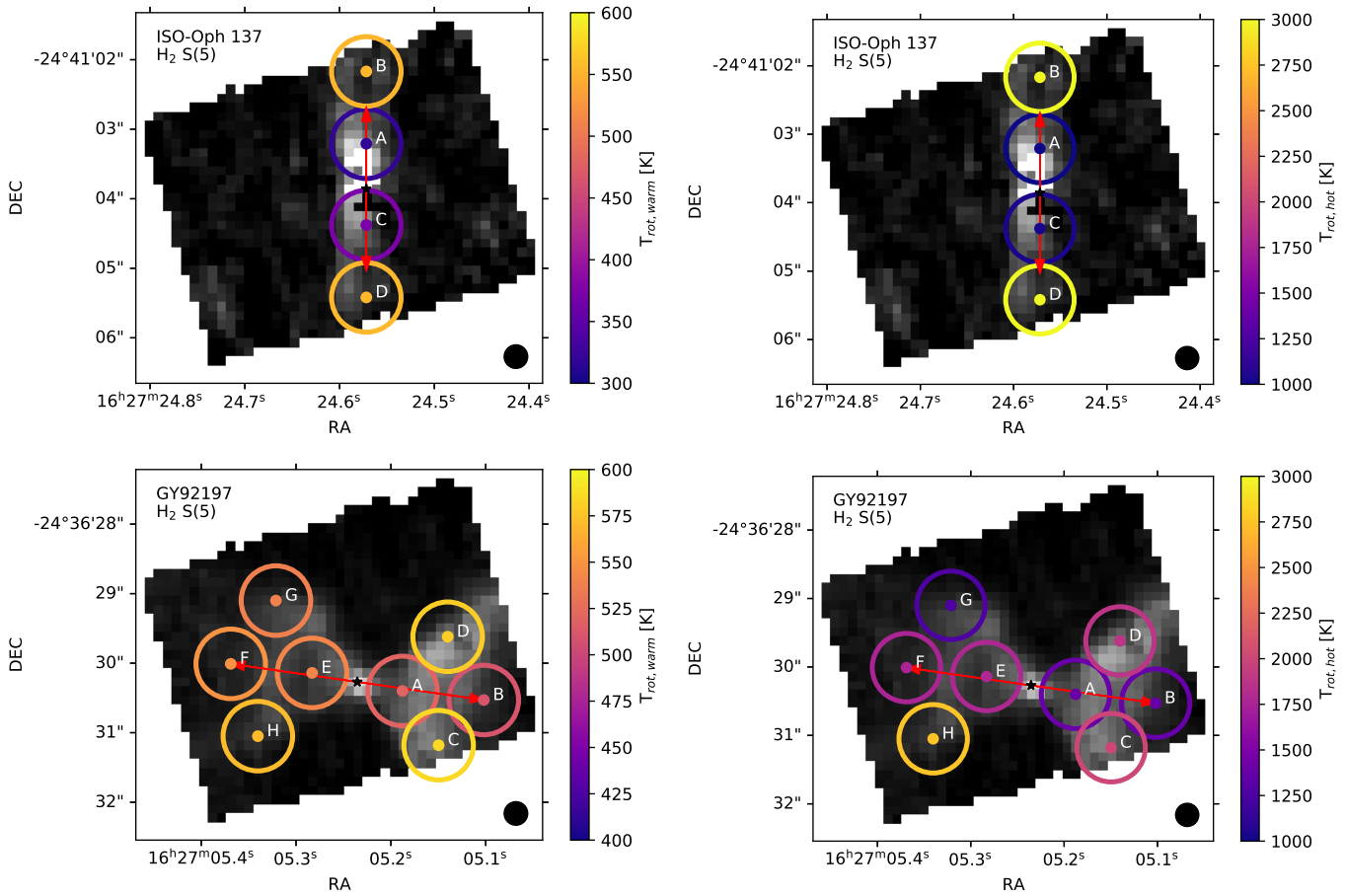


**Fig. 6.** Integrated emission of $H_2$ S(5) line toward ISO-Oph 137 (top) and [GY92] 197 (bottom) with circles color-coded with the rotational temperatures of warm (left) and hot (right) gas components, respectively. Red arrows show the outflow directions, and capital letters refer to apertures used for the spectra extraction.

### 4.2. Comparisons to shock models

In this section, we compare the measured $H_2$ intensities from our observations to the results of models of UV-irradiated shocks propagating in a broad range of physical conditions of the ISM (Kristensen et al. 2023). We aim to constrain the shock properties for the Ophiuchus protostars and identify the impact of external UV radiation from nearby B-type stars on the $H_2$ excitation in their outflows.

The model grid from Kristensen et al. (2023) was obtained using the Paris-Durham[3] shock code that simulates the changes in the chemical, thermal and dynamical conditions of interstellar matter due to steady state, plane parallel shocks (Flower & Pineau des Forêts 2003). In its latest version, the code accounts for the impact of external UV irradiation on the shock structure and chemistry (Lesaffre et al. 2013; Godard et al. 2019).

Kristensen et al. (2023) considers the following input parameters of the environment and shock properties: (i) the pre-shock gas density $n_H$, (ii) the traverse magnetic field strength, $B = b\sqrt{n_H}$ in units of $\mu$Gauss, where $b$ is a scaling factor for magnetic field, (iii) the shock velocity $v_{sh}$ (iv) the external UV radiation field in units of $G_0$, (v) the cosmic ray ionization rate $\zeta_{H_2}$, and (vi) the abundance of polycyclic aromatic hydrocarbons, $X$(PAH). The code calculates a chemical steady-state for a given gas density, $n_H$, and UV field (step 1), the chemical equilibrium results are used as input for a PDR calculation (step 2), and the resulting PDR conditions are used as inputs for the shock model (step 3), for details see Section 2 of Kristensen et al. (2023). The excitation of $H_2$ is subsequently calculated, taking into considerations collisions with H (Flower 1997; Flower & Roueff 1998; Martin & Mandy 1995), $H_2$ (Flower & Roueff 1998), and He (Flower et al. 1998). The resulting $H_2$ line intensities, along with a number of atomic line intensities, are provided in a machine-readable format on CDS[4].

The shock model predictions from Kristensen et al. (2023) are provided for the following ranges of parameters: $n_H$ from $10^2$ to $10^8$ cm$^{-3}$, $b$ from 0.1 to 10, $v_{sh}$ from 2 to 90 km s$^{-1}$, $G_0$ from 0 to $10^3$, $\zeta_{H_2}$ from $10^{-17}$ to $10^{-15}$ s$^{-1}$, and $X$(PAH) from $10^{-8}$ to $10^{-6}$. Here, we restrict the considered parameters to those expected in outflows from low-mass protostars. In particular, typical (post-shock) gas densities in outflows are in the range from $10^5$–$10^8$ cm$^{-3}$ (Mottram et al. 2014), given the high compression factors predicted in Kristensen et al. (2023) all available pre-shock densities, from $10^2$–$10^6$ cm$^{-3}$ are considered. For such densities, the $b$ scaling factor of 0.1–1 provide magnetic field strengths of the order of 0.001–1 mG, consistent with the recent measurements for the Ophiuchus molecular cloud (Lê et al. 2024). The shock velocities above 10 km s$^{-1}$ are expected based on the resolved profiles of $H_2O$ and high-$J$ CO lines with *Herschel* (Kristensen et al. 2012, 2017). Since the

[3] http://ism.obspm.fr/shock.html

[4] https://cdsarc.cds.unistra.fr/viz-bin/cat/J/A+A/675/A86#/article

**Table 3.** Rotational temperatures, column densities, extinction, and ortho-to-para ratios for all sources and apertures.

| Pos. | $T_{\rm warm}$ (K) | $T_{\rm hot}$ (K) | $N_{\rm warm}$ $(\times 10^{19}\,{\rm cm}^{-2})$ | $N_{\rm hot}$ $(\times 10^{17}\,{\rm cm}^{-2})$ | $A_K$ | OPR |
|---|---|---|---|---|---|---|
| | | | GSS30-IRS 1 | | | |
| A[a] | 679 ± 0.5 | – | 65.5±0.4 | – | 4.7 ± 2.0 | 3.0[b] |
| B[a] | 1495 ± 206 | – | 1.4 ± 0.8 | – | 2.0 ± 6.5 | 3.0[b] |
| C | 540 ± 126 | 1988 ± 1856 | 22.0 ± 18.0 | 31.0 ± 60.0 | 3.0 ± 1.2 | 3.0[b] |
| | | | [GY92] 197 | | | |
| A | 507 ± 41 | 1320 ± 190 | 12.0 ± 4.0 | 19.0 ± 12.0 | 2.9 ± 0.5 | 2.5 ± 0.3 |
| B | 444 ± 56 | 1269 ± 72 | 3.8 ± 0.7 | 17.0 ± 4.0 | 2.3 ± 0.5 | 2.1 ± 0.2 |
| C | 560 ± 10 | 1698 ± 84 | 6.1 ± 0.5 | 9.2 ± 1.5 | 2.8 ± 0.1 | 2.2 ± 0.1 |
| D | 545 ± 32 | 1607 ± 166 | 8.0 ± 1.6 | 19.0 ± 7.0 | 3.0 ± 0.3 | 2.1 ± 0.2 |
| E | 543 ± 55 | 2198 ± 2082 | 9.9 ± 1.9 | 4.0 ± 7.1 | 3.3 ± 0.7 | 2.2 ± 0.5 |
| F | 532 ± 164 | 1894 ± 2198 | 3.8 ± 4.2 | 5.2 ± 13.4 | 3.3 ± 1.6 | 2.0 ± 0.9 |
| G | 507 ± 116 | 1140 ± 325 | 6.1 ± 4.4 | 19.0 ± 29.0 | 3.4 ± 1.1 | 2.1 ± 0.6 |
| H | 566 ± 38 | 2520 ± 1194 | 4.0 ± 1.8 | 1.2 ± 1.1 | 2.9 ± 0.6 | 2.5 ± 0.4 |
| | | | WL 17 | | | |
| A | 607 ± 89 | 2156 ± 1616 | 4.7 ± 3.6 | 3.5 ± 6.5 | 2.4 ± 1.0 | 2.3 ± 0.7 |
| B | 600 ± 44 | 1964 ± 444 | 2.9 ± 0.9 | 4.8 ± 3.0 | 2.4 ± 0.4 | 2.3 ± 0.3 |
| C | 649 ± 73 | 1863 ± 746 | 3.5 ± 1.5 | 6.7 ± 8.5 | 2.4 ± 0.6 | 2.6 ± 0.5 |
| D | 532 ± 206 | 1185 ± 347 | 3.8 ± 2.8 | 28.0 ± 40.0 | 2.5 ± 1.3 | 2.9 ± 0.9 |
| E | 544 ± 65 | 1813 ± 608 | 7.0 ± 3.9 | 7.9 ± 7.9 | 2.2 ± 0.8 | 2.0 ± 0.4 |
| F | 460 ± 42 | 2456 ± 550 | 4.2 ± 1.6 | 3.2 ± 1.1 | 2.7 ± 0.6 | 2.2 ± 0.3 |
| G | 502 ± 69 | 1283 ± 120 | 4.0 ± 1.0 | 23.0 ± 9.0 | 1.8 ± 0.5 | 2.2 ± 0.2 |
| H | 541 ± 50 | 1993 ± 695 | 3.9 ± 2.0 | 2.6 ± 2.4 | 1.8 ± 0.7 | 2.3 ± 0.5 |
| | | | ISO-Oph 137 | | | |
| A | 317 ± 15 | 1000 ± 70 | 560.0 ± 100.0 | 230.0 ± 30.0 | 5.5 ± 0.3 | 2.7 ± 0.1 |
| B | 543 ± 40 | 2954 ± 1155 | 3.5 ± 1.5 | 2.1 ± 1.0 | 3.3 ± 0.6 | 2.5 ± 0.4 |
| C | 380 ± 40 | 1061 ± 100 | 84.0 ± 8.4 | 98.0 ± 9.9 | 4.3 ± 0.4 | 2.4 ± 0.2 |
| D | 541 ± 33 | 2787 ± 762 | 2.5 ± 0.8 | 1.9 ± 0.7 | 3.1 ± 0.4 | 2.5 ± 0.3 |

**Notes.** [(a)]Values derived from single temperature component fit due to the non-detection of the S(1), S(2) and S(8) lines in these apertures. [(b)]OPR equilibrium value of 3.0 assumed due to the non-detection of the S(1) and S(2) transitions in apertures A and B. For aperture C, an OPR ratio of 3 led to a better fit, and is therefore used.

line profiles are not resolved with MIRI, the maximum shock velocities are ~60 km s$^{-1}$, but more likely they are not exceeding ~30 km s$^{-1}$ if they trace a similar gas component as $H_2O$. The ionization by cosmic rays and PAH abundances are not known for the studied region in Ophiuchus; however, neither of these parameters have a significant impact on our analysis (Appendix H[5]). Here, we adopt the values from the low-end of the grid, $\zeta = 10^{-17}$ s$^{-1}$ and X(PAH) = $10^{-7}$.

Figure 8 shows the comparison of the shock model results with the S(2)/S(7) ratios measured in the outflows from Ophiuchus protostars (see Section 3). Depending on the assumed magnetic field strength, the S(2)/S(7) ratio shows significant differences for a given value of pre-shock density but varying UV fields. Here, we consider magnetic fields with $b = 0.1$, representative of predominantly dissociative *J*-type shocks where ionic and neutral fluids are well coupled (Neufeld & Dalgarno 1989; Flower & Pineau Des Forêts 2010), and $b = 1$, typically adopted for *C*-type shocks, where ions and neutrals are decoupled (Kaufman & Neufeld 1996; Flower & Pineau Des Forêts 2010).

The behavior of the S(2)/S(7) line ratio is notably different between the two types of shocks. For the lower density scenarios ($n_{\rm H} = 10^2$–$10^3$ cm$^{-3}$) *J*-type shocks appear capable to reproduce the observed line ratios for a range of relatively low shock velocities ($v_{\rm sh}$ = 10–20 km s$^{-1}$), which becomes smaller for higher pre-shock densities and is already below 15 km s$^{-1}$ at $n_{\rm H} = 10^3$ cm$^{-3}$. The models also require an external UV field strength in the range of 1–100 $G_0$ to match the observed line ratios. We note here that the external UV radiation field is either contributed to by the nearby stars or produced in accretion shocks and the radiation is escaping through the outflow cavity; the self-irradiation is negligible in such low-velocity shocks (Kristensen et al. 2023). For the same range of densities, *C*-type shocks only agree with the observed line ratios for a limited range of higher shock velocities ($v_{\rm sh}$ = 20–25 km s$^{-1}$). An exception to this limited velocity range is the case with $n_{\rm H} = 10^3$ cm$^{-3}$ and UV field of 100 $G_0$, which reproduces the observed ratios for $v_{\rm sh}$ = 10–25 km s$^{-1}$. The restricted velocity range in which *C* shocks are capable of reproducing the observed line ratios suggests that for pre-shock densities of $n_{\rm H} = 10^2$–$10^3$ cm$^{-3}$ *J* shocks are more likely responsible for the excitation of $H_2$.

At pre-shock densities above $10^4$ cm$^{-3}$, the model S(2)/S(7) ratios for the *J*-type shocks decrease and span less than 2 orders of magnitude, and are generally not consistent with the ratios observed in the Ophiuchus sources. The only exceptions are the models assuming $n_{\rm H} = 10^4$ cm$^{-3}$ and a complete absence of UV irradiation, or models with UV fields of $10^3$ $G_0$, which are too high for most low-mass star-forming regions (Karska et al. 2018; Kristensen et al. 2017; van Dishoeck et al. 2011). In contrast, the model ratios for the *C*-type shocks span several orders

[5] Appendix H is available online here.

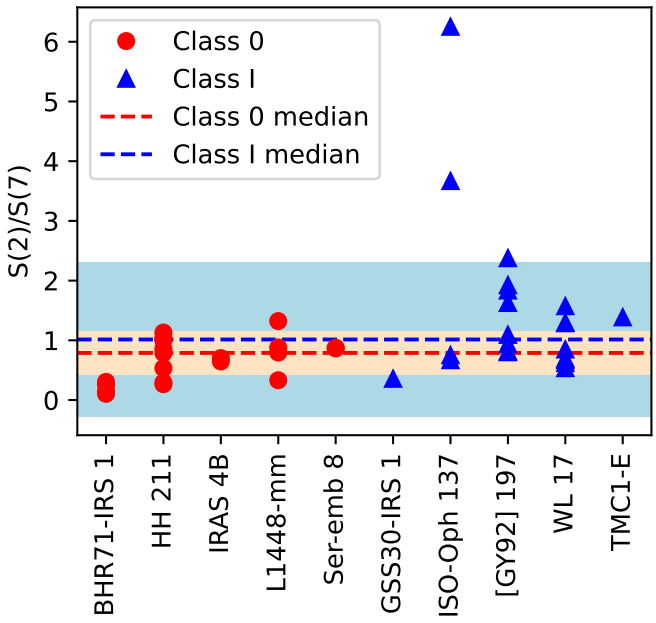


**Fig. 7.** Ratio of the S(2)/S(7) $H_2$ emission lines in different low-mass protostellar sources. Red points mark Class 0 sources from Francis et al. (2025) and blue points are Class I sources from this work and TMC1-E from Tychoniec et al. (2024). The dashed lines mark the median values, 0.3 for Class 0 (in red) and 1.0 (in blue). Colored areas mark the median ± standard deviation range.

of magnitude and reproduce the observations for an extended range of shock velocities ($v_{sh}$ = 10–25 km s$^{-1}$). At the pre-shock density of $10^4$ cm$^{-3}$, the S(2)/S(7) ratio decreases roughly by an order of magnitude with increasing values of UV field strengths. At the same time, the ratio does not depend strongly on the assumed shock velocity, facilitating meaningful comparisons with observations. For shock velocities in a broad range of values, from 10 to 20 km s$^{-1}$, the best-fit value of $G_0$ is 10–100. Slightly higher velocities would be also consistent with lower UV fields, but already at 25 km s$^{-1}$ none of the models would reproduce the observations; thus, lower UV fields are rather unlikely.

At the pre-shock densities of $10^5$–$10^6$ cm$^{-3}$, the model ratios for C-type shocks decrease strongly with the increasing UV field strength and shock velocity (right column, middle and bottom panels of Fig. 8). At 15 km s$^{-1}$, the best fit models suggest $G_0$ of 1–10 for the pre-shock density of $10^5$ cm$^{-3}$, and $G_0$ of 0 (a fully shielded scenario) for $10^6$ cm$^{-3}$. It is worth noting that $G_0$ of 100 is also consistent with observations for faster shocks ($v_{sh}$ of 25–30 km s$^{-1}$) at those higher pre-shock densities.

The sample of Class 0 sources from Francis et al. (2025) displays lower values for the observed S(2)/S(7) line ratios, suggesting higher excitation conditions within their outflows. The lower line ratios mean that the low-density, low-velocity *J*-type shocks require even higher values of UV irradiation (10–100 $G_0$) in order to reproduce the observations. In addition, both higher pre-shock density (up to $10^4$ cm$^{-3}$) *J*- shocks with low velocities, as well as, high-velocity ($v_{sh} \geq 20$ km s$^{-1}$), high-density $n_H \geq 10^4$ cm$^{-3}$ solutions with UV fields of 100–1000 $G_0$ are compatible with Class 0 sources.

In Appendix H[5], we show that the choice of other $H_2$ lines representing the warm and hot gas components does not significantly change the shock conditions required to reproduce the observations. We have also investigated various pairs of lines located either in the warm or in the hot component, but these ratios do not constrain well the shock models. A similar trend was noted with CO, where a broad range of shock conditions fit the observations of the warm component alone (Dionatos et al. 2013; Karska et al. 2013), whereas the inclusion of the external UV-irradiation of C-shocks allowed the curvature seen in rotational diagrams to be explained (Karska et al. 2018).

The shock model results presented in Kristensen et al. (2023) allow also for the reconstruction of full rotational diagrams, offering an alternate approach of comparing them to observations. Figure 9 shows a comparison between the rotational diagrams for two of the best models along with the extinction corrected rotational diagram from aperture A of WL 17 (see also Fig. 5), as an example among our observed rotational diagrams. The first model corresponds to a *C*-type shock with a pre-shock density of $n_H = 10^4$ cm$^{-3}$ that best reproduces the S(2)/S(7) ratio. The second model corresponds to a *J*-type shock with a pre-shock density of $n_H = 10^3$ cm$^{-3}$ that, in turn, best reproduces the two components rotational temperatures fit of the observations. Despite the *C*-shock model closely matching the observed S(2)/S(7) line ratio, in the range of velocities studied (10 km s$^{-1}$ < $v_{sh}$ < 30 km s$^{-1}$), it fails to reproduce the curvature seen in the rotational diagrams of our observations. Instead, it is best described by a single temperature component with $T_{rot} \sim 900$ K, a value that lies between that of the two components found in our observations. The *J*-shock model on the other hand, is best described by a two components fit, with $T_{warm} \sim 680$ K and $T_{hot} \sim 2000$ K, values similar to those measured in our sample, and also displays the shift between the two components at a similar $E_{up}$. Despite better predicting the shape of the rotational diagram, model 2 predicts column densities of $N_{hot} = 6.4 \times 10^{16}$ cm$^{-2}$ and $N_{warm} = 9.7 \times 10^{17}$ cm$^{-2}$, which are consistently one to two orders of magnitude lower than the values estimated for our Ophiuchus sources (see Table 3). In contrast, model 1 predicts $N_{tot} = 2.8 \times 10^{19}$ cm$^{-2}$, in line with the observed values. We note here though that column densities predicted in shock models depend heavily on the assumed geometry of the shocks. Since models in Kristensen et al. (2023) assume a simple planar shock morphology whereas real shocks have complex morphologies, the reported differences in column densities are not sufficient to dismiss *J*-shocks. Overall, while comparing the full rotational diagram produced by different shock models to the observations has the benefit of considering all the information from the available transitions, it comes with some significant caveats in terms of the column densities and total fluxes, which rely on the assumed shock sizes and area.

To summarize, $H_2$ observations of outflows from four Class I protostars in Ophiuchus and five Class 0 sources studied by Francis et al. (2025) are consistent with the line ratios in both *C*- and *J*-type shocks. For the examined range of shock velocities, *J*-type shocks are also better at reproducing the overall shape of rotational diagrams, although they seem to underpredict the total column densities. Regardless, both kinds of models show that external irradiation by UV fields of the order of 10–100 in $G_0$ units is required to best match the observations. As a next step, we determine UV radiation using other indirect methods to verify the results from shock models.

### 4.3. The impact of irradiation environment on the protostars in Ophiuchus

To assess the strength of the external UV irradiation on the protostars in Ophiuchus, we considered two additional methods:

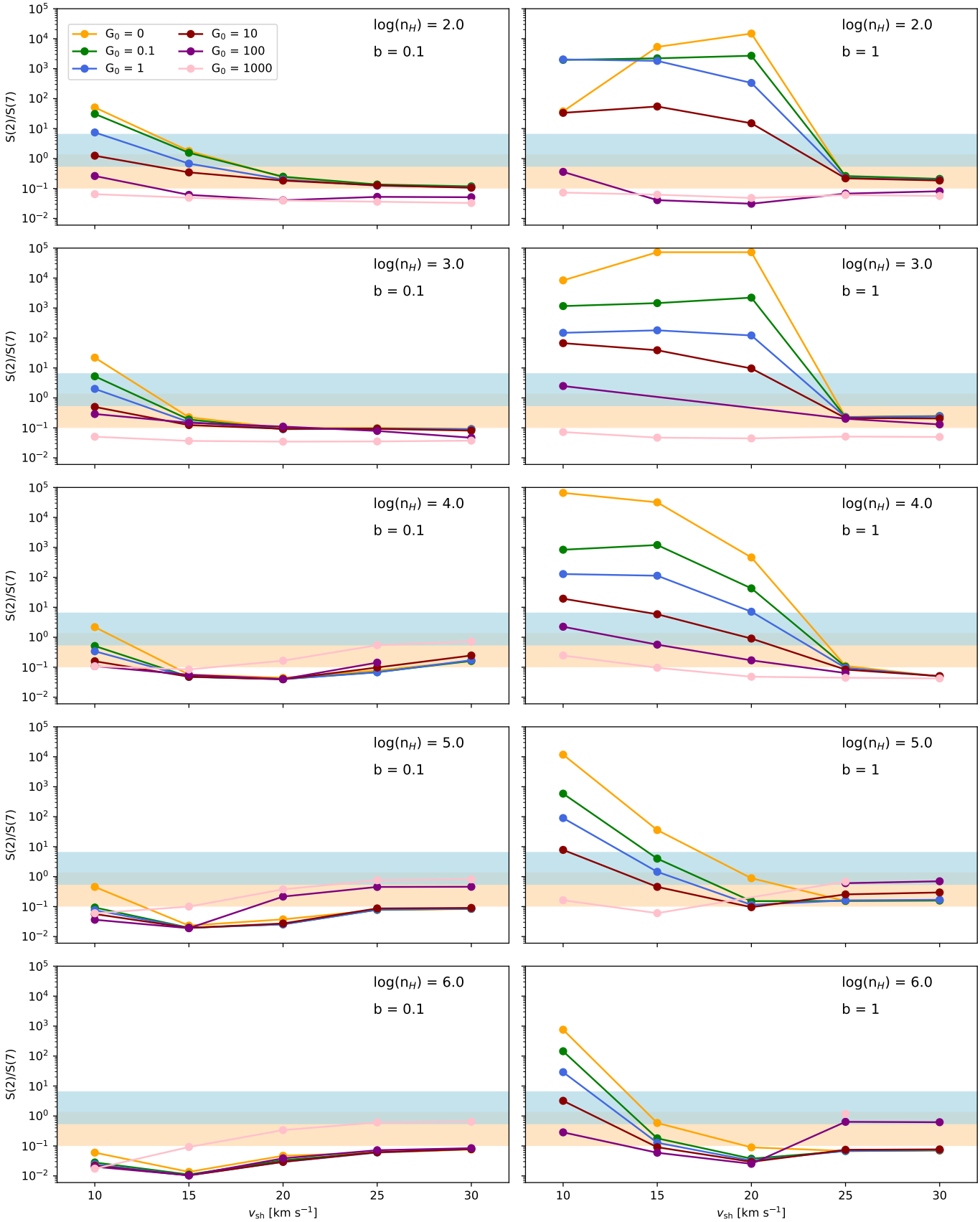


**Fig. 8.** Ratio of the S(2) over the S(7) transition of $H_2$ against the shock velocity for different UV field strengths. The $\log(n_H)$ ranges from 2 to 6 from top to bottom, while magnetic field strength is b = 0.1 for the left column and 1 for the right. For all panels $\zeta = 10^{-17}$ s$^{-1}$, and X(PAH)= $10^{-7}$ are used. The shaded blue region marks the observed range of S(2)/S(7) ratios for the sources in Ophiuchus, while the beige region marks the range for Class 0 sources from Francis et al. (2025). Note that line intensities from Kristensen et al. (2023) are not available for all combinations of model parameters covered in the figure.

**Table 4.** External UV field strengths in units of $G_0$.

| Protostar | HD147899 | S1 (GSS35) | $\sigma$-Sco | $\alpha$-Sco | $\rho$-Oph | UV fields (stars) | UV fields (dust) | Difference |
|---|---|---|---|---|---|---|---|---|
| GSS30-IRS 1 | 149 | 967 | 51 | 2 | 21 | 1190 | 3923 | 0.70 |
| ISO-Oph 21 | 176 | 552 | 52 | 2 | 20 | 803 | 528 | 0.34 |
| [GY92] 197 | 48 | 43 | 51 | 3 | 13 | 157 | 417 | 0.62 |
| WL 17 | 44 | 35 | 51 | 3 | 12 | 146 | 314 | 0.53 |
| ISO-Oph 137 | 31 | 21 | 49 | 3 | 11 | 115 | 344 | 0.67 |

**Notes.** Difference estimated as $1-(UV_{(stars)}/UV_{(dust)})$, except for ISO-Oph 21 where $1-(UV_{(dust)}/UV_{(stars)})$ was used since the UV field estimate from stars is higher.

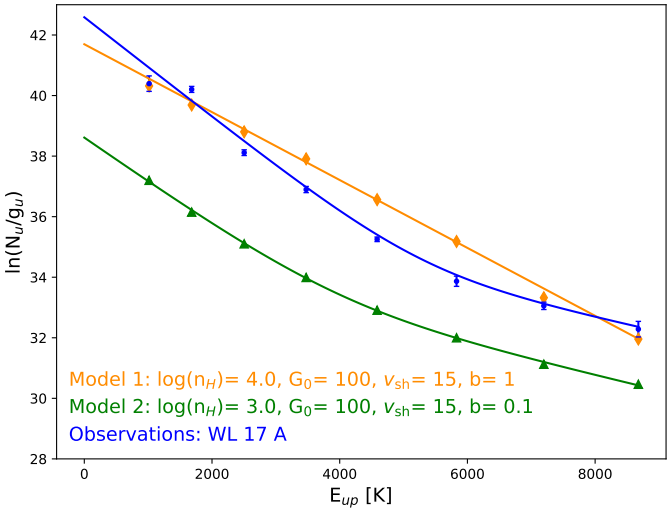


**Fig. 9.** Synthetic rotational diagrams based on the $H_2$ intensities predicted for different combinations of parameters in the Kristensen et al. (2023) shock models. Green triangles show model results for $n_H = 10^3\,cm^{-3}$, $G_0 = 100$, $v_{sh} = 15\,km\,s^{-1}$, $b = 0.1$, $\zeta = 10^{-17}\,s^{-1}$, and $X(PAH) = 10^{-7}$. Orange diamonds show the model with $n_H = 10^4\,cm^{-3}$, $G_0 = 100$, $v_{sh} = 15\,km\,s^{-1}$, $b = 1$, $\zeta = 10^{-17}\,s^{-1}$, and $X(PAH) = 10^{-7}$. Blue points correspond to the observed values for aperture A of WL 17. Solid lines represent the best fit in each case.

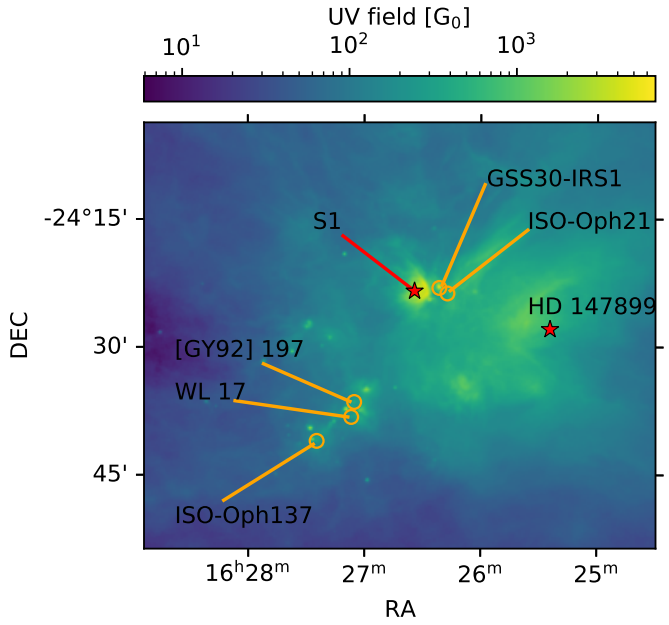


**Fig. 10.** Distribution of the interstellar UV radiation field estimated from the dust continuum emission from *Herschel* under the assumption that all UV radiation from nearby stars was absorbed and re-emitted in the far-IR. The $G_0$ values presented here are likely overestimated due to contribution from thermal dust emission to the FIR continuum. Orange circles mark the location of the protostars, while red stars mark the position of the massive stars S1 and HD147899. $\alpha$-Sco, $\sigma$-Sco, and $\rho$-Oph are located outside the FoV of this figure (similar to Fig. 1).

(i) UV radiation from nearby stars, and (ii) emission from dust assuming that all UV radiation was absorbed and re-emitted in the far-IR. We followed the procedure from Schneider et al. (2016, 2023) to calculate the UV flux at the position of each of our sources and originating from young, massive stars in the region. We considered several nearby stars and/or binaries: $\sigma$-Sco, a B1 III and B1 V type binary (Maíz Apellániz et al. 2021); $\alpha$-Sco, a M1.5 $I_{ab}$ and B2 V type binary (Maíz Apellániz et al. 2021); $\rho$-Oph, a B2 IV and B2 V type binary (Abt 2011); HD 147889, a B2 V type star (Chini 1981; Liseau et al. 1999); and S1 (GSS35), a B3 V type star (Wilking et al. 2005). The total UV luminosity emitted by each of those stars was calculated from

$$L_{UV} = 4\pi^2 r^2 \int_{\lambda_{910}}^{\lambda_{2066}} B(\lambda, T) d\lambda, \quad (4)$$

where $r$ is the stellar radius and $T$ is the effective temperature of the star. Values for the radius and effective temperature of each source are taken from Drilling & Landolt (2000), based on their spectral type. The integration between 910 and 2066 Å covers far-UV photons relevant for the star-forming regions, with energies between 6 and 13.6 eV.

To obtain the UV flux at the position of protostars, the total UV luminosity from nearby stars was scaled by a factor of $(4\pi R^2)^{-1}$, where $R$ is the distance between the source of UV radiation and the respective target in Ophiuchus. Due to the high uncertainties of line-of-sight distances, we assumed all considered objects to be at the same distance from Earth, and thus used the projected distances for the calculation (Schneider et al. 2016, 2023). The distances between the B-type stars and the protostars range between ~4.2–4.3 pc for $\sigma$-Sco, ~4.3–5.2 pc for $\alpha$-Sco, ~2.3–3.1 pc for $\rho$-Oph, ~0.6–1.3 pc for HD147899, and ~0.1–0.9 pc for S1. The resulting UV fluxes for each of our sources are presented in Table 4. It is worth noting that this approach does not correct for dust attenuation, which is significant in dusty molecular clouds, and thus represents only an upper limit to the radiation reaching our protostars.

Perhaps a more accurate way to estimate the UV radiation field in the region is by using the far-IR dust emission. Under the assumption that the UV emission of nearby massive stars is fully absorbed and re-emitted in the far-IR, the local UV radiation field can be estimated from the total FIR intensity between

60 and 200 μm (Kramer et al. 2008; Roccatagliata et al. 2013; Schneider et al. 2016). Here, we use the *Herschel*/PACS continuum intensities at 70 and 160 μm, collected as part of the *Herschel* Gould Belt Survey (Ladjelate et al. 2020), to obtain an estimate of the far-IR intensity ($I_{\rm FIR}$). Then, the total UV field, in units of $G_0$, is given by (Schneider et al. 2016)

$$F_{\rm UV} = \frac{4\pi I_{\rm FIR}\,1000}{1.6}. \quad (5)$$

Figure 10 shows the resulting map of the estimated $F_{\rm UV}$ in the Ophiuchus where our targets are located. To obtain an estimate for each of our sources, we calculated the average $F_{\rm UV}$ in a 12″ aperture around each protostar, corresponding to the resolution of the *Herschel*/PACS continuum (see Table 4).

The two methods presented above yield somewhat different results, with the general trend of the dust-based method predicting values higher by approximately a factor of 3, with the exception of ISO-Oph 21. Since the estimate from the nearby stars is expected to represent an upper limit of the $F_{\rm UV}$, the even higher values determined from the dust could be explained by the dust-based method accounting also for locally produced UV radiation, or from a significant contribution of thermal dust emission from the cloud (see also Schneider et al. 2016).

Both methods predict, however, that GSS30-IRS 1 stands apart from the other sources with a significantly higher $F_{\rm UV}$ flux of the order of $10^3$. ISO-Oph 21 has the second strongest $F_{\rm UV}$, with $F_{\rm UV} \sim 500\,G_0$ based on the $I_{\rm FIR}$ and $\sim$800 $G_0$ based on the stellar emission. The remaining three sources show consistently similar UV fields of $\sim$300–400 $G_0$ based on $I_{\rm FIR}$, and $\sim$100 $G_0$ based on the stellar emission.

These results confirm the presence of significant variance in the UV conditions among protostars in Ophiuchus, allowing us to examine its potential impact on the star formation process. They are consistent with the estimates from UV-irradiated shock models implying UV fields of 10–100 times the average interstellar radiation fields.

## 5. Discussion

### 5.1. Origin of $H_2$ emission in outflows from low-mass protostars

Mapping of pure rotational $H_2$ lines with ISO and the InfraRed Spectrograph (IRS) on board *Spitzer* Space Telescope was a stepping stone to understand the molecular excitation in low-mass protostellar outflows (e.g., van Dishoeck 2004; Neufeld et al. 2006, 2009; Tappe et al. 2012). The low-$J$ ($J < 4$) $H_2$ emission in the prototypical outflow L1157 was associated with the wider cold molecular outflow traced by CO, while that of higher-$J$ ($J > 7$) lines was connected to the precessing jet and more localized shocked regions (Nisini et al. 2010b). On the contrary, the morphology of outflows seen in various $H_2$ transitions was rather similar (Giannini et al. 2011). Such a pattern resembles also our observations of low-mass protostars in Ophiuchus, where only slight variations in extent and opening angles are seen over different transitions even at the much smaller scales probed with JWST (see Section 3.1 and also Fig. G.1[6]).

Detection of several $H_2$ transitions allowed the determination of excitation temperatures of the emitting gas, accounting also for the nonequilibrium $H_2$ ortho-to-para ratios (Neufeld & Yuan 2008; Neufeld et al. 2009). For an assumed power-law distribution of gas temperatures, with the column densities of material at temperature T to $T + dT$ proportional to $T^{-\beta}dT$, the best-fit power-law indices were found in the range 3.8–4.2 toward BHR71, L1448, and NGC 2071 (Giannini et al. 2011). The range of indices of 3.9–5.4 in L1157 indicated a large variation in the physical parameters along the outflows (Nisini et al. 2010b), in line with MIRI maps covering smaller spatial scales (Fig. 6).

Nisini et al. (2010b) and Giannini et al. (2011) also provide temperature estimates for selected locations along the outflows based on linear fits to the S(0)-S(2) and S(5)-S(7) lines, corresponding to a warm and hot gas component, respectively. The resulting values of $T_{\rm warm} \sim$ 240–400 K and $T_{\rm hot} \sim$ 1000–1500 K are lower than the ones estimated in this work: $540 \pm 70$ K and $2000 \pm 700$ K for warm and hot component, respectively (Section 4.1). However, the difference in temperature could be due to the inclusion of the S(0) line and the lack of detections of higher-$J$ lines due to limited sensitivity of *Spitzer*.

Important insights into the origin of hot molecular gas were enabled by *Herschel*, and the detection of high-$J$ CO lines up to $J = 48$ and at a resolution of 9.4″, even toward outflows from low-mass protostars (Herczeg et al. 2012). Similar to $H_2$, CO rotational diagrams revealed two dominant gas physical components with surprisingly similar temperatures of the warm component of ~300 K toward all low-mass protostars (Karska et al. 2013; Green et al. 2013; Manoj et al. 2013). This gas temperature is consistent with the *Spitzer* results, but about 200 K lower than the respective warm component seen in $H_2$ with MIRI (Section 4.1).

To investigate possible changes of gas temperature as the protostar evolves, Figure 11 shows a comparison of rotational temperatures of $H_2$ and CO toward Class 0 and I objects. The $H_2$ results for Class 0 objects are adopted from a recent study of on-source positions of five objects by Francis et al. (2025), whereas Class I temperatures refer to outflows from Ophiuchus protostars (Section 4), and a single source in Taurus – TMC1 (Tychoniec et al. 2024). The distribution of rotational temperatures based on CO and for Class 0 and I objects are adopted from a consistent analysis of ~90 protostars with *Herschel*/PACS (Karska et al. 2018).

We find that the distribution of $T_{\rm warm}$ and $T_{\rm hot}$ using $H_2$ is tentatively shifted toward higher values for less evolved protostars (top panel of Fig. 11). However, the range of the hot component temperature is relatively broad for both Class 0 and I objects, reaching values of up to 3000 K. The difference is reflected by the average $H_2$ rotational temperatures for the Class 0 objects of $660 \pm 100$ K (warm) and $2200 \pm 600$ K (hot) versus for the Class I objects of $520 \pm 70$ K (warm) and $1800 \pm 550$ K (hot).

Similar trend of decreasing rotational temperature with the evolutionary stage was not present using CO observations (bottom panel of Fig. 11). It is worth noting that the maximum temperatures obtained with CO did not exceed ~1100 K, and the distribution of the hot component temperatures with *Herschel* of $760 \pm 170$ K (Karska et al. 2018) suggests that high-$J$ CO lines might trace a less energetic part of the flow than $H_2$.

A combined analysis of $H_2O$ and CO from *Herschel* provided solid evidence that both gas temperature components discussed above originate in non-dissociative shocks, with the hot component additionally tracing regions irradiated by UV radiation (Karska et al. 2014a, 2018; Kristensen et al. 2017). The impact of far-UV photons was further confirmed by high abundances of OH and other hydrides in the immediate surrounding of both low- and high-mas protostars (Wampfler et al. 2013; Benz et al. 2016). The $H_2$ line ratios measured toward Ophiuchus protostars, favor the origin of $H_2$ emission in the UV-irradiated shocks (Section 4.2). The ratio of the S(2)/S(7) lines

[6] Appendix G is available online here.

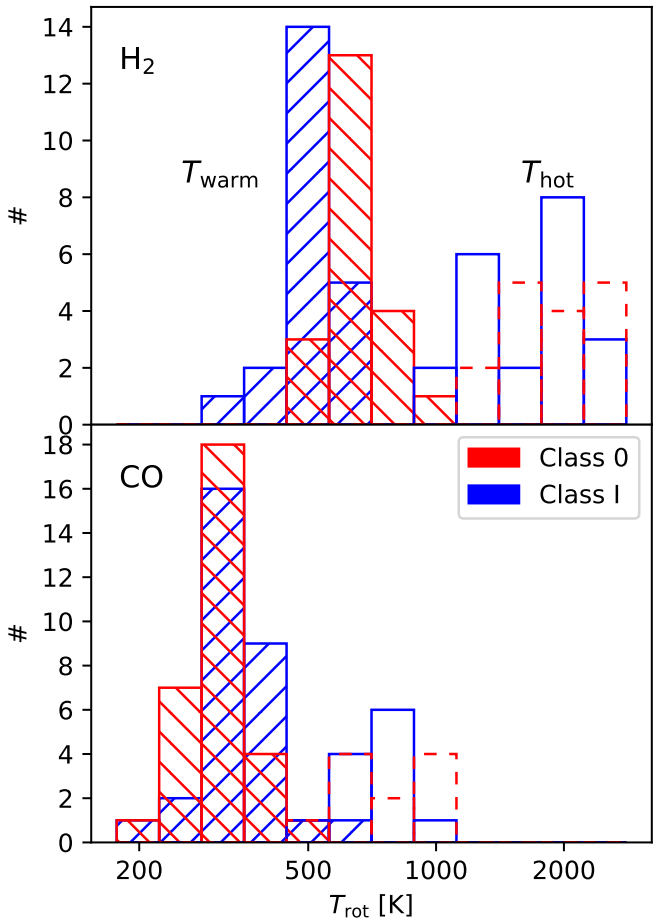


**Fig. 11.** Distribution of the rotational temperatures of $H_2$ (top) and high-$J$ CO (bottom) in low-mass protostars. Temperatures in Class 0 protostars are shown in red, and in Class I sources in blue. The warm gas component is shown in stripped bins, and the hot one in clear bins. $H_2$ results for Class 0 protostars are adopted from Francis et al. (2025), and CO results for both Class 0 and I are from Karska et al. (2018).

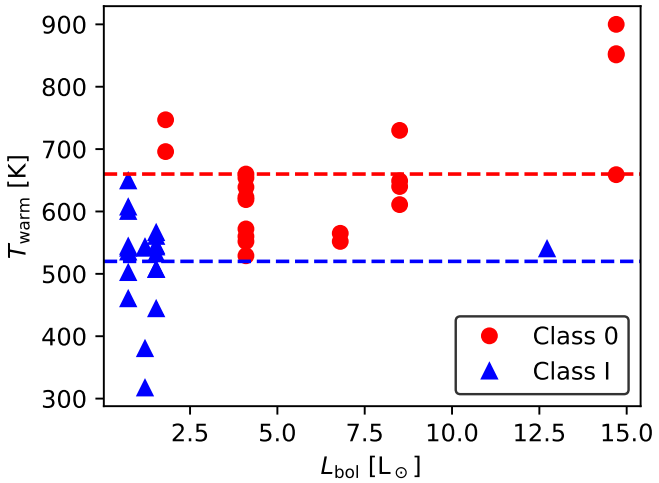


**Fig. 12.** Temperature of the warm gas component along the protostellar outflows over the bolometric luminosity of the corresponding driving source. Blue triangles show the Class I sources from this work and Tychoniec et al. (2024), while red circles show the Class 0 sample from Francis et al. (2025). Dashed blue and red lines show the mean values for the Class I and 0 sources, respectively.

for Class 0 objects is at the lower end of values for Class I objects (Fig. 7), which would imply higher UV-fields in those sources assuming the same gas densities (Fig. 8). Consequently, gas temperatures would be higher for Class 0 objects, consistent with the results of our rotational analysis (Fig. 11). However, the densities of the envelopes of Class 0 objects are typically higher than for Class I objects (e.g., Kristensen et al. 2012), which should reduce the impact of external UV radiation, in particular for the outflow positions closer to the central source. The small variation in excitation conditions among the Oph sources despite the significant difference of the UV field strength from the surrounding environment, as estimated in Sect. 4.3, suggests that the environmental UV radiation has little to no effect on the excitation within protostellar outflows. We note though that the positions examined in this work are located very close to the protostars, and therefore likely to be well shielded from the external UV radiation. In addition, some UV radiation can be also produced in-situ by the shock itself, but velocities above 30 km s$^{-1}$, higher than measured using velocity-resolved $H_2O$ lines for low-mass protostars, would be required (Lehmann et al. 2020, 2022; Kristensen et al. 2023). Hence, accretion shocks and high velocity shocks along the protostellar jets are more likely sources for the UV radiation required to reproduce the excitation conditions observed in the Oph sources. Such an origin for the UV radiation also aligns with the slightly higher excitation conditions seen in Class 0 sources, since they are in general believed to have higher accretion rates and drive more powerful jets. Prompt OH emission, shown to probe well the UV field within protostellar outflows (e.g., Neufeld et al. 2024), could serve as an independent approach to confirm such evolutionary trends. Regardless, observations of larger number of sources with additional line tracers are needed to confirm the trend of higher gas temperatures in Class 0 objects and its interpretation.

In addition to the evolutionary stage, source properties such as the bolometric luminosity or envelope mass have also been closely associated with outflow properties (e.g., Cabrit & Bertout 1992; Yıldız et al. 2015; Mottram et al. 2017; Skretas & Kristensen 2022). To explore whether the observed shifts in temperatures and excitation conditions are associated with source properties, instead of the evolutionary stage of the sources, we look into the comparison of the warm component temperature over the bolometric luminosity of the source, for the same sample that was used in Figs. 7 and 11. Even though the sample is small, Fig. 12 shows no clear correlation between the source properties and the resulting $H_2$ temperatures. In contrast, the slight shift between the Class I and Class 0 sources, initially noted in Fig. 11, is apparent. The lack of impact of the source properties on the excitation conditions within the outflows are further supported by the remarkable similarity of temperatures between low- and high-mass sources reported in Francis et al. (2025).

To summarize, $H_2$ emission from protostellar outflows in Ophiuchus likely originates in shocks irradiated by UV fields produced in shocks along the protostellar jets or by accretion onto the protostar. By comparisons with other protostars observed with JWST (Francis et al. 2025), we find a trend of decreasing $H_2$ rotational temperatures from Class 0 to Class I objects. In addition, we find no clear connection between the driving source properties and the excitation conditions within their outflows. The upcoming analysis of larger samples of

**Table 5.** Mass outflow rates and kinetic luminosities.

| | $\dot{M}$ ($\times 10^{-9}$ M$_\odot$ yr$^{-1}$) | $L_{\rm kin}$ ($\times 10^{-5}$ L$_\odot$) |
|---|---|---|
| GSS30-IRS 1 | 27.8 | 50.4 |
| [GY92] 197 | 5.0 | 9.1 |
| WL 17 | 4.2 | 7.5 |
| ISO-Oph 137 | 6.7 | 12.2 |

protostars with JWST will certainly allow us to draw more solid conclusions on the origin of $H_2$ emission.

### 5.2. Gas energetics in outflow shocks

Theoretical studies of line cooling from dense cores predict that most of the released energy is emitted in mid-IR emission from $H_2$, followed by far-IR lines fines structure lines of [O I], high-$J$ CO, and $H_2O$ rotational transitions (Goldsmith & Langer 1978; Takahashi et al. 1983; Neufeld & Kaufman 1993; Ceccarelli et al. 1996; Doty & Neufeld 1997). Similarly, $H_2$ emission is the most significant cooling pathway for shock excited gas in protostellar outflows (Kaufman & Neufeld 1996; Flower & Pineau Des Forêts 2010; Kristensen et al. 2023). Thus, JWST observations of $H_2$ lines allow us to study the energetics of protostars, at spatial scales significantly smaller than previously achieved with *Spitzer* (e.g., Nisini et al. 2010b; Giannini et al. 2011).

For a non-dissociative shock propagating in a medium with a pre-shock density of $n_{\rm H} \sim 10^4$ cm$^{-3}$ and $v_{\rm sh} \sim 10$–$50$ km s$^{-1}$, $H_2$ luminosity corresponds to ~20–70% of the total outflow cooling rate Kaufman & Neufeld (1996). This allows for the calculation of the total kinetic luminosity ($L_{\rm kin}$) of the outflow from the observed rotational lines of $H_2$ (Maret et al. 2009):

$$L_{\rm kin} = \frac{1}{2}\dot{M}v_{\rm sh}^2 = \frac{(1-f_m)}{f_c}L_{\rm H_2}, \quad (6)$$

where $(1-f_m)$ is the fraction of shock mechanical energy that is converted into internal excitation and $f_c$ is the fraction of cooling attributed to the $H_2$ emission. In turn, the outflow mass rate can be calculated as

$$\dot{M} = 1.24\times10^{-2}\frac{(1-f_m)}{f_c}\left(\frac{L_{\rm H_2}}{\rm L_\odot}\right)\left(\frac{v}{\rm km/s}\right)^{-2} {\rm M_\odot yr^{-1}}. \quad (7)$$

Adopting $f_c = 0.25$–$0.5$, $(1-f_m) = 0.75$, and $v_{\rm sh} \sim 15$–$35$ km s$^{-1}$, Maret et al. (2009) report mass loss rates of the order of $10^{-6}$ M$_\odot$ yr$^{-1}$ for five Class 0 sources in NGC 1333 in Perseus.

We calculated the mass loss rate for the four outflow sources in Ophiuchus, by summing up the $H_2$ line intensity measured in all the apertures (see Table C.1). In addition, we adopted $f_c = 0.5$ and $(1-f_m) = 0.75$, similar to Maret et al. (2009), and assumed $v_{\rm sh} = 15$ km s$^{-1}$, which best matches our observations (see Section 4.2). We find values of $\dot{M} \sim 4$–$7\times10^{-9}$ M$_\odot$ yr$^{-1}$, except for GSS30-IRS 1, where $\dot{M} = 2.8\times10^{-8}$ M$_\odot$ yr$^{-1}$. The significantly higher value measured for GSS30-IRS 1 reflects the much stronger $H_2$ emission compared to the rest of the sources, and could be partly due to inclusion of the extended and bright protostellar envelope in some of the apertures (Table 5).

It is worth noting that the values estimated here represent lower limits for the true $\dot{M}$ values for our outflows due to the limited FoV of MIRI. The mass loss rates of $\sim7.8\times10^{-7}$ M$_\odot$ yr$^{-1}$ were obtained using low-$J$ CO lines for the entire outflow from [GY92] 197 (van der Marel et al. 2013), so almost 2 orders of magnitude higher than the JWST estimates. However, those CO observations trace the entrained outflow gas, not the shocked gas inside the cavity seen in $H_2$. Nevertheless, Nisini et al. (2010b) found a good agreement between the outflow parameters estimated from $H_2$ and CO observations in L1157 (Bachiller et al. 2001), where the full extent of the outflow was considered. This study supported the scenario that the CO outflow is accelerated by the $H_2$ flow; however, the angular resolution of existing CO observations for protostars in Ophiuchus is too low for similar comparisons.

**Table 6.** Mass outflow rates using Eq. (8).

| | $\dot{M}_{\rm warm}$ $\left(\times10^{-8}{\rm M_\odot yr^{-1}}\right)$ | $\dot{M}_{\rm hot}$ $\left(\times10^{-10}{\rm M_\odot yr^{-1}}\right)$ |
|---|---|---|
| GSS30-IRS 1 | 11.4 | 14.0 |
| [GY92] 197 | 11.4 | 29.4 |
| WL 17 | 1.8 | 10.0 |
| ISO-Oph 137 | 0.6 | 0.7 |

**Notes.** The values for GSS30-IRS 1 are derived only for the single outflow lobe covered by our observations. For all other sources the values represent the sum over the two outflow lobes.

An alternative calculation method proposed by Delabrosse et al. (2024) offers a more direct approach to estimate mass loss rates using the $H_2$ lines within the MIRI range. For this method, the mass loss rate is given by

$$\dot{M} = 2m_{\rm H}N_{\rm H_2}l_{\rm perp}\frac{v_{\rm rad}}{cos(i)}, \quad (8)$$

where $m_{\rm H}$ is the hydrogen atom mass, $N_{\rm H_2}$ the column density of $H_2$, $l_{\rm perp}$ the width of the molecular outflow, $v_{\rm rad}$ the radial velocity of the flow, and $i$ the inclination angle of the outflow. Table 6 shows the resulting mass loss rates for all sources, calculated separately for the warm and hot components of the outflows. The mass loss rates were calculated independently for each lobe and then summed to give the total rate for each source. For GSS30-IRS 1, where only one lobe is covered by our FoV, the given value corresponds only to the observed outflow lobe. We used the column densities derived from the rotational diagram analysis (Table 3). For the wide angle outflows of [GY92] 197 and WL 17, we used the average column density of the three apertures spanning the width of the outflow lobes (In both cases, apertures A, C, and D and E, G, and H, respectively, for each lobe). For GSS30-IRS 1, we used the values derived from aperture C due to the higher uncertainties in the cold component properties in apertures A and B, caused by the non-detection of the S(1) and S(2) lines due to the bright continuum (see Sect. 3.2). For ISO-Oph 137, we used the values from the apertures further away from the source (B and D) as the column densities derived for apertures A and C are likely overestimated. The radial velocities for each source were estimated from the Gaussian fitting (Table 2) and using the same apertures (or averages) as for the $N_{\rm H_2}$. The width of the outflows ($l_{\rm perp}$) was measured directly from the integrated intensity maps, using the S(3) and S(7) transitions for the warm and hot components, respectively. Finally, for the inclination angle, we adopted the literature values of 60° for GSS30-IRS 1 (Artur de la Villarmois et al. 2019), and 34° for WL 17 (Shoshi et al. 2024), and for the edge-on disks of [GY92] 197 (Michel et al. 2023) and ISO-Oph 137 (van Kempen et al. 2009) we assumed $i = 80°$.

Overall, we find a broad range of mass loss rate among our sources, with values ranging from $\sim 10^{-7}$–$10^{-9}\,M_\odot\,yr^{-1}$ for the warm and $\sim 10^{-9}$–$10^{-11}\,M_\odot\,yr^{-1}$ for the hot component, respectively. Despite that fact that we only measure a single outflow lobe, the highest values are associated with the outflow of GSS30-IRS 1, the brightest source in our sample (see Table 1). Surprisingly, the outflow of [GY92] 197 also shows directly comparable mass loss rates, despite having an order of magnitude lower bolometric luminosity. In addition to that, the lowest mass loss rates we find are associated with ISO-Oph 137, a source with a comparable bolometric luminosity to that of [GY92] 197. This result may suggest that the morphology of the outflow, collimated or wide-angled, has an impact on the estimated outflow properties, with wide-angled outflows displaying higher outflow rates compared to collimated flows for sources with similar bolometric luminosities. Our sample though is extremely limited to draw any safe conclusions, and additional observations would be required to confirm or refute this suggestion.

In addition, we find that the warm component carries most of the mass in the outflow, with mass loss rates approximately two orders of magnitude higher that those of the hot component. This difference directly reflects the two orders of magnitude difference seen in the column densities of the two components. Comparing our results with previous works employing the same method we find that our results lie between the values estimated for the hot gas component of the Class I source DG Tau (Delabrosse et al. 2024) and those estimated for the Class 0 source HH211 (Caratti o Garatti et al. 2024). Namely, the mass loss rates for the hot component of ISO-Oph 137 ($\sim 10^{-11}\,M_\odot\,yr^{-1}$) are directly comparable to the results of Delabrosse et al. (2024), while the mass loss rates for the warn component of GSS30-IRS 1 and [GY92] 197 ($\sim 10^{-7}\,M_\odot\,yr^{-1}$) appear comparable to those of HH211. Finally, the mass loss rate for [GY92] 197, estimated using the "moving slab" method is also directly comparable to the low-$J$ CO estimate of $\sim 7.8 \times 10^{-7}\,M_\odot\,yr^{-1}$ (van der Marel et al. 2013). This results suggest that indeed, this method yields more accurate results, as it overcomes many of the limitations of the luminosity method discussed above. To summarize, our observations highlight the potential of JWST in constraining the energetics of outflows via the $H_2$ emission.

## 6. Conclusions

In this work, we present JWST MIRI/MRS observations of 5 Class I protostars in the Ophiuchus molecular cloud. We analyze the $H_2$ excitation associated with the protostellar outflows, and study the origin of the emission in shocks irradiated by external UV photons. The conclusions are as follows:

- $H_2$ outflows are detected in four out of five sources. These outflows display two distinct morphologies. Two of them appear narrow and well collimated (GSS30-IRS 1 and ISO-Oph 137), and the other two show wide opening angles with well-defined cavities (WL 17 and [GY92] 197).
- Several atomic and ionic emission lines are detected, with the most common being those of [Ne II], [Fe II], and [S I]. Their emission is associated with narrow, well-collimated jets, even in cases in which the $H_2$ emission traces outflow cavities.
- The line emission along the outflows shows no significant velocity shifts between the outflow lobes, constraining the line-of-sight velocity of the $H_2$ outflows to $v < 90\,km\,s^{-1}$. The only case in which a noticeable velocity shift is detected is the [Ne] II line at 12.8 μm in WL 17.
- Rotational diagram analysis reveals that the $H_2$ emission within the protostellar outflows is described well by a two-temperature-components model. The two components are found to have rotational temperatures in the range of $T_{warm} \sim 500$–$600\,K$ and $T_{hot} \sim 1000$–$3000\,K$.
- Based on shock model results from Kristensen et al. (2023), the external UV irradiation is found to have a significant impact on the S(2)/S(7) $H_2$ line ratios. By contrast, the cosmic ray ionization rate and PAH abundance appear to have minimal to no impact. The magnetic field strength seems to shift the observed behavior of the ratio to higher velocities, by allowing higher-velocity $C$-type shocks.
- The observed S(2)/S(7) ratios agree with predictions from $C$-type shocks at pre-shock densities of $n_H \geq 10^4\,cm^{-3}$, as well as with low-density ($n_H \leq 10^3\,cm^{-3}$), low-velocity ($v_{sh} \leq 15\,km\,s^{-1}$) $J$-type shocks. The $J$-type shocks reproduce the observed positive curvature of the rotational diagrams better but at the same time underestimate the column densities.
- The observations require the presence of substantial (∼10–100 $G_0$) UV irradiation in shock models. The strength of the UV fields is higher than that derived for the nearby diffuse cloud (van Dishoeck & Black 1986), suggesting that some UV photons originate from the accretion shocks in protostellar systems.

Overall, our results present a detailed view of four different protostellar outflows at close distances from their driving source, highlighting their morphological differences and physical properties. The lack of substantial variation in outflow properties, despite the predicted variation in external UV field and model results, suggests that more work is still required, both to observationally constrain the UV field strength and also to accurately model its impact.

## Data availability

Appendices D-H are available online on Zenodo.

*Acknowledgements.* We are grateful to Ewine F. van Dishoeck for useful insights and suggestions enhancing the overall quality of the manuscript. This work is based on observations made with the NASA/ESA/CSA James Webb Space Telescope. The data were obtained from the Mikulski Archive for Space Telescopes at the Space Telescope Science Institute, which is operated by the Association of Universities for Research in Astronomy, Inc., under NASA contract NAS 5-03127 for JWST. These observations are associated with program ID 1959. This publication is also based upon work from COST Action PLANETS CA22133, supported by COST (European Cooperation in Science and Technology). AK acknowledges support from the Polish National Science Center SONATA BIS grant No. 2024/54/E/ST9/00314. Astrochemistry in Leiden is supported by funding from the European Research Council (ERC) under the European Union's Horizon 2020 research and innovation programme (grant agreement No. 101019751 MOLDISK), by the Netherlands Research School for Astronomy (NOVA), and by grant TOP-1 614.001.751 from the Dutch Research Council (NWO). MF acknowledges support from the Polish National Agency for Academic Exchange grant No. BPN/BEK/2023/1/00036/DEC/01 and from the Polish National Science Centre SONATA grant No. 2022/47/D/ST9/00419. The material is based upon work supported by NASA under award number 80GSFC24M0006 (M.S.).

## References

Abt, H. A. 2011, AJ, 141, 165
Arce, H. G., Mardones, D., Corder, S. A., et al. 2013, ApJ, 774, 39
Argyriou, I., Glasse, A., Law, D. R., et al. 2023, A&A, 675, A111
Artur de la Villarmois, E., Jørgensen, J. K., Kristensen, L. E., et al. 2019, A&A, 626, A71
Assani, K. D., Harsono, D., Ramsey, J. P., et al. 2024, A&A, 688, A26

Bachiller, R., Pérez Gutiérrez, M., Kumar, M. S. N., & Tafalla, M. 2001, A&A, 372, 899
Bai, X.-N., Ye, J., Goodman, J., & Yuan, F. 2016, ApJ, 818, 152
Bally, J. 2016, ARA&A, 54, 491
Benz, A. O., Bruderer, S., van Dishoeck, E. F., et al. 2016, A&A, 590, A105
Bontemps, S., André, P., Kaas, A. A., et al. 2001, A&A, 372, 173
Brandner, W., Sheppard, S., Zinnecker, H., et al. 2000, A&A, 364, L13
Bushouse, H., Eisenhamer, J., Dencheva, N., et al. 2024, JWST Calibration Pipeline
Bussmann, R. S., Wong, T. W., Hedden, A. S., Kulesa, C. A., & Walker, C. K. 2007, ApJ, 657, L33
Cabrit, S., & Bertout, C. 1992, A&A, 261, 274
Caratti o Garatti, A., Ray, T. P., Kavanagh, P. J., et al. 2024, A&A, 691, A134
Ceccarelli, C., Hollenbach, D. J., & Tielens, A. G. G. M. 1996, ApJ, 471, 400
Chini, R. 1981, A&A, 99, 346
Christiaens, V., Gonzalez, C., Farkas, R., et al. 2023, J. Open Source Software, 8, 4774
Delabrosse, V., Dougados, C., Cabrit, S., et al. 2024, A&A, 688, A173
Dionatos, O., Jørgensen, J. K., Green, J. D., et al. 2013, A&A, 558, A88
Doty, S. D., & Neufeld, D. A. 1997, ApJ, 489, 122
Drilling, J. S., & Landolt, A. U. 2000, in Allen's Astrophysical Quantities, ed. A. N. Cox, 381
Duchêne, G., Bouvier, J., Bontemps, S., André, P., & Motte, F. 2004, A&A, 427, 651
Enoch, M. L., Evans, N. J. I., Sargent, A. I., & Glenn, J. 2009, ApJ, 692, 973
Evans, N. J. I., Dunham, M. M., Jørgensen, J. K., et al. 2009, ApJS, 181, 321
Fall, S. M., Krumholz, M. R., & Matzner, C. D. 2010, ApJ, 710, L142
Ferreira, J. 1997, A&A, 319, 340
Flower, D. R. 1997, MNRAS, 288, 627
Flower, D. R., & Pineau des Forêts, G. 2003, MNRAS, 343, 390
Flower, D. R., & Pineau Des Forêts, G. 2010, MNRAS, 406, 1745
Flower, D. R., & Roueff, E. 1998, J. Phys. B At. Mol. Phys., 31, 2935
Flower, D. R., Roueff, E., & Zeippen, C. J. 1998, J. Phys. B At. Mol. Phys., 31, 1105
Francis, L., van Dishoeck, E. F., Caratti o Garatti, A., et al. 2025, A&A, 694, A174
Frank, A., Ray, T. P., Cabrit, S., et al. 2014, in Protostars and Planets VI, eds. H. Beuther, R. S. Klessen, C. P. Dullemond, & T. Henning, 451
Friesen, R. K., Pon, A., Bourke, T. L., et al. 2018, ApJ, 869, 158
Giannini, T., Nisini, B., Neufeld, D., et al. 2011, ApJ, 738, 80
Godard, B., Pineau des Forêts, G., Lesaffre, P., et al. 2019, A&A, 622, A100
Goldsmith, P. F., & Langer, W. D. 1978, ApJ, 222, 881
Green, J. D., Evans, N. J. I., Jørgensen, J. K., et al. 2013, ApJ, 770, 123
Green, J. D., Yang, Y.-L., Evans, N. J. I., et al. 2016, AJ, 151, 75
Greenfield, P., & Miller, T. 2016, Astron. Comput., 16, 41
Harsono, D., Bjerkeli, P., Ramsey, J. P., et al. 2023, ApJ, 951, L32
Herczeg, G. J., Karska, A., Bruderer, S., et al. 2012, A&A, 540, A84
Karska, A., Herczeg, G. J., van Dishoeck, E. F., et al. 2013, A&A, 552, A141
Karska, A., Herpin, F., Bruderer, S., et al. 2014a, A&A, 562, A45
Karska, A., Kristensen, L. E., van Dishoeck, E. F., et al. 2014b, A&A, 572, A9
Karska, A., Kaufman, M. J., Kristensen, L. E., et al. 2018, ApJS, 235, 30
Kaufman, M. J., & Neufeld, D. A. 1996, ApJ, 456, 611
Kramer, C., Cubick, M., Röllig, M., et al. 2008, A&A, 477, 547
Kristensen, L. E., van Dishoeck, E. F., Bergin, E. A., et al. 2012, A&A, 542, A8
Kristensen, L. E., van Dishoeck, E. F., Mottram, J. C., et al. 2017, A&A, 605, A93
Kristensen, L. E., Godard, B., Guillard, P., Gusdorf, A., & Pineau des Forêts, G. 2023, A&A, 675, A86
Ladjelate, B., André, P., Könyves, V., et al. 2020, A&A, 638, A74
Law, D. R., E. Morrison, J., Argyriou, I., et al. 2023, AJ, 166, 45
Le Gouellec, V. J. M., Maury, A. J., & Hull, C. L. H. 2023, A&A, 671, A167
Lê, N., Tram, L. N., Karska, A., et al. 2024, A&A, 690, A191
Lee, C.-F. 2020, A&A Rev., 28, 1
Lehmann, A., Godard, B., Pineau des Forêts, G., & Falgarone, E. 2020, A&A, 643, A101
Lehmann, A., Godard, B., Pineau des Forêts, G., Vidal-García, A., & Falgarone, E. 2022, A&A, 658, A165
Leous, J. A., Feigelson, E. D., Andre, P., & Montmerle, T. 1991, ApJ, 379, 683
Lesaffre, P., Pineau des Forêts, G., Godard, B., et al. 2013, A&A, 550, A106
Lindberg, J. E., Charnley, S. B., Jørgensen, J. K., Cordiner, M. A., & Bjerkeli, P. 2017, ApJ, 835, 3
Liseau, R., White, G. J., Larsson, B., et al. 1999, A&A, 344, 342
Loren, R. B., Wootten, A., & Wilking, B. A. 1990, ApJ, 365, 269
Maíz Apellániz, J., Barbá, R. H., Fariña, C., et al. 2021, A&A, 646, A11
Mangum, J. G., & Shirley, Y. L. 2015, PASP, 127, 266
Manoj, P., Watson, D. M., Neufeld, D. A., et al. 2013, ApJ, 763, 83
Maret, S., Bergin, E. A., Neufeld, D. A., et al. 2009, ApJ, 698, 1244
Martin, P. G., & Mandy, M. E. 1995, ApJ, 455, L89
Melnick, G. J., & Kaufman, M. J. 2015, ApJ, 806, 227
Michel, A., Sadavoy, S. I., Sheehan, P. D., et al. 2023, AJ, 166, 184
Mirocha, A., Karska, A., Gronowski, M., et al. 2021, A&A, 656, A146
Motte, F., Andre, P., & Neri, R. 1998, A&A, 336, 150
Mottram, J. C., Kristensen, L. E., van Dishoeck, E. F., et al. 2014, A&A, 572, A21
Mottram, J. C., van Dishoeck, E. F., Kristensen, L. E., et al. 2017, A&A, 600, A99
Nakamura, F., Kamada, Y., Kamazaki, T., et al. 2011, ApJ, 726, 46
Narang, M., Manoj, P., Tyagi, H., et al. 2024, ApJ, 962, L16
Neufeld, D. A., & Dalgarno, A. 1989, ApJ, 344, 251
Neufeld, D. A., & Kaufman, M. J. 1993, ApJ, 418, 263
Neufeld, D. A., & Yuan, Y. 2008, ApJ, 678, 974
Neufeld, D. A., Melnick, G. J., Sonnentrucker, P., et al. 2006, ApJ, 649, 816
Neufeld, D. A., Nisini, B., Giannini, T., et al. 2009, ApJ, 706, 170
Neufeld, D. A., Manoj, P., Tyagi, H., et al. 2024, ApJ, 966, L22
Nisini, B. 2003, Ap&SS, 287, 207
Nisini, B., Benedettini, M., Codella, C., et al. 2010a, A&A, 518, L120
Nisini, B., Giannini, T., Neufeld, D. A., et al. 2010b, ApJ, 724, 69
Nisini, B., Navarro, M. G., Giannini, T., et al. 2024, ApJ, 967, 168
Nutter, D., Ward-Thompson, D., & André, P. 2006, MNRAS, 368, 1833
Ortiz-León, G. N., Loinard, L., Kounkel, M. A., et al. 2017, ApJ, 834, 141
Podio, L., Tabone, B., Codella, C., et al. 2021, A&A, 648, A45
Pontoppidan, K. M., Dullemond, C. P., van Dishoeck, E. F., et al. 2005, ApJ, 622, 463
Pontoppidan, K. M., Salyk, C., Banzatti, A., et al. 2024, ApJ, 963, 158
Pudritz,, R. E., Ouyed, R., Fendt, C., & Brandenburg, A. 2007, in Protostars and Planets V, eds. B. Reipurth, D. Jewitt, & K. Keil, 277
Pudritz, R. E., & Norman, C. A. 1983, ApJ, 274, 677
Ray, T. P., & Ferreira, J. 2021, New Astron. Rev., 93, 101615
Ray, T. P., McCaughrean, M. J., Caratti o Garatti, A., et al. 2023, Nature, 622, 48
Roccatagliata, V., Preibisch, T., Ratzka, T., & Gaczkowski, B. 2013, A&A, 554, A6
Schneider, N., Bontemps, S., Motte, F., et al. 2016, A&A, 591, A40
Schneider, N., Bonne, L., Bontemps, S., et al. 2023, Nat. Astron., 7, 546
Shoshi, A., Harada, N., Tokuda, K., et al. 2024, ApJ, 961, 228
Skretas, I. M., & Kristensen, L. E. 2022, A&A, 660, A39
Skretas, I. M., Karska, A., Wyrowski, F., et al. 2023, A&A, 679, A66
Takahashi, T., Silk, J., & Hollenbach, D. J. 1983, ApJ, 275, 145
Tamura, M., Sato, S., Suzuki, H., Kaifu, N., & Hough, J. H. 1990, ApJ, 350, 728
Tappe, A., Forbrich, J., Martín, S., Yuan, Y., & Lada, C. J. 2012, ApJ, 751, 9
Tychoniec, Ł., Manara, C. F., Rosotti, G. P., et al. 2020, A&A, 640, A19
Tychoniec, Ł., van Dishoeck, E. F., van't Hoff, M. L. R., et al. 2021, A&A, 655, A65
Tychoniec, Ł., van Gelder, M. L., van Dishoeck, E. F., et al. 2024, A&A, 687, A36
van der Marel, N., Kristensen, L. E., Visser, R., et al. 2013, A&A, 556, A76
van Dishoeck, E. F. 2004, ARA&A, 42, 119
van Dishoeck, E. F., & Black, J. H. 1986, ApJS, 62, 109
van Dishoeck, E. F., & Black, J. H. 1989, ApJ, 340, 273
van Dishoeck, E. F., Kristensen, L. E., Benz, A. O., et al. 2011, PASP, 123, 138
van Dishoeck, E. F., Kristensen, L. E., Mottram, J. C., et al. 2021, A&A, 648, A24
van Kempen, T. A., van Dishoeck, E. F., Salter, D. M., et al. 2009, A&A, 498, 167
Wampfler, S. F., Bruderer, S., Karska, A., et al. 2013, A&A, 552, A56
Weintraub, D. A., Kastner, J. H., Griffith, L. L., & Campins, H. 1993, AJ, 105, 271
White, G. J., Drabek-Maunder, E., Rosolowsky, E., et al. 2015, MNRAS, 447, 1996
Wilking, B. A., Lada, C. J., & Young, E. T. 1989, ApJ, 340, 823
Wilking, B. A., Meyer, M. R., Robinson, J. G., & Greene, T. P. 2005, AJ, 130, 1733
Wilking, B. A., Gagné, M., & Allen, L. E. 2008, in Handbook of Star Forming Regions, Volume II, ed. B. Reipurth, 5, 351
Wright, G. S., Rieke, G. H., Glasse, A., et al. 2023, PASP, 135, 048003
Yang, Y.-L., Green, J. D., Evans, N. J. I., et al. 2018, ApJ, 860, 174
Yıldız, U. A., Kristensen, L. E., van Dishoeck, E. F., et al. 2015, A&A, 576, A109

## Appendix A: Line detections

**Table A.1.** Line detections toward selected positions in the maps of low-mass protostars in Ophiuchus

| Lines | transition | GSS30-IRS 1 | | | ISO-Oph 21 | | | | | [GY92] 197 | | | | | | | | WL 17 | | | | | | | | ISO-Oph 137 | | | |
|---|---|---|---|---|---|---|---|---|---|---|---|---|---|---|---|---|---|---|---|---|---|---|---|---|---|---|---|---|---|
| | | A | B | C | A | B | C | D | E | A | B | C | D | E | F | G | H | A | B | C | D | E | F | G | H | A | B | C | D |
| $H_2$ S(1) | Iv0-J3-v0-J1 | - | - | + | + | + | + | + | + | + | + | + | + | + | + | + | + | + | + | + | + | + | + | + | + | - | + | - | + |
| $H_2$ S(2) | Iv0-J4-v0-J2 | - | - | + | + | + | + | + | + | + | + | + | + | + | + | + | + | + | + | + | + | + | + | + | + | + | + | + | + |
| $H_2$ S(3) | Iv0-J5-v0-J3 | + | + | + | - | - | - | - | - | + | + | + | + | + | + | + | + | + | + | + | + | + | + | + | + | + | + | + | + |
| $H_2$ S(4) | Iv0-J6-v0-J4 | + | + | + | - | - | - | - | - | + | + | + | + | + | + | + | + | + | + | + | + | + | + | + | + | + | + | + | + |
| $H_2$ S(5) | Iv0-J7-v0-J5 | + | + | + | - | - | - | - | - | + | + | + | + | + | + | + | + | + | + | + | + | + | + | + | + | + | + | + | + |
| $H_2$ S(6) | Iv0-J8-v0-J6 | + | + | + | - | - | - | - | - | + | + | + | + | + | + | + | + | + | + | + | + | + | + | + | + | + | + | + | + |
| $H_2$ S(7) | Iv0-J9-v0-J7 | + | + | + | - | - | - | - | - | + | + | + | + | + | + | + | + | + | + | + | + | + | + | + | + | + | + | + | + |
| $H_2$ S(8) | Iv0-J10-v0-J8 | + | + | + | - | - | - | - | - | + | + | + | + | + | - | - | - | + | + | + | + | + | + | + | + | - | + | - | + |
| [Ni II] 10.6 | $^4F_{9/2}$-$^4F_{7/2}$ | - | - | - | - | - | - | - | - | + | - | - | - | - | - | - | - | - | - | - | - | - | - | - | - | - | - | - | - |
| [Ni II] 6.63 | $^2D_{3/2}$-$^2D_{5/2}$ | + | + | + | - | - | - | - | - | + | - | - | - | - | - | - | - | - | - | - | - | - | - | - | - | - | - | - | + |
| [Ni II] 5.18 | $^3D_{5/2}$-$^2D_{3/2}$ | + | - | - | - | - | - | - | - | - | - | - | - | - | - | - | - | + | - | - | - | - | - | - | - | - | - | - | - |
| [Ni I] 14.8 | $^3D_3$-$^3D_2$ | - | - | - | - | - | - | - | - | + | - | - | - | - | - | - | - | - | - | - | - | - | - | - | - | - | - | - | - |
| [Ni I] 11.3 | $^3F_3$-$^3F_2$ | - | - | + | - | - | - | - | - | - | - | - | - | - | - | - | - | - | - | - | - | - | - | - | - | - | - | - | - |
| [Ni I] 5.89 | $^3D_1$-$^1D_2$ | - | + | - | - | - | - | - | - | - | - | - | - | - | - | - | - | - | - | - | - | - | - | - | - | - | - | - | - |
| [Fe II] 25.9 | $a^6D_{7/2}$-$a^6D_{9/2}$ | - | + | + | - | - | - | - | - | + | - | - | - | - | - | - | - | - | - | - | - | + | - | - | - | - | + | + | + |
| [Fe II] 22.9 | $a^4D_{7/2}$-$a^4D_{5/2}$ | - | - | - | - | - | - | - | - | - | - | - | - | - | - | - | - | - | - | - | - | - | - | - | - | - | + | - | - |
| [Fe II] 17.9 | $a^4F_{7/2}$-$a^4F_{9/2}$ | - | + | + | - | - | - | - | - | + | + | + | + | + | - | - | - | - | - | - | - | - | - | - | - | - | + | + | + |
| [Fe II] 6.72 | $a^4F_{9/2}$-$a^6D_{7/2}$ | + | - | - | - | - | - | - | - | + | - | - | - | - | - | - | - | - | - | - | - | - | - | - | - | - | - | - | - |
| [Fe II] 5.34 | $a^4F_{9/2}$-$a^6D_{9/2}$ | + | + | + | - | - | - | - | - | + | + | + | - | - | - | - | - | - | - | - | - | + | - | - | - | - | - | + | + |
| [Ne III] 15.5 | $^3P_2$-$^3P_1$ | - | - | - | - | - | - | - | - | + | + | + | + | + | - | - | - | - | - | + | - | - | - | - | - | - | - | - | - |
| [Ne II] 12.8 | $^2P_{3/2}$-$^2P_{1/2}$ | - | - | - | - | - | - | - | - | + | + | + | + | + | + | + | + | + | + | + | - | + | + | + | + | + | + | + | - |
| [S I] 25.2 | $3P_1$-$3P_2$ | - | + | + | - | - | - | - | - | - | - | - | - | + | - | - | - | - | - | - | - | + | + | + | - | + | + | + | + |
| [Co II] 25.6 | $a^5F_3$-$a^5F_2$ | - | + | - | - | - | - | - | - | - | + | - | - | - | - | - | - | - | - | - | - | - | - | - | - | - | - | - | - |
| [Co II] 14.7 | $a^5F_4$-$a^5F_5$ | - | - | - | - | - | - | - | - | - | - | - | - | - | - | - | - | - | - | + | - | - | - | - | - | - | - | - | - |
| [Ar II] 6.98 | $^2P1/2$-$^2P_{3/2}$ | - | + | - | - | - | - | - | - | + | + | + | + | + | - | - | - | - | - | + | - | - | - | - | - | - | - | - | - |
| [Ar III] 21.8 | $^3P_1$-$^3P_0$ | - | - | - | - | - | - | - | - | - | - | - | - | - | - | - | - | - | - | + | - | + | - | + | - | - | - | - | - |
| [Ar III] 8.99 | $^3P_1$-$^3P_2$ | - | - | - | - | - | - | - | - | - | - | - | - | - | - | - | - | - | - | - | - | - | - | - | + | - | - | - | - |

## Appendix B: Line fluxes

Table B.1 contains integrated line fluxes, corrected for the local extinction values, for all $H_2$ lines detected in each apertures of all sources in our sample. Table B.2 contains line integrated fluxes for all detected [Ne II], [Ne III], [Fe II] and [S I] transitions.

**Table B.1.** Integrated fluxes of $H_2$ lines in all sources and apertures, corrected for extinction

| Pos. | Integrated flux $\times 10^{-18}$ [W m$^{-2}$] | | | | | | | |
|---|---|---|---|---|---|---|---|---|
| | S(1) | S(2) | S(3) | S(4) | S(5) | S(6) | S(7) | S(8) |
| **GSS30-IRS 1** | | | | | | | | |
| A | – | – | 303.0 ± 73.0 | 50.2 ± 10.1 | 77.1 ± 15.6 | 10.9 ± 6.1 | 65.5 ± 9.0 | – |
| B | – | – | 6.8 ± 1.9 | 4.1 ± 1.3 | 19.5 ± 2.2 | 9.0 ± 1.7 | 15.3 ± 2.1 | – |
| C | 1.4 ± 0.3 | 1.6 ± 0.5 | 2.3 ± 0.6 | 2.4 ± 0.7 | 3.9 ± 0.7 | 2.1 ± 1.4 | 4.5 ± 1.2 | – |
| **ISO-Oph 21**[a] | | | | | | | | |
| A | 0.6 ± 0.1 | 0.9 ± 0.1 | – | – | – | – | – | – |
| B | 0.8 ± 0.1 | 1.1 ± 0.1 | – | – | – | – | – | – |
| C | 0.6 ± 0.1 | 1.1 ± 0.1 | – | – | – | – | – | – |
| D | 0.8 ± 0.1 | 1.1 ± 0.1 | – | – | – | – | – | – |
| E | 0.6 ± 0.1 | 1.1 ± 0.1 | – | – | – | – | – | – |
| **[GY92] 197** | | | | | | | | |
| A | 1.7 ± 0.1 | 2.4 ± 0.2 | 6.0 ± 0.5 | 1.8 ± 0.2 | 2.8 ± 0.2 | 0.7 ± 0.1 | 1.5 ± 0.2 | 0.3 ± 0.2 |
| B | 0.4 ± 0.1 | 0.6 ± 0.1 | 1.3 ± 0.2 | 0.6 ± 0.1 | 1.3 ± 0.1 | 0.5 ± 0.1 | 0.9 ± 0.2 | 0.2 ± 0.2 |
| C | 0.9 ± 0.1 | 1.3 ± 0.1 | 3.9 ± 0.4 | 1.5 ± 0.2 | 2.1 ± 0.2 | 0.8 ± 0.2 | 1.5 ± 0.2 | 0.5 ± 0.2 |
| D | 1.1 ± 0.1 | 1.9 ± 0.1 | 4.7 ± 0.4 | 1.9 ± 0.2 | 3.2 ± 0.2 | 1.2 ± 0.2 | 2.5 ± 0.3 | 0.8 ± 0.2 |
| E | 1.3 ± 0.3 | 2.4 ± 0.3 | 5.3 ± 0.5 | 1.5 ± 0.2 | 2.3 ± 0.2 | 0.6 ± 0.1 | 1.3 ± 0.2 | – |
| F | 0.4 ± 0.1 | 1.1 ± 0.1 | 1.7 ± 0.5 | 0.6 ± 0.2 | 1.4 ± 0.1 | 0.4 ± 0.1 | 1.0 ± 0.2 | – |
| G | 0.7 ± 0.1 | 1.6 ± 0.2 | 2.7 ± 0.5 | 1.0 ± 0.1 | 1.5 ± 0.2 | 0.4 ± 0.1 | 0.7 ± 0.1 | 0.1 ± 0.2 |
| H | 0.6 ± 0.1 | 1.1 ± 0.1 | 2.7 ± 0.4 | 0.7 ± 0.2 | 1.2 ± 0.1 | 0.2 ± 0.1 | 0.6 ± 0.2 | 0.2 ± 0.2 |
| **WL 17** | | | | | | | | |
| A | 0.6 ± 0.2 | 1.7 ± 0.2 | 3.5 ± 0.3 | 1.3 ± 0.1 | 2.3 ± 0.2 | 0.5 ± 0.1 | 1.4 ± 0.2 | 0.4 ± 0.1 |
| B | 0.5 ± 0.1 | 0.8 ± 0.1 | 2.4 ± 0.2 | 0.9 ± 0.1 | 1.8 ± 0.2 | 0.5 ± 0.1 | 1.2 ± 0.2 | 0.5 ± 0.2 |
| C | 0.6 ± 0.1 | 1.2 ± 0.1 | 4.1 ± 0.3 | 1.5 ± 0.1 | 3.1 ± 0.2 | 0.7 ± 0.1 | 2.0 ± 0.2 | 0.5 ± 0.1 |
| D | 0.6 ± 0.2 | 1.2 ± 0.2 | 3.2 ± 0.3 | 1.1 ± 0.1 | 2.6 ± 0.2 | 0.6 ± 0.1 | 1.8 ± 0.2 | 0.2 ± 0.1 |
| E | 0.8 ± 0.2 | 1.9 ± 0.2 | 3.5 ± 0.3 | 1.3 ± 0.1 | 2.1 ± 0.2 | 0.7 ± 0.1 | 1.6 ± 0.2 | 0.5 ± 0.1 |
| F | 0.5 ± 0.1 | 0.7 ± 0.1 | 1.2 ± 0.2 | 0.4 ± 0.1 | 0.8 ± 0.1 | 0.4 ± 0.2 | 1.3 ± 0.3 | 0.5 ± 0.3 |
| G | 0.5 ± 0.1 | 0.8 ± 0.1 | 2.3 ± 0.2 | 0.9 ± 0.1 | 2.2 ± 0.2 | 0.7 ± 0.1 | 1.1 ± 0.1 | 0.3 ± 0.1 |
| H | 0.5 ± 0.1 | 1.0 ± 0.1 | 2.1 ± 0.3 | 0.6 ± 0.1 | 1.1 ± 0.1 | 0.3 ± 0.1 | 0.6 ± 0.1 | 0.3 ± 0.1 |
| **ISO-Oph 137** | | | | | | | | |
| A | – | 21.3 ± 7.9 | 29.6 ± 5.9 | 5.0 ± 1.0 | 10.2 ± 1.1 | 2.5 ± 4.1 | 3.7 ± 2.3 | – |
| B | 0.5 ± 0.1 | 0.9 ± 0.2 | 2.1 ± 0.4 | 0.6 ± 0.2 | 1.2 ± 0.2 | 0.3 ± 0.2 | 1.2 ± 0.2 | 0.5 ± 0.2 |
| C | – | 6.6 ± 1.5 | 12.0 ± 2.0 | 3.0 ± 0.6 | 4.9 ± 0.8 | 1.5 ± 0.6 | 2.1 ± 1.1 | – |
| D | 0.4 ± 0.1 | 0.6 ± 0.1 | 1.5 ± 0.5 | 0.4 ± 0.1 | 0.9 ± 0.1 | 0.3 ± 0.1 | 0.9 ± 0.3 | 0.4 ± 0.3 |

**Notes.** [a] Values given for ISO-Oph 21 are uncorrected for extinction since the extinction value could not be estimated.

**Table B.2.** Integrated fluxes of detected Ne II, Ne III, Fe II, and S I lines in all sources and apertures, corrected for extinction

| Pos. | Integrated flux $\times 10^{-18}$ [W m$^{-2}$] | | | | | | | |
|---|---|---|---|---|---|---|---|---|
| | [Ne II] 12.8 $\mu$m | [Ne III] 15.5 $\mu$m | [Fe II] 5.34 $\mu$m | [Fe II]17.9 $\mu$m | [Fe II] 22.9 $\mu$m | [Fe II] 24.5 $\mu$m | [Fe II] 25.9 $\mu$m | [S I] 25.2 $\mu$m |
| **GSS30-IRS 1** | | | | | | | | |
| A | – | – | 15.6 ± 8.7 | – | – | – | – | – |
| B | 14.5 ± 4.2 | – | 8.7 ± 1.7 | 10.7 ± 3.4 | – | – | 26.3 ± 6.1 | – |
| C | 6.0 ± 2.5 | – | 8.9 ± 2.3 | 9.0 ± 0.9 | – | – | 32.4 ± 4.9 | – |
| **[GY92] 197** | | | | | | | | |
| A | 28.8 ± 1.7 | 1.8 ± 0.1 | 0.8 ± 0.1 | 2.3 ± 0.2 | – | – | 1.2 ± 0.3 | – |
| B | 3.9 ± 0.2 | 0.5 ± 0.04 | 0.5 ± 0.2 | 0.4 ± 0.04 | – | 0.2 ± 0.1 | 0.4 ± 0.4 | – |
| C | 3.5 ± 0.2 | 0.4 ± 0.05 | 0.5 ± 0.2 | 0.4 ± 0.04 | – | – | 0.3 ± 0.2 | – |
| D | 2.1 ± 0.2 | 0.2 ± 0.04 | – | 0.3 ± 0.04 | – | – | – | – |
| E | 10.0 ± 1.0 | 0.3 ± 0.1 | – | 0.5 ± 0.2 | – | – | – | 1.1 ± 0.4 |
| F | 0.7 ± 0.1 | – | – | – | – | – | – | – |
| G | 0.5 ± 0.1 | – | – | – | – | – | – | – |
| H | 0.3 ± 0.06 | – | – | – | – | – | – | – |
| **WL 17** | | | | | | | | |
| A | 1.2 ± 0.3 | – | – | – | – | – | – | – |
| B | 0.3 ± 0.05 | – | – | – | – | – | – | – |
| C | 0.1 ± 0.03 | 0.04 ± 0.02 | – | – | – | – | – | – |
| D | – | – | – | – | – | – | – | |
| E | 1.7 ± 0.2 | – | 0.3 ± 0.1 | – | – | – | – | – |
| F | 0.1 ± 0.08 | – | – | – | – | – | – | 0.3 ± 0.1 |
| G | 0.4 ± 0.06 | – | – | – | – | – | – | 0.5 ± 0.2 |
| H | 0.1 ± 0.04 | – | – | – | – | – | – | – |
| **ISO-Oph 137** | | | | | | | | |
| A | 4.3 ± 2.4 | – | – | – | – | – | – | 7.6 ± 2.5 |
| B | 0.3 ± 0.2 | – | – | 0.4 ± 0.1 | 0.4 ± 0.1 | – | – | 2.9 ± 0.6 |
| C | 5.5 ± 2.1 | – | 2.0 ± 0.7 | 7.0 ± 1.8 | – | – | 4.7 ± 1.9 | 8.0 ± 1.8 |
| D | – | – | 0.6 ± 0.2 | 0.9 ± 0.1 | – | – | 1.5 ± 0.3 | 0.2 ± 0.6 |

## Appendix C: Total mid-IR luminosities

Table C.1 shows the total mid-IR luminosities of $H_2$, [Fe II], [Ne II] and [S I], by summing up the intensities of all available transitions of each species in every given aperture. Values in parenthesis give the percentage of the total emission coming from each species.

**Table C.1.** Total mid-IR line luminosities for all detected $H_2$, Fe II, Ne II, and S I lines.

| Pos. | Line luminosities $\times 10^{-6}$ [$L_\odot$] | | | | |
|---|---|---|---|---|---|
| | $H_2$ | [Fe II] | [Ne II] | [S I] | Total |
| **GSS30-IRS 1** | | | | | |
| A | 294.04 (97.0%) | 9.05 (3.0%) | – | – | 303.09 |
| B | 31.74 (47.6%) | 26.52 (39.8%) | 8.41 (12.6%) | – | 66.67 |
| C | 10.56 (24.5%) | 29.19 (67.5%) | 3.48 (8.0%) | – | 43.23 |
| **[GY92] 197** | | | | | |
| A | 9.98 (34.2%) | 2.50 (8.5%) | 16.71 (57.2%) | – | 29.19 |
| B | 3.37 (51.8%) | 0.87 (13.4%) | 2.26 (34.8%) | – | 6.50 |
| C | 7.25 (72.6%) | 0.70 (7.0%) | 2.03 (20.3%) | – | 9.98 |
| D | 10.04 (87.8%) | 0.17 (1.5%) | 1.21 (10.6%) | – | 11.43 |
| E | 8.53 (55.9%) | 0.29 (1.9%) | 5.80 (38.0%) | 0.64 (4.2%) | 15.26 |
| F | 3.83 (90.3%) | – | 0.41 (9.7%) | – | 4.24 |
| G | 5.05 (94.6%) | – | 0.29 (5.4%) | – | 5.34 |
| H | 4.24 (96.1%) | – | 0.17 (3.9%) | – | 4.41 |
| **WL 17** | | | | | |
| A | 6.79 (90.7%) | – | 0.70 (9.3%) | – | 7.49 |
| B | 4.99 (96.7%) | – | 0.17 (3.3%) | – | 5.16 |
| C | 7.95 (99.3%) | – | 0.06 (0.7%) | – | 8.01 |
| D | 6.56 (100%) | – | – | – | 6.56 |
| E | 7.20 (86.1%) | 0.17 (2.0%) | 0.99 (11.8%) | – | 8.36 |
| F | 3.89 (94.4%) | – | 0.06 (1.5%) | 0.17 (4.1%) | 4.12 |
| G | 5.11 (90.8%) | – | 0.23 (4.1%) | 0.29 (5.1%) | 5.63 |
| H | 3.77 (98.4%) | – | 0.06 (1.6%) | – | 3.83 |
| **ISO-Oph 137** | | | | | |
| A | 41.96 (85.9%) | – | 2.50 (5.1%) | 4.41 (9.0%) | 48.86 |
| B | 4.24 (64.6%) | 0.46 (7.0%) | 0.17 (2.6%) | 1.68 (25.6%) | 6.56 |
| C | 17.47 (52.5%) | 7.95 (23.9%) | 3.19 (9.6%) | 4.64 (14.0%) | 33.25 |
| D | 3.13 (62.7%) | 1.74 (34.9%) | – | 0.12 (2.4%) | 4.99 |

# List of Figures


1.1 Illustration of the different evolutionary stages of a low-mass young stellar objects. Figure from Persson, 2014. . . . 3
1.2 Example spectral energy distributions of the four Classes of low-mass protostars. Figure from Persson, 2014. . . . 5
1.3 Illustration of the morphology of the cluster potential enabling the formation of massive stars in the competitive accretion scenario. Figure from Bonnell, Larson and Zinnecker, 2007. . . . 7
1.4 Illustration of the evolutionary scenario of high-mass stars. Image from Cormac Purcell. . . . 8
1.5 Example illustrating the classification of high-mass star forming regions. Panels on the left show three color images (red: ATLASGAL 870 $\mu$m, green: PACS 160 $\mu$m, blue: PACS 70 $\mu$m) of sources in each high-mass star formation class, while the corresponding SEDs are presented on the right. The Figure is taken from König et al., 2017. . . . 9
1.6 Qualitative illustration of the energy levels within a molecule. In order of increasing energy, molecular energy levels are divided into rotational, vibrational, and electronic. Figure taken from `https://commons.wikimedia.org/wiki/File:Molecular_energy_levels_en.svg` . . . 10
1.7 First detection of the L1551 outflow by Snell, Loren and Plambeck, 1980. The solid and dashed contours mark the blue- and red-shifted CO $J$ = 1-0 line emission respectively, overlaid on the continuum emission. . . . 14
1.8 Illustration of the outflow launching configuration predicted by the X-wind model (F. Shu et al., 1994). . . . 15
1.9 Illustration of the outflow structure as predicted by the disk-wind model (Pudritz and Norman, 1986). . . . 16
1.10 Illustration of the different components of a protostellar outflow. Background image is the jet of HH34 seen in H$\alpha$ emission (cyan) and [S II] (red). Figure from Bally, 2016. . . . 16
1.11 Example of outflow detections in the IR dark cloud G28.37+0.07 based on CO $J$=2-1 observations (Kong et al., 2019). . . . 18
1.12 The jet of HH212 as seen in SiO emission (green contours). The disk surrounding the protostar is also seen in the continuum emission. Figure from C.-F. Lee et al., 2017. . . . 19

1.13 Correlation of the outflow force with the envelope mass (left) and the bolometric luminosity (right) as presented by Bontemps, Andre et al., 1996. Empty circles mark Class 0 sources and filled circles Class I, while the dotted arrows mark model evolutionary tracks based on the model presented in the same work. . . . 21

1.14 The HH211 outflow as seen with JWST NIRCam. The different colors correspond to the different filters of NIRCam (Purple: F162M + F164N, Blue: F210M + F323N, Cyan: F335M, Green: F460M, Orange: F466N, Red: F470N). Figure taken from Ray et al., 2023. . . . . 23

1.15 Example two-component rotational diagram of the $H_2$ rotational transitions in the wavelength range of the MIRI/MRS on board the JWST. Figure by Tychoniec, van Gelder et al., 2024. . . . . 25

1.16 Example of the KP5 extinction curve between 5 and 20 $\mu$m. Marked in green are the locations of the pure rotational transitions of $H_2$ over the same range. . . . . 26

1.17 High velocity CO $J$ =2-1 emission from the prototypical explosive outflow BN/KL. Figure from Bally, Ginsburg, H. Arce et al., 2017. . . . . 27

1.18 Illustration of a two fluids shock for a range of magnetic field strengths. As the magnetic field becomes stronger (from top to bottom), the magnetic precursors becomes more significant, smoothening the transition between the pre- and post-shock regions, until the $J$-type shock is eventually converted into $C$-type. Figure taken from Draine, 2011. . . . . 28

1.19 The *Spitzer space telescope* view of the Cygnus-X molecular cloud complex. The 3.6-micron light is represented in blue color, the 4.5-micron light in blue-green, the 8.0-micron light in green, and the 24-micron light in red. Image credit: NASA/JPL-Caltech/Harvard-Smithsonian CfA, and Beerer et al., 2010. . . . . 30

1.20 Optical image of the $\rho$ Ophiuchus cloud complex and its surroundings. Adapted from (Wilking, Gagné and Allen, 2008), background image credit: Robert Gendler, Jim Misti, and Steve Mazlin. . . . . 31

2.1 Example of the three different emission morphologies seen among the different molecular tracers covered in the CASCADE range. The background emission is the 2.2 micron continuum emission from the United Kingdom Infra-Red Telescope (UKIRT) *Wide Field Camera* (WFCAM) probing shock excited $H_2$ emission from the outflow (Warren et al., 2007). The white contours mark the $5\sigma$ $HCO^+$ (left), $N_2H^+$ (middle) and SiO (right) emission, while intensities are integrated between -50 and 50, -20 and 10 ,and -20 and 20 km s$^{-1}$ for the $HCO^+$, $N_2H^+$ and SiO emission, respectively. Figure taken from Skretas, Karska, Wyrowski et al. (2023). 36

2.2 Contour of the redshifted (5 to 45 km s$^{-1}$) and blueshifted (-5 to -45 km s$^{-1}$) $HCO^+$ emission shown in red and blue respectively. The contours correspond to 5 $\sigma_{\rm rms}$ emission and the velocity ranges are given relative to the source velocity of -3 km s$^{-1}$. Background emission is the integrated $HCO^+$ emission from -50 to 50 km s$^{-1}$. Figure taken from Skretas, Karska, Wyrowski et al. (2023). . . . . 37

2.3 Distribution of gas velocities associated with the outflows in DR21 (left) and Orion KL (right, Bally, Ginsburg, H. Arce et al., 2017). Each point shows a local intensity peak of the $HCO^+$ emission (above 2 $\sigma$) integrated in velocity steps of 5 km $s^{-1}$. The color of the points signifies the corresponding velocity steps and are shared for the two plots. Background gray-scale shows the integrated $HCO^+$ (left panel) and CO emission (right panel) over the entire velocity range of the outflows (from −70 to 70 km $s^{-1}$ for DR21 Main and −100 to 100 km $s^{-1}$ for Orion KL). Figure taken from Skretas, Karska, Wyrowski et al. (2023). . . . . 38

2.4 [Left:] Zoom-in on the western lobe of the DR21 Main outflow, where it is interacting with a nearby dense molecular structure. Background grayscale shows the integrated $HCO^+$ emission, integrated between -50 and 50 km $s^{-1}$ relative to the source velocity. Red contours show line emission of $H_2CO$, blue contours show the emission of $N_2H^+$ and green contours show the emission of SiO. All contour levels are at 5, 10 and 20 $\sigma_{rms}$ of the corresponding emission. [Right:] Average integrated intensities of $HCO^+$ (in blue), $H_2CO$ (in red), and $N_2H^+$ (in green) across the interaction region in the western lobe of DR21. Intensities are integrated from -70 to 70, -20 to 20 and -20 to 10 km $s^{-1}$ for $HCO^+$, $H_2CO$ and $N_2H^+$, respectively. The x-axis shows the distance in arcseconds measured along the black lines shown in the left panel. The orange rectangle shows the area actively affected by the interaction and is also marked in the left panel. The intensities for $H_2CO$ and $N_2H^+$ are scaled up by a factor of 8 in order for their distributions to be more easily comparable to that of $HCO^+$. Figure adapted from Skretas, Karska, Wyrowski et al. (2023). . . . . 39

3.1 Combined NOEMA and GBT 3.6 mm continuum map of the DR21 filament region. Marked are the location of all dense clumps associated with the region (see Section 3.2.2). . . . . 44

3.2 Spectra of $HCO^+$ $J$=1-0 (blue) and $H^{13}CO^+$ $J$=1-0 (green) for clumps along DR21 Ridge: 5823, N55, N56, N44, N47 and N53. The spectra were averaged over the FWHM of the corresponding clumps (Table 3.2). Red and blue dashed lines mark the velocity range associated with outflow wing emission. The black dashed line marks the source velocity, $v_{source}$ = -3 km $s^{-1}$ for all sources except N56, which is located in a separate structure east of DR21, where $V_{source}$ = 18 km $s^{-1}$. . . . . 49

3.3 $HCO^+$ channel maps of the 3 different velocity components detected in the DR21 filament. The main component at -3 km $s^{-1}$ is shown on the left panel, the 9 km $s^{-1}$ component is shown in the middle, while the 18 km $s^{-1}$ component is on the right. The velocity width of the channels is 2.0 km $s^{-1}$. . . . . 50

3.4 Velocity-integrated maps of the red-shifted (red contours) and blue-shifted (blue contours) $HCO^+$ emission. Velocity ranges used for each source are given in table 3.3. Green contours show the integrated SiO intensity. The black cross and dashed circle indicate the location and size of the corresponding core (see Table 3.2). Orange and cyan arrows mark the most likely direction of the outflow, and the yellow star indicates the outflow origin. Finally, the grayscale background shows the 3.6 mm continuum from NOEMA and GBT. . . . . 51

3.5 Same as in Figure 3.4 . . . . . 52

3.6 Outflow mass over the envelope mass (left) and the bolometric luminosity (right) of the driving protostellar sources. Right facing triangles represent low-mass sources from Mottram et al. (2017), left facing triangles mark sources taken from Yıldız et al. (2015) and upwards are from van der Marel et al. (2013) while in blue are the Class I sources and in red the Class 0. Black diamonds mark intermediate mass sources (van Kempen, Hogerheijde et al., 2016), gray squares mark high-mass sources from Maud et al. (2015), green "×" mark high-mass sources from Beuther, Schilke et al. (2002), and orange stars mark the sources in the DR21 ridge (this work). The green star represents the DR21 Main outflow from Skretas, Karska, Wyrowski et al. (2023) and the dashed, black line shows the best fit to the outflow force - envelope mass correlation for all sources. The errorbars mark the possible variation of the outflow mass estimate due to the inclination correction factor. . . . . 57

3.7 Outflow mass rate versus envelope mass (left) and bolometric luminosity (right). The labels are the same as in Figure 3.6. . . . . 60

3.8 Outflow momentum versus envelope mass (left) and bolometric luminosity (right). The labels are the same as in Figure 3.6. . . . . 61

3.9 Outflow force versus envelope mass (left) and bolometric luminosity (right). The labels are the same as in Figure 3.6. . . . . 61

3.10 Outflow kinetic energy versus envelope mass (left) and bolometric luminosity (right). The labels are the same as in Figure 3.6. . . . . 62

3.11 Outflow kinetic luminosity versus envelope mass (left) and bolometric luminosity (right). The labels are the same as in Figure 3.6. . . . . 62

3.12 Outflow properties over source declination for all outflow sources in the sample. From top to bottom the outflow properties shown are: outflow mass (left) and outflow mass rate (right), outflow momentum (left) and outflow force (right), and outflow kinetic energy (left) and luminosity (right). Dashed lines mark the location of DR21 Main and DR21 (OH). The green square corresponds to the outflow of N56, which is located in a separate structure from the DR21 ridge. The errorbars mark the possible variation of the corresponding value due to the inclination correction factor. . . . . 65

3.13 Dynamical time over source declination for all outflows sources in the sample. The dynamical time shown here is the average between the dynamical times estimated for the two outflow lobes. Dashed lines mark the location of DR21 Main and DR21 (OH). The green square corresponds to the outflow of N56, which is located in a separate structure from the DR21 ridge. . . . . 66

3.14 $H_2$ column density map of the entire DR21 ridge from Marsh et al. (2017). Contour levels correspond to 2,3,5, and 10 $\sigma_{\rm rms}$ of the column density. Red stars mark the location of the most prominent outflow sources DR21 Main - N46, DR21 (OH)- N44, and N53. Red dotted lines mark the location of the accreting filaments, as identified by Hennemann et al. (2012). The saturated regions around DR21 Main and DR21 (OH) have been masked. . . . . 67

3.15 Orientation and extent of outflow lobes in the DR21 ridge. The colorscale of the lines corresponds to the maximum/minimum velocity measured for red and blueshifted lobes respectively. . . . . 68

3.16 Comparison of different outflow properties measured using the CASCADE $HCO^+$ observations (this work) and CO $J$ =3-2 observations taken with the SMA (Skretas and Kristensen, 2022). [Top]: Comparison between the outflow forces ($F$). [Left]: Maximum velocity ($v_{\rm max}$) in each lobe. [Right]: Radius of outflow lobes ($R_{\rm lobe}$). Square points, in top panel, represent values for the whole outflow, while circles and triangles, in the second and third panels correspond to the values of the blue- and red-shifted outflow lobes respectively. . . . . 69

4.1 Integrated emission of $H_2$ S(5) line at 6.91 $\mu$m toward GSS30-IRS 1, ISO-Oph 137, [GY92] 197, and WL 17. The positions of the protostars, measured from the line-free region at 6.9 $\mu$m, are shown with black stars. The red arrows shows the apparent outflow direction based on the $H_2$ emission. The black filled circle marks the spatial resolution of MIRI at $\lambda$ = 6.9 $\mu$m ($\sim 0.2''$). Figure from Skretas, Karska, Francis et al., 2025. . . . . 74

4.2 Example of $H_2$ rotational diagram for the outflow of WL 17. The extinction-corrected values are shown in red, and the ones before the correction in blue. The dashed and dotted lines mark the fits to the two gas components of the outflow (warm and hot respectively), while the black line marks the combined fit. Figure adapted from Skretas, Karska, Francis et al., 2025. . . . . 75

4.3 Distribution of the rotational temperatures of $H_2$ (top) and high-$J$ CO (bottom) in low-mass protostars. Temperatures in Class 0 protostars are shown in red, and in Class I sources in blue. The warm gas components is shown in stripped bins, and the hot one in clear bins. $H_2$ results for Class 0 protostars are adopted from Francis et al., 2025, and CO results for both Class 0 and I are from Karska, Kaufman et al., 2018. Figure taken from Skretas, Karska, Francis et al., 2025. . 76

4.4 Ratio of the S(2) over the S(7) transition of $H_2$ against the shock velocity for different UV field strengths. The $\log(n_H)$ ranges from 2 to 6 from top to bottom, while magnetic field strength is b = 0.1 for the left column and 1 for the right. For all panels $\zeta = 10^{-17}$ $s^{-1}$, and X(PAH)= $10^{-7}$ are used. The blue shaded region marks the observed range of S(2)/S(7) ratios for the sources in Ophiuchus, while the beige region marks the range for Class 0 sources from Francis et al., 2025. Note that line intensities from Kristensen, Godard et al., 2023 are not available for all combinations of model parameters covered in the figure. Figure taken from Skretas, Karska, Francis et al., 2025. . . . . 77

A.1 Spectra of $HCO^+$ $J = 1 - 0$ (blue) and $H^{13}CO^+$ $J = 1 - 0$ (green) for clumps N54, N52, and N51. The spectra were averaged over the FWHM of the corresponding clumps (Table 3.2). Red and blue dashed lines mark the velocity range associated with outflow wing emission. The black dashed line marks the source velocity, $v_{source}$ = -3 km $s^{-1}$ for all sources. . . . . 101

A.2 Spectra of $HCO^+$ $J = 1 - 0$ (blue) and $H^{13}CO^+$ $J = 1 - 0$ (green) for clumps N48, N46, N45, N43, N42, and N41. The spectra were averaged over the FWHM of the corresponding clumps (Table 3.2). Red and blue dashed lines mark the velocity range associated with outflow wing emission. The black dashed line marks the source velocity, $v_{source}$ = -3 km $s^{-1}$. . . . . 102

A.3 Spectra of $HCO^+$ $J = 1 - 0$ (blue) and $H^{13}CO^+$ $J = 1 - 0$ (green) for clumps N40, N39, N38, N37, N36, and N35. The spectra were averaged over the FWHM of the corresponding clumps (Table 3.2). Red and blue dashed lines mark the velocity range associated with outflow wing emission. The black dashed line marks the source velocity, $v_{source}$ = -3 km $s^{-1}$. . . . . 103

A.4 Spectra of $HCO^+$ $J = 1 - 0$ (blue) and $H^{13}CO^+$ $J = 1 - 0$ (green) for clumps N34, DR21-22, DR21-19, DR21-12, 7743, and 7189. The spectra were averaged over the FWHM of the corresponding clumps (Table 3.2). Red and blue dashed lines mark the velocity range associated with outflow wing emission. The black dashed line marks the source velocity, $v_{source}$ = -3 km $s^{-1}$. . . . . 104

A.5 Spectra of $HCO^+$ $J = 1 - 0$ (blue) and $H^{13}CO^+$ $J = 1 - 0$ (green) for clumps 2406, 3382, 2179, N50, N49, and N57. The spectra were averaged over the FWHM of the corresponding clumps (Table 3.2). Red and blue dashed lines mark the velocity range associated with outflow wing emission. The black dashed line marks the source velocity, $v_{source}$ = -3 km $s^{-1}$ except N57, which is located in a separate structure east of DR21, where $V_{source}$ = 18 km $s^{-1}$. . . . . 105

A.6 Same as in Fig. 3.4 but for sources with no clear outflow detection. . . . . 107

# List of Tables


1.1 Summary of the different criteria used in protostellar classification . . . . . 4
1.2 Spectroscopic designation of branches within ro-vibrational transitions . . . . . 12

3.1 Continuum and spectral line parameters for the lines studied in this work . . . . 43
3.2 Core properties for sources in the CASCADE field . . . . . 47
3.3 Outflow velocity ranges . . . . . 53
3.4 Inclination correction factors for the calculation of outflow forces using the Separation method . . . . . 56
3.5 Outflow properties . . . . . 59
3.6 Energy distances ($E_{\mathrm{dist}}$) and corresponding p-values for energy distance tests of the distributions of outflow parameters with respect to the source envelope mass 64
3.7 Energy distances ($E_{\mathrm{dist}}$) and corresponding p-values for energy distance tests of the distributions of outflow parameters with respect to the source bolometric luminosity . . . . . 66

A.1 Outflow force correlations best-fit results . . . . . 108
A.2 Outflow mass correlations best-fit results . . . . . 108
A.3 Outflow mass rate correlations best-fit results . . . . . 108
A.4 Outflow momentum correlations best-fit results . . . . . 109
A.5 Outflow kinetic energy correlations best-fit results . . . . . 109
A.6 Outflow kinetic luminosity correlations best-fit results . . . . . 109

# Acknowledgements

As I reach the end of my PhD journey, I feel the need to thank the many different people whose help was instrumental in its successful conclusion. First and foremost, I want thank the late Prof. Dr. Karl M. Menten, who offered me the opportunity to embark on this journey by inviting to do my PhD in his Millimeter and submillimeter Astronomy group at the Max Planck Institute for Radioastronomy. His sudden loss was strongly felt by all his students, but we will surely remember his wisdom and kindness fondly. Subsequently, I would like to thank Prof. Dr. Peter Schilke, for agreeing to succeed Karl as my primary supervisor, as well as, Prof. Dr. Amélie Saintonge for hosting me in her group for the final stretch of my PhD. In addition, I am grateful to Prof. Dr. Pavel Kroupa, Prof. Dr. Akaki Rusetsky, and Prof. Dr. Heiko Röglin for agreeing to participate in my thesis committee.

A very special thanks goes to Dr. Agata Karska and Dr. Friedrich Wyrowski, for their enormous help throughout my PhD work. Agata, I feel extremely fortunate that we met again in Bonn and had the opportunity to collaborate so closely over the past years. To everyone in the MPIfR, a massive thank you for all the help throughout my PhD, and for making the whole experience so much more enjoyable. A special mention of course needs to be made to all of my office-mates. Sharing the office with you guys was always a pleasure.

I am also grateful for all the friends I had the chance to meet over the years, both at the institute and outside of it. Thank you all for all the great times and the many board game sessions. Again, a special mention to my D&D crew. Thank you guys for letting me live out my fantasies, it was often a much needed distraction. I can promise that more adventures are coming in the future.

To my parents and siblings back in Greece, I will always be grateful for your support. It has always been crucial to allow me to complete this journey. Finally, Efi, thank you for embarking in this adventure with me, you have made it so much easier.

Cover page background image: The outflow of DR21 Main, as seen in the molecular hydrogen emission at 2.12 $\mu$m. The image was obtained using the Apache Point Observatory 3.5 meter telescope and NICFPS near-infrared camera using a 0.5 bandpass filter (PI: John Bally; published in Guzmán Ccolque, Fernández López et al., 2024).